**The Dissertation Committee for Kimberly Ann Homan Certifies that this is the approved version of the following dissertation:**

# Nanosystems for Combined Therapy and Imaging of Pancreatic Cancer

**Committee:**

Stanislav Emelianov, Co-Supervisor

Lisa Brannon-Peppas, Co-Supervisor

Konstantin Sokolov

Keith Stevenson

Richard Brown

James McGinity

James Tunnell

# Nanosystems for Combined Therapy and Imaging of Pancreatic Cancer

**by**

**Kimberly Ann Homan, B.S.Ch.E; M.S.E.**

**Dissertation**

Presented to the Faculty of the Graduate School of

The University of Texas at Austin

in Partial Fulfillment

of the Requirements

for the Degree of

**Doctor of Philosophy**

**The University of Texas at Austin**

**December 2010**

# Dedication

To my parents and husband.

For their love and never-ending support.

# Acknowledgements

I sincerely thank my advisors, Dr. Lisa Brannon-Peppas and Dr. Stas Emelianov, for their guidance and support during the course of my Ph.D. I am extremely grateful that both of you gave me a large creative license to explore my very varied and all-encompassing love of science and research. Furthermore, I am excited to continue pursuing ideas that we generated together over four years ago. Even more importantly, you served as excellent mentors and role models for balancing career objectives and family. I was truly lucky to have you both on my journey and I will take what I learned from you and make sure to mentor others with equal care and responsibility.

I am also grateful to my committee for their support over the last several years. First I would like to thank Dr. Brown. He was the first professor I met when being recruited to UT and he largely influenced my matriculation. His enthusiasm for science and music was inspiring then and remains so now. I will always appreciate his genuine nature, love for students, and grand ideas. Dr. Sokolov and his lab members have also been critical to me along the way. I learned many fine points of science and bioconjugation techniques from Dr. Sokolov, Tim Larson, Justina Tam, and Pratixa Joshi. I thank Dr. Tunnell for pioneering the laser-tissue interaction course that helped me understand nanoparticles in a new light. Moreover, many thanks to Dr. McGinity for his helpful discussions about drug-polymer interactions and to Dr. Stevenson who contributed significantly to my understanding of silver and its anisotropic shapes. Lastly, I would like to thank Dr. Nicolas Peppas. For several years I was invited to lab meetings with his group and I benefited greatly from that exposure. I learned a tremendous amount from Dr. Peppas, Dr. Fisher, Dr. Bayer, Maggie Phillips, Marty Gran, Dr. Marek, and

Brandon Slaughter. Furthermore, I am grateful for the loan of equipment from the Peppas lab that enabled completion of this thesis work.

I owe special thanks to my colleagues who have been by my side during the course of my studies. In particular, I would like to thank my graduate student mentors from both labs: Dr. Tania Betancourt, Dr. Amber Doiron, Dr. Jignesh Shah, and Dr. Valli Mallidi. So much of what I was able to accomplish was because you were willing to take the time to teach me important lab techniques and concepts. All of you are irreplaceable. Furthermore, in Stas' lab and the BME department there is no shortage of brilliant minds. I have had numerous important discussions with Dr. Iulia Graf, Dr. Frey, Alfred Song, Yun-Sheng Chen, Katie Wilson, Seungsoo Kim, Bo Wang, Geoff Luke, Mohammad Mehrmohammadi, and so many others. I must also thank Erika Cooley and Erin Baker. These two ladies stuck with me through some trying times over the last four years and their encouragement and support pulled me through.

I cannot write in words how fulfilling and important it was for me to work with undergraduates. Vanessa White, Uyai Umoren, Rohit Reddy, Sobeyda Gomez, Christopher Green, and Heidi Gensler were all there for me in the "science fiction" years. They really believed in the project, even when I was skeptical. In the later years, Adriane Schiano, Juan Pardo, Jeffrey Chen, Mike Souza, Ryan Truby, Mary Dockery, and Zachary Criss were instrumental in bringing the work past "science fiction" and into realistic published research. Working with all of you kept me on my toes the entire time and I was grateful to ride on the tails of your enthusiasm and curiosity. In particular, Christopher, Mike, and Ryan spent many years researching with me. I cannot thank each of you enough for your support, both personally and professionally.

Lastly, I must thank my family. I was blessed with parents who supported me no matter what I pursued in life. Their undying encouragement and support is the foundation

of any small success I have ever achieved. To my husband, I appreciate your patience and support through this process. Just knowing that you would be there, especially on my tough days meant everything to me.

**Nanosystems for Combined Therapy and Imaging of Pancreatic Cancer**

Publication No._____

Kimberly Ann Homan, Ph.D.

The University of Texas at Austin, 2010

Supervisors: Stanislav Emelianov and Lisa Brannon-Peppas

Pancreatic cancer remains a major unsolved health problem, with conventional cancer treatments having little impact on disease course. The objective of this thesis is to create innovative tools to better understand and improve chemotherapeutic treatment of pancreatic cancer. Towards this end, nanosystems were designed with a dual purpose: to carry chemotherapeutic drugs and act as photoacoustic imaging contrast agents. The overarching hypothesis is that these nanosystems can provide enhanced therapy for pancreatic cancer and enable visualization of drug delivery. Demonstrated in this dissertation is the design, synthesis, and characterization of two such nanosystems built to carry the chemotherapeutic agent gemcitabine while acting as a photoacoustic imaging contrast agent. The nanosystems were also shown to be multifunctional with possible application as photothermal therapy agents and cellular functional sensors. Although future research is required to fully investigate the clinical potential of these systems for pancreatic cancer, the work presented in this dissertation is a step towards creation of multifunctional nanosystems that will enable non-invasive, *in vivo* photoacoustic imaging of drug delivery.

# Table of Contents

List of Tables .....xv

List of Figures ..... xvi

Chapter 1: Introduction .....1

1.1 Pancreatic Cancer: Anatomy, Risk Factors, and Symptoms.....2

1.1.1 Current Treatment Strategies for Pancreatic Cancer .....3

1.1.2 Need for Imaging to Accurately Stage Pancreatic Cancer.....4

1.1.3 Endoscopic Ultrasound Imaging of Pancreatic Cancer .....8

1.2 Photoacoustic Imaging.....8

1.3 Nanosystems as Contrast Agents for Targeted Photoacoustic Imaging 11

1.4 Nanosystems as Combined Contrast Agents and Drug Delivery Vehicles .....13

1.5 Combined Endoscopic Ultrasound and Photoacoustic Imaging of Pancreatic Cancer .....16

1.6 Overall Research Goals.....17

1.7 References.....23

Chapter 2: Design of the Combined Imaging and Therapy Nanocage System (CIT-NS) .....31

2.1 CIT-NS Components .....32

2.1.1 Chemotherapeutic Drugs .....32

2.1.2 Poly(lactic-co-glycolic) Acid (PLGA).....33

2.1.3 Silver .....35

2.1.3.1 History of Silver as a Preservative.....37

2.1.3.2 History of Silver as a Therapeutic Agent.....38

2.1.3.3 Harmful Effects of Overexposure to Silver .....39

2.1.3.4 Cytotoxicity of Silver.....41

2.1.4 Exterior Coatings and Targeting Moieties .....42

2.2 Synergistic Aspects of the CIT-NS Design .....44

2.2.1 Combining the CIT-NS with Ultrasound.....44

2.2.2 Triggered Drug Release and other Photothermal Effects .....44
2.2.3 Silver Nanoparticles and Ionizing Radiation .....45
2.2.4 Biodegradation of the CIT-NS .....46
2.3 Limitations of the CIT-NS Design .....47
2.4 Conclusions .....48
2.5 References .....50

Chapter 3: Preliminary Testing of the CIT-NS design for enhancing PA Imaging58
3.1 Introduction .....58
3.2 Methods .....60
3.2.1 Coating Silica with a Porous Silver Layer .....60
3.2.2 Photoacoustic and Ultrasound Imaging of the Silver-Silica Nanosystem .....62
3.2.3 Preparing Samples of Set Concentrations of the Nanosystem for Imaging Studies .....63
3.2.4 Cytotoxicity Testing of the Nanosystem .....63
3.3 Results and Discussion .....65
3.3.1 The Silver-Silica Nanosystem .....65
3.3.2 Imaging of the Silver Nanosystem in Ex Vivo Pancreatic Tissue67
3.3.3 Imaging the Nanosystem Samples of Set Concentrations .....68
3.3.4 Cytotoxicity Tests Using the Silver-Silica Nanosystem .....70
3.4 Conclusions .....72
3.5 References .....80

Chapter 4: Synthesis and Characterization of the CIT-NS incorporating Doxorubicin .....83
4.1 Introduction .....83
4.2 Methods .....84
4.2.1 Materials .....84
4.2.2 Nanocage Synthesis with Doxorubicin .....85
4.2.3 Nanocage Characterization with Doxorubicin .....87
4.2.4 In Vitro DOX Release Studies .....87

4.2.5 Cytotoxicity Studies ..... 88
4.3 Results and Discussion ..... 91
4.3.1 CIT-NS incorporating Doxorubicin ..... 91
4.3.2 Doxorubicin Release Study ..... 93
4.3.3 Cytotoxicity Studies ..... 94
4.4 Conclusions ..... 95
4.5 References ..... 103
Chapter 5: Synthesis and Characterization of the CIT-NS incorporating Gemcitabine ..... 105
5.1 Introduction ..... 105
5.2 Methods ..... 106
5.2.1 Materials ..... 106
5.2.2 Gemcitabine Encapsulation in PLGA ..... 107
5.2.3 Synthesis of a Gemcitabine Prodrug ..... 108
5.2.4 Cytotoxicity Studies with the Gemcitabine Prodrug ..... 109
5.2.5 Gemcitabine Prodrug Encapsulation in PLGA ..... 110
5.3 Results and Discussion ..... 110
5.3.1 Gemcitabine loaded PLGA Microparticles ..... 111
5.3.2 Synthesis of a Gemcitabine Prodrug ..... 111
5.3.2.1 Synthesis and Characterization of Gemcitabine-$N^4$ Oleoyl Amide ..... 111
5.3.2.2 Failed Attempts to Synthesize Gemcitabine Prodrugs ..... 113
5.3.2.3 Gemcitabine-$N^4$ Oleoyl Amide Toxicity Compared to Native Gemcitabine ..... 116
5.3.3 Gemcitabine-$N^4$ Oleoyl Amide Encapsulation in PLGA ..... 117
5.4 Conclusions ..... 118
5.5 References ..... 128
Chapter 6: Design of the Combined Imaging and Therapy Nanoplate System (CIT-NpS) ..... 129
6.1 CIT-NpS Components ..... 129
6.2 Comparison of the CIT-NpS and the CIT-NS ..... 129

6.2.1 Optical Properties, Size, and Imaging Contrast .....129
6.2.2 Synthesis Techniques .....132
6.2.3 Drug Loading .....132
6.2.4 Stability .....133
6.3 Conclusions .....134
6.4 References .....136

Chapter 7: *In Vivo* Testing of the CIT-NpS Design for Enhanced Photoacoustic Imaging .....138
7.1 Introduction .....138
7.2 Methods .....140
7.2.1 Finite Difference Time Domain (FDTD) Modeling .....141
7.2.2 Silver Nanoplate Synthesis .....142
7.2.3 Silver Nanoplate Bioconjugation .....145
7.2.3.1 Antibody-Linker Synthesis .....145
7.2.3.2 Antibody and PEG Conjugation to Nanoplates .....146
7.2.4 *In Vitro* Characterization with Pancreatic Cancer Cells .....147
7.2.4.1 Cell Labeling .....147
7.2.4.2 Cytotoxicity .....148
7.2.5 Animal Model .....150
7.2.6 Biodistribution and Histology .....150
7.2.7 Combined Ultrasound and Photoacoustic (USPA) Imaging Set-up .....151
7.3 Results and Discussion .....152
7.3.1 FDTD Simulations of the Absorption and Scattering from Silver Nanoplates .....152
7.3.2 Silver Nanoplate “green” Synthesis and Bioconjugation .....153
7.3.3 *In Vitro* Characterization with Pancreatic Cancer Cells .....153
7.3.4 *In Vivo* Ultrasound and Photoacoustic (USPA) Imaging .....155
7.3.5 Biodistribution of Silver .....156
7.4 Conclusions .....157
7.5 References .....171

Chapter 8: Synthesis of the CIT-NpS and *In Vitro* Characterization.....174
8.1 Introduction.....174
8.2 Methods.....175
8.2.1 Gemcitabine-Thioamide Prodrug Synthesis and Characterization176
8.2.2 CIT-NpS Synthesis and Characterization .....177
8.2.3 *In Vitro* Characterization with Pancreatic Cancer Cells .....180
8.2.3.1 Cytotoxicity of the Gemcitabine-TA Prodrug .....181
8.2.3.2 CIT-NpS Therapeutic Efficacy and Cytotoxicity .....182
8.2.3.3 CIT-NpS Toxicity and Stability under Pulsed Laser Exposure .....182
8.2.3.4 CIT-NpS Toxicity under Continuous Wave Laser Exposure .....183
8.3 Results and Discussion .....183
8.3.1 Gemcitabine-TA Prodrug Synthesis and Characterization .....184
8.3.2 CIT-NpS Synthesis and Characterization .....185
8.3.3 Cytotoxicity of the Gemcitabine-TA Prodrug .....186
8.3.4 Therapeutic Efficacy of the CIT-NpS.....187
8.3.5 CIT-NpS Cytotoxicity under Pulsed Laser Exposure.....188
8.3.6 CIT-NpS Cytotoxicity under Continuous Wave Laser Exposure189
8.3.7 CIT-NpS Stability .....190
8.4 Conclusions.....193
8.5 References.....206

Chapter 9: Conclusions and Future Work.....208
9.1 Motivation.....208
9.2 The CIT-NS versus the CIT-NpS: Clinical Relevance .....209
9.2.1 Nanosystem Size and Drug Loading.....211
9.2.2 Triggered Drug Release .....211
9.2.3 Nanosystem Stability .....212
9.2.4 Silver versus Gold.....214
9.3 Future Directions for Nanosystems to Treat and Image Pancreatic Cancer .....215

9.4 Summary of Contributions to the Field .....216
9.5 References .....220
Bibliography .....222

# List of Tables

Table 1.1: A comparison of properties of currently available imaging technologies that compete with ultrasound and photoacoustic (USPA) imaging. .22

Table 7.1: Chart showing the growth solutions required for various growth stages of the stepwise nanoplate growth with their associated color changes and resulting longitudinal surface plasmon resonance (LSPR) peaks. Amounts of trisodium citrate (TSC) are from a 40 mM solution, and amounts of ascorbic acid (AA) are from a 40 mM solution. OD = optical density. .....159

Table 7.2: A comparison of absorbance cross section values for various nanoparticles at their longitudinal surface plasmon resonance. Data for the silver nanoplates and Au nanorods were simulated using FDTD modeling while data for the Au nanospheres and Au nanocages were previously reported.[12, 16, 22] .....161

Table 7.3: Size chart of Ag nanoplate edge length and thickness for each growth step along with the percent population of spheres grown alongside the nanoplates in each batch. .....163

# List of Figures

Figure 1.1: The anatomy of the pancreas as shown in relation to surrounding organs[97] (top) and in relation to its duct structure[98] (middle). Malignant tumor originating in the head of the pancreas[99] (bottom). .....19

Figure 1.2: EUS image of a pancreatic cancer (blue and yellow dotted lines show the extent of the tumor). EUS image provided by Dr. Jeffrey Lee, M.D. Anderson Cancer Center, Houston, TX. .....20

Figure 1.3: Optical absorption ($\mu_a$) or optical absorption plus scattering ($\mu_a + \mu_s$) for various absorbers in tissue ($HbO_2$ – oxygenated hemoglobin, Hb – deoxygenated hemoglobin). .....21

Figure 1.4: An illustration of how endoscopic ultrasound and photoacoustic (EUSPA) imaging would be implemented *in vivo*.....22

Figure 2.1: An illustration of the Combined Imaging and Therapy Nanocage System (CIT-NS) and its components. .....49

Figure 2.2: The chemical structure of poly(lactic-co-glycolic) acid where x represents the number of lactide units and y represents the number of glycolide units (x=y for the PLGA used in the CIT-NS).....49

Figure 3.1: An illustration of the Combined Imaging and Therapy Nanocage System (CIT-NS) and its components. .....73

Figure 3.2. Schematic of the combined ultrasound and photoacoustic (USPA) imaging system incorporating the array-based ultrasound transducer integrated with the fiber-optical light delivery system. .....74

Figure 3.3. Scanning electron micrograph (SEM) of the silver-silica nanosystem with silica core diameter of 180 nm (a), and corresponding coated 180 nm UV-vis spectrograph (b); a batch of sparsely coated 180 nm nanoparticles (c), and corresponding UV-vis spectrograph (d); a silver coated 520 nm silica core batch (d), and corresponding UV-vis spectrograph (e). All scale bars are 200 nm.....75

Figure 3.4. Ultrasound (a), photoacoustic (b), and combined (c) images of nanoparticles injected directly into an ex-vivo canine pancreas. All images were acquired from the same position as determined by the location of the ultrasound transducer. The images are 20 mm deep (y-axis) and 10.5 mm wide (x-axis).....76

Figure 3.5. Several views of a 3-D rendering of USPA imaging from the silver nanosystem injected directly into an ex-vivo canine pancreas. All images are 20 mm by 10.5 mm by 12 mm. For clarity, ultrasound signal from gelatin above the tissue was suppressed in these images.....77

Figure 3.6. Plot of fluence-normalized photoacoustic signal versus nanoparticle concentration for the four samples shown in the inset. Inset: photoacoustic images of gelatin phantom with PVA samples containing 0, $2\times10^7$, $2\times10^8$, $2\times10^9$ particles per ml from left to right where the white circle outlines the boundaries of the samples as determined by ultrasound imaging. All inset images are 12.5 mm by 10.5 mm. .....78

Figure 3.7. Cell viability data after 24 hr exposure to the silver-silica nanosystem at different concentrations in MDA-MB-231 cells (a) and MPanc96 cells (b).....79

Figure 4.1. An illustration of the Combined Imaging and Therapy Nanoplate System incorporating DOX. .....97
Figure 4.2. A schematic illustrating the steps required to synthesize the CIT-NS incorporating doxorubicin.....97
Figure 4.3. Doxorubicin loaded PLGA nanosphere (a) under scanning electron microscopy (b). .....98
Figure 4.4. Reaction schematic depicting how poly (vinyl alcohol) acts as a reducing agent in the presence of UV light (left). Scanning electron micrograph of silver seeded PLGA nanospheres (right). Scale bar is 200 nm. .....98
Figure 4.5. Different morphologies of the silver cage structure that was reduced on top of a PLGA core. .....99
Figure 4.6. The extinction spectrum of the tightly packed silver nanocages directly after synthesis.....99
Figure 4.7. A comparison of *in vitro* DOX release from DOX loaded PLGA nanospheres[1] (orange curve) versus DOX loaded PLGA nanospheres coated with a tightly packed silver nanocage (blue curve). .....100
Figure 4.8. Results of the MTT assay with four different conditions mixed in media relative to controls. Values lower than 1 indicate therapeutic efficacy (lower cell viability).....101

Figure 4.9. MDA-MB-231 breast cancer cells after 18 hr incubation with the CIT-NS incorporating DOX. (a) fluorescence image showing blue DAPI stained nuclei, (b) fluorescence image of the same cells in (a) showing red DOX flourescence, (c) a phase contrast image, and (d) a composite image of the three previous images showing purple nuclei – this indicates the co-location of DOX in the nucleus of these cells. Red DOX is also visible in the cytoplasm. All images are of the same FOV and the scale bars are all 20 μm.....102

Figure 5.1: An illustration of the desired Combined Imaging and Therapy Nanocage System (CIT-NS). .....120

Figure 5.2: The chemical structure of gemcitabine. In deoxycytidine the two fluorines circled in red are hydrogens.....120

Figure 5.3: A reaction schematic showing how Gemcitabine-$N^4$ Oleoyl Amide was synthesized. .....121

Figure 5.4: A schematic depicting the steps in the oil in water emulsion method required to encapsulate hydrophobic drugs in PLGA.....121

Figure 5.5: Gemcitabine loaded microparticles. Scale bar is 20 μm.....122

Figure 5.6: Progressive mass spectroscopy results as time continues in the reaction to form Gemcitabine-$N^4$ Oleoyl Amide. .....123

Figure 5.7: NMR of Gem (top) and the PD (bottom). The H shifts that are most noteworthy with the acylation of Gem are the CH6, CH5, and CH1 as labeled in blue, green, and purple, respectively. The PD spectrum shows major shifts in the doublet and triplet peaks associated with these positions, leaving no trace of Gem in the purified PD spectrum. ...124

Figure 5.8: MTS assay results showing the relative cell viability to control when L3.6pl pancreatic cancer cells were mixed with different concentrations of the native Gemcitabine (Gem) drug versus the Gemcitabine-$N^4$ Oleoyl Amide prodrug (PD). .....125

Figure 5.9: Gemcitabine loaded PLGA microparticles (left) and control PLGA nanoparticles with no drug loading (right).....126

Figure 5.10: Gemcitabine-$N^4$ Oleoyl Amide loaded PLGA microparticles. Scale bar is 2 μm. .....127

Figure 6.1: An illustration of the Combined Imaging and Therapy Nanoplate System (CIT-NpS) and its components. .....135

Figure 7.1: Surface grafting of directionally conjugated antibodies and PEG to the surface of silver nanoplates through thiol mediated chemistry. .....158

Figure 7.2: FDTD modeling of the extinction, scattering, and absorption cross-section for three silver triangular nanoplates of increasing edge length. 160

Figure 7.3: Silver nanoplates directly after step-wise growth adding edge length from S1 to S4 (a-d) with their corresponding extinction spectra (e) and color change in solution (f). Scale bars are 100 nm.....162

Figure 7.4: Darkfield microscopy of pancreatic cancer cells after incubation with no nanoplates (a), PEGylated nanoplates (b), and a-EGFR conjugated nanoplates (c). All scale bars are 20 μm. .....164

Figure 7.5: Results of the MTS assay for cell viability on three cell lines after incubation for 24 hr with a-EGFR conjugated Ag nanoplates at various concentrations. .....165

Figure 7.6: Blue circles highlight the position of the tumor in three different 2D cross-sectional planes *in vivo* prior to the silver nanoplate injection. Ultrasound (a-c) and photoacoustic images taken using 760 nm (d-f), 800 nm (g-i), and 900 nm (j-l) wavelengths of light are shown for each cross-section. All images are 17.5 mm by 10.5 mm. .....166

Figure 7.7: Ultrasound (a), photoacoustic (b-d), and combined PAUS (f-h) images of a 2D cross-section of the tumor at 5 hr post injection of a-EGFR and mPEG-SH conjugated Ag nanoplates. The tumor area is circled in blue. All images are 17.5 mm by 10.5 mm. (e) shows the optical extinction spectrum for the Ag nanoplates injected.....167

Figure 7.8: A 3D rendering of the entire mouse tumor and the accumulation of a-EGFR conjugated Ag nanoplates within the tumor volume. The image is 17.5 mm by 10.5mm by 12 mm. .....168

Figure 7.9: The biodistribution of silver in particular mouse organs 112 hr after silver nanoplate injection. Only ~15% of the initial injected dose was accounted for in all the organs tested.....169

Figure 7.10: Histological slices of the tumor stained with silver stain and hematoxylin (a) and nuclear fast red (b). The scale bar in (a) is 1 mm; scale bar in (b) is 200 μm.....170

Figure 8.1: Reaction scheme for thiolating Gemcitabine to create Gemcitabine-Thioamide (Gem-TA). .....194

Figure 8.2: Mass Spectroscopy results showing formation of the Gem-ATA prodrug. The large peaks at 496.25 and 518.17 m/z are unreacted Gem and SATA flying as one charged mass with either $H^+$ or $Na^+$. .....195

Figure 8.3: NMR of Gem (top) and the Gem-ATA prodrug (bottom). The H shifts that are most noteworthy for Gem-ATA formation are the CH6, CH5, and CH1 as labeled in blue, green, and purple, respectively. The Gem-ATA spectrum shows major shifts in the doublet peaks associated with the CH6 and CH5 hydrogens. The CH1 position shows two overlaid triplets in the Gem-ATA spectra showing that both Gem-ATA and Gem are both present in the sample.....196

Figure 8.4: UV-vis spectrographs showing (a) the difference in the supernatant after conjugation to Ag nanoplates for a Gem-ATA reaction staged with HA and without HA, and (b) Ag nanoplates after conjugation of antibodies and Gem-TA prodrugs. .....197

Figure 8.5: Energy-dispersive X-ray spectroscopy results captured using a scanning transmission electron microscope showing a silver nanoplate (a) with an elemental map of the elements Ag (b), F (c), and S (d). The coregistry of F and S with the location of the silver nanoplate in the image shows that Gem-TA is attached to the silver nanoplate.....198

Figure 8.6: X-ray photoelectron spectroscopy results showing the detection of F 1s at a binding energy of 688 eV on the surface of a silver nanoplate sample conjugated to Gem-TA. .....199

Figure 8.7: A comparison of L3.6pl cell viability after 48 hr of incubation with various concentrations of Gem and Gem-TA in their media. .....200

Figure 8.8: A comparison of L3.6pl cell viability after 48 hr of incubation with various drug concentrations either attached to silver nanoplates (Ag-Gem-TA) or free (Gem-TA) in the media. .....201

Figure 8.9: A comparison of L3.6pl cell viability after 1000 laser pulses at various light fluences. Cell viability was measured 48 hr after pulsed laser exposure for cells mixed with nanoplates conjugated to EGFR (Ag-EGFR) or nanoplates conjugated to EGFR and Gem-TA (Ag-EGFR-Gem-TA, 300 nM Gem-TA). The concentration of Ag nanoplates was kept constant for each condition at $1.5x10^{11}$ nanoplates per ml of media. .....202

Figure 8.10: Cell viability results for L3.6pl cells mixed with EGFR conjugated silver nanoplates ($1.5x10^{11}$ nanoplates per ml of media) at 48 hr after exposure to a continuous wave laser operating at 1.3 $W/cm^2$ for various times. .....203

Figure 8.11: High-resolution transmission electron microscope of one Ag nanoplate (a) and its corresponding diffraction pattern (b). .....204

Figure 8.12: Ultra-violet to visible (UV-vis) spectrophotometry results depicting various aspects of silver nanoplate stability with either time or pulsed laser exposure. The UV-vis with time for drug loaded (a) versus non-drug loaded nanoplates (b) kept in media at 37°C for 96 hr; the UV-vis with time for non-drug loaded, but EGFR conjugated nanoplates mixed with either L3.6pl cells (c) or HPNE cells (d); the UV-vis directly after 1000 laser pulses at various fluences for two sizes of nanoplates conjugated only to PEG (e and f).....205

Figure 9.1: Energy-dispersive X-ray spectroscopy results captured using a scanning transmission electron microscope showing a silica-coated silver nanoplate (a) with an elemental map of the elements Si (b) and Ag (c). The coregistry of Si and Ag with the location of the silver nanoplate in the image shows that Gem-TA is attached to the silver nanoplate. 218

Figure 9.2: Finite difference time domain (FDTD) modeling of the extinction, scattering, and absorption cross-sections for 90x12 nanoplates (a), 128x12 nanoplates (b), and 218x12 nanoplates (c) for silver and gold. .....219

# Chapter 1: Introduction

Pancreatic cancer remains a major unsolved health problem, with conventional cancer treatments having little impact on disease course. In 2010 an estimated 43,100 people will be diagnosed with pancreatic cancer.[1] Tragically, 36,800 people are expected to die from pancreatic adenocarcinoma in 2010, putting the yearly death rate painfully close to its incidence.[1, 2] In the United States, for men and women alike, pancreatic cancer represents the 4$^{th}$ leading cause of cancer-related deaths.[2] In fact, for all stages of pancreatic cancer combined, the 5 year survival rate remains at a low 5%, making it arguably the most lethal of all solid tumors.[3] In addition, the number of patients diagnosed with pancreatic cancer each year is rising;[4] this increase is in contrast to other diseases such as colorectal cancer, where a decrease in incidences can be attributed to investments in early detection.[5] It is clear that novel treatment and early detection methods are needed for pancreatic cancer.

The overarching hypothesis of this work is that nanosystems designed to be dual drug delivery and imaging contrast vehicles can provide enhanced therapy for pancreatic cancer and enable visualization of that drug delivery. The nanosystems that are designed, synthesized, and discussed in this dissertation are novel and patented.[6] Throughout this work, the prospect of using these nanosystems in conjunction with photoacoustic imaging techniques in pre-clinical settings is evaluated.

This introductory chapter outlines the current clinical treatment and imaging strategies for pancreatic cancer, introduces how nanotechnology can be incorporated with existing and future treatment and imaging techniques, and finally provides overall research goals for this dissertation.

## 1.1 Pancreatic Cancer: Anatomy, Risk Factors, and Symptoms

The pancreas is a gland that serves two main functions: it produces hormones, such as insulin, which are needed to use or store energy coming from food; and it produces enzymes, specifically digestive enzymes that are released through a system of ducts to the duodenum (the first part of the small intestine). As shown in Fig. 1.1, the pancreas is shaped like a six-inch long flat pear where its widest section represents the head, the middle is the body, and the thinnest section is the tail. The majority of pancreatic adenocarcinomas are 3 cm in diameter upon diagnosis[7] and present in the head of the pancreas.

Currently no routine screening for pancreatic cancer is performed in the United States, although several risk factors have been identified.[8] As with many cancers, smoking and age are the major risk factors, with pancreatic cancer being much more likely after 60 years of age. Furthermore, race is a factor. Pancreatic cancer is more prevalent in the African American population than the white population; however, some of this increased risk may be due to socioeconomic factors and to cigarette smoking. Diseases involving the pancreas such as chronic pancreatitis and diabetes are also risk factors. Interestingly, patients who have had a partial gastrectomy (part of their stomach removed) are also at increased risk. Additionally, as many as 10% of pancreatic cancers may be related to inherited DNA mutations. Finally, diets high in meats, fried foods, and nitrosamines increase the risk for this cancer; while diets high in fruits and vegetables decrease the risk.

Generally, pancreatic cancer symptoms do not present until late stages of disease progression. These symptoms are ambiguous at first and include weight loss, fatigue, loss of appetite, etc. Unfortunately, most often it is not until patients present with symptoms of jaundice that clinicians are generally triggered to check for pancreatic cancer. By this

time, only 10% of diagnosed patients have a localized tumor.[9] The other 30-40% of patients have locally advanced disease progression, and the remaining 50-60% have a metastatic form.[9]

### 1.1.1 Current Treatment Strategies for Pancreatic Cancer

Generally, treatment options for pancreatic cancer are surgery, chemotherapy, and radiation. In the following paragraphs each treatment option is presented in detail.

*Surgery.* Today surgical resection of pancreatic cancer offers the best chance for survival.[10] Sadly, only 10% of patients diagnosed with localized pancreatic tumors are candidates for this procedure.[11] Thus for the majority of patients who are diagnosed with inoperable tumors due to a locally advanced or metastic form of this disease, treatment options include chemotherapy followed by or in conjunction with radiation, if the patient is fit.[11] Unfortunately, these treatment options only extend the 3-10 month median survival range[12] by a few months. In some cases chemotherapy is used to shrink pancreatic tumors to an operable size,[13] and this neoadjuvant therapy has met with success in select cases.

*Chemotherapy.* Pancreatic carcinoma is inherently resistant to chemotherapeutic regimens, either alone or in combinations. The most effective drugs that have formed the basis of chemotherapeutic treatment for pancreatic cancer have been 5-fluorouracil (5-FU) and the more recently approved gemcitabine.[3] Current studies focus on biologic agents, such as antagonists to the epidermal growth factor receptor (EGFR), farnesyl transferase inhibitors, and antiangiogenic agents, and on newer chemotherapeutics. As with most chemotherapeutic regimens, treatment involves systemic intravenous injections. The concentrations of gemcitabine used per session is dose-limited by its cytotoxic effect on healthy bone marrow and epithelial tissue.[14] Some hypothesize that

the systemic approach is ineffective for most patients because drug concentrations accumulated within the tumor itself are not high enough to realize their estimated therapeutic potential.[15] In response to this issue several solutions have surfaced. A few groups have studied the use of endoscopic ultrasound guided fine needle injections of immunotherapies or tumor necrosis factors with gemcitabine directly into inoperable pancreatic tumors.[16] Shrinkage of the tumor to the point of resection was observed in 14% of patients in one cross-sectional study.[17] Other groups are employing different strategies altogether, such as gene therapy.[18-20] Yet another strategy involves encapsulation of a gemcitabine prodrug in liposomes[21] for targeted delivery strategies in the future.[22]

*Radiation therapy.* The third conventional treatment, radiation therapy (or external beam therapy) has little impact on pancreatic carcinoma. Some advocate combining radiation therapy with the radiosensitizing agents and 5-FU or gemcitabine.[23] A number of major oncologic centers recommend using neoadjuvant chemoradiation therapy for either all patients with potentially operable disease or for patients with locally advanced disease. After finishing this therapy, the patient is restaged, and if the disease still appears resectable, pancreatic resection is undertaken.[10] Some institutions use neoadjuvant chemotherapy and radiation therapy to try to improve the resectability potential of locally advanced cancers. Early results are promising[10]; however, no prospective, randomized, controlled trials have been conducted to offer support for this approach.

### 1.1.2 Need for Imaging to Accurately Stage Pancreatic Cancer

Diagnosis of pancreatic cancer in late developmental phases is very common as early-stage symptoms do not univocally indicate the cause. Since resection is the

preferred first treatment strategy, imaging for staging purposes is equally critical. A number of continually evolving imaging modalities are available to help diagnose pancreatic carcinoma in patients in whom the disease is suggested clinically. These include computed tomography (CT), transcutaneous ultrasonography (TUS), endoscopic ultrasonography (EUS), magnetic resonance imaging (MRI), and positron emission tomography (PET).[24]

*Computed tomography (CT)*. Because of its ubiquitous availability and ability to image the whole abdomen and pelvis, abdominal CT scanning is usually the mainstay of initial diagnostic modalities used for assessing patients suspected to have pancreatic carcinoma. The quality of CT scanners has been rapidly evolving. Unfortunately, 40-50% of tumors smaller than 3 cm are missed, and these are the tumors most likely to be resectable. Newer models using spiral (i.e., helical) CT scanning with multiple detectors and dual-phase contrast enhancement have significantly improved the sensitivity and specificity of abdominal CT findings in patients with pancreatic carcinoma. Dual-phase spiral CT findings are approximately 80% accurate for helping determine the resectability potential of pancreatic carcinoma. However, small tumors can still be missed even with the most advanced CT scanning currently available.[24]

*Transcutaneous ultrasonography (TUS).* Even though it is less expensive and generally more readily available than CT scanning, TUS has less utility in pancreatic carcinoma than CT scanning because the pancreas is often obscured by overlying gas. Additionally, the depth of the pancreas from the abdominal wall limits transcutaneous ultrasonic imaging to lower frequency (2-5 MHz), and thus, a lower-resolution ultrasonographic image is obtained. Therefore, TUS can help detect only 60-70% of pancreatic carcinomas, and similar to CT scanning, more than 40% of the lesions smaller than 3 cm are missed. TUS is very useful as an initial screening test in evaluating

patients who present with possible obstructive jaundice. By helping to detect intrahepatic or extrahepatic bile duct dilation, abdominal ultrasonography can help rapidly and accurately assess whether or not a patient has a biliary obstruction. However, other studies, such as abdominal CT scanning, EUS, or magnetic resonance cholangiopancreatography (MRCP), usually should then be performed to definitively diagnose the source of biliary obstruction.

*Endoscopic ultrasonography (EUS).* EUS obviates the physical limitations of TUS by placing a high-frequency ultrasonographic transducer on an endoscope, which is then positioned in the stomach or duodenum endoscopically to help visualize the head, body, and tail of the pancreas. Additionally, because of the proximity of the pancreas to the EUS transducer, high-frequency ultrasonography (7.5-12 MHz) can be used to produce very high-resolution (submillimeter) images. Where EUS is available, it has proven to be the most sensitive and specific diagnostic test for pancreatic cancer. In numerous series, EUS has detection rates of 99-100% for all pancreatic carcinomas, including those smaller than 3 cm. EUS is accurate for assessing the etiology of obstructive jaundice. An additional significant diagnostic advantage is EUS-guided fine-needle aspiration, which allows for the simultaneous cytologic confirmation of pancreatic carcinoma at the time of EUS diagnosis. EUS appears to be equivalent to dual-phase spiral CT scanning for assessing tumor resectability potential.

*Magnetic resonance imaging (MRI).* The role of MRI in pancreatic cancer has been less well studied than the role of CT scanning. It does not appear to be superior to spiral CT scanning. Because of the difficulty of working within intense magnetic fields, MRI is limited by the inability to perform MRI-directed needle aspirations; however, this technology is undergoing rapid change.

*Positron emission tomography (PET).* PET scanning uses 18F-fluorodeoxyglucose (FDG) to image both the primary tumor and metastatic disease. PET scanning can be especially useful in looking for occult metastatic disease. Its role in pancreatic cancer evaluation management is still under investigation. False-positive PET scans have been reported in patients with pancreatitis.[25]

A combination of imaging techniques are generally used to identify, visualize, and stage pancreatic cancer. Details of imaging and staging procedures are given below.

*Imaging procedure.* Most patients suspected of having pancreatic carcinoma are initially studied with TUS and/or spiral CT. If patients have obvious hepatic metastatic disease based on initial TUS or CT findings, they undergo an image-guided biopsy of one of the liver metastases and then proceed to palliative therapy. Patients with a suggested or definite pancreatic mass or those who are still considered to have pancreatic cancer but do not have an obvious pancreatic mass need to have more definitive imaging studies. These studies are most commonly done using endoscopic ultrasonography – EUS plays a central role in the definitive diagnosis and staging of patients with pancreatic carcinoma. If a pancreatic mass is observed on EUS images, the patient is staged using EUS to determine resectability potential. Patients thought to have resectable tumors based on EUS findings proceed directly to operative intervention. If tumors are deemed unresectable based on EUS findings, the patients proceed directly to chemotherapy, radiation therapy, or both.

***Staging:*** Once an imaging modality has helped establish a probable diagnosis of pancreatic cancer, the next issue is whether the lesion is amenable to surgical resection. Only 10% of all patients presenting with pancreatic cancer are ultimately found to have easily resectable tumors with no evidence of local advancement. No survival benefit is achieved for patients undergoing noncurative resections for pancreatic carcinoma. Thus,

to avoid operating on patients who cannot benefit from the operation, accurate preoperative staging is very important. Despite our best efforts, however, thousands of patients who were thought to be candidates for pancreatectomy, based on imaging results, were discovered to have unresectable tumors at surgery. Therefore, improving imaging of tumors is critical for clinicians to more accurately assess patient treatment options.

### 1.1.3 Endoscopic Ultrasound Imaging of Pancreatic Cancer

In most clinics a combination of imaging techniques are currently used to diagnose and stage pancreatic cancer. One preferred combination uses CT[7] to detect the presence of a pancreatic cancer mass, and EUS to find and stage small lesions.[26, 27] In fact, the role of EUS imaging for pancreatic cancer has increased dramatically in recent years due to its high sensitivity and ability to detect lesions as small as 2-3 mm.[27] Although EUS shows promise, the images produced by this modality remain difficult to read (Fig 1.2). In fact, only endosonographers who have completed over 100 examinations are generally trusted to stage pancreatic cancer using EUS.[28] EUS has only 70-80% accuracy for correctly staging pancreatic carcinoma.

Despite its limitations, EUS is a currently well-characterized and trusted clinical imaging modality. Part of our overall research goals is to further improve EUS by combining endoscopic ultrasound and photoacoustic (EUSPA) imaging to enhance imaging contrast which will improve tumor staging accuracy, and ultimately increase resectability prediction rates.

## 1.2 PHOTOACOUSTIC IMAGING

EUS currently uses the acoustic contrast between normal and abnormal tissue to differentiate between cancerous and normal masses. Optical absorption of tissue is another possible contrast mechanism to detect and stage pancreatic cancer. Malignant

tumors are associated with higher blood content due to enhanced microvascularization inside or around the tumor.[29-32] The absorption coefficient of blood equals approximately 1 to 10 $cm^{-1}$ in the near-infrared spectral range depending on laser wavelength and the level of oxygen saturation in hemoglobin, while background absorption is only about 0.03-0.05 $cm^{-1}$ in normal tissue.[33, 34] The increased concentration of strongly absorbing molecules (hemoglobin and other porphyrins) was shown to yield 2-8 fold optical contrast between tumors and normal tissues.[35] Furthermore, malignant tumors have enhanced and noticeably hypoxic blood content.[33, 34] In contrast, benign tumors have a normal level of blood oxygenation.[36, 37]

Therefore, a technique for remote measurements of tissue optical absorption would be an optimal method for staging pancreatic tumors. Such a technique – named photo/opto/thermo-acoustic imaging – exists, and aims to remotely estimate the optical properties of tissue at high spatial and temporal resolution.[38] Photoacoustic imaging was introduced for use in biomedical applications by Oraevsky[39-42] and Kruger[43-45] and then further developed by Wang[46, 47] and others. Now, photoacoustic imaging applications range from microscopy to whole organ imaging.[48]

During photoacoustic imaging the tissue is irradiated with short (5-10 ns) pulses of low energy laser light. The 15-20 $mJ/cm^2$ laser fluence of near-infrared irradiation is sufficient to deliver optical energy to the pancreas and adjacent tissue – this laser fluence is well within the safe level of laser irradiation of tissue defined by the American National Standards and FDA.[49] Therefore, a photoacoustic level of pulsed laser energy will not produce any thermal damage to the tissue, and will result in a negligible temperature increase.[50, 51] Next, through the processes of optical absorption followed by thermoelastic expansion, broadband acoustic waves are generated within the irradiated volume. Using an ultrasound detector, these waves can be detected and spatially resolved.

The received ultrasound signal contains information about both position (time of flight) and strength of the optical absorber (amplitude of the photoacoustic signal).

The amplitude of the thermoelastic response of the tissue is proportional to the optical absorption, i.e., the stronger the absorption, the stronger the signal. Putting these qualitative statements in terms of a mathematical expression, the change in acoustic pressure associated with the generation of photoacoustic pressure transients ($\Delta P$) is equal to the Grüneisen parameter $\Gamma$ (a dimensionless, temperature dependant factor representing the fraction of thermal energy converted into mechanical stress by the absorber) times the incident laser fluence ($H$) and the absorber's absorption coefficient ($\mu_a$), yielding the simplified expression[40, 52]:

$$\Delta P = \Gamma H \mu_a \tag{1}$$

Equation (1) is valid only if the stress confinement condition is met, that is, if the heat diffusion time ($\tau_D$) is significantly shorter than the stress relaxation time ($\tau_{SR}$), i.e., the time for the acoustic waves to propagate through the irradiated volume. This condition limits the duration of the laser pulse ($\tau_L$), implying that it must also be much shorter than the stress relaxation time. When the stress confinement condition is met, the input laser energy generates photoacoustic pressure with the greatest efficiency.

Therefore, contrast in photoacoustic imaging is primarily determined by the $\mu_a$ of tissue components, most of which are shown in Fig. 1.3. For pancreatic cancer imaging, the contrast mechanism in photoacoustic imaging offers the prospect of identifying both anatomical features and different functional activities of the pancreas that are indistinguishable using other imaging modalities such as ultrasound, MRI, PET or CT/X-ray alone.

The measurements of intrinsic optical properties of the pancreas and other relevant tissues are limited, quite variable and offer only an approximate guide to the optical behavior of tissues. However, several observations can be made from the typical absorption spectrum of tissue. In the near-infrared (2000-3000 nm) region, water is the dominant absorber; the light penetration depth (the distance through tissue over which diffuse light decreases in fluence to 1/e or 37% of its initial value) varies from about 1 mm to 0.1 mm. In the ultraviolet region near and below 300 nm, the absorption depth is shallow, owing to absorption by cellular macromolecules. In the central region as shown in Fig. 1.3, tissue absorption is modest while contrast between tissue components remains high. Within 750-1300 nm wavelengths, the average optical penetration depth is on the order of tens of millimeters – therefore, this spectral range is very suitable for photoacoustic imaging of the pancreas.

A simple form of photoacoustic imaging (i.e., without contrast agents) may already discriminate between cancer cells and surrounding healthy tissue by discriminating hypoxic regions in the pancreas. However, by using near infrared (NIR) laser light (700-1300 nm) and a targeted NIR absorbing nanosystem delivered to the tumor, the photoacoustic response will be further enhanced because healthy tissue will not absorb the NIR light strongly nor will they have any significant concentration of the absorber (nanoparticles). In contrast, nanoparticles accumulated in the tumor will efficiently convert light energy into acoustic pressure waves that can provide a large photoacoustic signal against the tissue background.

## 1.3 NANOSYSTEMS AS CONTRAST AGENTS FOR TARGETED PHOTOACOUSTIC IMAGING

A variety of metal nanoparticles including gold or silver nanospheres, rods, shells and crescents can be used as photoabsorbers (exogenous contrast agents).[53-56] Compared

to conventional dyes such as indocyanine green, the absorption cross-section of metal nanoparticles can be six orders of magnitude higher,[57] thus making them effective absorbers for photoacoustic imaging. In addition, gold and silver nanoparticles are nontoxic in certain formulations and have already been used in biological and some clinical applications.[58-62] Mono-disperse metal nanoshells, for instance, are easy to synthesize, and their peak optical absorption can be synthetically tuned from 700 nm to 1100 nm where light penetration in tissue is optimal.[63] Indeed, by varying the shape and aspect ratio of nanostructures, the particles can be manufactured to absorb light at a desired wavelength across a wide spectrum including the near infrared spectrum.[64, 65]

These nanoparticles can be administered intravenously and blood circulation transports them to the region of interest. When injected into the blood stream, hydrophobic particles get coated by plasma proteins and are rapidly removed from the circulation by the reticuloendothelial system. However, by grafting hydrophilic polymer chains such as polyethylene glycol (PEG), immunogenic responses can be suppressed and blood circulation time of the nanoparticles can be improved.[66, 67] It has been demonstrated that small particles extravasate and accumulate in tumors due to the enhanced permeability and retention effect.[68, 69] This effect is caused by the leaky nature of tumor vessels. Thus, by an injection of correctly sized photoabsorbers (metal nanoparticle contrast agents), passive accumulation in tumors can be achieved. Furthermore, the metal nanoparticles can be made tumor specific by bioconjugating them with monoclonal antibodies, antibody fragments, folates, aptamers, or integrins whose receptors on the surface of cancer cells are upregulated. These targeting moieties can be attached either directly to the nanoparticles or via linker segments. For example, gold nanoparticles have been specifically targeted to epidermal growth factor (EGFR), which is overexpressed in over 30% of all epithelial cancers.[70-73]

Therefore, using these metal nanoparticle contrast agents targeted to cancer cell surface receptors in conjunction with a photoacoustic and ultrasound imaging device will significantly enhance pancreatic cancer detection and staging.

## 1.4 NANOSYSTEMS AS COMBINED CONTRAST AGENTS AND DRUG DELIVERY VEHICLES

Research in nanotechnology has exponentially increased over the last decade.[74] Metal nanoparticles were discovered to be excellent optical contrast agents; and over the same time period, other types of nanoparticles, such as polymeric nanoparticles and liposomes, were proven as exceptional drug and therapeutic gene delivery vehicles.[75-77] These vehicles could also be targeted to cancer cell surface receptors similar to the metal nanoparticles described above. The overarching therapeutic scheme is for chemotherapeutic drugs to be packaged in the nanoparticles; the targeted nanoparticles are then delivered systemically, extravasate into the tumor area due to the EPR effect, and latch on preferentially to cancer cells. While latched on to cancer cells, the nanoparticles can either release their drug cargo in the extracellular space or be endocytosed into the cell where the drugs are released internally.[78] Researchers hope to accomplish the following two main objectives by packing chemotherapeutics in nanoparticles targeted to cancer cells versus using traditional systemic injections of chemotherapy: (1) to limit the chemotherapeutic damage to healthy tissue (less patient suffering and side effects) and (2) to maximize the drug dose delivered directly to the tumor, making the therapy more effective and subjecting the patient to a lower overall dose of drugs. These objectives have been accomplished by researchers with the chemotherapeutic drug doxorubicin, for instance, where it was encapsulated in either poly(lactic-co-glycolic) acid or liposomes and successfully delivered to cancer cells.[79-83] Liposomal doxorubicin is currently in clinical trials.

As nanotechnology matures, sophisticated nanoparticles are surfacing in the form of multifunctional drug carriers. Several triggered drug delivery systems have been synthesized where light or some other form of electromagnetic energy is used to trigger drug release once the therapeutic nanoparticles have accumulated at the diseased site.[84-86] In addition to triggered release, researchers have begun to make combined imaging contrast and drug delivery nanoparticles. Interestingly, these new nanoparticles provide clinicians with an ability never before realized: the visualization of drug delivery. In current clinical settings, when a patient receives an injection or takes a pill, doctors "hope" the drug is properly delivered. Using a multifunctional nanoparticle, that delivery can be monitored and eventually even quantified at the diseased site.

Some initial studies using nanoparticles as multifunctional carriers for drug delivery and MRI contrast enhancement have surfaced.[87] Similarly, research in using photoacoustic imaging to visualize drug delivery is in its infancy. Initial strategies proposed to combine drug delivery with photoacoustic imaging involve using traditional, metallic photoacoustic contrast agents as multiplexed drug carriers.

Gold nanorods are photoacoustic contrast agents that can be easily multiplexed by conjugating drugs, targeting moieties, or other molecules of interest to their surface.[88] Drugs can be chemically modified with a linker that allows for facile attachment to the gold surface. The linker can have a thiol group that readily attaches to the gold surface via thiolate bonds, or other photocleavable linkers are possible. For example, gold nanorods conjugated to Etanercept (a rheumatic drug) were intra-articularly injected into ex vivo rat tail joints, and photoacoustic tomography (PAT) was used to visualize the distribution of the conjugates. The sensitivity of photoacoustic imaging to detect the gold nanorods in this study was calculated to be at 10 pM concentrations in joint connective tissue.[89]

Other photoacoustic contrast agents with potential as drug carriers are hollow gold structures. Both hollow gold nanocages and nanoshells absorb NIR light and have the capacity to house large payloads of drugs in their interior while leaving their exterior available for surface functionalization with targeting moieties.[59, 90] It was shown that 63% of doxorubicin (a breast and ovarian chemotherapeutic agent) could be loaded by weight in hollow gold nanospheres.[86] NIR light was used to trigger release of the drug by using the light for heat conversion at the nanosphere surface. After heat triggered release, the doxorubicin exhibited cytotoxic effects on MDA-MB-231 breast cancer cells. Others demonstrated that the gold hollow nanospheres could double as photothermal agents, demonstrating an enhanced killing effect in vitro when both drugs and photothermal therapy were used in combination. These hollow gold structures have been used to enhance contrast in photoacoustic imaging[91], but their use as a multifunctional carrier capable of photoacoustic image-guided drug delivery has not yet been published.

Though using noble metal structures with drugs conjugated directly to their surface is a commonly used example of a multiplexed drug carrier, new hybrid carriers are also being explored. Traditionally, nano-forms of medicine involved encapsulation of drugs in polymers or liposomal complexes for delivery. Now hybrid polymer-silver or polymer-gold structures are being explored for this purpose where the drugs are housed in the polymer and the metal is used to heat the structure and trigger drug release.[92-95] In one approach, hollow gold nanoshells were either encapsulated in the liposome with drugs or tethered to the lipid bilayer via a linker, and NIR light was used to disrupt the stability of the lipid membrane, causing the inner contents to be released.[96] If the ratio of the noble metal content to the drugs and polymer or lipid system is known, photoacoustic imaging can be used to monitor drug release processes using these hybrid systems.

Very few studies on the topic of drug delivery monitored by photoacoustics exist since the field is young. However, the opportunity to visualize drug delivery and trigger drug release is exciting to researchers and clinicians alike. In the coming years, image-guided drug delivery using a combination of photoacoustics with multiplexed nanoparticles will be a rapidly expanding research area. The research presented in this dissertation is part of this growing field. The focus here is on synthesis and initial testing of nanosystems specifically designed to enhance photoacoustic imaging while delivering drugs.

## 1.5 Combined Endoscopic Ultrasound and Photoacoustic Imaging of Pancreatic Cancer

Using multifunctional nanoparticles in combination with ultrasound and photoacoustic (USPA) imaging to visualize drug delivery is a broad goal of this research project. For this goal to be realized for pancreatic cancer, the USPA imaging would need to be performed endoscopically to allow for the light source to get in close proximity to the pancreas, affording an effective photoacoustic response. Figure 1.4 provides an illustration of how endoscopic ultrasound and photoacoustic (EUSPA) imaging can be accomplished in vivo using an adapted EUS probe that can deliver light.

The goal to combine EUS and photoacoustic imaging is based on several major factors. First, endoscopic ultrasound and photoacoustic imaging are complementary and can be transparently integrated since both photoacoustic and ultrasound imaging systems utilize the same ultrasound sensor and associated receiver electronics. Second, since both anatomical (morphology) and functional (activity) properties of the pancreatic tissue are expected to change with malignancy, it is anticipated that EUSPA imaging may detect and stage pathology earlier than EUS examination alone or even in combination with CT. Furthermore, compared to other imaging modalities such as microCT, MRI, PET/SPECT

and diffuse optical tomography (described in section 1.1.2 and also see Table 1), only USPA is a high-resolution, high-sensitivity real-time imaging capable of simultaneous morphological, functional and molecular imaging. Third, ultrasonic and optical access is enhanced by the location of the pancreas (typically within a few centimeters from the transducer). High frequency, and hence high spatial resolution ultrasound imaging is possible in most cases. Since the same ultrasound transducer will be used to detect photoacoustic transients, the photoacoustic signal can be resolved with spatial resolution akin to that in EUS imaging. Fourth, based on current clinical criteria, EUS imaging is already widely used for staging of pancreatic cancer[4, 27, 28] and, therefore, all necessary pre-requisites for EUSPA imaging of the pancreas are readily available. Patients will not be subjected to any additional biopsies, and the examination time will not increase to perform EUSPA imaging of the pancreas. Fifth, both ultrasound and photoacoustic imaging techniques are non-ionizing imaging methods and there are no safety concerns associated with low-fluence, non-ionizing laser irradiation. In addition, EUSPA imaging can be relatively inexpensive and portable. Finally, an urgent need exists for more sensitive and specific imaging to detect and stage pancreatic cancer – nanoparticle-augmented EUSPA imaging may fill that need and become an important clinical tool for reliable staging of pancreatic cancer.

### 1.6 Overall Research Goals

The overall hypothesis of the research is that (1) multifunctional nanoparticle contrast agents capable of combined therapeutic and imaging contrast components targeted to pancreatic cancer can be produced and (2) using these multifunctional nanoparticles in conjunction with a EUSPA imaging system will ultimately accomplish

visualization of drug delivery, more effective therapy, and more accurate staging of pancreatic cancer.

Towards accomplishment of these overall goals, the research presented here evaluates the feasibility of (1) synthesizing multifunctional (imaging contrast + drug delivery) nanoparticles, (2) evaluating therapeutic efficacy of these nanoparticles *in vitro*, and (3) imaging these nanoparticles with lab prototype USPA systems. The building of an EUSPA probe and demonstration of EUSPA imaging augmented with nanoparticles will be the subject of future work meant to build on that presented here.

The research presented in the following chapters is organized by nanosystem. Two multifunctional nanosystems are described in detail from design (Chapters 2 and 6), to preliminary synthesis and photoacoustic testing (Chapters 3 and 7), to complete synthesis of the designed nanosystems and in vitro characterization (Chapters 4/5 and 8). Finally, overall conclusions combined with insights for future work (Chapter 9) are presented that summarize the broad implications of the research relative to the biomedical field and present new directions based on those findings.

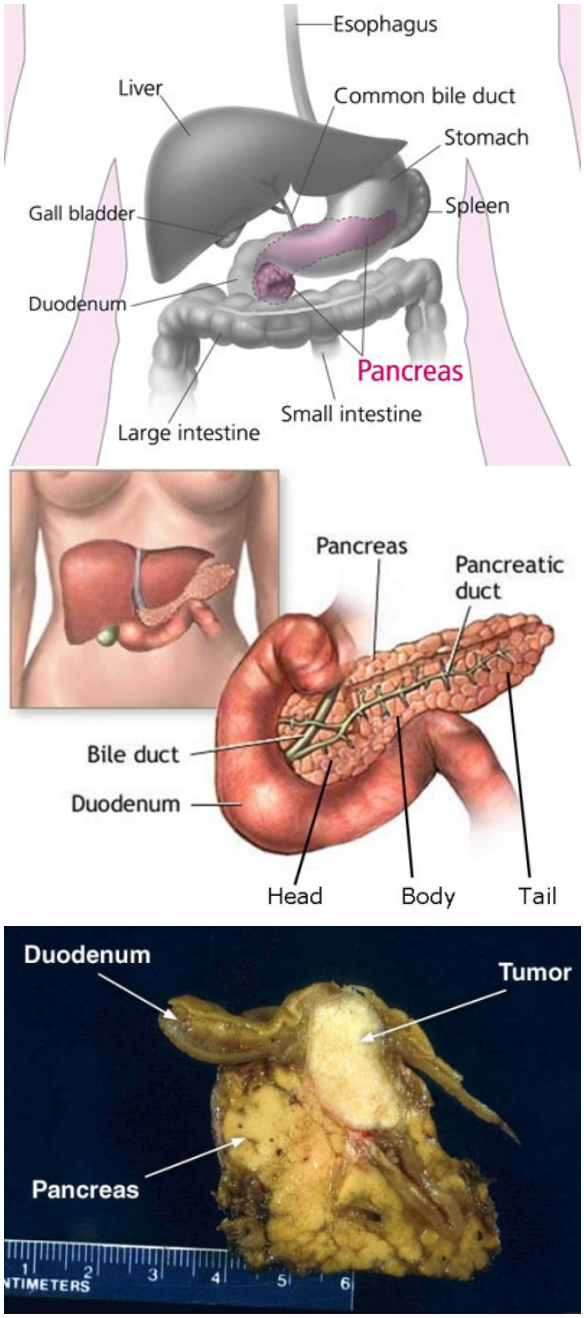


Figure 1.1: The anatomy of the pancreas as shown in relation to surrounding organs[97] (top) and in relation to its duct structure[98] (middle). Malignant tumor originating in the head of the pancreas[99] (bottom).

Figure 1.2: EUS image of a pancreatic cancer (blue and yellow dotted lines show the extent of the tumor). EUS image provided by Dr. Jeffrey Lee, M.D. Anderson Cancer Center, Houston, TX.

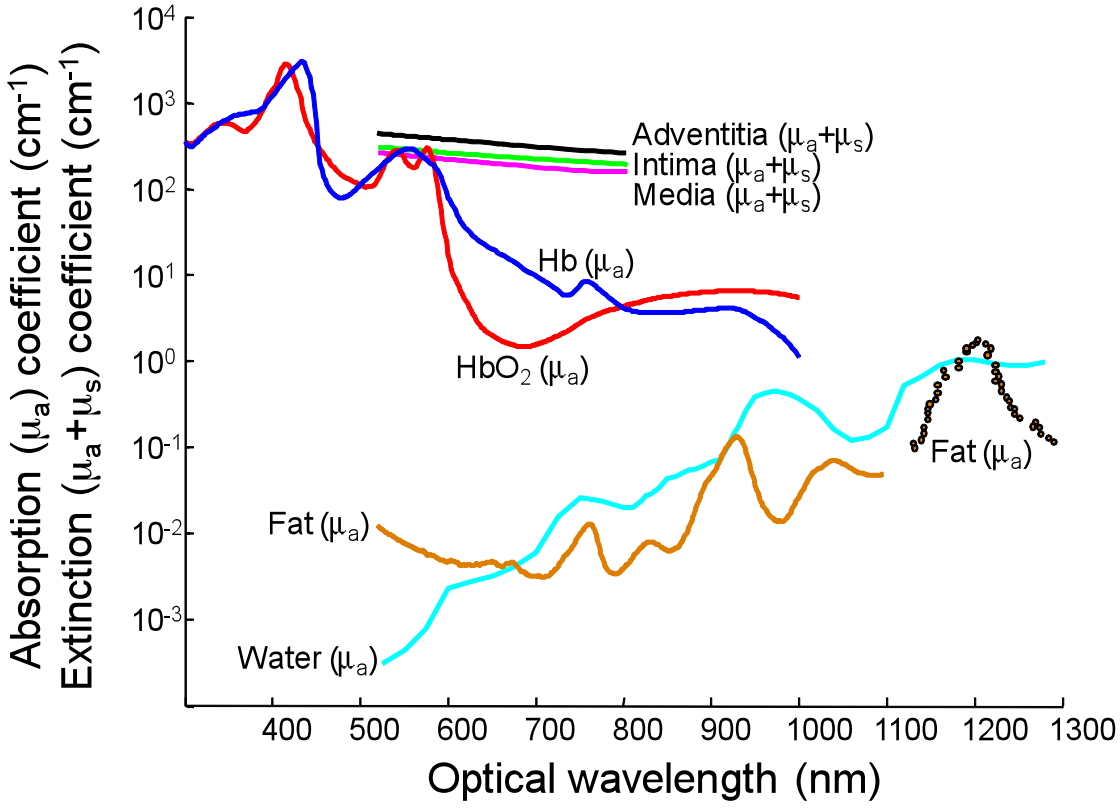


Figure 1.3: Optical absorption ($\mu_a$) or optical absorption plus scattering ($\mu_a+\mu_s$) for various absorbers in tissue ($HbO_2$ – oxygenated hemoglobin, Hb – deoxygenated hemoglobin).

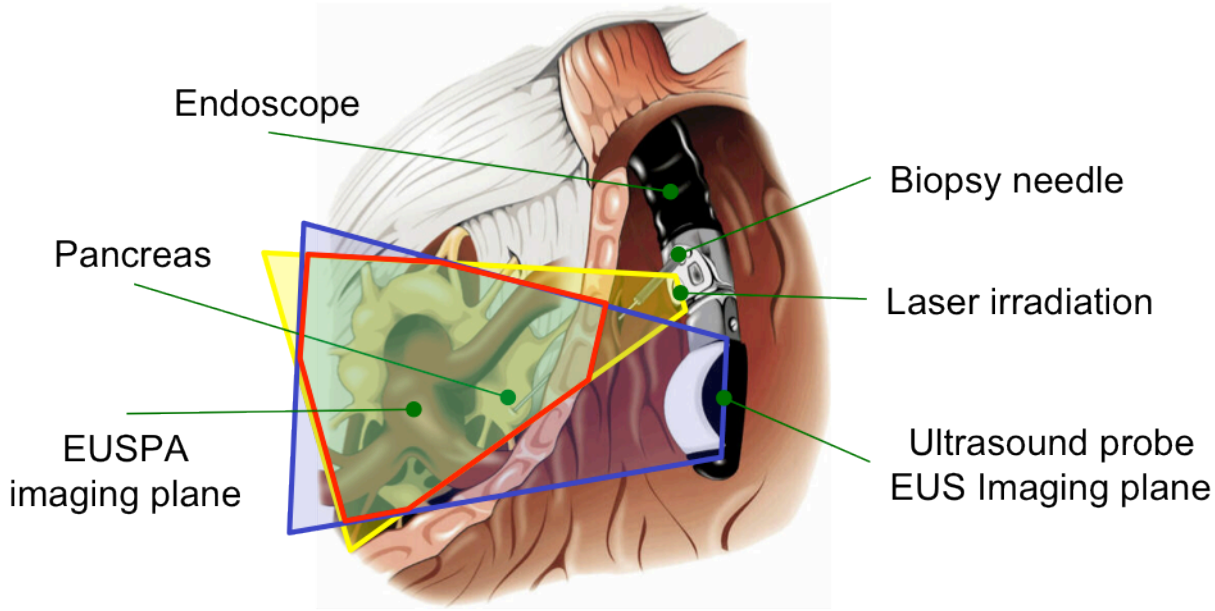


Figure 1.4: An illustration of how endoscopic ultrasound and photoacoustic (EUSPA) imaging would be implemented *in vivo*.

| | **Optical tomography** | **MicroCT** | **PET/SPECT** | **MRI** | **Ultrasound imaging** | **USPA imaging** |
|---|---|---|---|---|---|---|
| *Imaging depth* | Very good (up to 50 mm) | Excellent (50+ mm) | Excellent (50+ mm) | Excellent (50+ mm) | Very good (30-40 mm) | Very good (30-40 mm) |
| *Spatial resolution and anatomical imaging* | Poor (3-5 mm) | Excellent (0.01 mm) | Poor (2-3 mm) | Good (0.1-0.2 mm) | Very good (0.05-0.1 mm) | Very good (0.05-0.1 mm) |
| *Real-time* | No | No | No | No | Yes | Yes |
| *Endogenous contrast* | Poor | Very good | Poor | Excellent | Good | Excellent |
| *Molecular contrast* | Good | Poor | Excellent | Good | Poor | Excellent |
| *Safety* | No concerns | Concerns | Concerns | No concerns | No concerns | No concerns |
| *Longitudinal studies* | Very good | Poor | Poor | Good | Excellent | Excellent |
| *Blood perfusion* | Poor | Poor | Poor | Excellent | Good | Excellent |
| *Oxygen saturation* | Poor | Poor | Poor | Good | Poor | Excellent |
| *Portability* | Very good | Poor | Poor | Poor | Excellent | Excellent |
| *Cost effectiveness* | Very good | Poor | Poor | Poor | Excellent | Good |

Table 1.1: A comparison of properties of currently available imaging technologies that compete with ultrasound and photoacoustic (USPA) imaging.

## 1.7 REFERENCES


1. NCI, "Surveillance Epidemiology and End Results," in Secondary Surveillance Epidemiology and End Results Secondary NCI, Ed., Place Published (2010), http://seer.cancer.gov/statfacts/html/pancreas.html.
2. N. J. Nelson, "Pancreatic Cancer Research Matures," J. Natl. Cancer Inst. (2007)
3. E. Bria, M. Milella, A. Gelibter, F. Cuppone, M. S. Pino, E. M. Ruggeri, P. Carlini, C. Nistico, E. Terzoli, F. Cognetti and D. Giannarelli, "Gemcitabine-based combinations for inoperable pancreatic cancer: Have we made real progress?: A meta-analysis of 20 phase 3 trials," Cancer 110(3), 525-533 (2007)
4. C. De Angelis, A. Repici, P. Carucci, M. Bruno, M. Goss, L. Mezzabotta, R. Pellicano, G. Saracco and M. Rizzetto, "Pancreatic cancer imaging: the new role of endoscopic ultrasound," Journal of the Pancreas 8(1 Suppl), 85-97 (2007)
5. A. Jemal, L. X. Clegg, E. Ward, L. A. Ries, X. Wu, P. M. Jamison, P. A. Wingo, H. L. Howe, R. N. Anderson and B. K. Edwards, "Annual report to the nation on the status of cancer, 1975-2001, with a special feature regarding survival," Cancer 101(1), 3-27 (2004)
6. K. Homan, S. Emelianov and L. Brannon-Peppas, "Compositions for Therapy and Imaging of Cancer and Associated Methods," (2008)
7. B. Agarwal, E. Abu-Hamda, K. L. Molke, A. M. Correa and L. Ho, "Endoscopic ultrasound-guided fine needle aspiration and multidetector spiral CT in the diagnosis of pancreatic cancer," Am. J. Gastroenterol. 99(5), 844-850 (2004)
8. B. Simon and H. Printz, "Epidemiological trends in pancreatic neoplasias," Dig. Dis. 19(1), 6-14 (2001)
9. M. Reni and S. Cereda, "New therapies for pancreatic cancer: Current standard," Journal of the Pancreas 8(1 Suppl), 98-101 (2007)
10. H. G. Beger, B. Rau, F. Gansauge, B. Poch and K. H. Link, "Treatment of pancreatic cancer: Challenge of the facts," World J. Surg. 27(10), 1075-1084 (2003)
11. A. Mancuso, F. Calabro and C. N. Sternberg, "Current therapies and advances in the treatment of pancreatic cancer," Crit. Rev. Oncol. Hematol. 58(3), 231-241 (2006)
12. M. W. Saif, "Controversies in the adjuvant treatment of pancreatic adenocarcinoma," Journal of the Pancreas 8(5), 545-552 (2007)
13. G. R. Varadhachary, E. P. Tamm, J. L. Abbruzzese, H. Q. Xiong, C. H. Crane, H. Wang, J. E. Lee, P. W. Pisters, D. B. Evans and R. A. Wolff, "Borderline resectable pancreatic cancer: definitions, management, and role of preoperative therapy," Ann. Surg. Oncol. 13(8), 1035-1046 (2006)

14. T. Ishikawa, "Is it relevant that intra-arterial chemotherapy may be effective for advanced pancreatic cancer?," World J Gastroenterol 13(32), 4306-4309 (2007)

15. X. Yu, Y. Zhang, C. Chen, Q. Yao and M. Li, "Targeted drug delivery in pancreatic cancer," Biochim. Biophys. Acta (2009)

16. N. Pausawasdi and J. Scheiman, "Endoscopic evaluation and palliation of pancreatic adenocarcinoma: current and future options," Curr Opin Gastroenterol 23(5), 515-521 (2007)

17. J. J. Farrell, N. Senzer, J. R. Hecht, N. Hanna, T. Chung, J. Nemunaitis, A. Rosemurgy, M. Javle, T. Reid and M. Posner, "Long-Term data for endoscopic ultrasound (EUS) and percutanous (PTA) guided intratumoral TNFerade gene delivery combined with chemoradiation in the treatment of locally advanced pancreatic cancer (LAPC)," Gastrointest. Endosc. 63(5), AB93 (2006)

18. P. Fogar, F. Navaglia, D. Basso, E. Greco, C. F. Zambon, E. Fadi, A. Falda, A. Stranges, F. Vannozzi, R. Danesi, S. Pedrazzoli and M. Plebani, "Suicide gene therapy with the yeast fusion gene cytosine deaminase/uracil phosphoribosyltransferase is not enough for pancreatic cancer," Pancreas 35(3), 224-231 (2007)

19. A. Cascante, D. Abate-Daga, L. Garcia-Rodriguez, J. R. Gonzalez, R. Alemany and C. Fillat, "GCV modulates the antitumoural efficacy of a replicative adenovirus expressing the TAT8-TK as a late gene in a pancreatic tumour model," Gene Ther. 14(20), 1471-1480 (2007)

20. X. Xie, W. Xia, Z. Li, H. P. Kuo, Y. Liu, Z. Li, Q. Ding, S. Zhang, B. Spohn, Y. Yang, Y. Wei, J. Y. Lang, D. B. Evans, P. J. Chiao, J. L. Abbruzzese and M. C. Hung, "Targeted expression of BikDD eradicates pancreatic tumors in noninvasive imaging models," Cancer Cell 12(1), 52-65 (2007)

21. M. L. Immordino, P. Brusa, F. Rocco, S. Arpicco, M. Ceruti and L. Cattel, "Preparation, characterization, cytotoxicity and pharmacokinetics of liposomes containing lipophilic gemcitabine prodrugs," J Control Release 100(3), 331-346 (2004)

22. P. Brusa, M. L. Immordino, F. Rocco and L. Cattel, "Antitumor activity and pharmacokinetics of liposomes containing lipophilic gemcitabine prodrugs," Anticancer research 27(1A), 195-199 (2007)

23. H. R. Cardenes, E. G. Chiorean, J. Dewitt, M. Schmidt and P. Loehrer, "Locally advanced pancreatic cancer: current therapeutic approach," Oncologist 11(6), 612-623 (2006)

24. R. S. Kwon and J. M. Scheiman, "New advances in pancreatic imaging," Curr Opin Gastroenterol 22(5), 512-519 (2006)

25. R. Valinas, A. Barrier, F. Montravers, S. Houry, J. N. Talbot and M. Huguier, "18 F-fluorodeoxyglucose positron emission tomography for characterization and initial staging of pancreatic tumors," Gastroenterol. Clin. Biol. 26(10), 888-892 (2002)

26. E. Tamm and C. Charnsangavej, "Pancreatic cancer: current concepts in imaging for diagnosis and staging," Cancer J 7(4), 298-311 (2001)

27. P. Michl, S. Pauls and T. M. Gress, "Evidence-based diagnosis and staging of pancreatic cancer," Best Pract Res Clin Gastroenterol 20(2), 227-251 (2006)

28. F. G. Gress, R. H. Hawes, T. J. Savides, S. O. Ikenberry, O. Cummings, K. Kopecky, S. Sherman, M. Wiersema and G. A. Lehman, "Role of EUS in the preoperative staging of pancreatic cancer: a large single-center experience," Gastrointest. Endosc. 50(6), 786-791 (1999)

29. J. Folkman, "What is the evidence that tumors are angiogenesis dependent?," J. Natl. Cancer Inst. 82(1), 4-6 (1990)

30. M. A. Konerding, A. J. Miodonski and A. Lametschwandtner, "Microvascular corrosion casting in the study of tumor vascularity: A review.," Scanning Microscopy 9(4), 1233-1244 (1995)

31. M. A. Rubin, M. Buyyounouski, E. Bagiella, S. Sharir, A. Neugut, M. Benson, A. d. l. Taille, A. E. Katz, C. A. Olsson and R. D. Ennis, "Microvessel density in prostate cancer: lack of correlation with tumor grade, pathologic stage, and clinical outcome," J.Urology 53(3), 542-547 (1999)

32. A. E. d. l. Taille, E. Katz, R. Bagiella, S. Buttyan, C. A. Sharir, T. Olsson, R. D. Burchardt, M. A. Ennis and M. A. Rubin, "Microvessel density as a predictor of PSA recurrence after radical prostatectomy. A comparison of CD34 and CD31," Am. J. Clin. Pathol. 113(4), 555-562 (2000)

33. R. S. DaCosta, L.Lilge, J. Kost, M. Cirocco, R. Saidi, A. DuVall, S. Hassaram, N. Marcon and B. C. Wilson, " Confocal fluorescence microscopy/macroscopy and microspectrofluorimetry analysis of human colorectal tissues," J. Anal. Morphol. Cell Vision 4(24-29 (1997)

34. Wray, M. Cope, D. T. Deply, J. S. Wyatt and E. O. R. Reynolds, "Characterization of the near infrared absorption spectra of cytochrome aa3 and hemoglobin for the non-invasive monitoring of cerebral oxygenation," Biochim. et Biophys. Acta 933(184-192 (1988)

35. G. Diebold, M. Khan and S. Park, "Photoacoustic "Signatures" of Particulate Matter: Optical Production of Acoustic Monopole Radiation," Science 250(4977), 101 (1990)

36. W. H. Nau, R. J. Roselli and D. F. Milam, "Measurement of thermal effects on the optical properties of prostate tissue at wavelengths of 1,064 and 633 nm," Lasers in Surgery and Medicine 24(1), 38-47 (1999)

37. A. A. Oraevsky, S. L. Jacques and F. K. Tittel, " Measurement of tissue optical properties by time-resolved detection of laser-induced transient stress,," Appl. Optics 36(1), 402-415 (1997)

38. A. A. Oraevsky and A. A. Karabutov, Optoacoustic Tomography, CRC Press (2003).

39. A. Oraevsky, S. Jacques and F. Tittel, "Determination of tissue optical properties by time-resolved detection of laser-induced stress waves," (1993)

40. A. Oraevsky, S. Jacques, R. Esenaliev and F. Tittel, "Time-Resolved Optoacoustic Imaging in Layered Biological Tissues," in Advances in Optical Imaging and Photon Migration R. R. Alfano, Ed., pp. 161-165, Academic Press, New York (1994).

41. A. Oraevsky, R. Esenaliev, S. Jacques, S. Thomsen and F. Tittel, "Lateral and z-axial resolution in laser optoacoustic imaging with ultrasonic transducers," (1995)

42. A. A. Oraevsky, S. L. Jacques and F. K. Tittel, "Measurement of tissue optical properties by time-resolved detection of laser-induced transient stress," Appl Opt 36(1), 402-415 (1997)

43. R. A. Kruger, "Photoacoustic ultrasound," Medical physics 21(1), 127-131 (1994)

44. R. A. Kruger and P. Liu, "Photoacoustic ultrasound: pulse production and detection of 0.5% Liposyn," Medical physics 21(7), 1179-1184 (1994)

45. R. A. Kruger, P. Liu, Y. R. Fang and C. R. Appledorn, "Photoacoustic ultrasound (PAUS)--reconstruction tomography," Med. Phys. 22(10), 1605-1609 (1995)

46. G. Ku, X. Wang, X. Xie, G. Stoica and L. V. Wang, "Imaging of tumor angiogenesis in rat brains in vivo by photoacoustic tomography," Appl Opt 44(5), 770-775 (2005)

47. X. Wang, Y. Xu, M. Xu, S. Yokoo, E. S. Fry and L. V. Wang, "Photoacoustic tomography of biological tissues with high cross-section resolution: reconstruction and experiment," Med. Phys. 29(12), 2799-2805 (2002)

48. M. Xu and L. V. Wang, "Photoacoustic imaging in biomedicine," Rev. Sci. Instrum. 77(041101 (2006)

49. "American National Standard for Safe Use of Lasers," Laser Institute of America; ANSI Z136.1((2000)

50. J. Shah, S. R. Aglyamov, K. Sokolov, T. E. Milner and S. Y. Emelianov, "Ultrasound imaging to monitor photothermal therapy - feasibility study," Opt Express 16(6), 3776-3785 (2008)

51. J. Shah, S. Park, S. Aglyamov, T. Larson, L. Ma, K. Sokolov, K. Johnston, T. Milner and S. Y. Emelianov, "Photoacoustic imaging and temperature measurement for photothermal cancer therapy," J Biomed Opt 13(3), 034024 (2008)

52. L. E. Kinsler, A. R. Frey, A. B. Coppens and J. V. Sanders, Fundamentals of Acoustics, John Wiley and Sons, Inc., New York (2000).

53. X. Huang, I. H. El-Sayed, W. Qian and M. A. El-Sayed, "Cancer cell imaging and photothermal therapy in the near-infrared region by using gold nanorods," Journal Of The American Chemical Society 128(6), 2115-2120 (2006)

54. C. Loo, A. Lin, L. Hirsch, M. H. Lee, J. Barton, N. Halas, J. West and R. Drezek, "Nanoshell-enabled photonics-based imaging and therapy of cancer," Technology In Cancer Research & Treatment 3(1), 33-40 (2004)

55. Y. Lu, G. L. Liu, J. Kim, Y. X. Mejia and L. P. Lee, "Nanophotonic crescent moon structures with sharp edge for ultrasensitive biomolecular detection by local electromagnetic field enhancement effect," Nano Lett 5(1), 119-124 (2005)

56. J. Shah, S. R. Aglyamov, K. Sokolov, T. E. Milner and S. Y. Emelianov, "Ultrasound-based Thermal and Elasticity Imaging to Assist Photothermal Cancer Therapy - Preliminary Study," (2006)

57. J. A. Copland, M. Eghtedari, V. L. Popov, N. Kotov, N. Mamedova, M. Motamedi and A. A. Oraevsky, "Bioconjugated gold nanoparticles as a molecular based contrast agent: implications for imaging of deep tumors using optoacoustic tomography," Molecular Imaging And Biology: MIB: The Official Publication Of The Academy Of Molecular Imaging 6(5), 341-349 (2004)

58. M. L. Li, J. C. Wang, J. A. Schwartz, K. L. Gill-Sharp, G. Stoica and L. V. Wang, "In-vivo photoacoustic microscopy of nanoshell extravasation from solid tumor vasculature," J Biomed Opt 14(1), 010507 (2009)

59. S. E. Skrabalak, J. Chen, Y. Sun, X. Lu, L. Au, C. M. Cobley and Y. Xia, "Gold nanocages: synthesis, properties, and applications," Acc Chem Res 41(12), 1587-1595 (2008)

60. Y. F. Huang, K. Sefah, S. Bamrungsap, H. T. Chang and W. Tan, "Selective photothermal therapy for mixed cancer cells using aptamer-conjugated nanorods," Langmuir 24(20), 11860-11865 (2008)

61. L. R. Hirsch, A. M. Gobin, A. R. Lowery, F. Tam, R. A. Drezek, N. J. Halas and J. L. West, "Metal nanoshells," Ann. Biomed. Eng. 34(1), 15-22 (2006)

62. K. Homan, J. Shah, S. Gomez, H. Gensler, A. Karpiouk, L. Brannon-Peppas and S. Emelianov, "Silver nanosystems for photoacoustic imaging and image-guided therapy," Journal of Biomedical Optics 15(2), 021316 (2010)

63. M. S. Peterson, J. Bouwman, A. Chen and M. Deutsch, "Inorganic metallodielectric materials fabricated using two single-step methods based on the Tollen's process," J. Colloid Interface Sci. 306(1), 41-49 (2007)

64. S. Link and M. El-Sayed, "Spectral properties and relaxation dynamics of surface plasmon electronic oscillations in gold and silver nanodots and nanorods," J. Phys. Chem. B 103(40), 8410-8426 (1999)

65. J. West and N. Halas, "Engineered nanomaterials for biophotonics applications: improving sensing, imaging, and therapeutics," Annu. Rev. Biomed. Eng. 5(285-292 (2003)

66. R. Gref, A. Domb, P. Quellec, T. Blunk, R. H. Müller, J. M. Verbavatz and R. Langer, "The controlled intravenous delivery of drugs using PEG-coated sterically stabilized nanospheres," Long-circulating Drug Delivery Systems 16(2-3), 215-233 (1995)

67. R.-L. Hong, C.-J. Huang, Y.-L. Tseng, V. F. Pang, S.-T. Chen, J.-J. Liu and F.-H. Chang, "Direct Comparison of Liposomal Doxorubicin with or without Polyethylene Glycol Coating in C-26 Tumor-bearing Mice: Is Surface Coating with Polyethylene Glycol Beneficial?," Clin Cancer Res 5(11), 3645-3652 (1999)

68. S. K. Hobbs, W. L. Monsky, F. Yuan, W. G. Roberts, L. Griffith, V. P. Torchilin and R. K. Jain, "Regulation of transport pathways in tumor vessels: role of tumor type and microenvironment," Proceedings Of The National Academy Of Sciences Of The United States Of America 95(8), 4607-4612 (1998)

69. G. Kong, R. D. Braun and M. W. Dewhirst, "Hyperthermia enables tumor-specific nanoparticle delivery: effect of particle size," Cancer Research 60(16), 4440-4445 (2000)

70. S. Mallidi, T. Larson, J. Aaron, K. Sokolov and S. Emelianov, "Molecular specific photoacoustic imaging with plasmonic nanoparticles," Optics Express 15(11), 6583-6588 (2007)

71. K. Sokolov, J. Aaron, B. Hsu, D. Nida, A. Gillenwater, M. Follen, C. MacAulay, K. Adler-Storthz, B. Korgel, M. Descour, R. Pasqualini, W. Arap, W. Lam and R. Richards-Kortum, "Optical systems for in vivo molecular imaging of cancer," Technol Cancer Res Treat 2(6), 491-504 (2003)

72. K. Sokolov, M. Follen, J. Aaron, I. Pavlova, A. Malpica, R. Lotan and R. Richards-Kortum, "Real-time vital optical imaging of precancer using anti-epidermal growth factor receptor antibodies conjugated to gold nanoparticles," Cancer Res 63(9), 1999-2004 (2003)

73. S. Bhattacharyya, R. Bhattacharya, S. Curley, M. A. McNiven and P. Mukherjee, "Nanoconjugation modulates the trafficking and mechanism of antibody induced receptor endocytosis," Proc. Natl. Acad. Sci. U. S. A. 107(33), 14541-14546 (2010)

74. J. Youtie, P. Shapira and A. Porter, "Nanotechnology publications and citations by leading countries and blocs," J. Nanopart. Res. 10(6), 981-986 (2008)

75. X. Wang, L. Yang, Z. G. Chen and D. M. Shin, "Application of nanotechnology in cancer therapy and imaging," CA. Cancer J. Clin. 58(2), 97-110 (2008)

76. S. Nie, Y. Xing, G. J. Kim and J. W. Simons, "Nanotechnology applications in cancer," Annu Rev Biomed Eng 9(257-288 (2007)

77. L. Brannon-Peppas and J. O. Blanchette, "Nanoparticle and targeted systems for cancer therapy," Adv Drug Deliv Rev 56(11), 1649-1659 (2004)

78. I. Brigger, C. Dubernet and P. Couvreur, "Nanoparticles in cancer therapy and diagnosis," Adv Drug Deliv Rev 54(5), 631-651 (2002)

79. T. Betancourt, B. Brown and L. Brannon-Peppas, "Doxorubicin-loaded PLGA nanoparticles by nanoprecipitation: preparation, characterization and in vitro evaluation," Nanomedicine 2(2), 219-232 (2007)

80. H. S. Yoo, K. H. Lee, J. E. Oh and T. G. Park, "In vitro and in vivo anti-tumor activities of nanoparticles based on doxorubicin-PLGA conjugates," J Control Release 68(3), 419-431 (2000)

81. D. H. Xu, J. Q. Gao and W. Q. Liang, "Liposome-based intracellular kinetics of doxorubicin in K562/DOX cells," Pharmazie 63(9), 646-649 (2008)

82. M. J. Johnston, K. Edwards, G. Karlsson and P. R. Cullis, "Influence of drug-to-lipid ratio on drug release properties and liposome integrity in liposomal doxorubicin formulations," J Liposome Res 18(2), 145-157 (2008)

83. J. Yokoe, S. Sakuragi, K. Yamamoto, T. Teragaki, K. Ogawara, K. Higaki, N. Katayama, T. Kai, M. Sato and T. Kimura, "Albumin-conjugated PEG liposome enhances tumor distribution of liposomal doxorubicin in rats," Int. J. Pharm. 353(1-2), 28-34 (2008)

84. K. Wilson, K. Homan and S. Emelianov, "Synthesis of a dual contrast agent for ultrasound and photoacoustic imaging," Reporters, Markers, Dyes, Nanoparticles, and Molecular Probes for Biomedical Applications II Proc. SPIE 7576(75760M (2010)

85. G. Wu, A. Mikhailovsky, H. A. Khant, C. Fu, W. Chiu and J. A. Zasadzinski, "Remotely triggered liposome release by near-infrared light absorption via hollow gold nanoshells," J. Am. Chem. Soc. 130(26), 8175-8177 (2008)

86. J. You, G. Zhang and C. Li, "Exceptionally high payload of doxorubicin in hollow gold nanospheres for near-infrared light-triggered drug release," ACS Nano 4(2), 1033-1041 (2010)

87. A. Arepally, "Targeted drug delivery under MRI guidance," J. Magn. Reson. Imaging 27(2), 292-298 (2008)

88. X. Huang, S. Neretina and M. El-Sayed, "Gold nanorods: From synthesis and properties to biological and biomedical applications," Adv. Mater. 21(48), 4880-4910 (2009)

89. D. Chamberland, A. Agarwal, N. Kotov, J. Fowlkes, P. Carson and X. Wang, "Photoacoustic tomography of joints aided by an Etanercept-conjugated gold nanoparticle contrast agentóan ex vivo preliminary rat study," Nanotechnology 19(095101 (2008)

90. K. An and T. Hyeon, "Synthesis and biomedical applications of hollow nanostructures," Nano Today 4(4), 359-373 (2009)

91. X. Yang, S. Skrabalak, Z. Li, Y. Xia and L. Wang, "Photoacoustic tomography of a rat cerebral cortex in vivo with Au nanocages as an optical contrast agent," Nano Lett 7(12), 3798-3802 (2007)

92. C. Chu, Y. Wang, L. Tai, L. Wu and C. Yang, "Surface deformation of gold nanorod-loaded poly (dl-lactide-co-glycolide) nanoparticles after near infrared irradiation: an active and controllable drug release system," Journal of Materials Chemistry 20(16), 3260-3264 (2010)

93. C. M. Cobley, L. Au, J. Chen and Y. Xia, "Targeting gold nanocages to cancer cells for photothermal destruction and drug delivery," Expert Opin Drug Deliv 7(5), 577-587 (2010)

94. M. Das, N. Sanson, D. Fava and E. Kumacheva, "Microgels loaded with gold nanorods: photothermally triggered volume transitions under physiological conditions," Langmuir 23(1), 196-201 (2007)

95. K. Homan, S. Gomez, H. Gensler, J. Shah, L. Brannon-Peppas and S. Emelianov, "Design and development of multifunctional contrast agents for photoacoustic imaging," Reporters, Markers, Dyes, Nanoparticles, and Molecular Probes for Biomedical Applications: Proceedings of the SPIE 7190(71900I-71900I (2009)

96. G. Wu, A. Mikhailovsky, H. A. Khant, C. Fu, W. Chiu and J. A. Zasadzinski, "Remotely triggered liposome release by near-infrared light absorption via hollow gold nanoshells," Journal of the American Chemical Society 130(26), 8175-8177 (2008)

97. "Pancreas Anatomy," in Secondary Pancreas Anatomy Secondary, Place Published, http://www.cancer.gov/cancertopics/wyntk/pancreas/page2.

98. "Pancreas Duct Structure," in Secondary Pancreas Duct Structure Secondary, Place Published, http://health.allrefer.com/health/diabetes-pancreas.html.

99. "Pancreatic Tumor," in Secondary Pancreatic Tumor Secondary, Place Published, http://www.orienttumor.com/english/t&t/Pancreatic_Cancer.htm.

# Chapter 2: Design of the Combined Imaging and Therapy Nanocage System (CIT-NS)

The objective of this research project is to design and synthesize new multifunctional nanoparticle systems capable of drug delivery and enhancing imaging contrast. The design of one such nanosystem termed the Combined Imaging and Therapy Nanocage System (CIT-NS) is explained in depth in this chapter (note that the CIT-NS is also referred to as the nanocage system in the text). Each component of the CIT-NS and the reasons for its selection are discussed. Furthermore, synergistic elements in the overall design and its potential limitations are addressed.

The CIT-NS design, illustrated in Fig. 2.1, was inspired by two existing nanoparticles. As mentioned in Section 1.4, polymeric nanoparticles have been developed as efficient chemotherapeutic drug carriers.[1] The CIT-NS uses that design as the core of the system. Similarly, metal nanoshells have been designed as optical contrast agents possessing a core of silica and a noble metal outer shell.[2] These metal nanoshells could be synthetically tuned to absorb near infrared light by adjusting the thickness of the gold layer deposited on the silica surface.[3] Since these metal nanoshells have high absorption cross-sections in the near infrared (NIR) spectrum, they make excellent photoacoustic contrast agents. The CIT-NS design was born from the marriage of these two particles (Fig. 2.1). The core of the CIT-NS consists of drugs encapsulated in a polymeric matrix of poly(lactic-co-glycolic) (PLGA) acid surrounded by a silver "shell" that is instead named a cage since the metal layer may not be completely confluent in the CIT-NS design providing a metal "cage" for the polymer and drug components.

## 2.1 CIT-NS COMPONENTS

The various components of the CIT-NS are described in depth in this section, relating details about why they were chosen for inclusion in the design and which properties they impart to the CIT-NS as a whole.

### 2.1.1 Chemotherapeutic Drugs

Unfortunately, pancreatic adenocarcinoma is inherently resistant to chemotherapeutic regimens, either alone or in combinations. The most effective drugs that have formed the basis of chemotherapeutic treatment for pancreatic cancer have been 5-fluorouracil (5-FU) and the more recently approved gemcitabine.[4] As with most chemotherapeutic regimens, treatment involves systemic intravenous injections. The concentrations of gemcitabine and other drugs used per session is dose-limited by their cytotoxic effect on healthy bone marrow and epithelial tissue.[5] Some hypothesize that the systemic approach is ineffective for most patients because drug concentrations accumulated within the tumor itself are not high enough to realize their estimated therapeutic potential. In response to this issue several solutions involving packaging these chemotherapeutics in polymeric nanoparticles have surfaced.[6-8] It is anticipated that packaging drugs in this way allows for a more lethal dose to be targeted and delivered directly to the cancerous site where its therapeutic potential will be realized.

Since gemcitabine is the most effective and most highly prescribed chemotherapeutic drug to treat pancreatic cancer, it was chosen to be packaged in the CIT-NS. However, intrinsic properties of gemcitabine make it difficult to encapsulate in PLGA. For instance, gemcitabine is highly hydrophilic and PLGA is hydrophobic. Although hydrophilic molecules have previously been encapsulated in PLGA[9], hydrophobic molecules encapsulate with higher efficiency and do not experience the burst release effect upon introduction in a solvent as strongly as hydrophilic molecules in

PLGA. Therefore, modifications to gemcitabine were necessary to make it more hydrophobic, allowing for better encapsulation in PLGA. Various prodrug forms of gemcitabine are covered in Chapter 5.

The most significant restriction regarding what drugs the system can carry is dictated by the drugs' ability to encapsulate in PLGA. Most hydrophobic molecules encapsulate well in PLGA, and PLGA as a carrier for drugs and myriad contrast agents or hydrophobic molecules of interest has been well documented.[10-14] One example of a widely used chemotherapeutic agent that is naturally hydrophobic and encapsulates well in PLGA is Doxorubicin (DOX). Incorporation of DOX in the CIT-NS was tested and results can be found in Chaper 4.

### 2.1.2 Poly(lactic-co-glycolic) Acid (PLGA)

One of the most widely investigated materials in drug delivery is poly(lactic-co-glycolic) acid (PLGA) due to its long history in the field, many advantageous properties, ease of use and wide availability.[12, 15] PLGA makes up the bulk of the core of the CIT-NS, entrapping drug molecules within its matrix.

The PLGA used in the CIT-NS is an FDA-approved copolymer of 50:50 lactide and glycolide monomers (Fig. 2.2). PLGA is a bulk eroding, biodegradable polymer that is approved for use as suture material and in various drug delivery systems, including Lupron Depot®, ProLease® and Trelstar® Depot.[12, 16] PLGA degrades into lactic acid and glycolic acid through hydrolysis of the ester bond, and the material bulk erodes as water diffuses into the matrix more quickly than the polymer degrades.[17, 18] PLGA is biocompatible due to the uptake of lactide and glycolide post-degradation into the citric acid cycle, and this allows for the use of PLGA without the need for removal of the material after the intervention. Of all possible copolymer blends of PLGA, the 50:50

lactide:glycolide PLGA degrades the fastest. PLGA microparticles injected intramuscularly in the legs of rats were shown to degrade by 70% in 3 weeks and be completely degraded *in vivo* at ~10 weeks.[16] Nanoformulations of PLGA are expected to degrade even more quickly. PLGA particles have been formulated extensively for use in both oral and subcutaneously-injected delivery systems.[19, 20] Furthermore, as discussed above, biodegradable PLGA nanoparticles have been utilized as successful delivery systems.[12, 17, 21-23]

PLGA is also a popular material due to its intracellular trafficking. Some groups have shown that cellular internalization of PLGA nanoparticles is through both fluid phase pinocytosis and clathrin-coated pits in vascular smooth muscle cells (VSMCs). Within 10 min of incubation with cells *in vitro*, PLGA nanoparticles rapidly escape endo-lysosomes and enter the cytoplasm.[24] At neutral pH, PLGA nanoparticles exhibit a negatively charged surface due to the presence of the carboxylic acid end groups on the copolymer. Interestingly, following cellular internalization (via endocytosis) PLGA nanoparticles undergo surface charge reversal (anionic to cationic) in the acidic pH of endo-lysosomal compartments.[24] The charge reversal facilitates an interaction of PLGA with the vesicular membranes, leading to transient and localized destabilization of the membrane, thereby resulting in the escape of nanoparticles into the cytosol.[25] A significant fraction of the PLGA nanoparticles undergo exocytosis - only 15% of the internalized nanoparticles escape into the cytosolic compartment. However, the fraction of nanoparticles that escape the endosome seem to remain in the cytoplasm and release the encapsulated therapeutic in a sustained manner as the polymer degrades slowly. This intracellular trafficking pathway might explain why DOX-loaded PLGA nanoparticles exhibited greater cytotoxic effects relative to free drugs at low concentrations.[26] Drugs

that require cytosolic delivery to have a therapeutic effect benefit from carriers like PLGA.

Due to their size and shape, PLGA nanoparticles and microparticles are popular for the encapsulation and delivery of active agents. PLGA particles can travel through blood vessels or be injected into other physiological areas, such as the peritoneum, and protect the encapsulated agent until delivery. Particles of PLGA can be formulated in many ways,[12, 27-29] yet emulsion and nanoprecipitation techniques[30-33] are facile and can be used to encapsulate both hydrophilic and hydrophobic agents. The advantages of the emulsion techniques are simplicity, flexibility in nanoparticle size by adjusting chemical interactions between starting materials, and the ability to encapsulate an agent without chemically linking it to the carrier. The optimization[31] and scale up production[32] of PLGA particles up to 100 g per batch has been reported.

To summarize, PLGA was chosen as the core of the CIT-NS due to its proven biocompatibility and biodegradation properties, its ability to sequester and protect active agents such as drugs, its intracellular cytosol trafficking, and the ease of using emulsion techniques to potentially produce large quantities of drug-loaded PLGA nanoparticles.

### 2.1.3 Silver

The core of the CIT-NS is surrounded by a silver studded or seeded cage. The function of silver in the CIT-NS is to increase the nanosystem's light absorption in the NIR spectrum, making it a suitable photoacoustic contrast agent. Silver on the surface of PLGA will have similar optical properties to the metal nanoshell structures mentioned previously that can act as photoacoustic contrast agents.[2]

The deposition of a thin layer of gold on the surface of a dielectric material (silica) to create a nanoshell allows for unique optical properties. At the nanoscale, as the

ratio of the silica core diameter to the thickness of the Au coating changes, the nanoshells' scattering and absorption properties change. Since the layer of gold is so thin, and the mean free path of electrons on the surface of gold is tens of nanometers, light can excite the conduction band of electrons in the metal to oscillate almost in unison across the nanoshell surface in response to light. This collective oscillation is termed the surface plasmon resonance (SPR) of the nanoparticle and is akin to mechanical or acoustic resonance but at the electronic scale. In the case of nanoshells, as the ratio of the core to shell thickness is changed, the SPR peak can be tuned from the visible to the NIR spectrum of light.[34]

Silver on the surface of PLGA yields similar plasmonic effects as gold nanoshells since PLGA is a dielectric similar to silica and the silver cage coating on the PLGA surface is comparable to a gold shell configuration. In fact, gold is used by the majority of researchers to impart photoacoustic contrast properties to nanosystems.[35, 36] Silver was incorporated in the CIT-NS because it has slightly stronger and sharper plasmon resonance properties (by 10 to 15%)[37], making it theoretically a better absorber and producer of photoacoustic transients. Furthermore, silver can be reduced onto the surface of PLGA in a cage-like, porous or semi-porous fashion so that controlled drug release through the silver cage is possible.

Currently, the use of silver in biomedical applications from nano to orthopedic is a controversial topic.[38] Some clinicians and researchers believe silver is toxic, while others see it as benign. Thus, the next few sections are provided as background on the use of silver throughout history and in the biomedical realm.

### *2.1.3.1 History of Silver as a Preservative*

The use of silver in biomedical applications is far from new. As early as 400 B.C., Hippocrates wrote of the healing and anti-disease properties of silver.[39] Ancient Egyptian writings also mention using silver for medical purposes.[40] Throughout history, well before the mechanism behind silver's germicidal and antibiotic properties were known, people had been using silver for its medical, preservative, and restorative powers. For instance, Herodotus recorded that to prevent sickness, the King of Persia carried with him boiled water in a silver flagon.[41, 42] In ancient Roman and Greek societies, the wealthy would commonly store their water, wine, and food stuffs in silver vessels to prevent bacterial growth. The known use of silver as a preservative in this way led to its incorporation in the making of utensils and goblets. Many, like the Chinese emperor and his court, would eat with silver chopsticks. In the Middle Ages, silver became the material of choice for the making of most tableware settings. This use of silver came to the upper class' advantage since their daily employment of silver utensils helped shield them from experiencing the full brunt of the plague.[40] In fact, the crude form of silver used to make early utensils contributed to the bluish skin discoloration seen in most wealthy folks at that time, resulting in their label as "royal blue bloods." Furthermore, it is possible that the phrase "born with a silver spoon" was coined during this time, and represented not only the wealth of the "royal blue bloods" class but also their good health and fortune.[41] The use of silver as an anti-spoilage agent continued through the ages. The first Australian outback settlers suspended their silverware in water jugs to reduce spoilage. Early American pioneers traveling westward in search of good fortune did the same. Even in the early 1900's, our grandparents and great-grandparents would place silver dollars in milk jugs to preserve freshness.[40]

Our use of silver as a preservative continues today. Switzerland now manufactures silver water purification tablets and filters employed in many international airlines. Silver is also used in swimming pools in place of chlorine to reduce the growth of algae and bacteria. These progressive swimming pool owners use "electrical ionization units that impregnate the water with silver and copper ions" to help sanitize their pool water.[43] Another current day application of silver is in toilets.[44] Vitra started a line of toilets and plumbing that have silver ions embedded in the glaze that covers these fixtures in order to kill germs. In February of 2006, Samsung introduced washing machines that expel silver ions during a final rinse cycle, which are supposed to provide anti-bacterial protection to clothes for up to several days.[45] Lastly, silver nanoparticles are now being considered for use in chitosan bionanocomposite films which will be used in food packaging to preserve freshness and prevent bacterial adhesion.[46]

#### *2.1.3.2 History of Silver as a Therapeutic Agent*

In addition to its use as a preservative and germicide, silver enjoys a long history as a therapeutic agent for early medical applications. Hippocrates specifically referenced it as a treatment for ulcers, saying that "the flowers of silver alone, in the finest powder" should be employed.[39] Later in 78 A.D., Pliny the Elder mentions it in his survey of the world's knowledge, saying that when silver is used as an ingredient in plasters, it enhances the quick closure of wounds.[41] In Ayurvedic medicine, an old form of alternative medicine in India, small amounts of silver were used as an active ingredient in an elixir given to patients stricken with disease or old age as a restorative or rejuvenative agent. In the 1800's, silver sutures were used with successful results.[40] In addition, around that same time, the use of hardened silver nitrate in the treatment of ulcers became widespread. Silver nitrate pencils were becoming standard equipment for surgeons in the

19th century. Also in that same era, J. N. Rust was the first to treat third degree burns with a dilute solution of silver nitrate. Rust claimed that the application of silver nitrates immediately gave rise to an artificial epidermis. Early in the 20th century, silver foil was used to treat burns as well. Doctors appreciated the foil's pain-killing effects, anti-bacterial properties, and good cosmetic results.[47] In 1884, German obstetrician C.S.F. Crede administered a 1% silver nitrate eye solution to infants to reduce cases of ophthalmia neonatorum. His treatment was so effective that the incidence of eye disease in infants dropped to 0.2%, almost preventing infant blindness. Crede's remedy is still used today.[40, 41, 48] Before 1939, over 96 different silver medicinals were marketed in topical, intravenous, and oral applications.[41] Silver compounds, like silver nitrate, were also used extensively during World War I and part of World War II to prevent infection.[40] In the late 1960's a new compound, silver sulphadiazine, was introduced by Charles Fox Jr. and it eventually became the new gold standard in burn treatment. It was originally thought that sulphadiazine itself imparted antimicrobial properties. However, when silver nitrate and sodium sulphadiazine were combined to form silver sulphadiazine, it was discovered that the sulphadiazine acted to keep silver ions in solution. Sulphadiazine allowed for slow release of silver ions into the wound at just high enough concentrations to still be an effective biocide.[49, 50] Additionally, by keeping silver ions in solution, sulphadiazine prevented the skin blackening effects experienced with silver nitrate products.[44] It is clear that the medicinal benefits of silver have been known for centuries and are being exploited to this day.

#### *2.1.3.3 Harmful Effects of Overexposure to Silver*

The use of silver was clearly on the rise in the 1900's. At about this time, harmful side effects from overexposure to silver were publicized. Excessive use of protein-bound

silver compounds was found to cause a notable discoloration of the skin called argyria. A large number of the argyria cases observed were caused by improperly prepared and unstable silver present in many of the early silver medicines .[40] The discoloration usually came after years of drinking colloidal silver formulations. Researchers subsequently learned that excess silver deposition in the form of silver granules (perhaps silver sulfide) precipitates in the dermis and mucous membranes, causing that irreversible blue-gray discoloration.[51] Once deposited in skin, silver remains immobile and accumulates with age and use of the silver product.[52] Argyria is rare and most sources site that other than discoloration, overexposure to silver is fairly innocuous, although some disagree.[53, 54]

The US Food and Drug Administration has stated that over-the-counter products containing silver are frequently misbranded and are not always safe or effective.[55] This debate has spawned many discussions, and an excellent summary of the health effects of silver has been prepared by the Committee for the Responsible Use of Silver in Health. The reader is directed to the Committee's sponsored site at www.silverfacts.com for more information.

As discussed above, silver has a long history of use as an antibacterial and therapeutic agent. Although its use in excess can have unwanted effects, many researchers have renewed interest in employing it for an amazing variety of different applications. Recent advances demonstrate the use of silver, silver alloys, conjugates, and complexes as dental biomaterials[56, 57], anti-bacterial agents used in conjunction with biomedical implants[58-61], therapeutic agents in the treatment of burns[62], and anti-viral[63, 64] (even anti-HIV) agents.

### *2.1.3.4 Cytotoxicity of Silver*

Despite the widespread use of silver over the centuries and its resurgence for use in antibacterial applications, the use of silver in biomedical applications remains controversial as some *in vitro* studies have shown silver to exhibit cytotoxic effects.[65, 66] Despite these findings, silver continues to be used in myriad applications such as silver coated catheters, orthopedic implants, and many medical devices.[61, 67, 68] Other studies have shown silver to be non-cytotoxic[38, 69, 70] in these formulations *in vitro*, but no concrete finding or consensus has been reached in the community. Most probably, the surface properties of the silver compound being used and the form of silver (i.e. nanosilver, bulk silver, or silver salts) ultimately determine its impact on nearby cells. Therefore, whatever specific silver formulation that is proposed must be tested extensively *in vitro* and *in vivo* before it can be accepted as safe. *In vitro* cytoxicity results with the various silver nanosystems tested here can be found in Chapters 3, 4, and 8.

In conclusion, silver was incorporated into the CIT-NS design to impart light absorption properties in the NIR, making the nanocage system a photoacoustic contrast agent. Silver has other properties that can also be exploited. Silver is more reactive than gold, which is possibly why it has cytotoxic effects in some cases. But that same reactivity also leads to silver degradation in the body. Details of degradation are covered in Chapter 8; but it is possible that if silver degrades, the entire CIT-NS represents one of the first degradable photoacoustic contrast nanosystems. Furthermore, noble metals like silver and gold bind readily to free thiol groups in solution, making covalent thiolate bonds.[71] Therefore, free thiol groups on a targeting moiety or polymer coating can be grafted to the surface of silver with ease. In summary, silver imparts photoacoustic contrast properties to the CIT-NS, it degrades in the body, and it provides a surface for

facile bioconjugation; furthermore, despite the controversy over its use, silver remains a viable solution to several biomedical problems.

### 2.1.4 Exterior Coatings and Targeting Moieties

In order to successfully navigate through the bloodstream and find its intended target cells, the CIT-NS must have exterior coatings and targeting moieties grafted directly on its surface. These exterior coatings help accomplish two goals: (1) to increase the circulation time of the nanosystem in the bloodstream by limiting recognition and clearance by the reticuloendothelial system (RES) and (2) to increase the likelihood of the nanosystem reaching and interacting with its intended target cells or diseased site.

Grafting poly(ethylene glycol) (PEG) chains to the surface of a nanosystem is one of the most well characterized methods for increasing its circulation time in the bloodstream. Once the surface of a nanosystem is covered with a brush[71] layer of hydrophilic PEG chains, the zeta potential of the system decreases to zero and thus, the nanoparticle surface is neutrally charged. This neutral, non-reactive surface helps repel proteins by steric repulsion forces, limiting opsonization in the bloodstream. Opsonization is the depositing of opsonin proteins on the surface of a foreign body. It is the first step in a long cascade of biological events that leads to recognition by the RES and clearance of the nanosystem out of the bloodstream by macrophages of the mononuclear phagocytic system. PEG chains in the molecular weight range above 2000 Da are effective in limiting opsonization and increasing blood circulation time for various nanosystems.[72, 73] As mentioned above, grafting PEG chains to the surface of the CIT-NS can be easily accomplished through using methyl-PEG-SH molecules that readily form thiolate bonds at the silver surface.

When designing nanoystems it is challenging to construct a nanoparticle that has both limited uptake by the RES in the bloodstream and yet excellent recognition and interaction with its intended target site (i.e. cancerous cells, angiogensis, etc.). Unfortunately, many targeting moieties, namely antibodies or antibody fragments, will induce a RES response *in vivo*. Therefore, most nanosystem designs aim to tightly control and limit the number of targeting moieties on the surface of the nanosystem so that large brush layers of PEG can still be incorporated on the surface. Combining the targeting moiety and PEG on the surface in this way strikes a balance between the long circulation time needed in the bloodstream and the molecular specificity required for the target.

Several different targeting moieties have been proposed to make nanosystems molecularly sensitive to pancreatic cancer cells. This molecular sensitivity is usually accomplished by grafting a protein, antibody, or molecule to the nanosystem that can recognize and interact with receptors or upregulated proteins on the surface of cancer cells. Listed here are several cell surface molecules known to be upregulated by pancreatic cancer cell lines: Mucin 1 (a transmembrane glycoprotein)[74], F19 antigen (a cell surface glycoprotein called fibroblast activation protein that is highly expressed by the stromal tissue of pancreatic cancer)[75], claudin-4 (a cell surface protein found in tight junctions that is overexpressed in both primary and metastatic pancreatic cancer cell lines)[76-78], CD71 (transferrin receptors)[77], gastrin receptors[79], IGF-1R (an insulin-like growth factor receptor)[80], and EGFR (epidermal growth factor receptor).[6, 81] Because EGFR is overexpressed throughout the various stages of pancreatic cancer growth and metastasis, the antibody to the EGFR (anti-EGFR) was chosen as the first intended targeting moiety for the CIT-NS.

## 2.2 SYNERGISTIC ASPECTS OF THE CIT-NS DESIGN

The combination of the CIT-NS with photoacoustic imaging provides several synergies that could be exploited to better treat cancer. These effects range from synergies resulting from integration with ultrasound technologies, lasers, and from the CIT-NS design itself.

### 2.2.1 Combining the CIT-NS with Ultrasound

Ultrasound can sonoporate cell membranes, making them more permeable to drugs or nanoparticles. Studies have shown increased killing effects when chemotherapeutic drugs were delivered in the presence of ultrasound.[82-84] To realize its full potential for imaging contrast enhancement, the CIT-NS must be used in conjunction with a photoacoustic imaging device which uses ultrasound transducers by design. Therefore, once the CIT-NS has accumulated in the tumor site, the cancer cells can be sensitized to nanoparticle and chemotherapeutic drug delivery using that same ultrasound system. Furthermore, high intensity, focused ultrasound (HIFU) can also be used to help enhance nanoparticle accumulation in the cancer region. HIFU creates cavitation, forcing holes to form between cells in the endothelial lining of blood vessels. However, HIFU treatment has also caused increased metastasis *in vivo*[85], so its use with the CIT-NS should be approached with caution. Overall, combining the CIT-NS with ultrasound provides a means to increase the drug's therapeutic effect and uptake in cancerous cells.

### 2.2.2 Triggered Drug Release and other Photothermal Effects

The CIT-NS is designed to work in conjunction with a photoacousic imaging device that is reliant on laser light delivery. This laser light can have synergistic effects when combined with the CIT-NS. Interestingly, PLGA has a glass transition temperature (Tg) of ~40-45°C. This Tg is only several degrees above body temperature. When

irradiated with laser light at the peak plasmon resonance of the CIT-NS, the temperature of the nanosystem is expected to instantaneously and temporarily rise to several hundred degrees Kelvin[86], well above the Tg for PLGA. Therefore, this heating could cause the polymer to become glassy and release drugs from its matrix. Thus, drug delivery from the CIT-NS, which would usually be carried out by simple diffusion, could be enhanced and even triggered at the diseased site using light. Furthermore, the heat generated by the CIT-NS absorbing the laser light has other therapeutic benefits. For instance, a pulsed laser that only induces temporary changes in temperature could be replaced with a continuous wave (CW) laser. That CW laser can be used to make the CIT-NS heat up and cause hyperthermia in the cancer cells around them. This process of heating nanoparticles near cells to induce cell death is a well-known procedure called photothermal therapy. Photothermal therapy using gold nanoshells[87] on patients with head and neck cancers is already in Phase I clinical trials. In short, laser light can be used to enhance cancer therapy in two ways: (1) to trigger drug delivery from the CIT-NS and (2) to use the CIT-NS as a photothermal therapy agent, killing cancer cells via hyperthermia.

### 2.2.3 Silver Nanoparticles and Ionizing Radiation

In addition to silver serving as a multifunctional imaging contrast and photothermal agent, silver nanoparticles can also sensitize cells to ionizing radiation (IR). When IR is incident upon cells labeled with silver nanoparticles, some hypothesize that silver ions elute from the nanoparticles and interact with ATP, causing production of reactive oxygen species that ultimately leads to cell death. Interestingly, silver nanoparticles sensitized cells to IR induced killing, while gold nanoparticles of similar size had no sensitizing effects.[88] Therefore, if the CIT-NS was used in combination with

common radiation therapy techniques, silver labeled cancer cells would be sensitized, enhancing the IR's therapeutic effect.

### 2.2.4 Biodegradation of the CIT-NS

The CIT-NS was designed to degrade over time in the body. All of the organic components of the nanosystem from the drugs to the PLGA, anti-EGFR, and PEG will eventually break down and clear the body through natural mechanisms such as the citric acid cycle, RES or renal clearance, etc. However, silver's degradation *in vivo* in nano form is not well characterized or understood. Once the CIT-NS enters a cell, lysosomes will likely tear the exterior coatings from the silver surface, creating a bare "naked" silver interface.[89] This surface will likely oxidize and pit in the acidic lysosomal compartment and if the silver is not completely degraded in the cell, it will most likely get recycled out of the cell into the extracellular space. Interactions with other enzymes or proteins in that space will further degrade silver. Unlike gold, which is unreactive and known to not degrade in the body, silver is more reactive and is known to degrade in salt solutions. Degradation products of metallic nano silver formulations likely include silver oxides or $Ag^+$ ions. Silver oxides can be cleared by the body, but $Ag^+$ ions are very reactive and will interact with proteins and enzymes, possibly causing them to lose function – this is one of the suspected mechanisms of silver's controversial cytotoxicity.[90] However, the antibacterial properties of $Ag^+$ ions have been well understood for centuries[39, 42], which explains the extensive use of silver coated catheters, orthopedic implants, and many medical devices[61, 67, 68]. In fact, having silver in place in the pancreas following tumor resection could help fight bacterial infections should they arise. In short, the entire CIT-NS is expected to degrade over weeks in the body, making this system one of the few degradable nanosystems that incorporate metal contrast agents.

## 2.3 LIMITATIONS OF THE CIT-NS DESIGN

The CIT-NS is limited by two properties: size and drug diffusion. The size of the endothelial gap junctions through which nanoparticles must extravasate to reach cancer were reported to be between 300 nm to 700 nm.[91] Therefore, the diameter of the CIT-NS should be designed to remain below this size range. PLGA core particles with entrapped drugs synthesized via emulsion techniques are generally between 150 nm and 250 nm in diameter. Adding a layer or silver and exterior coatings to the PLGA could increase the diameter by up to 100 nm. Therefore, keeping the nanosystem small by synthesizing smaller PLGA cores with thin silver layers is critical for this nanosystem to be viable *in vivo*. Even at these small sizes, large amounts of the CIT-NS are expected to accumulate in the liver and spleen, in addition to the tumor. Thus, organ specific toxicity will need to be assessed prior to *in vivo* application. Furthermore, the larger the nanosystem becomes, the more difficult it is to keep attractive forces between the particles from causing agglomeration or flocculation between nanoparticles in solution.

The other limiting factor in the CIT-NS design is the mechanism of drug delivery. In the absence of triggering drug release using electromagnetic energy and heating, drug release will occur via diffusion out of the bulk eroding PLGA polymer matrix. This drug diffusion will start the instant the CIT-NS is suspended in an aqueous environment. Therefore, ways to control or to limit drug diffusion prior to the nanosystem reaching its intended disease site are critical. One way to limit drug release through the CIT-NS is to control the confluency of the silver on the surface of PLGA. In theory, if the silver were a completely confluent shell with no holes around PLGA, then no drug diffusion would take place. Therefore, if the silver seeds coating the PLGA core exterior are very close together, this design could help limit and considerably slow drug release out of the

nanosystem. Controlling the drug release will allow the nanosystem time to accumulate in the tumor before significant drug is lost.

## 2.4 CONCLUSIONS

The CIT-NS is a complex nanosystem inherently built for functionality and synergy between it and USPA imaging. The advantage of such a system clinically is the ability to visualize drug delivery to pancreatic cancer *in vivo*, non-invasively. Furthermore, the ability of the nanosystem to also act as both a photothermal agent and an IR-sensitizing agent gives clinicians even more therapeutic options using this nanosystem. The limitations of the nanosystem are its overall size and drug delivery method, but these obstacles can be mitigated if synthetic techniques are employed to keep the nanosystem small and its silver tightly packed on the surface (see Chapter 4 for more synthesis details).

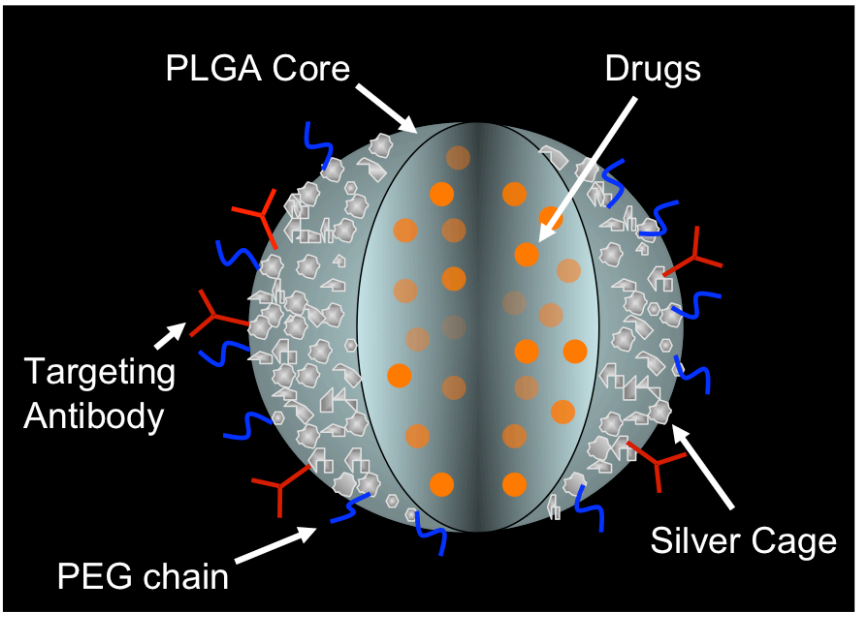


Figure 2.1: An illustration of the Combined Imaging and Therapy Nanocage System (CIT-NS) and its components.

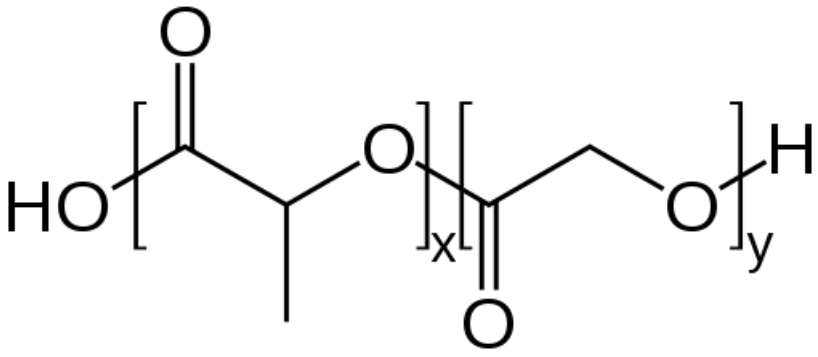


Figure 2.2: The chemical structure of poly(lactic-co-glycolic) acid where x represents the number of lactide units and y represents the number of glycolide units (x=y for the PLGA used in the CIT-NS).

## 2.5 REFERENCES


1. L. Brannon-Peppas and J. O. Blanchette, "Nanoparticle and targeted systems for cancer therapy," Adv Drug Deliv Rev 56(11), 1649-1659 (2004)
2. L. R. Hirsch, A. M. Gobin, A. R. Lowery, F. Tam, R. A. Drezek, N. J. Halas and J. L. West, "Metal nanoshells," Ann. Biomed. Eng. 34(1), 15-22 (2006)
3. Z. Liu, H. Song, L. Yu and L. Yang, "Fabrication and near-infrared photothermal conversion characteristics of Au nanoshells," Appl. Phys. Lett. 86(113109 (2005)
4. E. Bria, M. Milella, A. Gelibter, F. Cuppone, M. S. Pino, E. M. Ruggeri, P. Carlini, C. Nistico, E. Terzoli, F. Cognetti and D. Giannarelli, "Gemcitabine-based combinations for inoperable pancreatic cancer: Have we made real progress?: A meta-analysis of 20 phase 3 trials," Cancer 110(3), 525-533 (2007)
5. T. Ishikawa, "Is it relevant that intra-arterial chemotherapy may be effective for advanced pancreatic cancer?," World J Gastroenterol 13(32), 4306-4309 (2007)
6. C. R. Patra, R. Bhattacharya, E. Wang, A. Katarya, J. S. Lau, S. Dutta, M. Muders, S. Wang, S. A. Buhrow, S. L. Safgren, M. J. Yaszemski, J. M. Reid, M. M. Ames, P. Mukherjee and D. Mukhopadhyay, "Targeted delivery of gemcitabine to pancreatic adenocarcinoma using cetuximab as a targeting agent," Cancer Res. 68(6), 1970-1978 (2008)
7. X. Wang, L. Yang, Z. G. Chen and D. M. Shin, "Application of nanotechnology in cancer therapy and imaging," CA. Cancer J. Clin. 58(2), 97-110 (2008)
8. S. Nie, Y. Xing, G. J. Kim and J. W. Simons, "Nanotechnology applications in cancer," Annu Rev Biomed Eng 9(257-288 (2007)
9. A. L. Doiron, K. Chu, A. Ali and L. Brannon-Peppas, "Preparation and initial characterization of biodegradable particles containing gadolinium-DTPA contrast agent for enhanced MRI," Proc. Natl. Acad. Sci. U. S. A. 105(45), 17232-17237 (2008)
10. A. L. Doiron, K. A. Homan, S. Emelianov and L. Brannon-Peppas, "Poly(Lactic-co-Glycolic) Acid as a Carrier for Imaging Contrast Agents," Pharm. Res. 26(3), 674-682 (2009)
11. F. Danhier, N. Lecouturier, B. Vroman, C. Jerome, J. Marchand-Brynaert, O. Feron and V. Preat, "Paclitaxel-loaded PEGylated PLGA-based nanoparticles: in vitro and in vivo evaluation," J Control Release 133(1), 11-17 (2009)
12. R. C. Mundargi, V. R. Babu, V. Rangaswamy, P. Patel and T. M. Aminabhavi, "Nano/micro technologies for delivering macromolecular therapeutics using poly(D,L-lactide-co-glycolide) and its derivatives," J Control Release 125(3), 193-209 (2008)

13. I. Bala, S. Hariharan and M. N. Kumar, "PLGA nanoparticles in drug delivery: the state of the art," Crit. Rev. Ther. Drug Carrier Syst. 21(5), 387-422 (2004)

14. S. Zhou, X. Liao, X. Li, X. Deng and H. Li, "Poly-D,L-lactide-co-poly(ethylene glycol) microspheres as potential vaccine delivery systems," J Control Release 86(2-3), 195-205 (2003)

15. L. Brannon-Peppas, "Polymers in Controlled Drug Delivery," Medical Plastics and Biomaterials 4(34-44 (1997)

16. M. S. Shive and J. M. Anderson, "Biodegradation and biocompatibility of PLA and PLGA microspheres," Adv Drug Deliv Rev 28(1), 5-24 (1997)

17. L. Brannon-Peppas, "Recent advances on the use of biodegradable microparticles and nanoparticles in controlled drug delivery," International Journal of Pharmaceutics 116(1), 1-9 (1995)

18. M. Chasin and R. S. Langer, Biodegradable polymers as drug delivery systems, Marcel Dekker, New York (1990).

19. D. Blanco and M. Alonso, "Protein encapsulation and release from poly (lactide-co-glycolide) microspheres: Effect of the protein and polymer properties and of the co-encapsulation of surfactants," Eur. J. Pharm. Biopharm. 45(3), 285-294 (1998)

20. M. Vert, S. Li and H. Garreau, "Recent advances in the field of lactic acid/glycolic acid polymer-based therapeutic systems," Macromol Symp 98(633 (1995)

21. S. S. Feng, L. Mu, K. Y. Win and G. Huang, "Nanoparticles of biodegradable polymers for clinical administration of paclitaxel," Current medicinal chemistry 11(4), 413-424 (2004)

22. R. A. Jain, "The manufacturing techniques of various drug loaded biodegradable poly(lactide-co-glycolide) (PLGA) devices," Biomaterials 21(23), 2475-2490 (2000)

23. J. Panyam and V. Labhasetwar, "Biodegradable nanoparticles for drug and gene delivery to cells and tissue," Advanced drug delivery reviews 55(3), 329-347 (2003)

24. J. K. Vasir and V. Labhasetwar, "Biodegradable nanoparticles for cytosolic delivery of therapeutics," Adv Drug Deliv Rev 59(8), 718-728 (2007)

25. J. Panyam, W. Z. Zhou, S. Prabha, S. K. Sahoo and V. Labhasetwar, "Rapid endo-lysosomal escape of poly(DL-lactide-co-glycolide) nanoparticles: implications for drug and gene delivery," FASEB J. 16(10), 1217-1226 (2002)

26. T. Betancourt, B. Brown and L. Brannon-Peppas, "Doxorubicin-loaded PLGA nanoparticles by nanoprecipitation: preparation, characterization and in vitro evaluation," Nanomedicine 2(2), 219-232 (2007)

27. V. Lassalle and M. Ferreira, "PLA nano and microparticles for drug delivery: An overview of the methods of preparation," Macromol. Biosci. 7(6), 767-783 (2007)

28. G. Silva, P. Ducheyne and R. Reis, "Materials in particulate form for tissue engineering. 1. Basic concepts," Journal of Tissue Engineering and Regenerative Medicine 1(1), 4-24 (2007)

29. C. E. Astete and C. M. Sabliov, "Synthesis and characterization of PLGA nanoparticles," J. Biomater. Sci. Polym. Ed. 17(3), 247-289 (2006)

30. T. Betancourt, B. Brown and L. Brannon-Peppas, "Doxorubicin-loaded PLGA nanoparticles by nanoprecipitation: preparation, characterization and in vitro evaluation," Nanomedicine (London, England) 2(2), 219-232 (2007)

31. D. T. Birnbaum, J. D. Kosmala and L. Brannon-Peppas, "Optimization of preparation techniques for poly(lactic acid-co-glycolic acid) nanoparticles," Journal of Nanoparticle Research 2(173-181 (2000)

32. L. Brannon-Peppas and D. T. Birnbaum, "Process to scale-up the production of biodegradable nanoparticles," Abstract, American Institute of Chemical Engineers Meeting (2000)

33. A. L. Doiron, K. Chu, A. Ali and L. Brannon-Peppas, "Preparation and initial characterization of biodegradable particles containing gadolinium-DTPA contrast agent for enhanced MRI," Proceedings of the National Academy of Sciences (in press)

34. C. Loo, A. Lin, L. Hirsch, M. H. Lee, J. Barton, N. Halas, J. West and R. Drezek, "Nanoshell-enabled photonics-based imaging and therapy of cancer," Technol Cancer Res Treat 3(1), 33-40 (2004)

35. L. R. Hirsch, R. J. Stafford, J. A. Bankson, S. R. Sershen, B. Rivera, R. E. Price, J. D. Hazle, N. J. Halas and J. L. West, "Nanoshell-mediated near-infrared thermal therapy of tumors under magnetic resonance guidance," Proc. Natl. Acad. Sci. U. S. A. 100(23), 13549-13554 (2003)

36. H. Liao, C. Nehl and J. Hafner, "Biomedical applications of plasmon resonant metal nanoparticles," Nanomedicine 1(2), 201-208 (2006)

37. Z.-j. Jiang and C.-y. Liu, "Seed-mediated growth technique for the preparation of a silver nanoshell on a silica sphere," J. Phys. Chem. B 107(12411-12415 (2003)

38. D. W. Brett, "A discussion of silver as an antimicrobial agent: alleviating the confusion," Ostomy/wound management 52(1), 34-41 (2006)

39. Hippocrates, "On Ulcers," (1994-2000), http://classics.mit.edu/Browse/browse-Hippocrates.html

40. F. Key, "A brief history of the health support uses of silver," in Secondary A brief history of the health support uses of silver Secondary F. Key, Ed., Place Published, http://www.silver-colloids.com/Pubs/history-silver.html.

41. E. Rentz, "Historic perspectives on clinical use and efficacy of silver," in Secondary Historic perspectives on clinical use and efficacy of silver Secondary E. Rentz, Ed., Place Published, http://lifesilver.com/history.htm.

42. J. L. Clement and P. S. Jarrett, "Antibacterial silver," Metal-Based Drugs 1(467-482 (1994)

43. J. Hill, "Colloidal silver: a literature review: medical uses, toxicology & manufacture," (2004), http://www.clspress.com/publications.html.

44. S. Silver, T. Phung le and G. Silver, "Silver as biocides in burn and wound dressings and bacterial resistance to silver compounds," Journal of industrial microbiology & biotechnology 33(7), 627-634 (2006)

45. SAMSUNG, "SAMSUNG Laundry Featuring SilverCare™ Technology," in Secondary SAMSUNG Laundry Featuring SilverCare™ Technology Secondary SAMSUNG, Ed., Place Published (2006), http://www.samsung.com/PressCenter/PressRelease/PressRelease.asp?seq=20060213_0000233684.

46. J. W. Rhim, S. I. Hong, H. M. Park and P. K. Ng, "Preparation and characterization of chitosan-based nanocomposite films with antimicrobial activity," Journal of agricultural and food chemistry 54(16), 5814-5822 (2006)

47. H. J. Klasen, "Historical review of the use of silver in the treatment of burns. I. Early uses," Burns 26(2), 117-130 (2000)

48. J. Brussieux, A. Boisivon, H. P. Theron, C. Faidherbe, N. Machado and B. Michelon, "Prevention of neonatal conjunctivitis. A comparative clinical and bacteriologic study of 2 eyedrops: Silver nitrate and oxytetracycline chlorhydrate," Annales de Pediatrie 38(9), 637-641 (1991)

49. H. J. Klasen, "A historical review of the use of silver in the treatment of burns. II. Renewed interest for silver," Burns 26(2), 131-138 (2000)

50. C. L. Fox, Jr. and S. M. Modak, "Mechanism of silver sulfadiazine action on burn wound infections," Antimicrobial Agents and Chemotherapy 5(6), 582-588 (1974)

51. S. Silver, "Bacterial silver resistance: molecular biology and uses and misuses of silver compounds," FEMS Microbiology Reviews 27(2-3), 341-353 (2003)

52. M. Walker, C. A. Cochrane, P. G. Bowler, D. Parsons and P. Bradshaw, "Silver deposition and tissue staining associated with wound dressings containing silver," Ostomy Wound Management 52(1), 42-44, 46-50 (2006)

53. P. L. Drake and K. J. Hazelwood, "Exposure-related health effects of silver and silver compounds: A review," The Annals of Occupational Hygiene 49(7), 575-585 (2005)

54. K. D. Rosenman, A. Moss and S. Kon, "Argyria: Clinical implications of exposure to silver nitrate and silver oxide," J Occup Med 21(6), 430-435 (1979)

55. A. Gupta and S. Silver, "Silver as a biocide: will resistance become a problem?," Nature Biotechnology 16(10), 888 (1998)

56. F. Eichmiller, "Research into non-mercury containing metallic alternatives," Operative Dentistry 6(111-118 (2001)

57. H. J. Mueller, "In vitro tarnish and corrosion of a consolidated silver material for direct filling applications," Dent Mater 17(1), 60-70 (2001)

58. R. O. Darouiche, "Anti-infective efficacy of silver-coated medical prostheses," Clin Infect Dis 29(6), 1371-1377 (1999)

59. R. O. Darouiche, "Treatment of infections associated with surgical implants," The New England Journal of Medicine 350(14), 1422-1429 (2004)

60. F. Furno, K. S. Morley, B. Wong, B. L. Sharp, P. L. Arnold, S. M. Howdle, R. Bayston, P. D. Brown, P. D. Winship and H. J. Reid, "Silver nanoparticles and polymeric medical devices: A new approach to prevention of infection?," The Journal of Antimicrobial Chemotherapy 54(6), 1019-1024 (2004)

61. J. M. Schierholz, L. J. Lucas, A. Rump and G. Pulverer, "Efficacy of silver-coated medical devices," The Journal of Hospital Infection 40(4), 257-262 (1998)

62. B. S. Atiyeh, M. Costagliola, S. N. Hayek and S. A. Dibo, "Effect of silver on burn wound infection control and healing: Review of the literature," Burns 33(2), 139-148 (2007)

63. J. L. Elechiguerra, J. L. Burt, J. R. Morones, A. Camacho-Bragado, X. Gao, H. H. Lara and M. J. Yacaman, "Interaction of silver nanoparticles with HIV-1," Journal of Nanobiotechnology [electronic resource] 3(6 (2005)

64. R. W. Sun, R. Chen, N. P. Chung, C. M. Ho, C. L. Lin and C. M. Che, "Silver nanoparticles fabricated in Hepes buffer exhibit cytoprotective activities toward HIV-1 infected cells," Chemical Communications (Cambridge, England) 40), 5059-5061 (2005)

65. R. G. Seipelt, J. F. Vazquez-Jimenez, I. M. Seipelt, A. Franke, K. Chalabi, F. A. Schoendube and B. J. Messmer, "The St. Jude "Silzone" valve: Midterm results in

treatment of active endocarditis," The Annals of Thoracic Surgery 72(3), 758-762; discussion 762-753 (2001)

66. C. N. Kraft, M. Hansis, S. Arens, M. D. Menger and B. Vollmar, "Striated muscle microvascular response to silver implants: A comparative in vivo study with titanium and stainless steel," Journal of Biomedical Materials Research 49(2), 192-199 (2000)

67. C. A. Collinge, G. Goll, D. Seligson and K. J. Easley, "Pin tract infections: silver vs uncoated pins," Orthopedics 17(5), 445-448 (1994)

68. G. Gosheger, J. Hardes, H. Ahrens, A. Streitburger, H. Buerger, M. Erren, A. Gunsel, F. H. Kemper, W. Winkelmann and C. Von Eiff, "Silver-coated megaendoprostheses in a rabbit model--an analysis of the infection rate and toxicological side effects," Biomaterials 25(24), 5547-5556 (2004)

69. L. C. Fung, A. E. Khoury, S. I. Vas, C. Smith, D. G. Oreopoulos and M. W. Mittelman, "Biocompatibility of silver-coated peritoneal dialysis catheter in a porcine model," Perit Dial Int 16(4), 398-405 (1996)

70. M. Bosetti, A. Masse, E. Tobin and M. Cannas, "Silver coated materials for external fixation devices: in vitro biocompatibility and genotoxicity," Biomaterials 23(3), 887-892 (2002)

71. C. S. Levin, S. W. Bishnoi, N. K. Grady and N. J. Halas, "Determining the conformation of thiolated poly(ethylene glycol) on Au nanoshells by surface-enhanced Raman scattering spectroscopic assay," Anal. Chem. 78(10), 3277-3281 (2006)

72. D. E. Owens, 3rd and N. A. Peppas, "Opsonization, biodistribution, and pharmacokinetics of polymeric nanoparticles," Int. J. Pharm. 307(1), 93-102 (2006)

73. G. von Maltzahn, J. H. Park, A. Agrawal, N. K. Bandaru, S. K. Das, M. J. Sailor and S. N. Bhatia, "Computationally guided photothermal tumor therapy using long-circulating gold nanorod antennas," Cancer Res. 69(9), 3892-3900 (2009)

74. R. F. Chen, Z. H. Li, Q. H. Pan, J. J. Zhou, Q. B. Tang, F. Y. Yu, Q. B. Zhou, J. Wang and J. S. Chen, "In vivo Radioiodide Imaging and Treatment of Pancreatic Cancer Xenografts after MUC1 Promoter-Driven Expression of the Human Sodium-Iodide Symporter," Pancreatology 7(5-6), 505-513 (2007)

75. W. Eck, G. Craig, A. Sigdel, G. Ritter, L. J. Old, L. Tang, M. F. Brennan, P. J. Allen and M. D. Mason, "PEGylated gold nanoparticles conjugated to monoclonal F19 antibodies as targeted labeling agents for human pancreatic carcinoma tissue," ACS Nano 2(11), 2263-2272 (2008)

76. L. S. Nichols, R. Ashfaq and C. A. Iacobuzio-Donahue, "Claudin 4 protein expression in primary and metastatic pancreatic cancer: Support for use as a therapeutic target," Am. J. Clin. Pathol. 121(2), 226-230 (2004)

77. J. Qian, K. T. Yong, I. Roy, T. Y. Ohulchanskyy, E. J. Bergey, H. H. Lee, K. M. Tramposch, S. He, A. Maitra and P. N. Prasad, "Imaging pancreatic cancer using surface-functionalized quantum dots," J Phys Chem B 111(25), 6969-6972 (2007)

78. P. Michl, C. Barth, M. Buchholz, M. M. Lerch, M. Rolke, K. H. Holzmann, A. Menke, H. Fensterer, K. Giehl, M. Lohr, G. Leder, T. Iwamura, G. Adler and T. M. Gress, "Claudin-4 expression decreases invasiveness and metastatic potential of pancreatic cancer," Cancer Res. 63(19), 6265-6271 (2003)

79. B. M. Barth, R. Sharma, E. I. Altinoglu, T. T. Morgan, S. S. Shanmugavelandy, J. M. Kaiser, C. McGovern, G. L. Matters, J. P. Smith, M. Kester and J. H. Adair, "Bioconjugation of calcium phosphosilicate composite nanoparticles for selective targeting of human breast and pancreatic cancers in vivo," ACS Nano 4(3), 1279-1287 (2010)

80. D. B. Ulanet, D. L. Ludwig, C. R. Kahn and D. Hanahan, "Insulin receptor functionally enhances multistage tumor progression and conveys intrinsic resistance to IGF-1R targeted therapy," Proc. Natl. Acad. Sci. U. S. A. 107(24), 10791-10798 (2010)

81. S. Bhattacharyya, R. Bhattacharya, S. Curley, M. A. McNiven and P. Mukherjee, "Nanoconjugation modulates the trafficking and mechanism of antibody induced receptor endocytosis," Proc. Natl. Acad. Sci. U. S. A. 107(33), 14541-14546 (2010)

82. I. V. Larina, B. M. Evers, T. V. Ashitkov, C. Bartels, K. V. Larin and R. O. Esenaliev, "Enhancement of Drug Delivery in Tumors by Using Interaction of Nanoparticles with Ultrasound Radiation," Technology in Cancer Research and Treatment 4(2), 217-226 (2005)

83. I. V. Larina, B. M. Evers and R. O. Esenaliev, "Optimal drug and gene delivery in cancer cells by ultrasound-induced cavitation," Anticancer Res. 25(1A), 149-156 (2005)

84. T. Yoshida, T. Kondo, R. Ogawa, L. B. Feril, Jr., Q. L. Zhao, A. Watanabe and K. Tsukada, "Combination of doxorubicin and low-intensity ultrasound causes a synergistic enhancement in cell killing and an additive enhancement in apoptosis induction in human lymphoma U937 cells," Cancer Chemother. Pharmacol. (2007)

85. H. Hancock, M. R. Dreher, N. Crawford, C. B. Pollock, J. Shih, B. J. Wood, K. Hunter and V. Frenkel, "Evaluation of pulsed high intensity focused ultrasound exposures on metastasis in a murine model," Clin. Exp. Metastasis 26(7), 729-738 (2009)

86. C. M. Pitsillides, E. K. Joe, X. Wei, R. R. Anderson and C. P. Lin, "Selective cell targeting with light-absorbing microparticles and nanoparticles," Biophys. J. 84(6), 4023-4032 (2003)

87. A. M. Gobin, M. H. Lee, N. J. Halas, W. D. James, R. A. Drezek and J. L. West, "Near-infrared resonant nanoshells for combined optical imaging and photothermal cancer therapy," Nano Lett 7(7), 1929-1934 (2007)

88. R. Xu, J. Ma, X. Sun, Z. Chen, X. Jiang, Z. Guo, L. Huang, Y. Li, M. Wang, C. Wang, J. Liu, X. Fan, J. Gu, X. Chen, Y. Zhang and N. Gu, "Ag nanoparticles sensitize IR-induced killing of cancer cells," Cell Res. 19(8), 1031-1034 (2009)

89. A. E. Nel, L. Madler, D. Velegol, T. Xia, E. M. Hoek, P. Somasundaran, F. Klaessig, V. Castranova and M. Thompson, "Understanding biophysicochemical interactions at the nano-bio interface," Nat Mater 8(7), 543-557 (2009)

90. R. Bhattacharya and P. Mukherjee, "Biological properties of "naked" metal nanoparticles," Adv Drug Deliv Rev 60(11), 1289-1306 (2008)

91. I. Brigger, C. Dubernet and P. Couvreur, "Nanoparticles in cancer therapy and diagnosis," Adv Drug Deliv Rev 54(5), 631-651 (2002)

# Chapter 3: Preliminary Testing of the CIT-NS design for enhancing PA Imaging

The CIT-NS introduced in Chapter 2 is a complex nanosystem requiring significant research to synthesize. Before such a complex nanosystem is built, it is prudent to first test aspects of the design with similar nanosystems that are easier to synthesize. This chapter is the result of one such test in which a silver cage is deposited on a silica core instead of a PLGA core. The purpose of this preliminary test is to prove that a silver-silica nanocage can (1) be biocompatible and (2) provide imaging contrast enhancement for photoacoustic imaging. If a large near infrared absorption cross-section is demonstrated for these silver-silica (cage-core) particles, and if they create strong photoacoustic transients in *ex vivo* studies without signs of cytotoxicity, then building the CIT-NS with all its complexity is warranted.

## 3.1 INTRODUCTION

Photoacoustic contrast agent development has grown with the adoption of the photoacoustic imaging technique over the last decade. The surge of research in the fields of nanoscience and nanotechnology has yielded inorganic nanoparticles of various shapes and forms including shells, rods, and crescents with tunable absorption properties.[1-5] These nanosystems absorb light strongly in the near infrared (NIR) spectrum, where absorption from native tissue is minimized.[6] They are ideally suited as photoacoustic contrast agents since the absorption cross-section of myriad nanostructures can be multiples to orders of magnitude higher than the surrounding native tissue at NIR wavelengths. Reviews of the basic theory and principles of using nanotechnology in conjunction with photoacoustics are available[7, 8] and were highlighted in Chapter 1.

Most often, nanoparticles for photoacoustic imaging contrast are administered intravenously. They accumulate at a diseased site via both "passive" and "active" mechanisms, as discussed in Chapter 1. In the case of using photoacoustic imaging to highlight cancerous tissue, passive accumulation of nanoparticles in a solid tumor occurs due to the enhanced permeability and retention (EPR) effect, where the nanoparticles get essentially trapped in the leaky and disorganized nature of the tumor vasculature and eventually extravasate through endothelial junctions into the cancerous vasculature.[9, 10] Active targeting is achieved by covalently attaching antibodies or other signaling molecules to the nanoparticles.[10-12] In the active case, in addition to the passive EPR effect, the nanoparticles accumulate in diseased tissue due to the specific affinity of the antibody for its antigen: an upregulated cell-surface receptor on the diseased cells. Nanoparticles that accumulate directly at the site of disease can provide the necessary photoacoustic contrast with healthy tissue that is critical for disease detection and diagnosis.

Photoacoustic contrast agents are naturally multifunctional since low NIR pulsed light can be used for detection and diagnosis, while continuous wave light delivery modes can be used to create photothermal tissue damage from nanoparticle heating.[13, 14] The nanosystems can be functionalized further to expand their therapeutic capability beyond photothermal mechanisms. For instance, core-shell nanoparticles[15] with tunable optical absorption properties are currently in clinical trials for photothermal therapy. These nanoshells possess an inert silica core. The CIT-NS introduced in Chapter 2 is a new multifunctional nanosystem that results from replacing the inert silica with a core capable of carrying drugs or other contrast agents (see Fig. 3.1 and note that Fig. 3.1 is a different illustration of the CIT-NS already depicted in Fig. 2.1 minus the targeting moiety

depiction). The CIT-NS could have enhanced sensitivity to multimodal imaging or treatment strategies.

The benefits of the CIT-NS could be profound; but first, a detailed analysis of the optical properties of a porous layer versus the traditional confluent noble metal shell must be performed. These preliminary experiments are necessary to prove that a silver nanocage coating similar to that in the CIT-NS design will provide near infrared absorption and hence photoacoustic contrast. Therefore, in this chapter, a porous silver "cage" coating was reduced onto a silica core and the feasibility of using this silver-silica nanosystem as a photoacoustic imaging contrast agent was evaluated. Furthermore, the biocompatibility of the silver nanosystem was explored by performing cytotoxicity tests *in vitro*.

## 3.2 METHODS

### 3.2.1 Coating Silica with a Porous Silver Layer

Various sizes of the silver-silica nanosystem were produced by reducing silver onto silica spheres ranging in diameter from 180 nm to 520 nm. The procedures for coating the smallest (180 nm) and the largest (520 nm) spheres are presented along with generalized rules for scaling the synthesis to any size in between. The silica amine (-$NH_2$ surface groups) was purchased from two vendors: Corpuscular, Inc. or Bangs Laboratories, Inc. A modified stoichiometrically controlled method[16] was used to reduce silver onto silica in a porous, cage-like fashion. The silica spheres (20 $\mu$l of 2.5 wt% 180 nm spheres or 1.5 mg of the 520 nm spheres) were suspended via sonication in polypropylene vials containing 30 ml of deionized ultra-filtered (18.2mΩ-cm) (DIUF) water (in all diameters of silica attempted, the total surface area of all spheres in solution was kept constant at $6.5\times10^{-3}$ $m^2$). The 180 nm spheres were placed in a 15°C water bath,

while the 520 nm spheres were placed in a 11°C bath; both batches were stirred continuously at 500 rpm (the temperature was varied according to the diameter: 15°C for spheres roughly in the 100's of nm, 14°C for spheres in the 200's of nm, and so on). Silver in the form of 0.15 M silver nitrate was added to the stirring spheres in the amount of 0.4 ml for the 180 nm spheres and 0.8 ml for the 520 nm spheres. Note that the amount (mmol) of silver to add based on silica diameter, assuming constant surface area of $6.5\times10^{-3}$ $m^2$, can be calculated as:

$$y = 0.000176x + 0.02824 \qquad (3.1)$$

where y is the mmol of silver to add and x is the diameter of silica in nm. Lastly, 50 μl of 36% glucose, and 50 μl of 3% $NH_4OH$ solutions were added. Color changes from yellow to orange-brown, and finally to grey-black were noted between 2 and 13 min after adding $NH_4OH$. The pH of the solutions initially rose to 9 upon addition of the $NH_4OH$, but then fell to 7 when the silver reduction was complete. To suppress aggregation, 200 $\mu$l of 50 mM of poly(ethylene glycol) (mPEG-SH of 5000 g/mol from Laysan Bio) was added. The nanosystem was collected and cleaned 3 times using DIUF water and a 100 kDa Millipore centrifugal filter spun at 1500g for 4 min. The nanosystem can be suspended in DIUF water and stored in a plastic vial in the dark for several weeks.

The silver-silica nanosystem was analyzed using a LEO 1530 scanning electron microscope. The ultraviolet to visible (UV-vis) absorption spectrum of the as prepared nanosystem suspended in DIUF water was captured using a Shimadzu UV-1201 spectrophotometer (the spectra obtained represent either ~$2.0\text{x}10^9$ 180 nm core particles per ml or ~$2.6\text{x}10^8$ 520 nm core particles per ml).

### 3.2.2 Photoacoustic and Ultrasound Imaging of the Silver-Silica Nanosystem

To test the feasibility of using the silver-silica nanosystem as a contrast agent for combined ultrasound and photoacoustic (USPA) imaging, a custom-made imaging system was employed (Fig. 3.2). This system inherently contained two parts: a pulsed laser system with light delivery assembly interfaced with an ultrasound array-based transducer operated by an ultrasound system capable of capturing radio frequency (RF) signals. Pulsed light was generated by an optical parametric oscillator (OPO), tunable within a 680-950 nm range. For all studies, a wavelength of 800 nm with 7 ns laser pulse duration at 10 Hz pulse repetition rate was used. The maximum laser energy per pulse was 15 $mJ/cm^2$, which is well below the maximum permissible exposure standard set by the American National Standards Institute.[17] From the OPO system, light was directed into a fiber optic bundle containing 18 individual fibers. These fibers surrounded the ultrasound transducer (7.5 MHz center frequency, 10.5 mm wide, 128 element linear array), and allowed light irradiation and sound delivery to overlap within the imaging plane. The ultrasound transducer was interfaced with a Cortex ultrasound imaging engine (Winprobe Corporation, North Palm Beach, FL, USA) capable of RF data acquisition. The pulsed laser system, integrated imaging probe, and ultrasound system with RF signal acquisition together made up the USPA system that could capture spatially co-registered photoacoustic and ultrasound RF signals needed to form both ultrasound and photoacoustic images.

To evaluate the nanosystem as a contrast agent for photoacoustic imaging, the USPA system was employed to image the nanoparticles directly injected into an *ex-vivo* canine pancreas. Specifically, the pancreas was set in a gelatin mold (only for structural stability and ease of imaging). The 180 nm silica core, silver coated particles (50 $\mu$l of $10^9$ particles/ml suspended in a warm 8% gelatin solution) were injected via needle into

the chilled pancreas, approximately 8-10 mm below the pancreas surface. The solution with nanoparticles quickly gelled inside the organ, mimicking accumulation of the nanosystem in a small tumor. Spatially co-registered ultrasound and photoacoustic RF signals were captured using the USPA system. All RF data was then beamformed and the images were plotted using conventional logarithmic (ultrasound) and linear (photoacoustic) scales.

### 3.2.3 Preparing Samples of Set Concentrations of the Nanosystem for Imaging Studies

Samples of the silver-silica nanosystem were created by incorporating the 180 nm silica core, silver coated particles in poly(vinyl alcohol) (PVA) at concentrations of $2\times10^7$, $2\times10^8$, and $2\times10^9$ particles per ml. Specifically, under continuous stirring, 8 wt% PVA (165 sf from Celvol) was dissolved in water at 70°C containing a colloidal suspension of nanoparticles. After 15 min, the solution was pulled into a 1 cc syringe. The syringes were put through four freeze-thaw cycles in which they were held at -20°C for 12 hr and then at room temperature for 12 hr. During these cycles, the PVA formed physical cross-links with itself. At the conclusion of the four cycles, firm 5 mm diameter cylindrical samples of suspended nanoparticles were removed from the syringes. Setting the nanoparticles in these PVA samples provided a physical construct that held the various concentrations of nanoparticles in place for imaging.

### 3.2.4 Cytotoxicity Testing of the Nanosystem

The breast cancer cell line MDA-MB-231 and the pancreatic cancer cell line MPanc96 were both incubated with nanoparticles and tested for cell viability. Both cell lines were cultured in vitro using Dulbecco's Modified Eagle Medium (with 4500 mg glucose/L, L-glutamine, $NaHCO_3$ and pyridoxine HCl) supplemented with 10% fetal

bovine serum and 1% HEPES buffer and were maintained at 37°C under 5% $CO_2$ in a humidified incubator. All cell culture products were purchased from Sigma. For cell viability studies, cells were seeded in a 96 well plate (each well had 5,000 cells per 100 μl of media). The cells were allowed to attach and grow in the 96 well plate for 24 hr, after which the cell media was removed and replaced with suspensions of PEGylated, silver coated 180 nm silica spheres at various concentrations representing 2 mg/ml, 1 mg/ml, 0.5 mg/ml, 0.25 mg/ml, 0.125 mg/ml, and 0 mg/ml of silver specifically (at least 5 wells were seeded with each concentration). Note that the highest silver concentration at 2 mg/ml represented ~$2\times10^{10}$ particles per ml, while the lowest silver concentration at 0.125 mg/ml represented ~$1\times10^{9}$ particles per ml. After 24 hr of incubation, the media containing the silver-silica nanosystem was removed and replaced with fresh media containing no nanoparticles. The absorbance of each well in the plate was measured at 490 nm using a Synergy HT Multimode Microplate Reader from BioTek. Then, 20 μl of a tetrazolium compound [3-(4,5-dimethylthiazol-2-yl)-5-(3-carboxymethoxyphenyl)-2-(4-sulfophenyl)-2H-tetrazolium (MTS) and an electron coupling reagent (phenazine methosulfate) PMS from the CellTiter 96® $AQ_{ueous}$ Non-Radioactive Cell Proliferation Assay (a Promega product) was added to each well. Over a period of 1.5 hr in the incubator, the MTS was bioreduced by cells into a formazan product that had an absorbance peak at 490 nm. Dehydrogenase enzymes found in metabolically active cells were responsible for the conversion of MTS into the soluble formazan product. Therefore, the absorbance of each well at 490 nm was directly proportional to the number of viable cells. Values for the absorbance of each well at 490 nm taken before adding MTS were subtracted from the after MTS incubation values. Cell viability was determined by comparing the resulting absorbance of wells containing no nanoparticles to wells containing nanoparticles using an F test for a one-way ANOVA.

## 3.3 RESULTS AND DISCUSSION

### 3.3.1 The Silver-Silica Nanosystem

Porous, cage-like silver coatings built around sizes of silica cores ranging in diameter from 180-520 nm were produced. A scanning electron micrograph of a typical batch of 180 nm particles and its corresponding UV-vis spectrum are shown in Figs. 3.3a and 3.3b. The extinction spectrum is broad and extends into the near infrared wavelength region; this ultimate broadening is comparable to results from other researchers who created similar coatings with different methods.[18, 19] To achieve this broad extinction, sufficient silver coverage of the silica core is required. Indeed, when only half of the recommended moles of silver were reacted with 180 nm silica cores, insufficient coating of the particles resulted as shown in Fig. 3.3c. The corresponding extinction spectrum for these sparsely coated particles is similar to solid silver spheres in solution as shown in Fig. 3.3d. These results suggest that the cage-like coatings of silver over silica must reach a minimal confluency on the surface of silica for plasmonic effects to be observed in near infrared (NIR) wavelengths of light. Previous research has suggested that particles on the surface must be no more than 3 radii apart for nanoparticle plasmonic coupling to happen, shifting extinction to the NIR spectrum.[20-22]

Silica core sizes up to 520 nm were coated with silver as shown in Fig. 3.3e. Interestingly, the corresponding extinction spectrum (Fig. 3.3f) was similar to that of the coated 180 nm particles (Fig. 3.3b), despite the large difference in silica core size. Research from the West and Halas groups have shown that by changing the thickness of a confluent layer of metal over a silica core, the absorption peak of the resulting nanoparticles can be tuned.[23] Since a rough layer of silver over silica was built, it follows that the silver-silica nanosystem consists of particles with varying silver coating thickness. Therefore, the nanosystem is made up of nanoparticles, each of which is

resonating at a slightly different wavelength. At a macroscopic level, this results in the ultimate broadening on the extinction spectra since the spectra represents the contribution from all these roughly coated nanoparticles. Adding to this resonance effect is the action of single silver spheres in close proximity. On the surface of many nanoparticles, the coating is semi-confluent, but on others there is evidence of single silver spheres all attached to the silica and packed closely together. As mentioned previously, plasmon coupling effects take place when metal nanoparticles are within several radii of each other.[20-22]

The silver-silica nanosystems described here are large with core diameters ranging from 180 nm to 520 nm; Mie theory calculations show that the extinction spectra for traditional shell-core, silver-silica particles are dominated by scattering. In fact, Jain et al[2] described that for core-shell particles of this size, the scattering cross section divided by the absorption cross section is expected to be much greater than 6. However, the principal requirement for an excellent photoacoustic contrast agent is high optical absorption, which is represented by the absorption coefficient $\mu_a$. The absorption coefficient is defined as

$$\mu_a = N \cdot \sigma_{abs,} \tag{3.2}$$

where N is the number concentration of particles and $\sigma_{abs}$ is the absorption cross section of one particle. Furthermore, $\sigma_{abs} = Q_{abs} \cdot \sigma_g$ where $Q_{abs}$ is the absorption efficiency, and $\sigma_g$ is the geometric cross section of one particle. The $Q_{abs}$ for a 30 nm gold sphere is 2 at 532 nm[24], and $Q_{abs}$ for a silica-silver core shell structure (180 nm core, 60 nm shell) at 800 nm as calculated from publicly available Miecoated software developed by Christian Matzler at the University of Bern[25] is ~2 orders of magnitude lower at 0.018. The geometric cross section, however, of the silver-silica nanosystem is almost two orders of magnitude greater than the gold spheres. Therefore, as it follows from Eq. 3.2, for the same

concentration of the two nanosystems, the absorption coefficient $\mu_a$ is on the same order of magnitude. This simple comparison elucidates why larger nanosystems can enhance photoacoustic imaging contrast to the same degree as smaller nanosystems which inherently possess higher absorption efficiencies. Therefore, when comparing nanosystems for enhancement of photoacoustic contrast, a critical parameter to consider is the absorption cross section, $\sigma_{abs}$. It is important to note that these Mie theory calculations are limited to shell-core particles and do not adequately describe the rough coatings purposefully built here, but these sample calculations were provided to convey the significance of the $\sigma_{abs}$ parameter in the design of photoacoustic contrast agents.

### 3.3.2 Imaging of the Silver Nanosystem in Ex Vivo Pancreatic Tissue

One of the advantages of photoacoustic imaging is its ability to detect nanoparticles deep in tissue. This capability was tested by performing USPA imaging *ex-vivo* on a canine pancreas after injecting 50 $\mu$l of 180 nm silica core, silver coated particles at a concentration of $10^9$ particles/ml. The ultrasound image (Fig. 3.4a) defines the pancreas area, the photoacoustic image (Fig. 3.4b) shows the signal received primarily from the nanosystem interrogated by the pulse of scattered laser light, and the combined image (Fig. 3.4c) clearly depicts the location of the nanosystem against the background ultrasonic image of the organ. This series of images demonstrates the ability of combined USPA imaging to locate accumulated nanoparticles inside tissue and spatially register their location relative to the anatomical structures of the background tissue. In this case, strong photoacoustic signal from nanoparticles located 1 cm deep in tissue was detected. By translating the USPA imaging probe across the tissue surface, a 3-D rendering of the entire nanoparticle injection region in the tissue could be generated (Fig. 3.5). Thus, if the silver nanosystem were injected in the bloodstream systematically

and accumulated in a cancerous mass, then combined USPA imaging could be used to locate the nanoparticles inside tissue, helping clinicians to better define and characterize diseased areas.

### 3.3.3 Imaging the Nanosystem Samples of Set Concentrations

In addition to the imaging performed on the pancreas, some fundamental properties of the photoacoustic signal from these nanoparticles were analyzed using samples of silver coated silica suspended in poly(vinyl alcohol) (PVA). Before describing the results of these studies in detail, the following relationships are provided for completeness. First, the photoacoustic pressure (P) generated from an absorbing source immediately following a laser pulse can be defined as follows,[26]

$$P \propto \frac{\beta v^2}{C_p} \mu_a F \tag{3.3}$$

where $\beta$ is the thermal expansion coefficient, $v$ is the acoustic velocity in the medium, $\mu_a$ is the absorption coefficient (as defined in Eq. 3.2), $F$ is the fluence of light reaching the absorber, and $C_p$ is the specific heat at constant pressure. Note that absorption from native tissue and/or PVA was assumed to be constant in our calculations, so changes in $\mu_a$ should solely reflect changes in nanoparticle concentration. Given these relationships and minimal temperature increases during PAUS imaging,[13, 14, 27] a plot of $P/F$ versus $N$ should be linear. To test this hypothesis, PVA samples with different concentrations of nanoparticles were imaged and analyzed.

The PVA samples, set in a gelatin mold for structural stability during photoacoustic imaging trials, were imaged using the USPA imaging setup similar to that shown in Fig. 3.2, except that samples were irradiated using a diffuse air beam outputted

directly from the OPO (i.e., no optical fibers were used). Furthermore, the air beam and ultrasound imaging plane were perpendicular to each other, not co-axial as shown in Fig. 3.2. Specifically, an 800 nm, 4 mJ per pulse laser beam, diffused over an ~ 1 $cm^2$ spot size, was directed at the circular end of the cylindrical nanoparticle samples. The 7.5 MHz, 128 elements linear array transducer was set to image a traverse plane about ~2.5 mm away from the circular end of the cylindrical samples. Such an imaging setup was needed to ensure homogeneous irradiation of the samples with known laser fluence (4 $mJ/cm^2$), thus allowing the analysis of the photoacoustic pressure dependence on the concentration of nanoparticles.

Photoacoustic imaging of the samples resulted in a visible increase in signal as the concentration of nanoparticles increased, as shown in Fig. 3.6. To measure the changes in photoacoustic pressure quantitatively, areas inside the white circular regions of interest labeled in the inset images on Fig. 3.6 were set into grids of 60 by 50 pixels, inside which, a box of 30 by 30 pixels was defined. The mean photoacoustic signal value of the 30 by 30 pixel area was calculated for 21 different positions inside the 60 by 50 grid. The average of those different means was taken as the relative photoacoustic pressure for each sample. The relative fluence-compensated pressure values (per Eq. 3.3) versus concentration for each sample was linear ($R^2$ = 0.999). This result confirms the fundamental relationship that for a reasonable range of concentration of absorbers (nanoparticles), the photoacoustic signal from the nanosystem increases linearly with the concentration of nanoparticles.

Imaging the silver-silica nanosystem with set concentrations of particles not only allowed for testing this linear relationship, but also allowed for testing the sensitivity of our photoacoustic imaging system. Sensitivity was accessed by comparing the lowest concentration sample at $2x10^7$ particles per ml to the control containing no particles.

Using a balanced one-way ANOVA test, the means of the signals gathered per the 21 box positions were compared between the control sample (no particles) and the lowest concentration sample tested ($2x10^7$ particles per ml). With a p value < 0.000001, the means of the two signal sets were statistically significantly different. Therefore, our photoacoustic imaging system is sensitive to concentrations at least as low as $2x10^7$ particles per ml. This detection limit is more than one order of magnitude lower than that reported for gold nanorods ($7.5x10^8$ nanorods per ml as reported by Eghtedari et al[28]). However, a direct comparison of these two sensitivity figures is not fully meaningful since the experimental conditions (i.e., the medium and distance traveled by light) were different in the two experimental set-ups. Nonetheless, the comparison does indicate that the silver-silica nanosystem was able to enhance photoacoustic signal at low concentrations similar to a well-known standard such as gold nanorods.

In future *in vivo* experiments, the linear relationship between photoacoustic pressure and concentration of nanoparticles can be used to quantify the accumulation of the nanoparticles inside the tissue. If these nanoparticles were carrying drugs or other molecules of interest, performing photoacoustic imaging over time could provide noninvasive, quantifiable, image-guided monitoring of delivery and therapy.

### 3.3.4 Cytotoxicity Tests Using the Silver-Silica Nanosystem

There is much debate in the literature over the toxicity of silver.[29] Its use in burn wound treatment and as an antimicrobial in general are well known and characterized, but questions over toxicity still remain.[30-32] Due to these debates, it was critical for cytotoxicity tests to be performed using the silver-silica nanosystem. According to testing on two different cell lines (MDA-MB-231 and MPanc96), concentrations of silver in the silver coated silica particles up to 2 mg/ml (~$2\times10^{10}$ particles per ml in media) were not

exhibiting toxic effects. As shown in Fig. 3.7, cells exposed to no nanoparticles and cells exposed to concentrations of up to 2 mg/ml silver content showed no statistically significant variation in cell viability. The ANOVA tests on these populations showed p-values of 0.6 and 0.4 with the MDA-MB-231 and MPanc96 cells lines, respectively. These p-values suggest that there is no reason to reject the null hypothesis that the means of the populations (absorbance values) tested were different. Thus, the cell viability of all the wells are the same, and the silver nanosystem did not exhibit cytotoxic effects, even at concentrations as high as 2 mg/ml content of silver.

This work represents the first demonstration of photoacoustic imaging using a contrast agent incorporating silver in biological tissue. Further biodistribution and biocompatibility studies should be performed to evaluate the use of nanosilver in the body,[33] but this work clearly demonstrates its potential as a photoacoustic contrast agent.

The developed silver-silica nanosystem also has potential in image-guided therapy approaches. Once a diseased tissue or tumor is identified with traditional imaging techniques and the need for therapy is established, the delivery of these nanoparticles to the diseased site of interest could be image-guided to assist different therapy approaches. For example, photoacoustic imaging could be used to detect the presence and concentration of the particles in the tumor while they are simultaneously used for photothermal therapy. Furthermore, different types of therapy can be employed. Indeed, the particles could be used for guidance and monitoring of cavitation therapy in which nanoparticles are used to create nanobubbles. These bubbles can act alone or they can be further exploited in ultrasound therapy. Moreover, when the particles contain chemotherapeutic drugs in their core (the CIT-NS design),[34] then drug release could be controlled or monitored using this nanosystem augmented by USPA imaging. By tailoring the silver coating and the properties of the polymeric core used to make the

nanosystem, light may be used to induce a shape change in the structure of the nanosystem. This shape change should cause extensive release of the drug only where light interrogates the tissue with accumulated nanoparticles. Thus, the CIT-NS can serve simultaneously as an imaging contrast agent and therapeutic delivery and release device, enhancing our capabilities to effectively treat patients.

## 3.4 CONCLUSIONS

Rough silver coatings around silica nanospheres can be built and their optical extinction at near infrared wavelengths is high and broad. The breadth of the spectrum allows for a multitude of near infrared wavelengths to be used in photoacoustic imaging of these agents. Using 800 nm light, the silver-silica nanosystem was detected at least 1 cm deep in *ex vivo* pancreatic tissue using combined ultrasound and photoacoustic imaging. Furthermore, the photoacoustic signal from the nanosystem was found to increase linearly with nanoparticle concentration, as theory suggested. Therefore, since (1) the silver-silica nanosystem was found to be non-toxic and (2) strong photoacoustic transients were generated by the silver-silica nanosystem and detected deep in *ex vivo* tissue, then the preliminary results suggest that the CIT-NS has the potential to provide image-guided therapy monitoring, opening up a host of applications in which imaging and therapy are performed simultaneously.

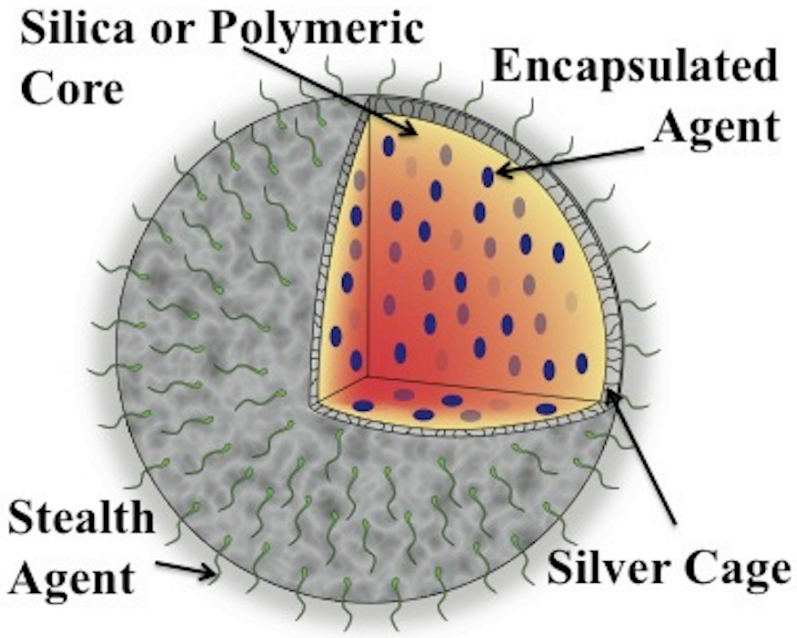


Figure 3.1: An illustration of the Combined Imaging and Therapy Nanocage System (CIT-NS) and its components.

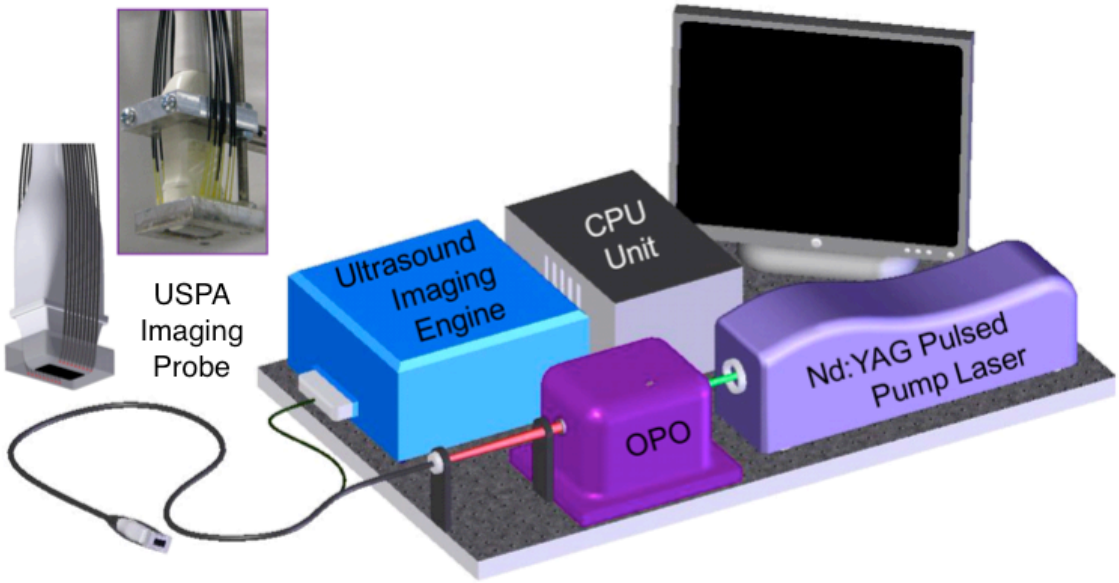


Figure 3.2. Schematic of the combined ultrasound and photoacoustic (USPA) imaging system incorporating the array-based ultrasound transducer integrated with the fiber-optical light delivery system.

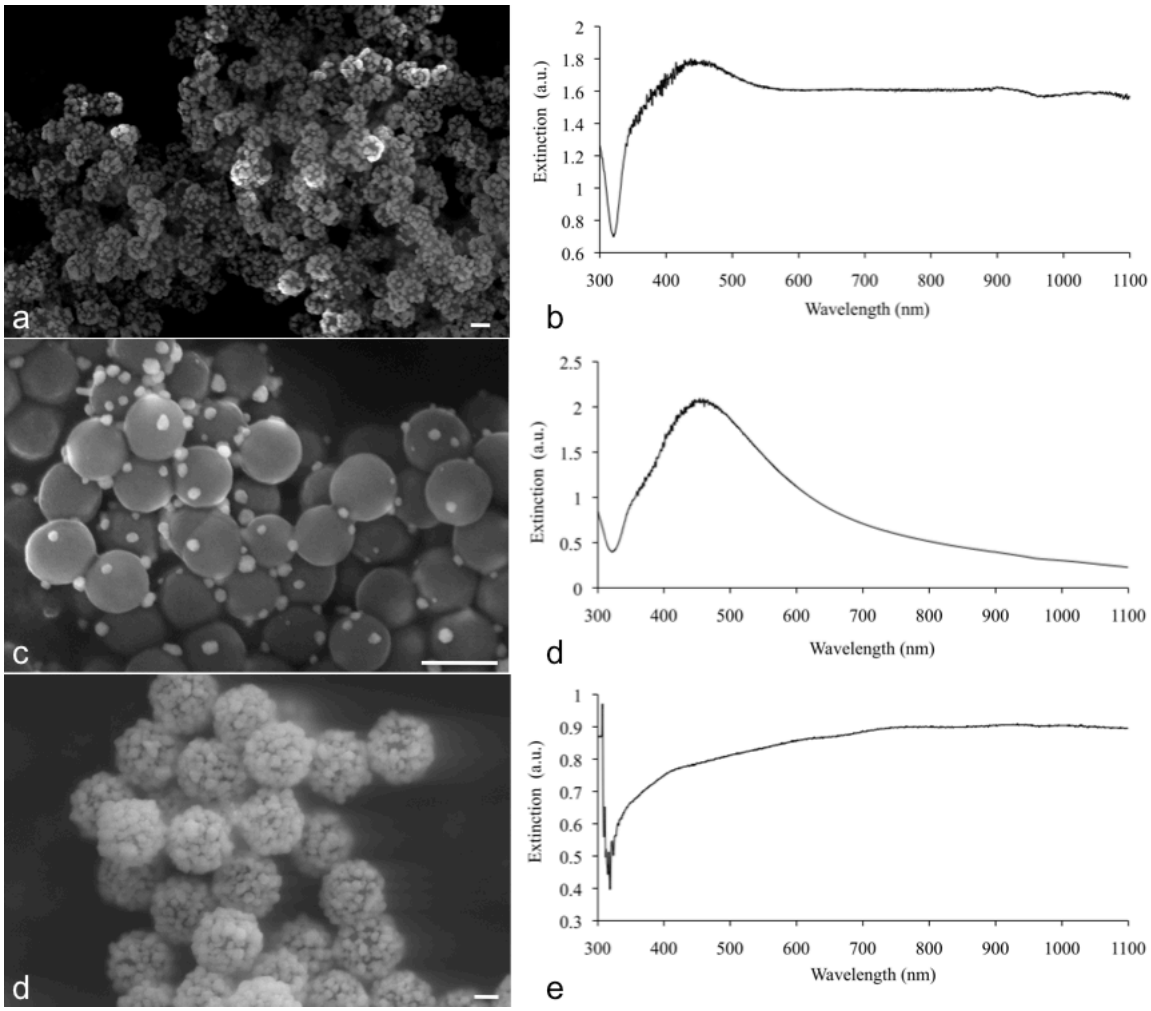


Figure 3.3. Scanning electron micrograph (SEM) of the silver-silica nanosystem with silica core diameter of 180 nm (a), and corresponding coated 180 nm UV-vis spectrograph (b); a batch of sparsely coated 180 nm nanoparticles (c), and corresponding UV-vis spectrograph (d); a silver coated 520 nm silica core batch (d), and corresponding UV-vis spectrograph (e). All scale bars are 200 nm.

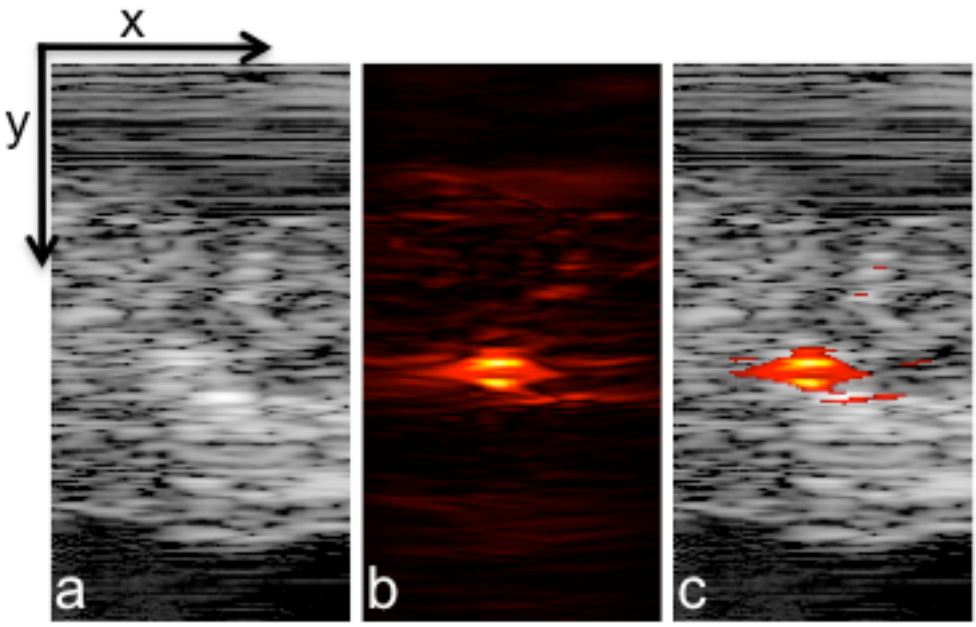


Figure 3.4. Ultrasound (a), photoacoustic (b), and combined (c) images of nanoparticles injected directly into an ex-vivo canine pancreas. All images were acquired from the same position as determined by the location of the ultrasound transducer. The images are 20 mm deep (y-axis) and 10.5 mm wide (x-axis).

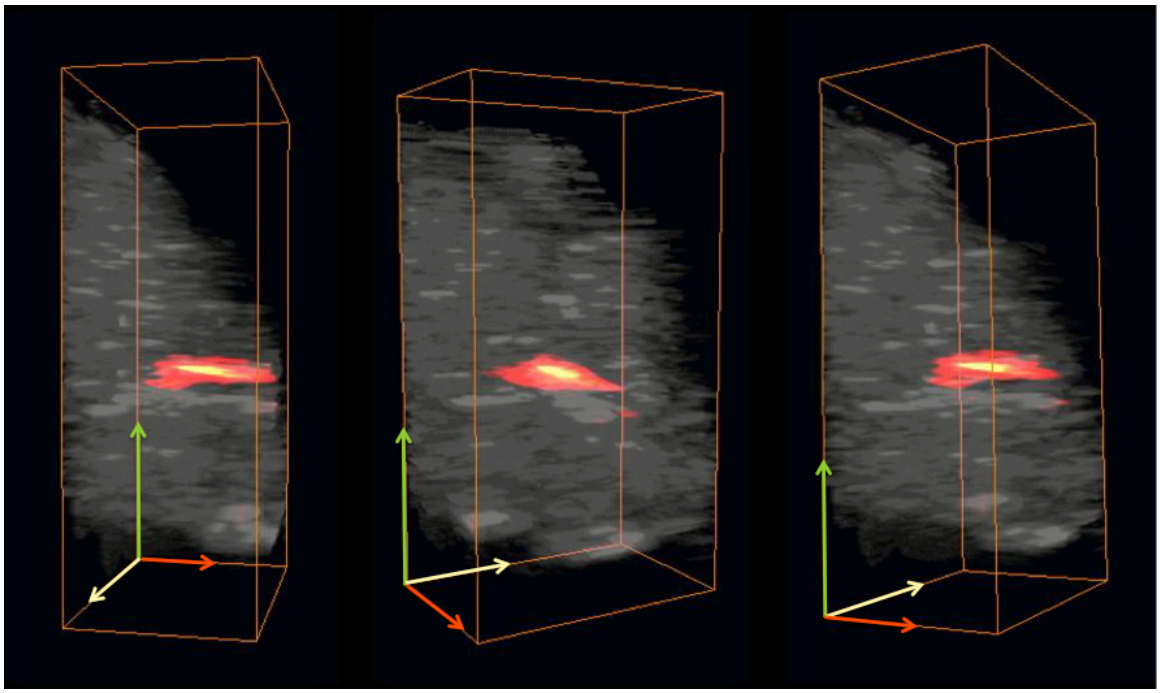

Figure 3.5. Several views of a 3-D rendering of USPA imaging from the silver nanosystem injected directly into an ex-vivo canine pancreas. All images are 20 mm by 10.5 mm by 12 mm. For clarity, ultrasound signal from gelatin above the tissue was suppressed in these images.

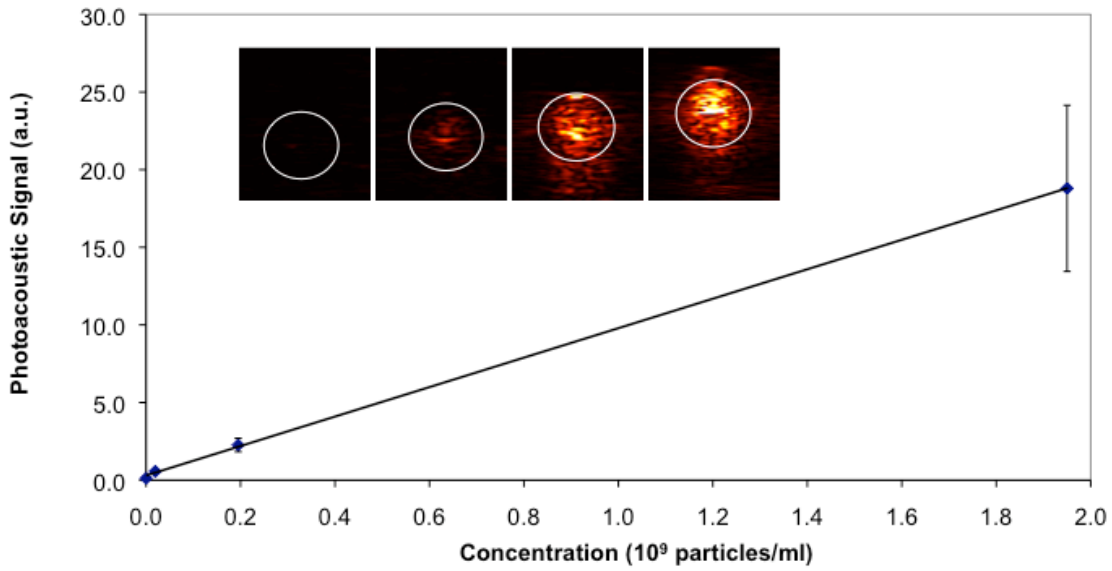


Figure 3.6. Plot of fluence-normalized photoacoustic signal versus nanoparticle concentration for the four samples shown in the inset. Inset: photoacoustic images of gelatin phantom with PVA samples containing 0, $2\times10^{7}$, $2\times10^{8}$, $2\times10^{9}$ particles per ml from left to right where the white circle outlines the boundaries of the samples as determined by ultrasound imaging. All inset images are 12.5 mm by 10.5 mm.

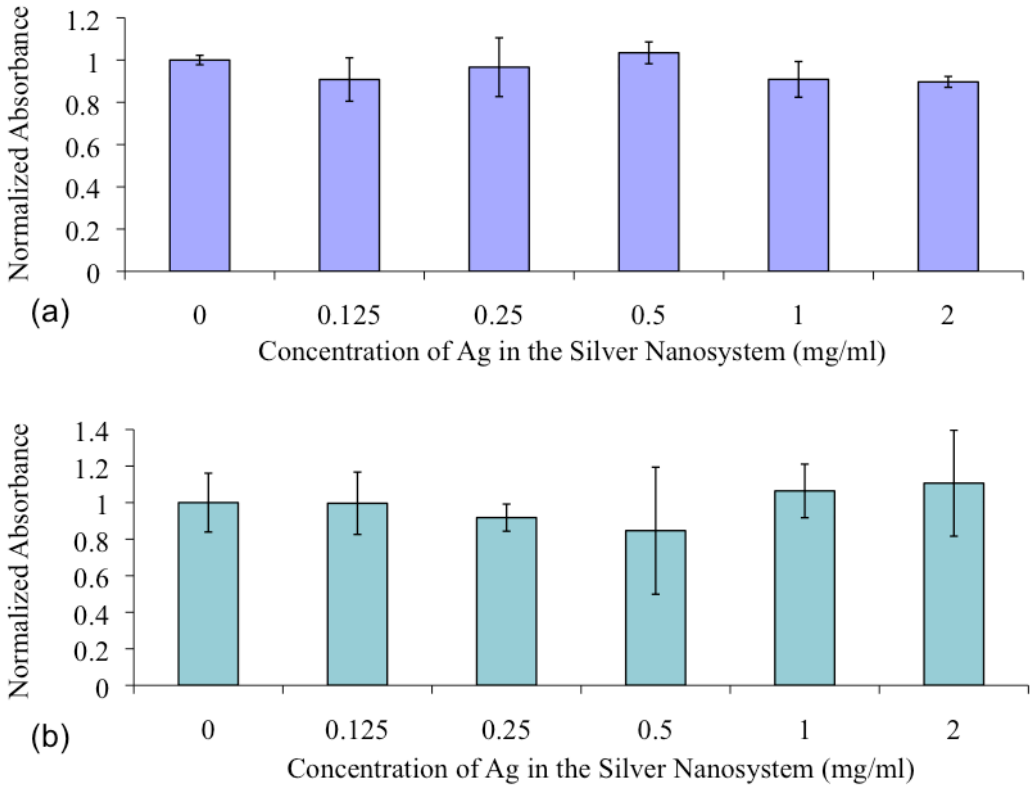


Figure 3.7. Cell viability data after 24 hr exposure to the silver-silica nanosystem at different concentrations in MDA-MB-231 cells (a) and MPanc96 cells (b).

### 3.5 REFERENCES


1. C. J. Murphy, T. K. Sau, A. M. Gole, C. J. Orendorff, J. Gao, L. Gou, S. E. Hunyadi and T. Li, "Anisotropic metal nanoparticles: Synthesis, assembly, and optical applications," J Phys Chem B 109(29), 13857-13870 (2005)
2. P. K. Jain, K. S. Lee, I. H. El-Sayed and M. A. El-Sayed, "Calculated absorption and scattering properties of gold nanoparticles of different size, shape, and composition: Applications in biological imaging and biomedicine," J Phys Chem B 110(14), 7238-7248 (2006)
3. T. Jennings and G. Strouse, "Past, present, and future of gold nanoparticles," Adv. Exp. Med. Biol. 620(34-47 (2007)
4. J. A. Copland, M. Eghtedari, V. L. Popov, N. Kotov, N. Mamedova, M. Motamedi and A. A. Oraevsky, "Bioconjugated gold nanoparticles as a molecular based contrast agent: Implications for imaging of deep tumors using optoacoustic tomography," Mol Imaging Biol 6(5), 341-349 (2004)
5. A. Oraevsky, A. Karabutov and E. Savateeva, "Enhancement of optoacoustic tissue contrast with absorbing nanoparticles," Proc of SPIE (2001)
6. R. Weissleder, "A clearer vision for in vivo imaging," Nat. Biotechnol. 19(4), 316-317 (2001)
7. A. A. Oraevsky, "Gold and silver nanoparticles as contrast agents for optoacoustic imaging," in Photoacoustic imaging and spectroscopy L. V. Wang, Ed., Taylor and Francis Group, New York (2009).
8. K. Homan, S. Mallidi, E. Cooley and S. Emelianov, "Combined Photoacoustic and Ultrasound Imaging of Metal Nanoparticles In Vivo," in Nanoimaging B. Goins and W. Phillips, Eds., Pan Stanford Publishing, Singapore (2010).
9. R. K. Jain, "Transport of molecules, particles, and cells in solid tumors," Annu Rev Biomed Eng 1(241-263 (1999)
10. L. Brannon-Peppas and J. O. Blanchette, "Nanoparticle and targeted systems for cancer therapy," Adv Drug Deliv Rev 56(11), 1649-1659 (2004)
11. I. H. El-Sayed, X. Huang and M. A. El-Sayed, "Surface plasmon resonance scattering and absorption of anti-EGFR antibody conjugated gold nanoparticles in cancer diagnostics: Applications in oral cancer," Nano Lett 5(5), 829-834 (2005)
12. S. Kumar, J. Aaron and K. Sokolov, "Directional conjugation of antibodies to nanoparticles for synthesis of multiplexed optical contrast agents with both delivery and targeting moieties," Nat Protoc 3(2), 314-320 (2008)
13. J. Shah, S. R. Aglyamov, K. Sokolov, T. E. Milner and S. Y. Emelianov, "Ultrasound imaging to monitor photothermal therapy - feasibility study," Opt Express 16(6), 3776-3785 (2008)

14. J. Shah, S. Park, S. Aglyamov, T. Larson, L. Ma, K. Sokolov, K. Johnston, T. Milner and S. Y. Emelianov, "Photoacoustic imaging and temperature measurement for photothermal cancer therapy," J Biomed Opt 13(3), 034024 (2008)

15. D. P. O'Neal, L. R. Hirsch, N. J. Halas, J. D. Payne and J. L. West, "Photo-thermal tumor ablation in mice using near infrared-absorbing nanoparticles," Cancer Lett. 209(2), 171-176 (2004)

16. M. S. Peterson, J. Bouwman, A. Chen and M. Deutsch, "Inorganic metallodielectric materials fabricated using two single-step methods based on the Tollen's process," J. Colloid Interface Sci. 306(1), 41-49 (2007)

17. ANSI, "Orlando: Laser Institute of America " American National Standard for Safe use of Lasers, ANSI Z136.1 (2000)

18. M. Zhu, G. Qian, G. Ding, Z. Wang and M. Wang, "Plasma resonance of silver nanoparticles deposited on the surface of submicron silica spheres," Mater. Chem. Phys. 96(489-493 (2006)

19. K. T. Yong, Y. Sahoo, M. T. Swihart and P. N. Prasad, "Synthesis and plasmonic properties of silver and gold nanoshells on polystyrene cores of different size and of gold–silver core–shell nanostructures," Colloids Surf. Physicochem. Eng. Aspects 290(1-3), 89-105 (2006)

20. J. Aaron, N. Nitin, K. Travis, S. Kumar, T. Collier, S. Y. Park, M. Jose-Yacaman, L. Coghlan, M. Follen, R. Richards-Kortum and K. Sokolov, "Plasmon resonance coupling of metal nanoparticles for molecular imaging of carcinogenesis in vivo," J Biomed Opt 12(3), 034007 (2007)

21. P. K. Jain and M. A. El-Sayed, "Universal scaling of plasmon coupling in metal nanostructures: extension from particle pairs to nanoshells," Nano Lett 7(9), 2854-2858 (2007)

22. S. Mallidi, T. Larson, J. Tam, P. P. Joshi, A. Karpiouk, K. Sokolov and S. Emelianov, "Multiwavelength photoacoustic imaging and plasmon resonance coupling of gold nanoparticles for selective detection of cancer," Nano Lett 9(8), 2825-2831 (2009)

23. L. R. Hirsch, A. M. Gobin, A. R. Lowery, F. Tam, R. A. Drezek, N. J. Halas and J. L. West, "Metal nanoshells," Ann. Biomed. Eng. 34(1), 15-22 (2006)

24. C. M. Pitsillides, E. K. Joe, X. Wei, R. R. Anderson and C. P. Lin, "Selective cell targeting with light-absorbing microparticles and nanoparticles," Biophys. J. 84(6), 4023-4032 (2003)

25. C. Matzler, "MATLAB Functions for Mie Scattering and Absorption," in Secondary MATLAB Functions for Mie Scattering and Absorption Secondary C.

Matzler, Ed., Place Published (2002), www.iap.unibe.ch/publications/download/199/en/.

26. C. K. N. Patel and A. C. Tam, "Pulsed optoacoustic spectroscopy of condensed matter," Reviews of Modern Physics 53(3), 517-550 (1981)

27. S. Sethuraman, S. R. Aglyamov, R. W. Smalling and S. Y. Emelianov, "Remote temperature estimation in intravascular photoacoustic imaging," Ultrasound Med. Biol. 34(2), 299-308 (2008)

28. M. Eghtedari, A. Oraevsky, J. Copland, N. Kotov, A. Conjusteau and M. Motamedi, "High sensitivity of in vivo detection of gold nanorods using a laser optoacoustic imaging system," Nano Lett 7(7), 1914-1918 (2007)

29. D. W. Brett, "A discussion of silver as an antimicrobial agent: alleviating the confusion," Ostomy Wound Manage 52(1), 34-41 (2006)

30. J. L. Clement and P. S. Jarrett, "Antibacterial silver," Metal-Based Drugs 1(467-482 (1994)

31. M. Ip, S. L. Lui, V. K. M. Poon, I. Lung and A. Burd, "Antimicrobial activities of silver dressings: An in vitro comparison," Journal of Medical Microbiology 55(59-63 (2006)

32. L. G. Ovington, "The value of silver in wound management," Podiatry Today 12(59-62 (1999)

33. P. V. AshaRani, G. Low Kah Mun, M. P. Hande and S. Valiyaveettil, "Cytotoxicity and Genotoxicity of Silver Nanoparticles in Human Cells," ACS Nano 3(2), 279-290 (2009)

34. A. L. Doiron, K. A. Homan, S. Emelianov and L. Brannon-Peppas, "Poly(Lactic-co-Glycolic) Acid as a Carrier for Imaging Contrast Agents," Pharm. Res. 26(3), 674-682 (2009)

# Chapter 4: Synthesis and Characterization of the CIT-NS incorporating Doxorubicin

Preliminary testing in Chapter 3 showed that a silver cage-like coating over a dielectric core, a structure optically similar to the CIT-NS, could provide photoacoustic imaging contrast, thus indicating that synthesis of the CIT-NS is indeed warranted. However, building the CIT-NS incorporating the drug gemcitabine is especially challenging since the native drug is hydrophilic and difficult to encapsulate in poly(lactic-co-glycolic) acid (PLGA) (see Chapter 5 for details). For that reason, the CIT-NS was first built incorporating a model hydrophobic drug, namely the chemotherapeutic agent doxorubicin (DOX); which is known to encapsulate well in PLGA using oil in water emulsion techniques.[1] This chapter details the experimental steps in synthesis and characterization of the CIT-NS incorporating DOX. The basic understanding of properties and synthesis techniques gained from making the CIT-NS with DOX proved that the design of the CIT-NS system is valid and producible, and provided the insight required for preparation of the ideal CIT-NS incorporating gemcitabine (Chapter 5).

## 4.1 Introduction

Since its discovery in 1971, the use of DOX as a chemotherapeutic agent has been rapidly expanding.[2] DOX is currently FDA approved to treat lymphoma, acute leukemia, soft-tissue carcinoma and breast, ovarian, testicular, lung, bladder and gastric cancers.[1] It is an anthracyline antibiotic that intercalates with DNA, blocking synthesis and transcription by sterically disturbing DNA nucleotides and inhibiting the enzyme topoisomerase II.[1]

Because of DOX's well characterized cardiotoxicity and nephrotoxicity[2, 3], the maximum lifetime dose limit for this drug is 550 mg/m$^2$ (note that m$^2$ is the body surface

area of the patient).[1] The damage to healthy cells caused by DOX has led to research by numerous groups on methods to encapsulate DOX in nanocarriers or make conjugates of DOX that can target the diseased site directly.[1, 2, 4-14] In previous work from our group[1], PLGA was used as a biodegradable carrier for DOX. Other groups have also proposed similar strategies for a combination of PLA or PLGA with DOX for cancer treatment.[3, 15]

DOX is a popular model drug in nanocarrier research for several reasons: (1) it is FDA approved to treat numerous cancers, (2) it is hydrophobic (soluble in methanol and minimally soluble in aqueous salt solutions), (3) it is orange-red in color (absorbs light at 480 nm), and (4) it is inherently fluorescent. All of these factors make it a suitable model drug for the CIT-NS system. Its hydrophobic nature should facilitate DOX's incorporation into the CIT-NS system. Once incorporated, DOX's fluorescence and light absorption properties should enable drug release profile characterization by spectroscopy and studies of DOX's interaction with cells by microscopy. This chapter covers the experimental methods and results of incorporating DOX as a model drug into the CIT-NS without a targeting antibody (Fig 4.1). Understanding how this model drug performs in the CIT-NS represents a significant step towards synthesis and understanding of the ideal CIT-NS incorporating the drug gemcitabine.

## 4.2 METHODS

Each step in the synthesis and characterization of a DOX loaded CIT-NS are described separately below. For reader clarity, the sources for all materials are consolidated here.

### 4.2.1 Materials

All chemicals were used without further purification and were at minimum ACS grade. PLGA 50:50DL 2A was purchased from Lakeshore Biomaterials (Birmingham,

AL, USA) and Medisorb (Cincinnati, OH, $M_n$ = 11 kD). ACS grade L(+) ascorbic acid and ultrapure silver nitrate were products of Acros (Morris Plains, NJ, USA). Polyvinyl alcohol (PVA) was purchased from Sigma-Aldrich (St. Louis, MO, USA, ~30 kDa). Dimethyl sulfoxide (DMSO) and acetone were purchased from Fisher Scientific (Fair Lawn, NJ, USA). Slide mounting media, Vectashield with DAPI stain, was from Vector Laboratories (Burlingame, CA, USA). Sodium hydroxide was purchased from J.T. Baker (Phillipsburg, NJ, USA). Dulbecco's phosphate buffered saline (DPBS) came from Mediatech, Inc. (Herndon, VA, USA). Doxorubicin hydrochloride was purchased from Fisher Scientific (Fair Lawn, NJ, USA). All cell culture products were purchased from Invitrogen (Carlsbad, CA, USA) unless otherwise specified. The MTT assay (Toxicology Assay Kit TOX-1) and the bovine serum albumin (BSA) were from Sigma (St. Louis, MO, USA). Finally, the methyl-poly(ethylene glycol)-thiol (mPEG-SH of 5 kDa) was from Laysan Bio (Arab, AL, USA).

### 4.2.2 Nanocage Synthesis with Doxorubicin

The CIT-NS was built in a step-wise, bottom up approach. An overall schematic describing the steps in synthesis required for the CIT-NS incorporating DOX are shown in Fig 4.2 and are described in sequence below.

Step 1: Synthesizing the PLGA Core with Encapsulated DOX: An oil in water nanoprecipitation method, modified from that reported by Betancourt et al.[1], was employed. Briefly, 10 mg of DOX was dissolved in 2 ml methanol. Separately, 100 mg of poly(lactic-co-glycolic) acid (PLGA) (50:50 DL, MW~12 kDa) was dissolved in 3 ml acetone. The co-solvent oil phase was created by mixing 1 ml of the DOX solution with all of the PLGA solution. The water phase consisted of a 10 ml surfactant solution of 1

mg/ml poly(vinyl alcohol) (PVA) and 10 mg/ml bovine serum albumin (BSA) in deionized and ultrafiltrated to 18.2 MΩ-cm (DIUF) water.

The oil phase was pipetted quickly into the water phase and sonicated briefly for 15 seconds. The resulting nanoprecipitation was stirred rigorously under slight vacuum for 30 min to remove the organic solvents. The resulting DOX loaded PLGA nanoparticles were collected via centrifugation at 48,000xg in a Beckman J2-21 refrigerated centrifuge running at 4°C for 15 min. The particles were washed once with a 10 mg/ml PVA solution and then resuspended in 20 ml DIUF water. The supernatants from all washes were retained for spectrophotometry analysis.

Step 2: Nucleating Ag on the Surface of PLGA: The DOX-loaded PLGA nanoparticles from step 1 (250 µl of the total 20 ml) were placed in a round shallow glass dish with 30 ml DIUF water (the water level was no greater than 3 mm high in the shallow dish). While stirring at 400 rpm, 300 µl of 0.15 M silver nitrate was added. The entire dish was then subjected to 254 nm light from an 8 W source for 15 min. During that 15 min, the light activated the PVA to act as a photoreducing agent for silver, nucleating silver on the surface of PLGA.

Step 3: Ag Nanocage Formation Around PLGA: Following from Step 2, the UV light was removed and the solution was transferred to a 50 ml polyethylene beaker. While stirring, 100 µL of 18wt% ascorbic acid was added. Within 30 seconds the solution turned from pink (native color of DOX-loaded PLGA) to tan-brown and finally grey-black, indicating that the silver had been reduced. Directly following reduction, 0.1 ml of a 30 mg/ml solution of methyl-poly(ethylene glycol)–thiol (mPEG-SH) was added and allowed to stir for 15 min. The resulting nanocages were collected via centrifugation at 48,000xg in a Beckman J2-21 refrigerated centrifuge running at 4°C for 15 min. The supernatant was retained for spectrophotometry analysis.

### 4.2.3 Nanocage Characterization with Doxorubicin

Several methods were used to characterize the nanocages: scanning electron microscopy (SEM), ultraviolet to visible (UV-vis) spectrophotometry, zeta potential, and dynamic light scattering. For all stages of CIT-NS development, preparation for SEM involved aliquoting the nanosystem directly from the reaction vessel and placing a drop on carbon conductive tape attached directly to an SEM platform tab. The drop was allowed to dry prior to examination using a 10 kV accelerating voltage on a LEO 1530 scanning electron microscope. Note that to observe the DOX loaded PLGA cores using SEM, the sample was sputter coated with a 20 nm thick layer of gold. Observation of the CIT-NS after any level of reduction of silver no longer required sputter coating for SEM preparation.

The optical properties of the CIT-NS were examined using a Shimadzu UV-1201 spectrophotometer. The CIT-NS was suspended in DI water in a plastic 10 mm pathlength cuvette. The spectrophotometer was used in absorbance mode to read the attenuation of light passing through the sample at wavelengths from 300 to 1100 nm.

The surface charge and size distribution of DOX loaded PLGA particles produced using the nanoprecipitation technique were characterized using a ZetaPlus instrument with accompanying software (Brookhaven Instruments Corp., Holtsville, NY) on suspensions of 1 mg/mL nanoparticles in water.

### 4.2.4 In Vitro DOX Release Studies

To perform DOX release studies, the entire procedure described in 4.2.2 had to be scaled up in order have enough DOX released from nanocages to allow for proper spectrophotometry measurements over long time periods. Specifically, the procedure was modified as follows. In Step 1 directly after the oil-in-water emulsion, 5 ml of 0.15 M silver nitrate was added and 254 nm light from an 8 W source irradiated the mixture

while stirring during the vacuum distillation of the organic phases (the acetone and methanol). Following vacuum distillation, the Ag nucleated DOX-PLGA nanoparticles were collected via centrifugation at 48,000xg in a Beckman J2-21 refrigerated centrifuge running at 4°C for 15 min. The resulting pellet of particles was resuspended in 20 ml DIUF water and the supernatant was retained for spectrophotometric analysis. Then 5 ml of the particle solution was added to each of four large beakers prefilled with 300 ml of DIUF water each. With vigorous stirring, 2.5 ml of 0.15 M silver nitrate was added to each beaker. To reduce the silver into cages over the DOX-PLGA, 0.3 ml of 18wt% ascorbic acid was added to each beaker. Over the course of 30 s, the solution turned from pink (native color of DOX-loaded PLGA) to tan-brown and finally grey-black, indicating that the silver had been reduced. Directly following reduction, 0.25 ml of a 30 mg/ml mPEG-SH solution was added. The resulting nanocages were collected via centrifugation at 48,000xg in a Beckman J2-21 refrigerated centrifuge running at 4°C for 15 min. The pellet was resuspended in 15 ml of DIUF water and equal aliquots of the suspension were loaded into 3 centrifuge tubes. These tubes were kept in a 37°C water bath over a period of 1 week. During that week, the tubes were periodically spun down at 48,000xg in a Beckman J2-21 refrigerated centrifuge running at 4°C for 15 min. After each centrifugation, the pellet was resuspended via sonication in 5 ml of fresh DIUF water and placed back in the warm water bath. The supernatants from each round of centrifugation were kept and analyzed to determine how much DOX was releasing into the water over time.

### 4.2.5 Cytotoxicity Studies

Cell Maintenance and Preparation: The *in vitro* therapeutic efficacy of the various PLGA-DOX nanoparticles were tested against human mammary gland epithelial

adenocarcinoma cells (MDA-MB-231). The breast cancer cells were maintained in Dulbecco's Modified Eagle Medium supplemented with 10% fetal bovine serum, 1% HEPES buffer, 1% L-glutamine, and 1% sodium pyruvate. They were kept at 37°C in a humidified 5% $CO_2$ incubator. For cell studies, 4500 cells per well were seeded in a 96 well plate and allowed to attach and grow for 1 day in media prior to the cytotoxicity experiment.

Nanoparticle Preparation: Three types of nanoparticles were tested for toxicity: the CIT-NS with DOX, the CIT-NS without DOX, and the DOX loaded PLGA nanoparticles. Following Step 3 explained in 4.2.2, the nanocages (CIT-NS with DOX) were suspended in 3.1 ml of MDA-MB-231 cell media and sterilized by sending the entire solution with nanocages through a 0.45 μm syringe filter. This suspension of nanocages in media represented a 12 μg/ml concentration of DOX. To get the other concentrations of 1.2 and 0.12 μg/ml DOX that were tested, the nanocages were diluted 1:10 in media. To test nanocages with no drugs (CIT-NS without DOX), the exact same procedures were followed, but DOX was not included during the formulation. Finally, to obtain a similar concentration of DOX in the DOX-PLGA nanoparticles (with no nanocage), 80 μl of the 20 ml suspension of DOX-PLGA nanoparticles (after Step 1 in 4.2.2) were suspended in 1 ml of MDA-MB-231 media. The DOX-PLGA particles were also diluted 1:10 in media as appropriate to obtain the 1.2 and 0.12 μg/ml DOX concentrations for cell testing.

MTT Assay: After cells were allowed to grow for 24 hr in the 96 well plate, their media was aspirated off and media containing the prepared nanoparticles was added. The media containing nanoparticles was allowed to interact with the cells for 4 hrs, after which the media with nanoparticles was removed and replaced with fresh, unadulterated media. Each condition was repeated in 4 separate wells, each containing 100 μl of media.

To assess the therapeutic efficacy of the interaction between the nanoparticles and the cells, the cells were allowed to incubate and grow for another 48 hr after the nanoparticles were removed. At 48 hr the activity of the mitochondria in each well was tested by adding 10 μl of the MTT product (3-[4,5-dimethylthiazol-2-yl]-2,5-diphenyl tetrazolium bromide). This MTT product was incubated with the cells for 4 hr, at which time the yellow tetrazole product was reduced by active mitochondria into insoluble purple formazan crystals. After adding 100 μl of the isopropanol/HCl mixture provided in the kit to each well in the 96 well plate and pipetting extensively, the formazan product dissolved. The absorbance of the formazan product at 570 nm could be determined for each well using a spectrophotometer, and a comparison with control wells provided a measure of therapeutic efficacy of the nanoparticles. To test whether conditions (wells with nanoparticles) were statistically significantly different from controls, an F test for a one-way analysis of variance (ANOVA) was used.

Microscopy Studies: MDA-MB-231 cells were grown on microscope slide coverslips. The highest concentration of nanocages (representing 12 μg/ml DOX in cell media) were incubated with these cells on the coverslips for 18 hr. After 18 hr, the media containing nanocages was removed and the coverslip was washed 3x with 2 ml of DPBS. Then a solution of 1% formalin in DPBS was incubated for 20 min with the cells on the coverslips. Finally the formalin-DPBS was aspirated away and the coverslips were mounted on slides using Vectashield with DAPI nuclear stain and sealed on the edges with nail polish. Images of the cells were captured using a Leica Inverted Microscope at 40X equipped with epi-fluorescence, brightfield, and phase contrast modes.

## 4.3 RESULTS AND DISCUSSION

The CIT-NS incorporating the model drug DOX is an important first step in building a prototype of the CIT-NS design and proving that it can be functional *in vitro*. In this section, results of the DOX loaded CIT-NS are presented and described from synthesis through characterization with breast cancer cells.

### 4.3.1 CIT-NS incorporating Doxorubicin

The synthesis of the CIT-NS started with an oil in water emulsion to load DOX in PLGA nanospheres (Step 1 in Section 4.2.2). A typical scanning electron microscope (SEM) micrograph of DOX loaded PLGA cores is shown in Fig 4.3. These particles averaged 210 nm in mean diameter with a polydispersity index of 0.09 and a zeta potential of -7 mV as measured using a ZetaPlus instrument. The negative zeta potential of these particles indicates their propensity to repel each other in solution, leading to a stable colloid. Furthermore, 65% encapsulation efficiency (mg of DOX encapsulated per mg of DOX in the preparation) was observed. In this case, we attempted to load 5 mg of DOX in 100 mg of PLGA and the encapsulation of 3.25 mg was observed and is comparable to previous studies.[1]

The next step in building the CIT-NS is to form nucleation sites for Ag on the surface of PLGA (Step 2 in Section 4.2.2). To nucleate silver on PLGA cores, a photoreduction method was employed. A diluted solution of the as prepared DOX-loaded PLGA nanospheres was placed in a round shallow dish and irradiated with 254 nm light. During this time, the PVA surfactant, still present on the surface of the PLGA nanospheres from the emulsion, acted as a reducing agent for $Ag^+$ in solution, as shown mechanistically in Fig 4.4, while also serving as macroscopic support for the forming silver seeds. An image of these PLGA cores with silver nucleation sites is shown on the right side of Fig 4.4. Recall that preparation of these samples for SEM involved drop

casting them on a SEM tab with no metal sputter coating. Therefore, as the SEM image in Fig. 4.4 was acquired, the PLGA cores were ballooning in response to the electron beam, and thus, the sizes shown in the image are up to 100% greater than actual size and degradation of some silver nucleated cores is evident.

The final step in building the CIT-NS involved the reduction of a silver cage around PLGA (Step 3 in Section 4.2.2). The photoreduction step (Step 2) only reduced a small percentage of the total $Ag^+$ to $Ag^0$ on the surface of PLGA, and therefore a final step using a stronger reducing agent was required to reduce all the $Ag^+$ and produce a cage layer of silver around PLGA. The final reducing agent, ascorbic acid, was added under continued vigorous stirring at room temperature. Examples of two different cage morphologies produced after ascorbic acid reduction around PLGA are shown in Fig 4.5. Interestingly, the cages in Fig 4.5a were produced when half of the silver was used (only 150 μl of 0.15 M silver nitrate) and the temperature was 1°C, whereas the almost fully confluent layer of silver in Fig 4.5b was produced at room temperature with 300 μl of 0.15 M silver nitrate. From SEM analysis, the size of the silver cage varied in thickness from 20 nm to 60 nm.

An ultraviolet to visible (UV-vis) spectrum of these nanocages was taken directly after synthesis and is shown in Fig 4.6. Interestingly, unlike nanoshells, the absorbance spectrum for the CIT-NS is broad and relatively uniform across the 400-1100 nm wavelength range. This extinction pattern is different from other nanoparticles, such as nanoshells, defined by a confluent layer of metal over a dielectric core. The light absorbance properties, specifically the longitudinal surface plasmon resonance peak, of these nanoshells can be tuned by changing the thickness of their metallic layer.[16] It could follow that since our metallic layer is, by design, not confluent or of uniform thickness and there is polydispersity in the size of the PLGA cores, an ultimate broadening or

flattening of the spectrum results. Furthermore, plasmon coupling between adjacent silver nanostructures on the PLGA surface can further broaden the spectrum.[17, 18] Thus, the CIT-NS absorbs and scatters light strongly across a wide range of the wavelengths. The extinction spectrum of the nanocage system confers two important properties: (1) the nanocages can be used as a photoacoustic contrast agent since they absorb light in the near infrared spectrum where tissue absorption is minimal (Fig 1.3) and (2) a pulsed laser of any near infrared wavelength can be used for photoacoustic imaging with the nanocage system.

The successful synthesis of the silver cage around a DOX loaded PLGA core represents the first known prototype of the novel CIT-NS. Post synthesis, an analysis of the *in vitro* functionality of the nanocage system was conducted and that discussion is provided in the next two sections.

### 4.3.2 Doxorubicin Release Study

The CIT-NS system was designed with the intent that the silver cage built surrounding the PLGA core should slow the release of drug by limiting its diffusion out of the core. The DOX release study shown in Fig 4.7 addresses this hypothesis. DOX release from DOX-PLGA nanospheres and the CIT-NS are compared. Both nanosystems show a characteristic burst release profile[19, 20], but the profile was significantly delayed for the nanocage system. In the first 5 hours, the nanocage system released less than 10% of DOX, while the DOX-PLGA system had released over 50% of its contents. Since the nanocage system being tested was the system with the most confluent layer of silver (Fig 4.5b), then the release profile shown in Fig 4.7 represents the slowest release profile achievable with the CIT-NS for the model drug DOX. The delayed drug release obtained with the CIT-NS is significant since maximum accumulation of nanosystems in tumors

using mouse models have been observed at ~5 hr (see Chapter 7). Therefore, if the CIT-NS were systemically injected, it would elute less than 10% of its drug into the bloodstream in the first five hours while its circulating and accumulating at a cancer site. In comparison, the DOX-PLGA nanospheres would release greater than 50% into the blood stream, making that nanosystem hardly more effective than systemic injections of free drug as is currently performed in the clinic.

### 4.3.3 Cytotoxicity Studies

The cytotoxicity results obtained by mixing the CIT-NS and its various components with breast cancer cells were highly encouraging. As shown in Fig 4.8, the formulation with only PLGA and silver showed no statistically significant loss of cell viability relative to control. These results are contrary to literature reporting on the cytotoxicity of silver.[21] The highest concentration tested here was 1.3 mg/ml of silver mixed with the cells – a high concentration. Therefore, silver in this form as part of the CIT-NS with a PLGA core and surrounding PEG layer was not cytotoxic. My hypothesis is that a size and surface property dependence on the toxicity of silver exists. Specifically, the silver ion is the most reactive form of silver and is likely responsible for its toxicity (see Chapter 2). When silver is in the form of small (5-10 nm), unstable seeds or in the form of a salt, the likelihood of silver ion release into the cellular environment is higher than that for the CIT-NS structure that has a much larger, more passivated silver surface. Therefore, since all the reports in the literature tested silver nanoseeds or silver salts[22-24], it is feasible that larger, more stable silver nanostructures present an exception. Since they are more stable and less reactive, the basal level of silver ions eluted into the cellular space is low – low enough not to induce toxicity. Further work would be required to

address this hypothesis directly, but the hypothesis is provided as a possible explanation for the lack of toxicity observed here.

In addition to the lack of toxicity from silver, other encouraging results are shown in Fig 4.8. For instance, in every formulation involving DOX, a corresponding loss of cell viability was observed. This loss of viability was concentration dependent and statistically significant with a $p < 0.02$ in the conditions with higher DOX concentrations. Therefore, encapsulating the drug in the CIT-NS is not hurting the *in vitro* efficacy of the drug and losses in cell viability are comparable to free drug. These results prove that the CIT-NS can function as designed and exhibit cytotoxic effects in a concentration dependent manner as expected.

To further prove that DOX can be delivered to cells using the CIT-NS, microscopy studies with cells grown on coverslips was performed. Fig 4.9 shows co-location of DOX fluorescence in the nucleus of breast cancer cells after 18 hr of incubation with the CIT-NS. The red DOX fluorescence was also seen in the cytoplasm near the nuclei. These results indicate that DOX can be delivered to cells by the CIT-NS and DOX does traffic through the cell, reaching the nucleus where it intercalates with DNA and exhibits its cytotoxic effect.

## 4.4 CONCLUSIONS

The CIT-NS incorporating the model drug DOX was successfully synthesized. Analysis of the *in vitro* properties of the system, such as control over the drug release profile and broad extinction in the near infrared spectrum, indicate that the nanosystem is viable for *in vivo* applications. Relating to the goals of the overall thesis, the results detailed in this chapter indicate that: (1) the design of the CIT-NS is valid and (2) that a prototype of the CIT-NS incorporating DOX can be synthesized with the expected

functional properties of drug delivery and light absorbance in the near infrared spectrum. Since the CIT-NS was successfully built with the model drug DOX, the ideal CIT-NS incorporating the drug gemcitabine will be the subject of Chapter 5.

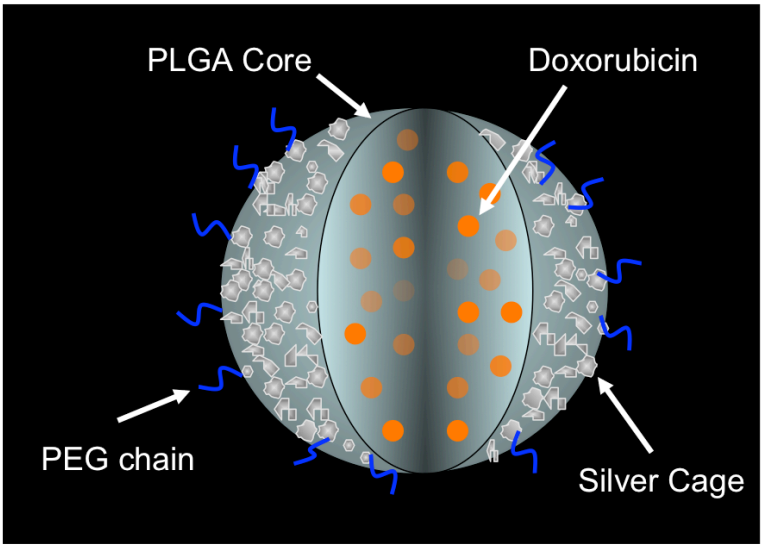


Figure 4.1. An illustration of the Combined Imaging and Therapy Nanoplate System incorporating DOX.

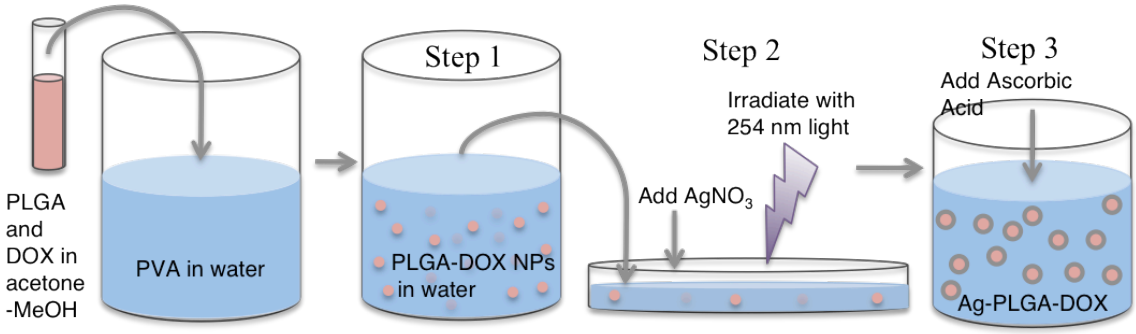


Figure 4.2. A schematic illustrating the steps required to synthesize the CIT-NS incorporating doxorubicin.

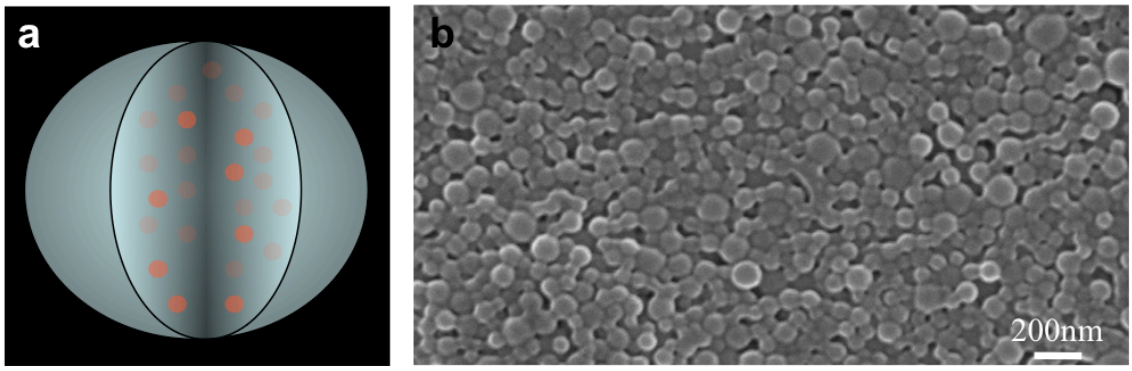


Figure 4.3. Doxorubicin loaded PLGA nanosphere (a) under scanning electron microscopy (b).

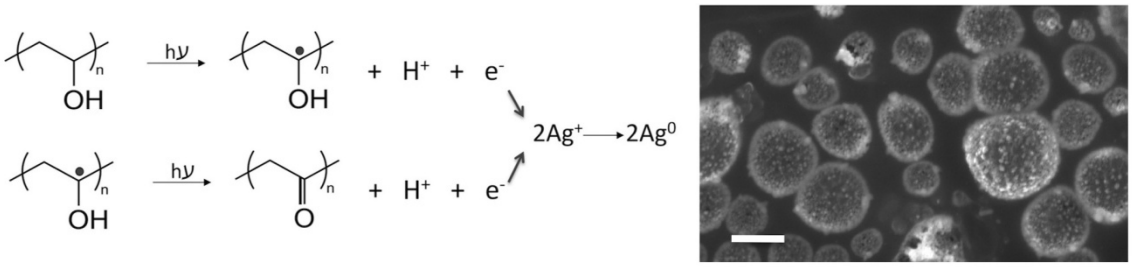


Figure 4.4. Reaction schematic depicting how poly (vinyl alcohol) acts as a reducing agent in the presence of UV light (left). Scanning electron micrograph of silver seeded PLGA nanospheres (right). Scale bar is 200 nm.

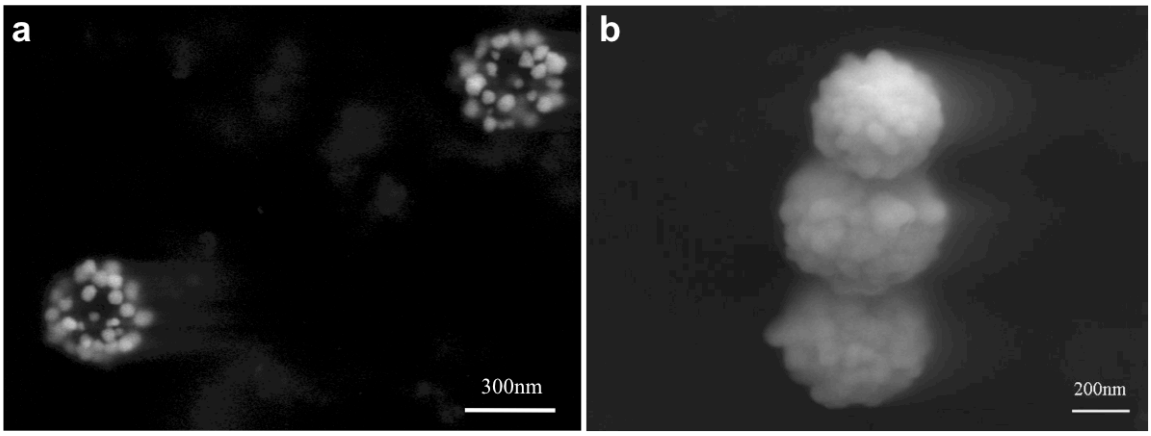


Figure 4.5. Different morphologies of the silver cage structure that was reduced on top of a PLGA core.

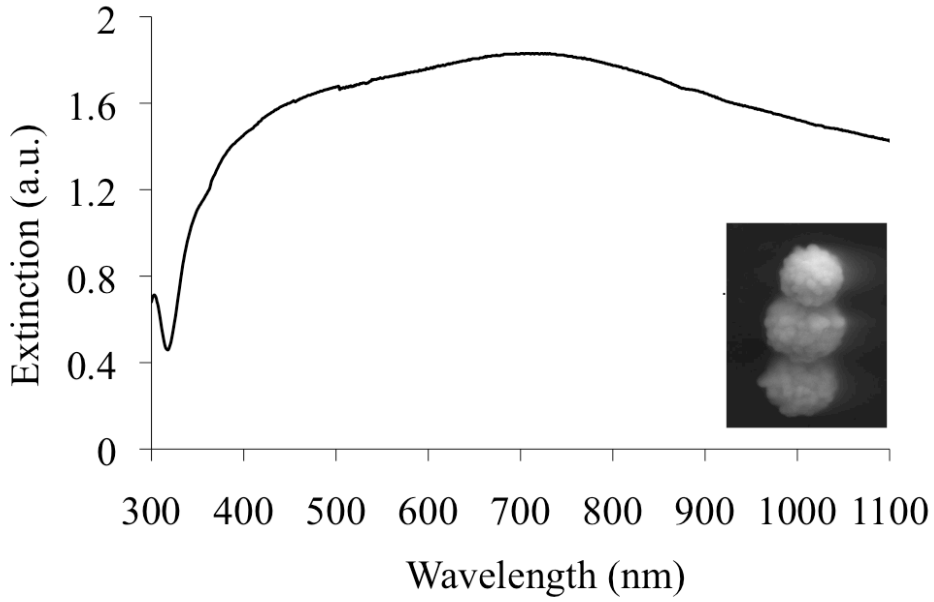


Figure 4.6. The extinction spectrum of the tightly packed silver nanocages directly after synthesis.

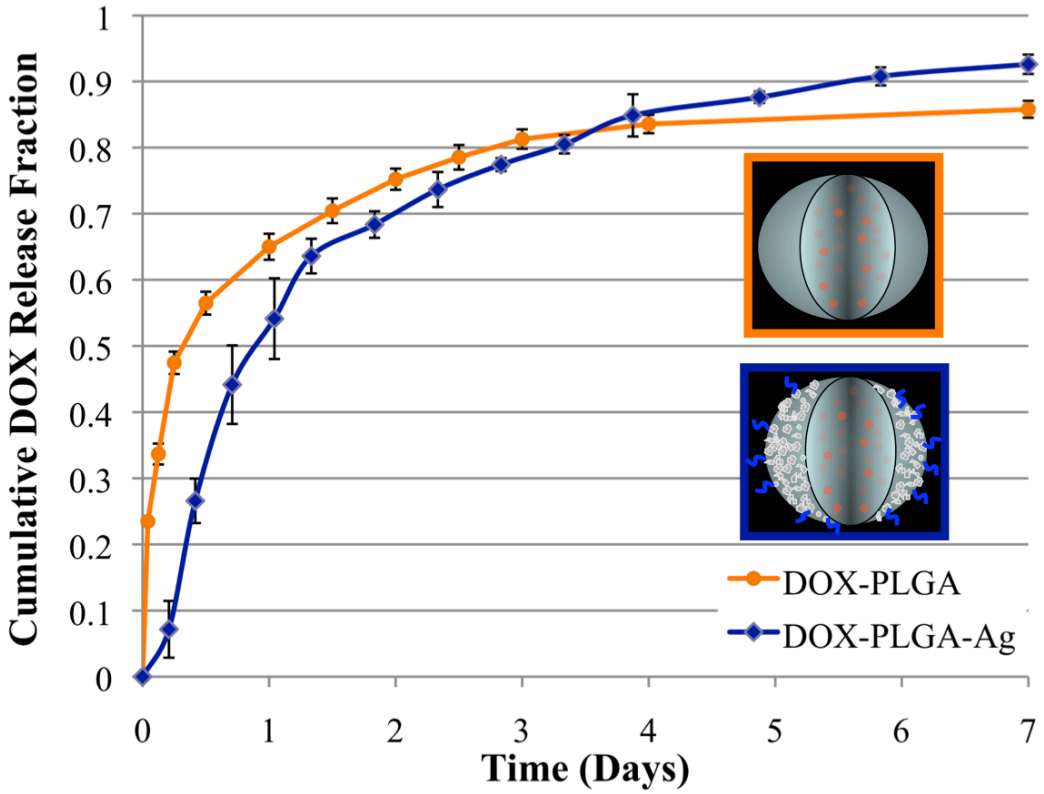


Figure 4.7. A comparison of *in vitro* DOX release from DOX loaded PLGA nanospheres[1] (orange curve) versus DOX loaded PLGA nanospheres coated with a tightly packed silver nanocage (blue curve).

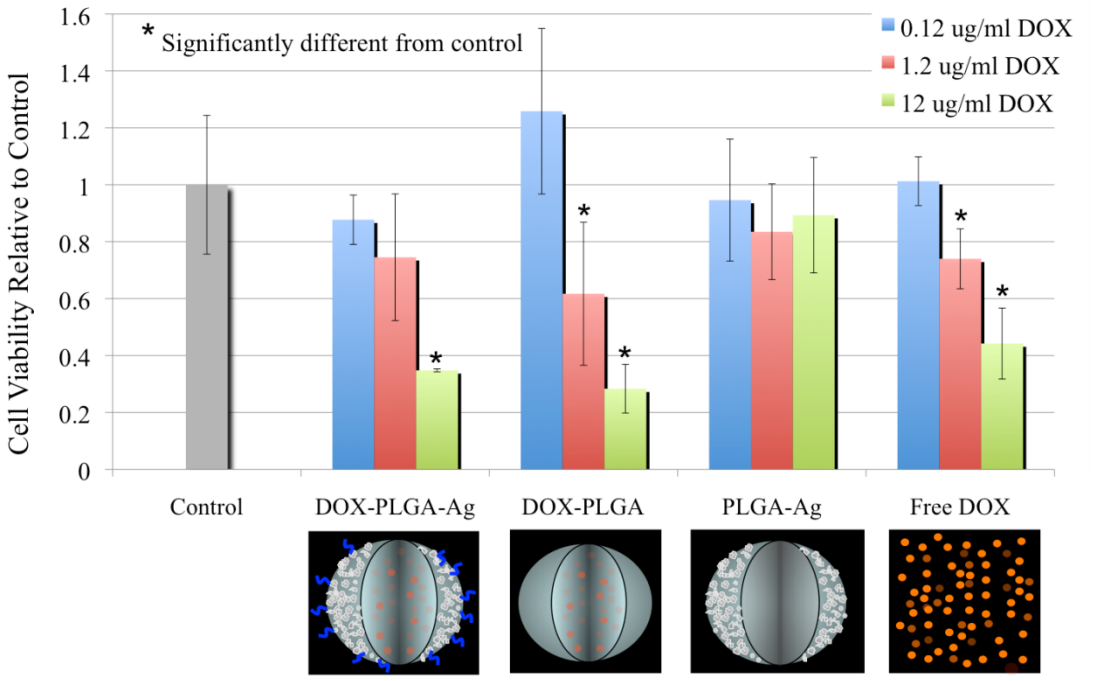


Figure 4.8. Results of the MTT assay with four different conditions mixed in media relative to controls. Values lower than 1 indicate therapeutic efficacy (lower cell viability).

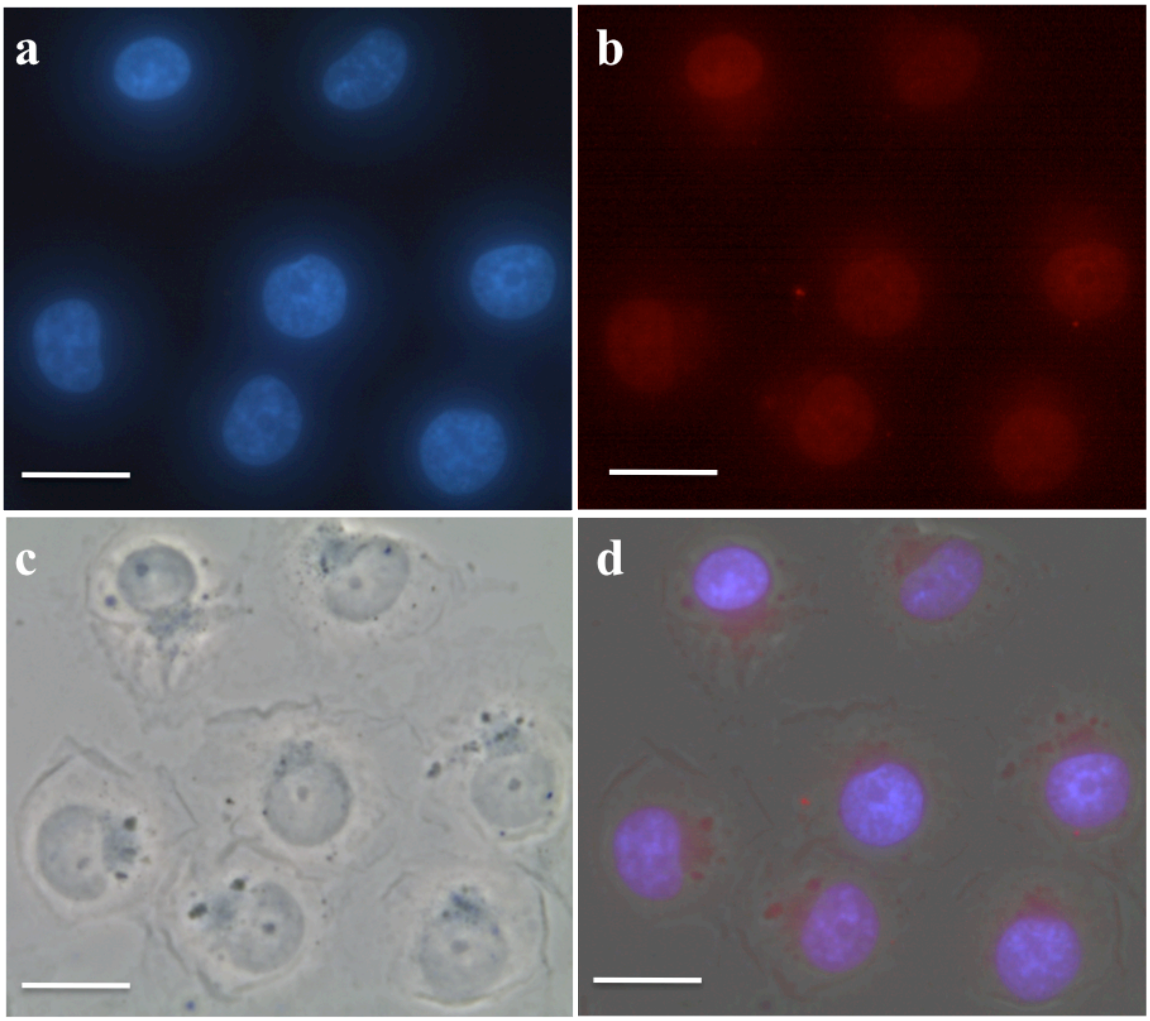


Figure 4.9. MDA-MB-231 breast cancer cells after 18 hr incubation with the CIT-NS incorporating DOX. (a) fluorescence image showing blue DAPI stained nuclei, (b) fluorescence image of the same cells in (a) showing red DOX flourescence, (c) a phase contrast image, and (d) a composite image of the three previous images showing purple nuclei – this indicates the co-location of DOX in the nucleus of these cells. Red DOX is also visible in the cytoplasm. All images are of the same FOV and the scale bars are all 20 μm.

## 4.5 REFERENCES


1. T. Betancourt, B. Brown and L. Brannon-Peppas, "Doxorubicin-loaded PLGA nanoparticles by nanoprecipitation: preparation, characterization and in vitro evaluation," Nanomedicine 2(2), 219-232 (2007)
2. R. R. Patil, S. A. Guhagarkar and P. V. Devarajan, "Engineered nanocarriers of doxorubicin: a current update," Crit. Rev. Ther. Drug Carrier Syst. 25(1), 1-61 (2008)
3. H. S. Yoo, K. H. Lee, J. E. Oh and T. G. Park, "In vitro and in vivo anti-tumor activities of nanoparticles based on doxorubicin-PLGA conjugates," J Control Release 68(3), 419-431 (2000)
4. S. Cai, S. Thati, T. R. Bagby, H. M. Diab, N. M. Davies, M. S. Cohen and M. L. Forrest, "Localized doxorubicin chemotherapy with a biopolymeric nanocarrier improves survival and reduces toxicity in xenografts of human breast cancer," J Control Release 146(2), 212-218 (2010)
5. X. Cheng, F. Zhang, G. Zhou, S. Gao, L. Dong, W. Jiang, Z. Ding, J. Chen and J. Zhang, "DNA/chitosan nanocomplex as a novel drug carrier for doxorubicin," Drug Deliv 16(3), 135-144 (2009)
6. M. J. Johnston, K. Edwards, G. Karlsson and P. R. Cullis, "Influence of drug-to-lipid ratio on drug release properties and liposome integrity in liposomal doxorubicin formulations," J Liposome Res 18(2), 145-157 (2008)
7. D. Lu, X. Wen, J. Liang, Z. Gu, X. Zhang and Y. Fan, "A pH-sensitive nano drug delivery system derived from pullulan/doxorubicin conjugate," J Biomed Mater Res B Appl Biomater 89(1), 177-183 (2009)
8. A. Mahmud, X. B. Xiong and A. Lavasanifar, "Development of novel polymeric micellar drug conjugates and nano-containers with hydrolyzable core structure for doxorubicin delivery," Eur. J. Pharm. Biopharm. 69(3), 923-934 (2008)
9. S. Park and H. S. Yoo, "In vivo and in vitro anti-cancer activities and enhanced cellular uptakes of EGF fragment decorated doxorubicin nano-aggregates," Int. J. Pharm. 383(1-2), 178-185 (2009)
10. M. Prokopowicz, J. Lukasiak and A. Przyjazny, "Utilization of a sol-gel method for encapsulation of doxorubicin," J. Biomater. Sci. Polym. Ed. 15(3), 343-356 (2004)
11. Y. J. Son, J. S. Jang, Y. W. Cho, H. Chung, R. W. Park, I. C. Kwon, I. S. Kim, J. Y. Park, S. B. Seo, C. R. Park and S. Y. Jeong, "Biodistribution and anti-tumor efficacy of doxorubicin loaded glycol-chitosan nanoaggregates by EPR effect," J Control Release 91(1-2), 135-145 (2003)

12. N. Tang, G. Du, N. Wang, C. Liu, H. Hang and W. Liang, "Improving penetration in tumors with nanoassemblies of phospholipids and doxorubicin," J. Natl. Cancer Inst. 99(13), 1004-1015 (2007)

13. R. Tong, L. Tang, L. Yala and J. Cheng, "Controlled formulation of doxorubicin-polylactide nanoconjugates for cancer drug delivery," Conf Proc IEEE Eng Med Biol Soc 2009(2400-2402 (2009)

14. D. H. Xu, J. Q. Gao and W. Q. Liang, "Liposome-based intracellular kinetics of doxorubicin in K562/DOX cells," Pharmazie 63(9), 646-649 (2008)

15. J. J. Yu, H. A. Lee, J. H. Kim, W. H. Kong, Y. Kim, Z. Y. Cui, K. G. Park, W. S. Kim, H. G. Lee and S. W. Seo, "Bio-distribution and anti-tumor efficacy of PEG/PLA nano particles loaded doxorubicin," J. Drug Target. 15(4), 279-284 (2007)

16. L. R. Hirsch, A. M. Gobin, A. R. Lowery, F. Tam, R. A. Drezek, N. J. Halas and J. L. West, "Metal nanoshells," Ann. Biomed. Eng. 34(1), 15-22 (2006)

17. J. Aaron, N. Nitin, K. Travis, S. Kumar, T. Collier, S. Y. Park, M. Jose-Yacaman, L. Coghlan, M. Follen, R. Richards-Kortum and K. Sokolov, "Plasmon resonance coupling of metal nanoparticles for molecular imaging of carcinogenesis in vivo," J Biomed Opt 12(3), 034007 (2007)

18. P. K. Jain and M. A. El-Sayed, "Universal scaling of plasmon coupling in metal nanostructures: extension from particle pairs to nanoshells," Nano Lett 7(9), 2854-2858 (2007)

19. B. Arica and A. Lamprecht, "In vitro evaluation of betamethasone-loaded nanoparticles," Drug Dev. Ind. Pharm. 31(1), 19-24 (2005)

20. F. Danhier, N. Lecouturier, B. Vroman, C. Jerome, J. Marchand-Brynaert, O. Feron and V. Preat, "Paclitaxel-loaded PEGylated PLGA-based nanoparticles: in vitro and in vivo evaluation," J Control Release 133(1), 11-17 (2009)

21. P. V. AshaRani, G. Low Kah Mun, M. P. Hande and S. Valiyaveettil, "Cytotoxicity and Genotoxicity of Silver Nanoparticles in Human Cells," ACS Nano 3(2), 279-290 (2009)

22. P. V. Asharani, M. P. Hande and S. Valiyaveettil, "Anti-proliferative activity of silver nanoparticles," BMC Cell Biol 10(65 (2009)

23. X. Chen and H. J. Schluesener, "Nanosilver: a nanoproduct in medical application," Toxicol. Lett. 176(1), 1-12 (2008)

24. A. B. Lansdown, "Critical observations on the neurotoxicity of silver," Crit. Rev. Toxicol. 37(3), 237-250 (2007)

# Chapter 5: Synthesis and Characterization of the CIT-NS incorporating Gemcitabine

At this point in the dissertation, all preliminary steps towards creating the CIT-NS have been described. Chapter 3 showed proof of concept for photoacoustic imaging using an optically similar nanosystem. Chapter 4 provided *in vitro* characterization of the CIT-NS, incorporating the model drug doxorubicin. This chapter details attempts to incorporate gemcitabine, the pancreatic cancer chemotherapeutic agent, into the CIT-NS (Fig 5.1).

## 5.1 Introduction

Gemcitabine (Gem) remains the gold standard in chemotherapeutic treatment of pancreatic cancer.[1] Gem (2',2'-diflourodeoxycytidine) is a pyrimidine antimetabolite whose structure is an analogue to deoxycytidine (Fig 5.2). The two fluorine atoms on Gem that differentiate it from deoxycytidine make it a potent analogue base.

Once in the cell, Gem must undergo phosphorylation to the active 5'-triphosphate; this conversion is mediated by deoxycytidine kinase. Once in this active form, gemcitabine triphosphate gets incorporated in an elongating DNA strand. Once it is added, however, no further bases can attach, DNA synthesis halts, and there is further inhibition of ribonucleoside reductase.[2] Thus, Gem's mode of action is to mimic the C-base of DNA, use the cell's native enzymes to put it in an active 5'-triphosphate form, and halt DNA synthesis, leading to cell death via apoptosis.

Unfortunately, Gem could not be incorporated in poly(lactic-co-glycolic) acid (PLGA), which is the core of the desired CIT-NS system. Like all DNA bases, Gem is hydrophilic. This hydrophilic property makes it difficult to entrap in hydrophobic carriers such as poly(lactic-co-glycolic) acid (PLGA). Thus, a prodrug form of Gem was sought.

Another reason for seeking a prodrug form of Gem is that Gem has a short half life in plasma (on the order of minutes). Therefore large doses of the drug are required to achieve therapeutic levels. Gem's short half life is caused by cytidine deaminase in the blood, liver, and other tissues. Cytidine deaminase converts Gem to the inactive metabolite 2',2'-diflourodeoxyuridine, which is excreted in the urine.[2]

Synthesizing prodrug forms of Gem can solve both the solubility and deamination challenges. Making 4-(N)-acyl derivative prodrug forms of Gem can (1) make the drug more hydrophobic and (2) provide enough stability of the amine to significantly increase its half life *in vivo*.[2, 3] Researchers have shown that acyl derivative of Gem are just as active or more active than the native drug since cathepsin enzymes B and D do cleave the amide bond on the prodrug, recovering native Gem in the intracellular space.[2] Therefore, Gem prodrugs represent a viable option for incorporation in the desired CIT-NS.

In this chapter, encapsulation of native gemcitabine and a prodrug form of gemcitabine in PLGA using emulsion techniques is presented. Furthermore, the implications of incorporating these gemcitabine derivatives in the CIT-NS design is broadly addressed.

## 5.2 METHODS

Each step in the synthesis and characterization of gemcitabine derivatives loaded in PLGA are described separately below. For reader clarity, the sources for all materials are consolidated here.

### 5.2.1 Materials

All chemicals were used without further purification and were at minimum ACS grade. PLGA 50:50DL 2A was purchased from Lakeshore Biomaterials (Birmingham,

AL, USA, ~12 kDa) and Medisorb (Cincinnati, OH, $M_n$ = 11 kD). Bovine serum albumin, polyvinyl alcohol (PVA, ~30 kDa), mineral oil, oleoyl chloride, pyridine, and methanol were purchased from Sigma-Aldrich (St. Louis, MO, USA). Dimethyl sulfoxide (DMSO) and acetone were purchased from Fisher Scientific (Fair Lawn, NJ, USA). Dulbecco's phosphate buffered saline (DPBS) came from Mediatech, Inc. (Herndon, VA, USA). Lecithin was a product of Acros (Morris Plains, NJ, USA). Gemcitabine hydrochloride was purchased from Chemiceuticals LLC (Research Triangle Park, NC, USA). All cell culture products, including the MTS assay, were purchased from Invitrogen (Carlsbad, CA, USA) unless otherwise specified.

### 5.2.2 Gemcitabine Encapsulation in PLGA

In spite of its hydrophilic properties, encapsulation of Gem in PLGA was achieved. A water-in-oil-in-oil double emulsion method was used, similar to that previously described.[4, 5] An inner aqueous phase was created by dissolving 24 mg of Gem in 500 µl of a 10 mg/ml polyvinyl alcohol (PVA) solution. This phase was slowly added onto an organic phase (inner oil) containing 100 mg of PLGA in 1.25 ml of acetone, and the system was sonicated for 1 min. This first emulsion was poured into 35 ml of the external oil phase which contained mineral oil with dissolved lecithin (1.25 mg/ml) and sonicated again for 1 min. Organic solvent was removed while stirring under vacuum, the particles were collected by centrifugation at 45,000xg for 15 min, and the supernatant was removed. Gem loaded PLGA particles were washed repeatedly by suspension in hexane containing lecithin (1.25 mg/ml) to remove mineral oil. Storage of the particles involved adding 120 mg of trehalose (cryoprotectant) to the particle pellet and freezing overnight in a -80°C freezer. The resulting solution was then lyophilized in a Freeze Dryer 4.5 (Labconco, Kansas City, MO, USA) and the particles stored at -20°C. For Gem

release studies, the particles were suspended in 40 ml of Dulbecco's phosphate buffered saline (DPBS) and allowed to sit in a 37°C water bath. At various times, the particles were spun down at 45,000xg for 15 min and their supernatants collected. Drug release was quantified using spectrophotometric analysis of the supernatants at the peak absorbance of Gem (269 nm).

### 5.2.3 Synthesis of a Gemcitabine Prodrug

Many methods were used in attempts to make Gemcitabine-$N^4$ Oleoyl Amide (see Section 5.3.2.2). The greatest yield was achieved by a method adapted from a gemcitabine derivatives patent which described a similar procedure using elaidic acid chloride.[3] The reaction schematic is shown in Fig 5.3. Specifically, Oleoyl Chloride (OC) was reacted in 2.5 molar excess to Gem by the following method. Gem (100 mg, 0.333 mmol) was dissolved in 3.0 ml of pyridine and placed under an Ar environment with vigorous stirring. Then 55 μl of OC (0.167 mmol) was added using a microneedle at successive time points of 0, 1, 2, 3, and 4 hr into the reaction. The reaction was characterized using electrospray ionization mass spectroscopy at the time points of 1, 2, 3, 4, and 5 hr into the reaction. To separate unreacted OC from the PD, the entire crude reaction mixture was rotovaped until only an orange gooey precipitant remained. The precipitant was then suspended in 10 ml methanol. Remaining unreacted OC and oleic acid collected as a clear/white pellet at the bottom of the flask. The methanol containing PD was collected and rotovaped 3x with methanol suspensions to remove any excess pyridine. The final product was characterized by rotovaping again, drying overnight in a vacuum oven, and resuspending in deuterated pyridine for $H^1$ Nuclear Magnetic Resonance (NMR) analysis at 600 MHz. Spiking the mixture for NMR with a known

amount of dioxane allowed for quantification of the amount of PD present, and thus the yield of this synthesis method.

### 5.2.4 Cytotoxicity Studies with the Gemcitabine Prodrug

The human pancreatic cancer cell line L3.6pl (a generous gift from the Pancreatic Cancer Group at M.D. Anderson Cancer Center) was incubated with both Gem and the PD in cell media to test the therapeutic efficacy (cell viability) of both drugs relative to each other and relative to control conditions with no drugs. The L3.6pl cells were cultured using Dulbecco's Modified Eagle Medium (DMEM) (with 4500 mg glucose/L, L-glutamine, $NaHCO_3$ and pyridoxine HCl) supplemented with 10% fetal bovine serum (FBS) and 1% Penicillin-Streptomycin (Pen/Strep) while maintained at 37°C and 5% $CO_2$ in a humidified incubator. For cell viability studies, cells were seeded in a 96 well plate (each well had 5,000 cells per 100 μl of media). The cells were allowed to attach and grow in the 96 well plate for 24 hr, after which the cell media was removed and replaced with suspensions of Gem and PD in media at various concentrations (300 nM, 30 nM, 3 nM and 0 nM). Note that to get the PD suspended properly in media, Tween 20 was added as a biocompatible surfactant. After 48 hr of incubation, 20 μl of a tetrazolium compound [3-(4,5-dimethylthiazol-2-yl)-5-(3-carboxymethoxyphenyl)-2-(4-sulfophenyl)-2H-tetrazolium (MTS) and an electron coupling reagent (phenazine methosulfate) PMS from the CellTiter 96® $AQ_{ueous}$ Non-Radioactive Cell Proliferation Assay (a Promega product) was added to each well. Over a period of 1.5 hr in the incubator, the MTS was bioreduced by cells into a formazan product that had an absorbance peak at 490 nm. After 1.5 hr, the absorbance of each well in the plate was measured at 490 nm using a Synergy HT Multimode Microplate Reader from BioTek. Dehydrogenase enzymes found in metabolically active cells were responsible for the conversion of MTS into the soluble

formazan product. Therefore, the absorbance of each well at 490 nm was directly proportional to the number of viable cells (at least 6 wells were tested per condition). Cell viability was determined by comparing the resulting absorbance of wells containing no drugs to wells containing Gem and PDs using an F test for a one-way ANOVA.

### 5.2.5 Gemcitabine Prodrug Encapsulation in PLGA

An oil in water emulsion technique was used to entrap the PD in PLGA similar to that previously described[6] and used for Doxorubicin encapsulation in Chapter 4. This technique is appropriate since the PD is soluble in methanol. The steps in this technique are described below and shown in Fig 5.4.

Briefly, 100 mg of PLGA was dissolved in 2 ml acetone. Then 225 μl of an 11.11 mg/ml solution of the PD in methanol was added to the PLGA solution in acetone to form the oil phase. The water phase consisted of a 10 ml surfactant solution of 5 mg/ml poly(vinyl alcohol) (PVA) and 5 mg/ml bovine serum albumin (BSA) in deionized and ultrafiltrated to 18.2 MΩ-cm (DIUF) water.

The oil phase was pipetted quickly into the water phase and sonicated for 15 seconds. The resulting white cloudy nanoprecipitation was stirred vigorously under slight vacuum for 30 min to remove the organic solvents. The resulting PD loaded PLGA nanoparticles were collected via centrifugation at 48,000xg in a Beckman J2-21 refrigerated centrifuge running at 4°C for 15 min. The supernatants from all washes were retained for spectrophotometric analysis.

## 5.3 Results and Discussion

The first step in synthesizing the CIT-NS system with Gem is to encapsulate Gem in PLGA. The results of several methods to entrap Gem and a PD of Gem in PLGA are detailed below.

### 5.3.1 Gemcitabine loaded PLGA Microparticles

Gem was successfully loaded in PLGA using a water-in-oil-in-oil emulsion was successful. Encapsulation efficiencies (percent of Gem loaded versus that used in preparation) of up to 70% with loadings of up to 17 mg Gem per 100 mg PLGA, as determined by spectrophotometric assay, were observed. Unfortunately, the Gem loaded PLGA particles were larger than desired; they were actually *micro*particles (Fig 5.5). Furthermore, release studies showed all of the Gem releasing from the microparticles within the first half hour of being in an aqueous PBS solution. The water-in-oil-in-oil technique tends to produce larger particles, such as these Gem loaded PLGA microparticles.[4] Smaller particles can be synthesized if high sonication powers (up to 120 W probe sonicators) are used during the emulsion, but ultimately the Gem release profile is too fast for *in vivo* applications. Therefore, synthesis of a prodrug form of Gem that allows for better encapsulation in *nano*particles and slower release from PLGA, as detailed in the next section, was necessary.

### 5.3.2 Synthesis of a Gemcitabine Prodrug

This section describes three important results: (1) the successful synthesis of Gemcitabine-$N^4$ Oleoyl Amide, (2) many failed attempts to synthesize and purify various gemcitabine prodrugs, and (3) characterization of the PD's toxicity to a pancreatic cancer cell line *in vitro*.

#### *5.3.2.1 Synthesis and Characterization of Gemcitabine-$N^4$ Oleoyl Amide*

Gemcitabine-$N^4$ Oleoyl Amide (PD) was successfully synthesized using acyl halide chemistry. As reaction time increased, formation of the PD at 528 m/z in the mass spectroscopy results (Fig 5.6) was evident, along with a corresponding decrease in Gem at 264 m/z. A peak absorbance shift was also noted in the ultraviolet spectrum from the

peak for Gem (269 nm) to a peak for the PD (251 nm). Note that lower yields of the PD were obtained when OC was not added in succession during the reaction. Successive additions of OC may have helped maintain the activity of the very reactive OC species, reducing unwanted side reactions and increasing PD yield.

The Gem-OC reaction proceeded by a standard $S_N2$ mechanism. Again, OC is a very reactive species, with its Cl being an excellent leaving group. The excellent leaving group on OC helped facilitate a reaction with the nucleophilic primary amine on Gem, forming an amide bond. Fortunately, this synthesis involved a benign reactant, OC, that readily forms biocompatible oleic acid derivatives in the presence of methanol or water. Therefore, the synthesis worked as expected where the only toxic agent left in the final formulation was the PD itself.

The purification and yield of the PD was determined by NMR. Most peaks in the NMR spectrum correspond with those cited for the Gemcitabine-$N^4$ Elaidic Amide described elsewhere.[3] The NMR spectra for Gem and the PD are shown in Fig 5.7. Shifts in the CH6, CH5, and CH1 positions are seen in the PD spectrum; no peaks associated with the Gem control are seen in the PD spectrum. Since a liquid separation/precipitation method was used to separate the PD from the initial reactants, the retention of small impurities from the initial two reactants was expected (small unexplained peaks in the PD NMR in Fig 5.7). More rigorous methods of purification such as preparative liquid chromatography (LC) using a silica column with a mobile phase of 10% methanol in chloroform was attempted, but the separation was poor and overall yield suffered greatly. Note that yields of other processes to make and purify gemcitabine prodrugs with these LC techniques have been reported between 15-50%.[2, 3] The benefit of the simple separation method presented here is high yield. Using just liquid separation, yields as high as 90% were obtained. Yields were determined by spiking the NMR sample with a

known amount of dioxane and comparing the area under the dioxane peak at 3.61 ppm with that of CH6 on the PD at 8.51 ppm (this procedure was repeated with several controls and the experimental error between the NMR machine and the dioxane spiking was 13%). High yield is important because Gem is expensive. Furthermore, since our ultimate goal is to encapsulate the PD in PLGA, any Gem impurities left in the PD formulation will be expelled in the water phase during processing. The rare oleic acid derivatives left might encapsulate in PLGA, but they will have no cytotoxic effects and will not preclude a solid preliminary study on the synthesis of the CIT-NS.

#### *5.3.2.2 Failed Attempts to Synthesize Gemcitabine Prodrugs*

Synthesis of a Gem prodrug took 3.5 years of effort and resulted in numerous failed attempts. The methods attempted fall into two categories: synthetic methods in wet phase and synthetic methods involving solid phase organic chemistry.

Wet Chemistry Methods: Using techniques described by Immordino et al[2], the synthesis of 4-N-stearoyl-gemcitabine was attempted. The reaction was performed in dioxane with the reactant stearic anhydride. The reaction was monitored with spectrophotometry, thin layer chromatography, and mass spectroscopy; and none of these characterization tools indicated the presence of 4-N-stearoyl-gemcitabine. Aside from the reaction conditions specified by Immordino et al, reaction times for up to 63 hr at elevated temperatures up to 60°C were attempted, and still no prodrug was formed. The main difference between our experimental conditions and that of Immordino et al was the Gem used. They synthesized Gem in house, while we were using Gem that was packed as a salt with HCl as purchased from Chemiceuticals LLC. It is possible that the added HCl in our formulation inhibited the reaction by lowering the overall pH and making conditions unfavorable for 4-N-stearoyl-gemcitabine to be formed.

Solid Phase Chemistry Methods: Long polypeptide chains and libraries of DNA can now be synthesized using solid phase organic chemistry.[7-9] Solid phase organic chemistry takes place in solution on the surface of polystyrene beads (~150 to 400 μm in diameter).[8] Generally these polystyrene beads, also called resin, are surface functionalized with linker molecules that can react with functional groups on a molecule of interest. Once a molecule is attached to the resin, further organic chemistry reactions can be performed on the molecule at the bead surface. The beauty of solid phase organic synthesis is the ability to perform repeated washes while the product is immobilized on the resin, and then easily recover the reacted compound. For instance, using a Teflon fritted syringe, the beads can be trapped and cleaned with multiple solvents ad infinitum. Usually, detaching a product from the bead is simple since most linkers are acid labile. Therefore, placing a small amount of triflouroacetic (TFA) acid (1%) in dichloromethane (DCM) could cleave any supported compound from the bead, and that product would then be easily collected and separated from the beads. Since conventional LC methods were proving challenging for recovering large yields of pure PD, these solid phase organic synthesis methods were attempted in the hopes of retrieving high yields of purified prodrug.

The first solid phase organic chemistry strategy attempted was to couple dihydropyran-functionalized (DHP) resin to the primary alcohol on Gem. This strategy involved immobilizing Gem through its primary alchohol, leaving Gem's primary amine free for acylation in subsequent steps. Two preliminary steps were taken towards this strategy: (1) since Gem must be cleaved off the resin using TFA (a strong acid), Gem degradation in the presence of TFA was tested and (2) since high yield, high purity synthesis was the goal of this strategy, the loading and release of just Gem was tested prior to performing the acylation step. In the first test, Gem was incubated with a 5%

TFA solution in water for 5 min. After evaporating off the TFA and water, mass spectroscopy and NMR results showed no appreciable differences between Gem incubated with TFA and control Gem. Therefore, the second preliminary test was initiated using methods described by Thompson et al.[10] Briefly, 489.1 mg of DHP resin was placed in a round bottom flask with 5 ml of dichloroethane (DCE). The beads were allowed to swell for 15 min while heating in an 80°C oil bath under reflux. Finally, 230.6 mg of pyridinium p-toluenesulfonate PPTS (a 2.7 fold molar excess greater than the available linker sites on the resin surface) and 50.6 mg of Gem were added and the solution was stirred under reflux for 48 hr at 80°C. After the reaction, the beads were transferred to a fritted syringe where they were washed with DCM (1x), 1:1 dimethylformamide (DMF):water (4x), DMF (3x), DCM (3x), and lastly 95:5 TFA:water for bead cleavage and collection. Mass spectroscopy confirmed the presence of intact Gem cleaved from the beads, but spectrophotometric analysis only showed a 13% yield. Furthermore, a ninhydrin test was used to look for the presence of the primary amine on Gem after cleavage. The ninhydrin compound should turn blue in the presence of a primary amine, but in both the test sample and Gem controls, the ninhydrin never exhibited a blue color. It is possible that the ninhydrin test works better with less hindered primary amines. Overall, after varying many parameters (amount of resin vs PPTS, temperature, etc) the highest loading and release yield of Gem was only 13%. This yield wasn't high enough to warrant further exploration of coupling Gem to DHP resin. The next strategy was to try a more nucleoside friendly resin.

After the DHP resin failed to load Gem in high yield, a resin used commonly in DNA synthesis was attempted, the dimethoxytrityl (DMT) resin. It is known that primary amines readily attach to DMT-functionalized resins.[11] Therefore, the strategy here was to block the primary amine site by performing the acyl halide reaction (Section 5.3.2.1), and

then use the beads to sift out the Gemcitabine-$N^4$ Oleoyl Amide prodrug from its reactant mixture by coupling to DMT through its primary alcohol. If higher resin loading could be achieved with this method, then cleaning and purification of the PD could be facilitated by using the resin. Briefly, Gemcitabine-$N^4$ Oleoyl Amide was synthesized using the methods described in Section 5.3.2.1. Then 1 g of DMT resin was placed in the reaction vessel with 8.5 ml of dry DMF, 45.46 mg of imidazole, 43.36 μl of methanesulfonic acid, and 116.32 μl of diisopropylethylamine. Under an Ar environment, the mixture was shaken on an orbital shaker for 24 hr. This method of coupling nucleosides to DMT using mesylates had been previously reported.[12] The resin was then transferred to a fritted syringe and cleaned using DMF (3x) and DCM (2x) before cleaving using a 0.5vol% TFA in DCM solution. Unfortunately, the yield of the PD was so low that it was immeasurable with spectrophotometers, although it was detected with mass spectrometry. Furthermore, even though the resin product manufacturers claim that the DMT cleaves from the nucleotide, we observed significant amounts of DMT eluting off the beads and into the cleavage solution, creating impurities in our final product. Even worse, however, was that the OC reactant had formed oleic acid and the oleic acid coupled to the beads in large quantities. Therefore, using DMT beads to clean unreacted OC away from the PD was simply not possible and the strategy of using solid phase chemistry was abandoned.

#### *5.3.2.3 Gemcitabine-$N^4$ Oleoyl Amide Toxicity Compared to Native Gemcitabine*

Even though many strategies for prodrug synthesis had failed, the acyl halide approach creating Gemcitabine-$N^4$ Oleoyl Amide as described in Section 5.3.2.1 was successful. Using that synthesis, a PD was created that could be characterized and tested. One such *in vitro* test was the cytotoxicity studies with pancreatic cancer cells detailed below.

The available literature reports the cytotoxic activity of Gem prodrugs to be between two- and five-fold better than native gemcitabine.[2] Most references site the stability of the prodrug forms in plasma as the main reason for increased therapeutic efficacy.[2, 3] The tests performed in the literature were with different cells lines than those used here and measured inhibition of protein synthesis. In comparison, the MTS assay presented here (Fig 5.8) is a cell viability study only, measuring the function of active mitochondria. The results shown in Fig 5.8 indicate that the PD and Gem have toxic effects proportionate to concentration. However, this MTS assay performed on L3.6pl pancreatic cancer cells demonstrated no evidence of enhanced cytotoxicity with the PD. Instead, these results indicated that the PD and Gem are equally effective. The contradiction between these results and the literature might stem from either the type of cytotoxicity tests performed or the differences between individual cells lines. Protein inhibition testing would need to be performed on the L3.6pl cell line to further elucidate the reason for this difference.

### 5.3.3 Gemcitabine-$N^4$ Oleoyl Amide Encapsulation in PLGA

Unfortunately, encapsulation of the PD Gemcitabine-$N^4$ Oleoyl Amide in PLGA via the oil in water emulsion technique was unsuccessful. Immediately after the oil phase was added to the water phase, the white milky solution began to aggregate. Two solutions are shown in Fig 5.9 – the left one was PD loaded PLGA and the right was a control with no drug loading. Aggregation is clear in the PD loaded PLGA sample. Encapsulation efficiencies were only 50% for PD loaded PLGA and the resulting PLGA particles were non-spherical in shape with a large polydispersity (Fig 5.10). Different combinations of surfactants ranging from 1 to 10 mg/ml of BSA and 1 to 10 mg/ml PVA combinations were attempted, but all trials suffered from similar microparticle results with low

encapsulation efficiencies. While these hydrophobic forms of Gem load well in carriers such as liposomes[2], in the case of PLGA they might be acting as a plasticizer. Recall from Chapter 2 that the Tg of PLGA is 40-45°C. If Gem and/or Gem prodrugs are acting as a plasticizer and lowering the Tg significantly, then amorphous shapes of PLGA, as shown in Fig 5.10, would result. Further work using either differential scanning calorimetry or thermo-mechanical analysis could be used to test the plasticizer hypothesis. The fact that a stable colloidal suspension of PD loaded PLGA nanoparticles could not be produced with the methods tested, meant that further progress towards building the CIT-NS incorporating Gem was simply not feasible or that further research incorporating Gem or PD into other polymeric carriers would need to be investigated.

## 5.4 CONCLUSIONS

In its native form, Gem did encapsulate in PLGA, but the resulting PLGA particles exhibited a large polydispersity in size from 200 nm to 20 μm; and all of the Gem released from these particles after just 30 min in aqueous solution. Thus, Gem prodrugs that might encapsulate in PLGA and release slowly were considered as a viable alternative. Furthermore, prodrugs, being more stable in plasma than native Gem, might also provide a therapeutic benefit. A prodrug of Gem, Gemcitabine-$N^4$ Oleoyl Amide, was successfully synthesized; but contrary to the literature, it showed no enhanced therapeutic efficacy over the free native Gem and did not encapsulate well in PLGA. Using oil in water emulsion techniques, only 50% encapsulation efficiencies were achieved, and the PLGA particles aggregated extensively. These findings might indicate that synthesizing the CIT-NS incorporating Gem is not feasible. Solutions to this problem could involve updating the CIT-NS design. For instance, the polymer used for encapsulation could be changed to one unaffected by Gem, or liposomes could be used as

the core of the CIT-NS. One could also consider completely new designs for the CIT-NS that incorporate silver and Gem without the polymer. The design of such a system is the subject of the next chapter.

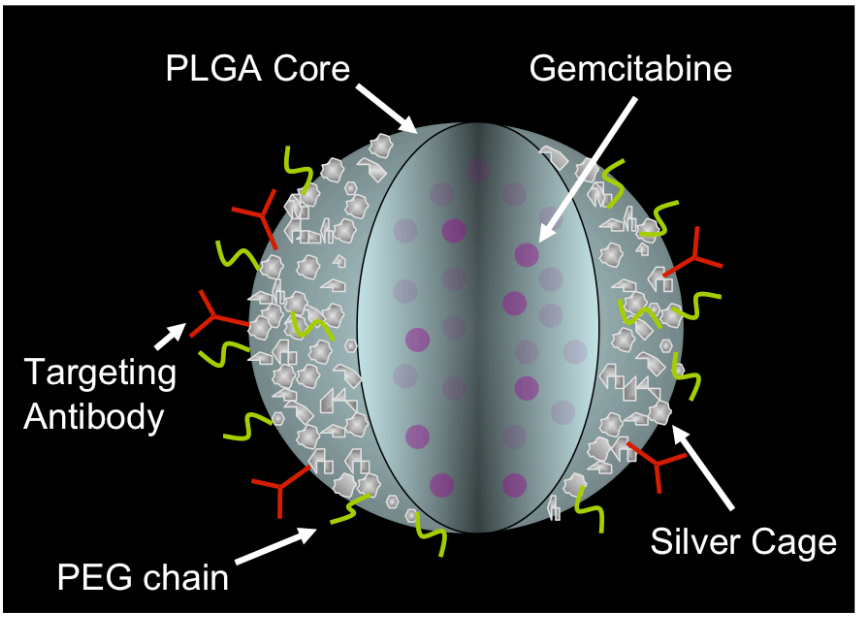


Figure 5.1: An illustration of the desired Combined Imaging and Therapy Nanocage System (CIT-NS).

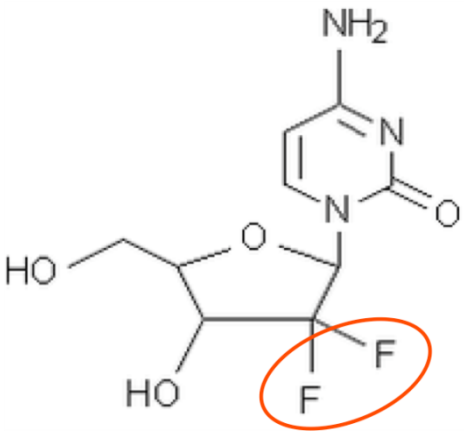


Figure 5.2: The chemical structure of gemcitabine. In deoxycytidine the two fluorines circled in red are hydrogens.

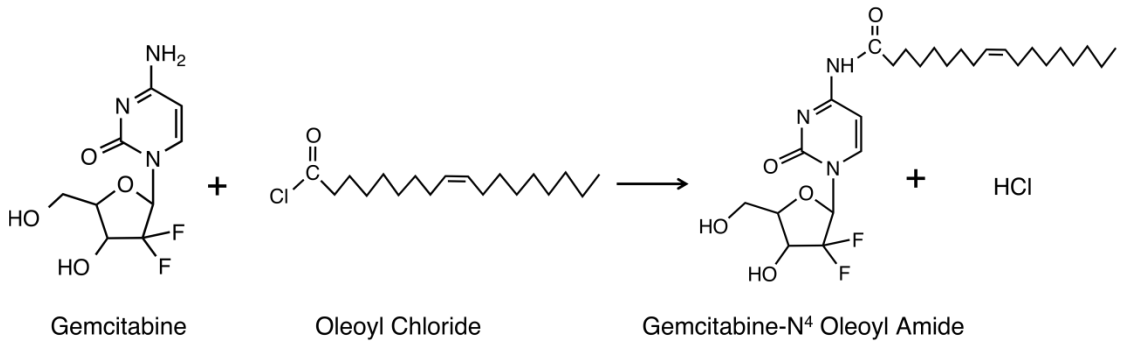


Figure 5.3: A reaction schematic showing how Gemcitabine-$N^4$ Oleoyl Amide was synthesized.

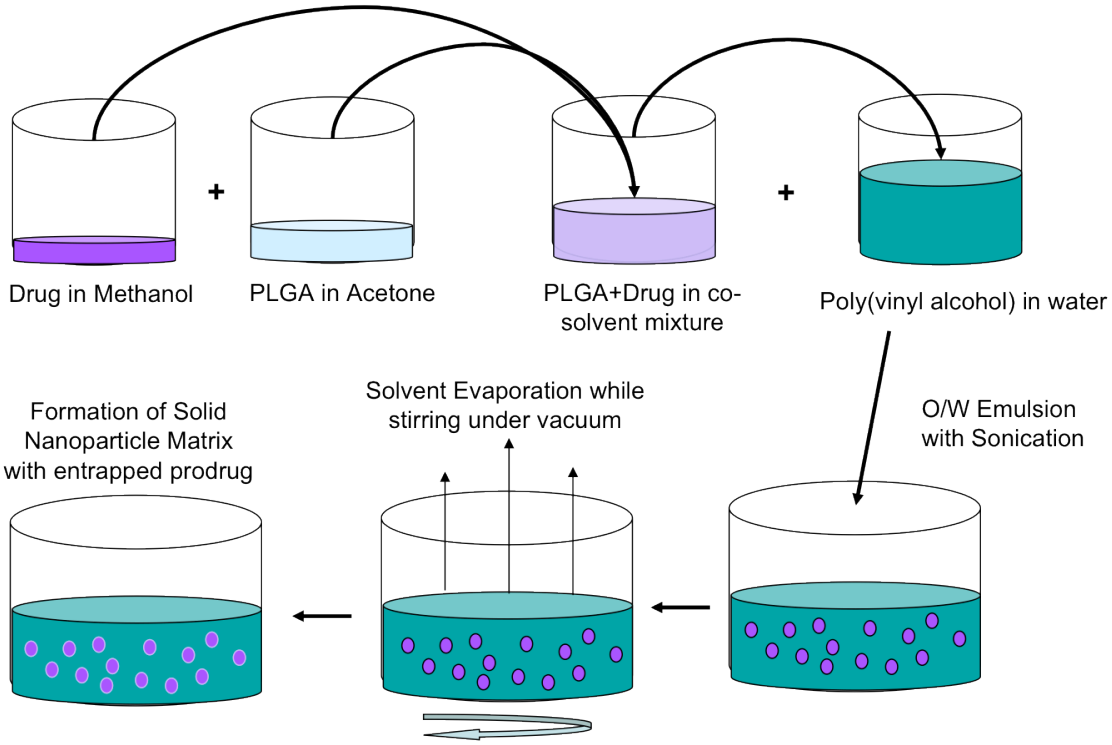


Figure 5.4: A schematic depicting the steps in the oil in water emulsion method required to encapsulate hydrophobic drugs in PLGA.

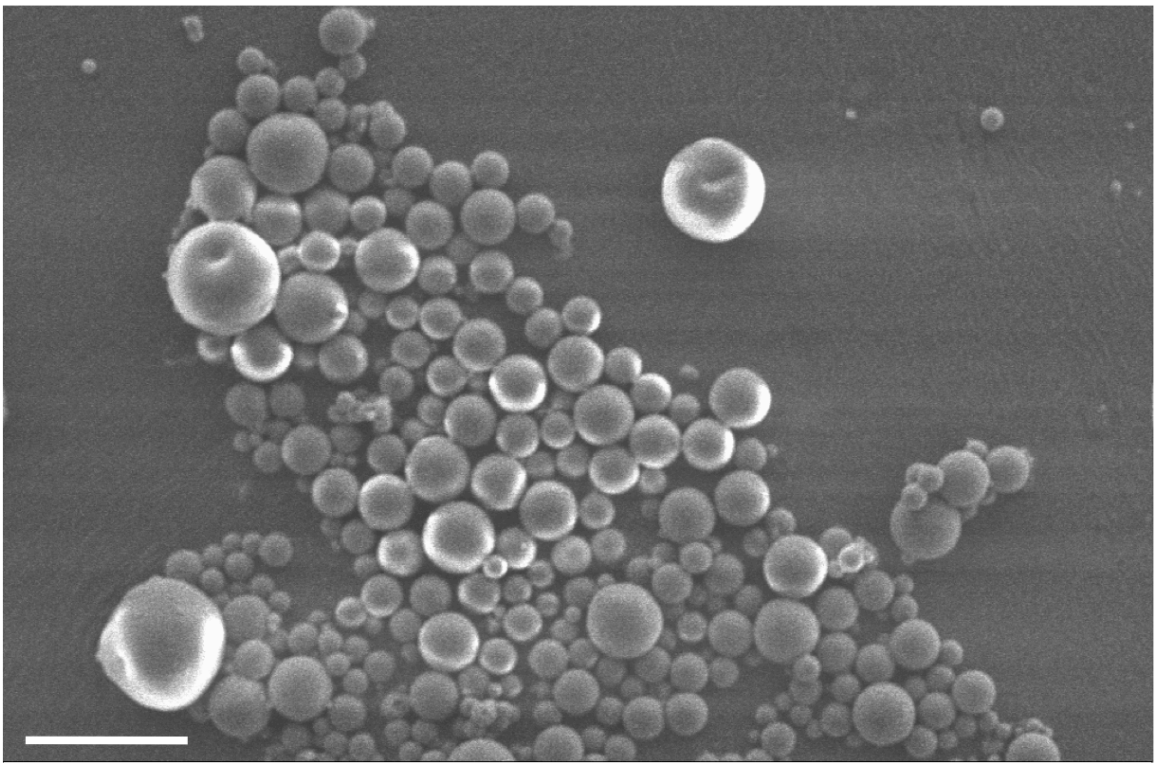

Figure 5.5: Gemcitabine loaded microparticles. Scale bar is 20 μm.

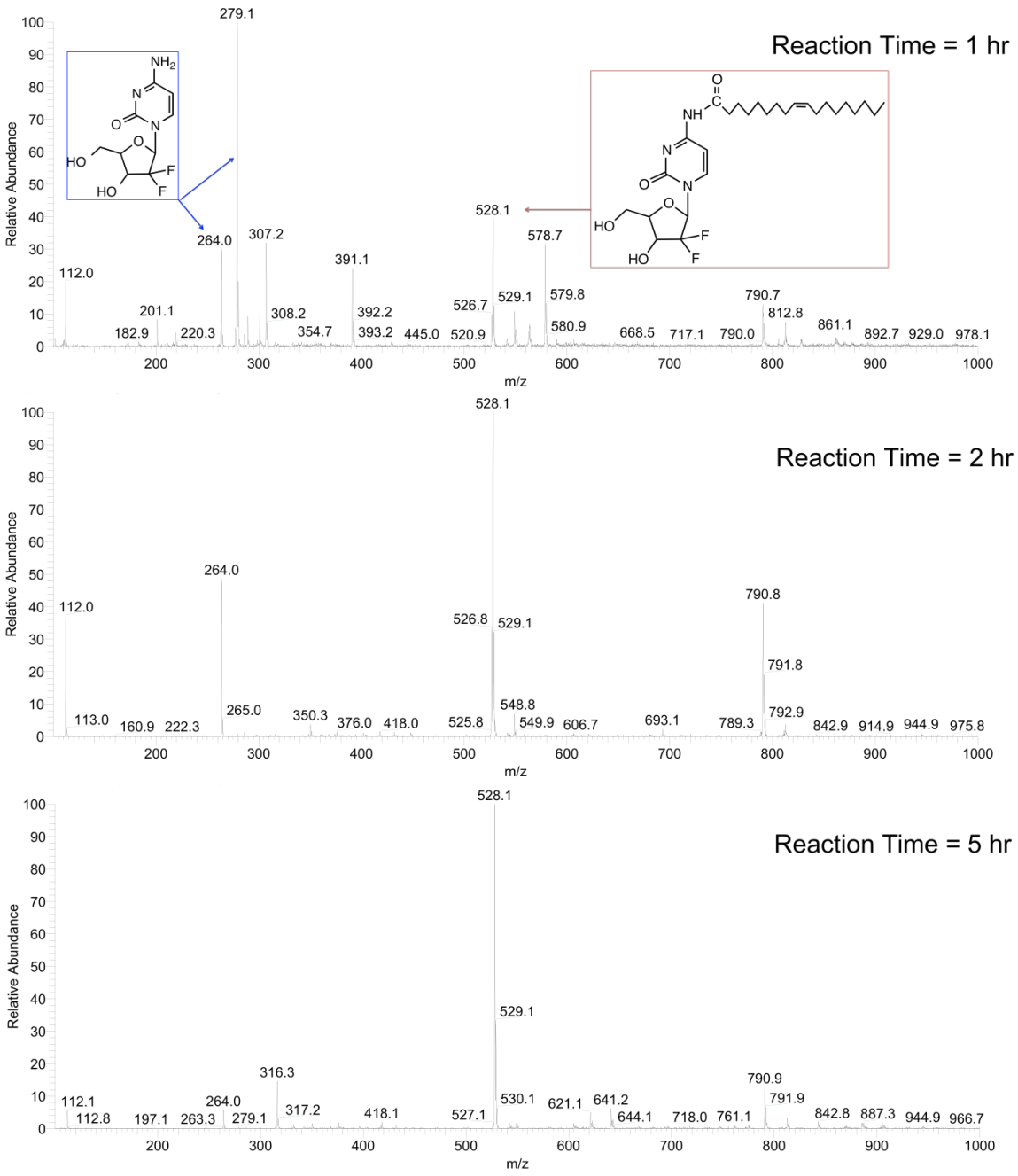


Figure 5.6: Progressive mass spectroscopy results as time continues in the reaction to form Gemcitabine-$N^4$ Oleoyl Amide.

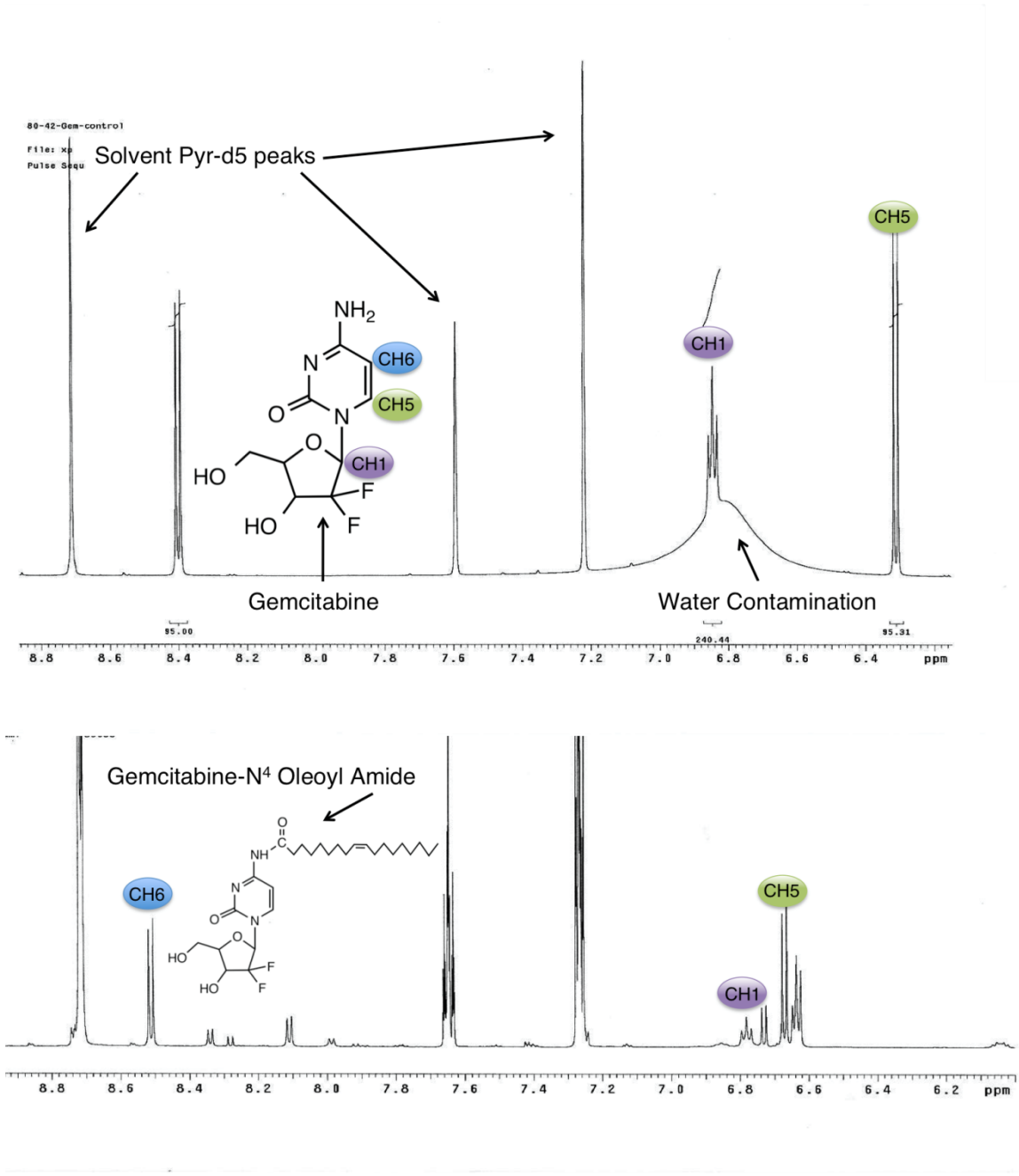


Figure 5.7: NMR of Gem (top) and the PD (bottom). The H shifts that are most noteworthy with the acylation of Gem are the CH6, CH5, and CH1 as labeled in blue, green, and purple, respectively. The PD spectrum shows major shifts in the doublet and triplet peaks associated with these positions, leaving no trace of Gem in the purified PD spectrum.

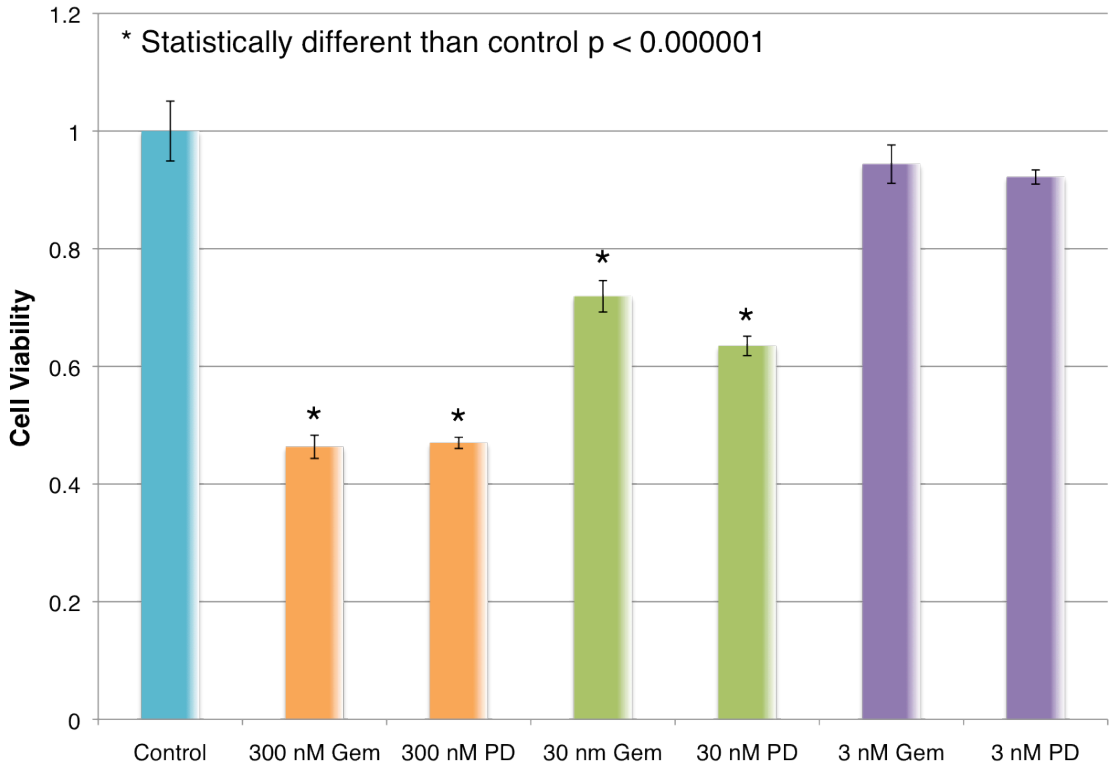


Figure 5.8: MTS assay results showing the relative cell viability to control when L3.6pl pancreatic cancer cells were mixed with different concentrations of the native Gemcitabine (Gem) drug versus the Gemcitabine-$N^4$ Oleoyl Amide prodrug (PD).

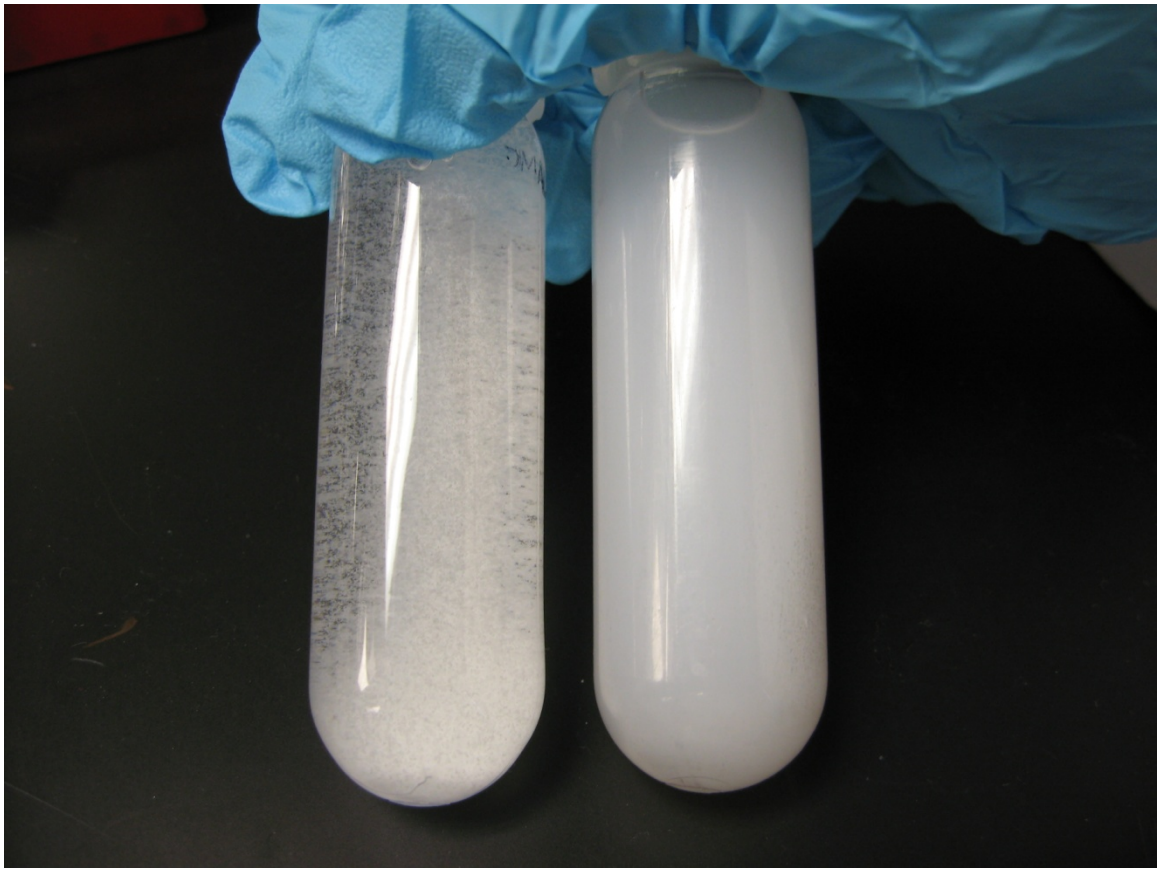

Figure 5.9: Gemcitabine loaded PLGA microparticles (left) and control PLGA nanoparticles with no drug loading (right).

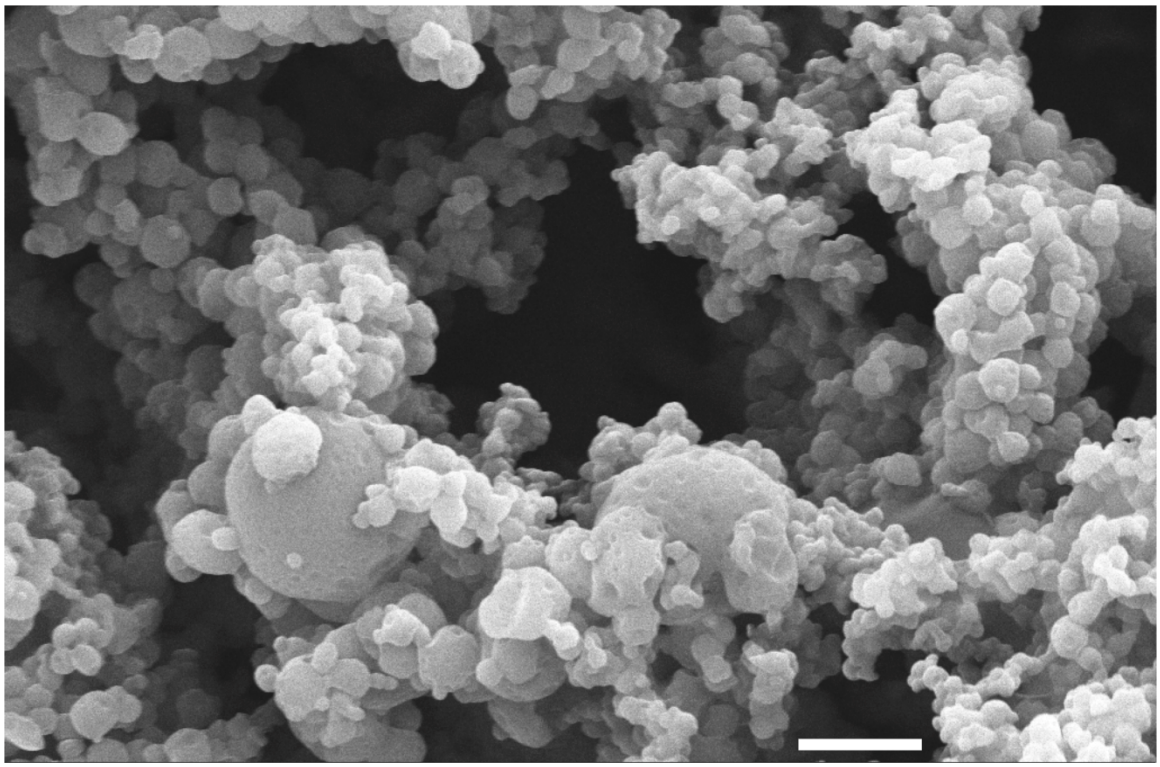

Figure 5.10: Gemcitabine-$N^4$ Oleoyl Amide loaded PLGA microparticles. Scale bar is 2 μm.

## 5.5 REFERENCES


1. Y. J. Chua and D. Cunningham, "Chemotherapy for advanced pancreatic cancer," Best Pract Res Clin Gastroenterol 20(2), 327-348 (2006)
2. M. L. Immordino, P. Brusa, F. Rocco, S. Arpicco, M. Ceruti and L. Cattel, "Preparation, characterization, cytotoxicity and pharmacokinetics of liposomes containing lipophilic gemcitabine prodrugs," J Control Release 100(3), 331-346 (2004)
3. F. Myhren, B. Brretzen, A. Dalen and M. L. Sandvold, "Gemcitabine derivatives ", (2002)
4. A. L. Doiron, K. Chu, A. Ali and L. Brannon-Peppas, "Preparation and initial characterization of biodegradable particles containing gadolinium-DTPA contrast agent for enhanced MRI," Proc. Natl. Acad. Sci. U. S. A. 105(45), 17232-17237 (2008)
5. A. L. Doiron, K. A. Homan, S. Emelianov and L. Brannon-Peppas, "Poly(Lactic-co-Glycolic) Acid as a Carrier for Imaging Contrast Agents," Pharm. Res. 26(3), 674-682 (2009)
6. T. Betancourt, B. Brown and L. Brannon-Peppas, "Doxorubicin-loaded PLGA nanoparticles by nanoprecipitation: Preparation, characterization and in vitro evaluation," Nanomedicine 2(2), 219-232 (2007)
7. S. L. Dax, J. J. McNally and M. A. Youngman, "Multi-component methodologies in solid-phase organic synthesis," Curr. Med. Chem. 6(3), 255-270 (1999)
8. F. Dorwald, Organic synthesis on solid phase: Supports, linkers, reactions, Wiley-VCH Verlag GmbH (2002).
9. M. Steger, C. Hubschwerlen and G. Schmid, "Solid-and solution-Phase synthesis of highly-Substituted-Pyrrolidine libraries," Bioorg. Med. Chem. Lett. 11(18), 2537-2540 (2001)
10. L. Thompson and J. Ellman, "Straightforward and general method for coupling alcohols to solid supports," Tetrahedron Lett. 35(50), 9333-9336 (1994)
11. A. Frutos, J. Brockman and R. Corn, "Reversible protection and reactive patterning of amine-and hydroxyl-terminated self-assembled monolayers on gold surfaces for the fabrication of biopolymer arrays," Langmuir 16(5), 2192-2197 (2000)
12. M. Kataoka and Y. Hayakawa, "A convenient method for the synthesis of N-free 5-O-(p, p-Dimethoxytrityl)-2-deoxyribonucleosides via the 5-O-Selective tritylation of the parent substances," J. Org. Chem 64(16), 6087-6089 (1999)

# Chapter 6: Design of the Combined Imaging and Therapy Nanoplate System (CIT-NpS)

Since the CIT-NS proved challenging to synthesize using gemcitabine, a design is presented here for a different multifunctional nanosystem with gemcitabine. The new nanosystem is called the Combined Imaging and Therapy Nanoplate System (CIT-NpS) and will be referred to as the CIT-NpS or the nanoplate system in this text.

## 6.1 CIT-NpS Components

The design of the CIT-NpS is illustrated in Fig. 6.1. The CIT-NpS is a triangular silver nanoplate with three components attached to its exterior (1) gemcitabine, (2) antibodies that target upregulated cancer cell surface receptors, and (3) poly(ethylene glycol) (PEG) chains. The antibody and the PEG chains serve the same purposes in the CIT-NpS as they did in the CIT-NS of targeting and limiting immune system recognition, respectively, as outlined in Chapter 2. Gemcitabine continues to serve as chemotherapy, but in the new design it is attached to the nanoplate surface instead of being entrapped inside of a polymer core.

## 6.2 Comparison of the CIT-NpS and the CIT-NS

The CIT-NpS provides both advantages and disadvantages when compared to the CIT-NS in terms of optical properties, size and synthesis, drug loading, and stability. All of these various properties and characteristics are compared in this section.

### 6.2.1 Optical Properties, Size, and Imaging Contrast

The shape of the nanoplate system (CIT-NpS) and the nanocage system (CIT-NS) are vastly different. In general, shape and size differences of the noble metal component in the nanosystem will dictate both its optical properties and the cellular response.

The optical properties of plasmonic noble metals like silver and gold are highly dependent on size and shape. For instance, the longitudinal surface plasmon resonance (LSPR) peak of gold nanorods depends on the aspect ratio of the longitudinal (length of the rod) versus the transverse (diameter of the rod) dimensions. For example, gold nanorods with an aspect ratio, R (defined as the length/diameter of the rod), of 3.1 will have a LSPR peak at a wavelength of 740 nm, while an R of 3.9 yields a LSPR peak at 800 nm.[1] The phenomena of red-shifting, or right-shifting, of the LSPR to longer wavelengths as R increases is also true for other anisotropic shapes of noble metals, such as silver. In the case of silver nanoplates, the aspect ratio, calculated by the side length (longitudinal dimension) of the plate divided by the plate width (transverse dimension) will determine the LSPR of the nanosystem.[2] These noble metal anisotropic shapes of particular aspect ratios yield sharp, well-defined extinction spectra peaks with wavelength when measured using a spectrophotometer.

Nanocages of silver, in contrast to nanoplates or nanorods, have much broader extinction spectra since a mixture of aspect ratios inherently exists in the sample. For a nanoshell or nanocage the R is defined as the core diameter divided by the metal thickness. The broadened extinction spectra result from inherent lack of size control during synthesis. When the nanocage system is built, silver is reduced onto cores of PLGA. The PLGA is not completely monodispersed, so a variation in core diameters is already present in the sample. Furthermore, the silver thickness around those PLGA cores is not uniform within each individual nanoparticle and particle to particle variation also exists, thus adding to the diversity of aspect ratios in the sample. The polydispersity of R's in the sample ultimately led to very broad extinction spectra for the CIT-NS as demonstrated in Chapter 4.

The difference in optical properties between the CIT-NpS that has a sharp LSPR peak, and the CIT-NS that has a broad LSPR, will cause these systems to behave slightly differently as imaging contrast agents for photoacoustic imaging. An important property of a nanosystem for photoacoustic imaging contrast is the absorption cross-section. Nanosystems with high absorption cross-sections, and thus high $\mu_a$, as defined in Eq. 1.1, will create high amplitude photoacoustic transients. Per nanoparticle, the nanoplate system will have higher individual absorption cross-sections at the LSPR peak wavelength; and therefore, per particle, the nanoplate system is a superior contrast agent. However, the geometric size also plays a role in the probability of light absorption in an *in vivo* situation (see Chapter 3). Even though the absorption cross-section of the nanocage system is lower per particle, the probability of light absorption events is increased due to their greater geometric size. Thus, the photoacoustic contrast created by these drastically different systems can be similar.[3] Therefore, enhancement of photoacoustic imaging from nanoparticles depends on both geometric size and absorption cross-section.

While geometric size and absorption cross-section are the important factors in the physics of photoacoustic signal generation, the concentration of the nanosystem that accumulates in the diseased area ultimately determines its applicability *in vivo*. Photoacoustic signal is linearly proportional to nanoparticle concentration[3], so high accumulation of the nanosystem at the diseased site is critical for detection and high signal to noise imaging.

The biology of the diseased site or tumor determines the uptake of nanoparticles into both the extracellular and intracellular spaces. Since both the nanoplate and the nanocage systems are designed for systemic delivery, the structure of the tumor vasculature must allow for extravasation of the nanoparticles into the tumor area.

Extravasation is dependent on the size of the gap junctions between endothelial cells in the lining of the tumor vasculature (generally between 300 nm and 700 nm for most tumors).[4] Smaller particles have a greater chance of navigating through these junctions, and therefore the nanoplate system with an overall size less that 200 nm has a greater change of accumulating in high concentrations. Furthermore, nanoparticle interactions with cells are size and shape dependent;[5, 6] generally smaller particles get internalized to a greater extent. Therefore, the nanoplate system is advantageous to the nanocage system because (1) per particle it has a higher absorption cross section and (2) its smaller size allows it to accumulate in a tumor and interact with cancer cells to a greater extent.

### 6.2.2 Synthesis Techniques

The CIT-NS is a complex structure requiring several individual steps for synthesis (see Chapters 4 and 5). Synthesis of the CIT-NpS is simpler since silver nanoplate synthesis techniques are readily available[2, 7-10], and since conjugation of moieties to the surface of silver can be easily accomplished using thiol-mediated chemistries.[11, 12] In order to encapsulate gemcitabine in a polymer matrix for the CIT-NS, a prodrug form of gemcitabine is required (see Chapter 5). Similarly, a prodrug form of gemcitabine containing a thiol is required for the CIT-NpS to enable covalent bonding of gemcitabine to the surface of silver. In both cases, the prodrug form needs to be tested to ensure it is as active as the native drug. Overall, the nanoplate system is more facile because it has fewer components and fewer steps in its synthesis.

### 6.2.3 Drug Loading

The methods of drug loading/release and the drug loading capacities of the CIT-NS versus the CIT-NpS systems are disparate. The method of drug loading in the CIT-NS is via entrapment in a polymer matrix core, whereas drug loading in the CIT-NpS is via

covalent bonds to the surface of silver. Each of these methods presents advantages and disadvantages. The distinct advantage of the CIT-NS is that large payloads of drug can be encapsulated in the polymer core. The disadvantage is that drug release from the nanocage system will happen by diffusion. Therefore, once the nanocage system is suspended in any aqueous fluid, it will release drugs slowly. The drug release profile can be controlled by varying the silver cage confluency (Chapter 4), but ultimately the polymer will experience bulk erosion and elution of the drug. The advantage of the CIT-NpS is that drugs are attached to the nanoplates via covalent bonds. As long as silver remains stable in solution (i.e. it doesn't erode into AgO or $A^+$ ions), then the drugs will remain conjugated to the surface and will not diffuse out during systemic delivery or while in storage in a buffered solution. In summary, the nanocage system offers high drug loading capacity, but poor control over release; whereas, the nanoplate system has low drug loading capacity, but great control over release.

### 6.2.4 Stability

As with most noble metals, silver is most stable as a spherical nanoparticle; it is the lowest energy configuration. Making anisotropic shapes of metals, like nanoplates, requires specific capping agents and reaction conditions since those shapes have higher surface energies.[13] Therefore, from a surface energy perspective, the silver nanoplate system is much less stable than the silver nanocage system; because the nanoplate is a highly anisotropic shape and the nanocage is built from nanospheres of silver packed closely around a polymer core. Silver nanoplates that are not passivated on the surface will dissolve in salt solutions and react readily with proteins and enzymes. Thus, one of the challenges for both systems, but even more so for the nanoplate system, is to passivate the surface of silver to make it more biocompatible and less reactive. The best

way to accomplish this goal is to conjugate polymers such as PEG to the surface. Additionally, allowing the surface to oxidize will also reduce reactivity. In the CIT-NS these conjugations are not challenging since the surface will only contain a few antibodies and mostly PEG. However, since drug molecules, that will not inherently stabilize the silver surface, are occupying the same sites that stabilizing molecules would normally bind, the CIT-NpS is more difficult to stabilize. Therefore, to stabilize the nanoplate system, the design must incorporate an optimized balance between the ratio of drugs and antibodies attached to the surface versus the coverage of passivating PEG molecules.

## 6.3 CONCLUSIONS

The CIT-NpS may be a superior combined imaging and therapy nanosystem since it has the advantages of higher absorption cross section per particle, sharper and more defined LSPR peaks, simplified synthesis, and smaller size that allows for better accumulation and intracellular trafficking at a tumor site. However, the large disadvantage of the nanoplate system is its reduced drug loading capacity compared to the CIT-NS. Furthermore, the CIT-NpS is more difficult to stabilize since it inherently has a high energy surface that is prone to dissolution and side reactions if not properly passivated. All of the advantages and challenges of the CIT-NpS are explored experimentally in the next several chapters.

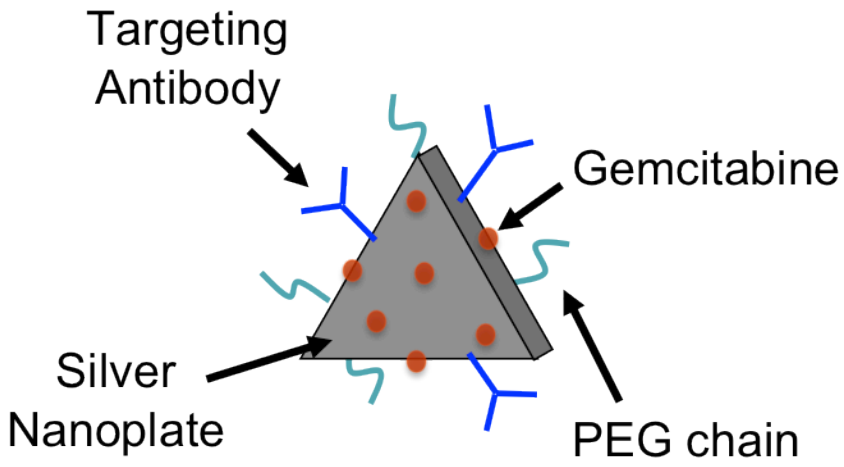


Figure 6.1: An illustration of the Combined Imaging and Therapy Nanoplate System (CIT-NpS) and its components.

## 6.4 REFERENCES


1. P. K. Jain, K. S. Lee, I. H. El-Sayed and M. A. El-Sayed, "Calculated absorption and scattering properties of gold nanoparticles of different size, shape, and composition: applications in biological imaging and biomedicine," J Phys Chem B 110(14), 7238-7248 (2006)
2. X. Zou, E. Ying, H. Chen and S. Dong, "An approach for synthesizing nanometer-to micrometer-sized silver nanoplates," Colloids Surf. Physicochem. Eng. Aspects 303(3), 226-234 (2007)
3. K. Homan, J. Shah, S. Gomez, H. Gensler, A. Karpiouk, L. Brannon-Peppas and S. Emelianov, "Silver nanosystems for photoacoustic imaging and image-guided therapy," Journal of Biomedical Optics 15(2), 021316 (2010)
4. I. Brigger, C. Dubernet and P. Couvreur, "Nanoparticles in cancer therapy and diagnosis," Adv Drug Deliv Rev 54(5), 631-651 (2002)
5. P. Decuzzi, R. Pasqualini, W. Arap and M. Ferrari, "Intravascular delivery of particulate systems: does geometry really matter?," Pharm. Res. 26(1), 235-243 (2009)
6. W. Jiang, B. Y. Kim, J. T. Rutka and W. C. Chan, "Nanoparticle-mediated cellular response is size-dependent," Nat Nanotechnol 3(3), 145-150 (2008)
7. X. C. Jiang, C. Y. Chen, W. M. Chen and A. B. Yu, "Role of Citric Acid in the Formation of Silver Nanoplates through a Synergistic Reduction Approach," Langmuir (2009)
8. D. Aherne, D. Ledwith, M. Gara and J. Kelly, "Optical properties and growth aspects of silver nanoprisms produced by a highly reproducible and rapid synthesis at room temperature," Adv. Funct. Mater. 18(14), 2005-2016 (2008)
9. C. Metraux and C. Mirkin, "Rapid thermal synthesis of silver nanoprisms with chemically tailorable thickness," Adv. Mater. 17(4), 412-415 (2005)
10. C. Xue, G. S. Metraux, J. E. Millstone and C. A. Mirkin, "Mechanistic study of photomediated triangular silver nanoprism growth," J. Am. Chem. Soc. 130(26), 8337-8344 (2008)
11. S. Kumar, J. Aaron and K. Sokolov, "Directional conjugation of antibodies to nanoparticles for synthesis of multiplexed optical contrast agents with both delivery and targeting moieties," Nat Protoc 3(2), 314-320 (2008)
12. C. S. Levin, S. W. Bishnoi, N. K. Grady and N. J. Halas, "Determining the conformation of thiolated poly(ethylene glycol) on Au nanoshells by surface-enhanced Raman scattering spectroscopic assay," Anal. Chem. 78(10), 3277-3281 (2006)

13. C. J. Murphy, T. K. Sau, A. M. Gole, C. J. Orendorff, J. Gao, L. Gou, S. E. Hunyadi and T. Li, "Anisotropic metal nanoparticles: Synthesis, assembly, and optical applications," J Phys Chem B 109(29), 13857-13870 (2005)

# Chapter 7: *In Vivo* Testing of the CIT-NpS Design for Enhanced Photoacoustic Imaging

Since the CIT-NS proved challenging to synthesize using gemcitabine, a new design was presented in Chapter 6 called the Combined Imaging and Therapy Nanoplate System (CIT-NpS). The CIT-NpS consists of silver nanoplate carriers with gemcitabine, poly(ethylene glycol) (PEG), and targeting antibodies grafted to its surface (Fig 6.1). Analogous to how the CIT-NS was explored, the intention of this chapter is to first prove the feasibility of using silver nanoplates as imaging contrast agents for photoacoustic imaging. Therefore, this chapter details all aspects of the CIT-NpS design and synthesis except the attachment of drugs to the nanoplates' surface, while Chapter 8 covers drug conjugation to the plates.

## 7.1 Introduction

Noble metal nanoparticles have garnered particular interest from researchers in recent years because of their unique and tunable surface plasmon resonance properties.[1] As discussed in Chapters 1 and 6, confinement of the surface electrons in these metals when synthesized on the nanoscale leads to interesting light absorption and scattering properties within the visible to near infrared (NIR) wavelength ranges. Both the size and shape of metallic nanoparticles contribute strongly to this plasmon resonance effect.[2-4] In many cases, as the aspect ratio in the dimensions of a nanoparticle is increased, the longitudinal surface plasmon resonance peak (LSPR) shifts to higher wavelengths across the visible to NIR wavelength spectrum.[3, 5, 6]

Silver nanoplates represent one such nanoparticle where large aspect ratios are readily achievable and therefore the LSPR is easily tuned from the visible to the NIR. Particles like silver nanoplates whose resonance can be tuned into the NIR are of

particular interest for biomedical sensing applications, since absorption of light from tissue is minimized at NIR wavelengths.[7] Another advantage of using silver over other common noble metals such as gold is that silver has at least 10% sharper and stronger resonances.[8] The large disadvantage to using silver nanoparticles is their lack of stability in nanoform. Silver is inherently more reactive than gold and this activity leads to shape deformation of anisotropic nano-colloidal silver solutions (see Chapter 8 for details concerning silver nanoplate stability).

Applications using metallic nanoparticles as contrast agents depend on the stability of the nanoparticles' LSPR to provide meaningful, interpretable signals. Some of these applications include two-photon microscopy, surface enhanced Raman scattering (SERS), and a myriad of other optical based techniques. Another emerging technique with the same restriction is photoacoustic (PA) imaging.[9, 10] As discussed in Chapter 1, PA imaging is based on the principle of sound generation following light absorption. In short, PA imaging can detect nanoparticles in tissue by shining pulsed light on the nanoparticle-laden tissue, and measuring the resulting sound transients using an ultrasound (US) transducer.[11] The US transducer can also then be used to capture a co-registered US image of the interrogated area. When the US and PA images are combined, the location of nanoparticles can be displayed relative to the anatomical information provided by US. This PA technique is powerful because it only requires that light travel in one direction, and therefore the penetration depths at which PA imaging can detect nanoparticles is at least three times that of purely optical imaging methods. Since the absorption cross sections of metallic nanoparticles can be orders of magnitude higher than the surrounding native tissue, these nanoparticles are excellent photoacoustic imaging contrast agents.[12-15]

Since silver has exceptional optical properties suitable for many biomedical applications from sensors to contrast agents, it was chosen as the basic carrier in the CIT-NpS. While silver is known to have these exceptional optical properties, no one has attempted to use silver, in any form, as a PA contrast agent. The silver-silica nanosystem presented in Chapter 3 was the first use of silver for PA imaging enhancement.[16] In this chapter, silver nanoplates are presented as a different, and potentially better, nanosystem for enhancing PA imaging. The synthesis of silver nanoplates and methods of bioconjugation are presented along with studies testing the molecular sensitivity of these agents *in vitro* against pancreatic cancer cells. Furthermore, the cytotoxicity of these silver nanoplates is explored. Finally, the efficacy of silver nanoplates as contrast agents for USPA imaging in an *in vivo* mouse xenograft cancer model is evaluated. Therefore, the entire CIT-NpS is synthesized and characterized without drugs in this chapter. These initial tests prove that silver nanoplates are excellent PA contrast agents; the building of the entire CIT-NpS with attached drugs is described in Chapter 8.

## 7.2 METHODS

Each step in the synthesis and characterization of silver nanoplates is described separately below. For reader clarity, the sources for all materials are consolidated here.

Materials: All chemicals were used without further purification and were at minimum ACS grade. Silver nitrate (>99%), trisodium citrate (TSC), sodium periodate, the antibody to Epidermal Growth Factor Receptor (EGFR) clone C225, poly(ethylene glycol) bisphenol A epichlorohydrin $M_n$ = 14 kDa, and Bis (p-sulfonatophenyl) phenylphosphine dihydrate dipotassium salt (BSPP) were purchased from Sigma-Aldrich (St. Louis, MO, USA). ACS grade L(+) ascorbic acid was a product of Acros (Morris Plains, NJ, USA). Dulbecco's phosphate buffered saline (DPBS) came from Mediatech,

Inc. (Herndon, VA, USA). The methyl-poly(ethylene glycol)-thiol (mPEG-SH of 5 kDa) was from Laysan Bio (Arab, AL, USA). All cell culture products, including the MTS assay, were purchased from Invitrogen (Carlsbad, CA, USA) unless otherwise specified. Slide mounting media, Vectashield with DAPI stain, was from Vector Laboratories (Burlingame, CA, USA). The linker hydrazide-polyethylene glycol-dithiol (SPT-014B) was a product of Sensopath (Bozeman, MT, USA).

### 7.2.1 Finite Difference Time Domain (FDTD) Modeling

An effective PA contrast agent will have a high absorption cross-section. Recall that PA imaging contrast is generated by differences in the optical absorption map of the interrogated tissue. Further, Eqn 1 in Chapter 1 shows that photoacoustic pressure is directly proportional to the absorption coefficient of the tissue. To generate PA imaging contrast that is greater than the native tissue, an exogenous contrast agent must have a large absorption coefficient. Since the absorption coefficient is equal to the number of absorbers times the absorption cross-section of a single absorber, then it follows that absorption cross-section is a critical parameter for a PA contrast agent. Before synthesizing a new photoacoustic contrast agent such as a silver nanoplate, it is prudent to first model the absorption cross-section of a silver nanoplate and compare it to the absorption cross-sections of other existing photoacoustic contrast agents, such as gold nanospheres and nanocages.

Modeling of the extinction, scattering, and absorption cross-sections of triangular silver nanoplates with uniform thickness of 12 nm and triangle edge lengths of 25 nm, 60 nm, 90 nm, 128 nm, and 218 nm was accomplished using the commercially available program Lumerical Solutions. Lumerical FDTD uses finite difference time domain (FDTD) modeling to solve Maxwell's equations for each point in a simulation space with

a user defined, non-uniform mesh. In the simulation space, a silver triangular nanoplate was situated in water (index of refraction for water was taken as 1.33 with no imaginary component simulated). Silver dielectric data were based on Johnson and Christy and fitted by a multi-Lorentzian sum. A wave packet of light with a Gaussian distribution of the field amplitude of light frequencies in a wavelength range of 300 nm to 1400 nm was simulated. The light source was chosen to be a total-field/scattered-field source (TFSF), defined as a volume where the light is injected on one face, and the total field is determined at every mesh point inside the TFSF volume, while outside the TFSF volume only the scattered filed is calculated. Such a light source reduces calculation noise and prevents artifacts of diffraction due to a finite source (aperture effect). Monitors were set up inside and outside of the TFSF volume to measure optical cross-sections. To obtain final total optical cross-sections, the results from all directions were added, and then three separate simulations using light polarized along three directions (two longitudinal directions and one transverse direction) were averaged.

### 7.2.2 Silver Nanoplate Synthesis

Silver nanoplates were formed via a seed-mediated growth process. Silver seeds were synthesized via procedures previously described by Xue et al.[17] Specifically, a 250 ml flask was placed in an ice bath and filled with 95 ml of deionized and ultrafiltrated (up to 18.2 MΩ-cm) (DIUF) water. In an Ar environment, 1 ml of 30 mM TSC and 0.5 ml of 20 mM $AgNO_3$ were added. The mixture was stirred at 500 rpm for 20 min. To reduce the silver, 1 ml of ice cold 50 mM $NaBH_4$ was added quickly and the solution immediately turned bright yellow. One more ml of the 50 mM $NaBH_4$ was then added over the following 15 min at a rate of 0.067 ml/min. In a separate ice cold vial, a solution of 1 ml of 50 mM $NaBH_4$ was added to 1 ml of 5 mM Bis(p-

sulfanatophenyl)phenylphosphine dehydrate dipotassium salt (BSPP). That 2 ml mixture of $NaBH_4$ and BSPP was slowly dropped into the vigorously stirring silver seed solution over a period of 5 min (Ar environment was maintained throughout the procedure and the flask was wrapped in foil to minimize light exposure). The Ag seeds were then stirred at 350 rpm and kept at 0°C for 5 hr. Finally, the seeds were transferred to a 4°C refrigerator in their original flask and allowed to age undisturbed in a sealed Ar environment overnight.

The seeds were used to grow nanoplates within 14 days after synthesis, with the peak efficacy (largest translation to plates) obtained on the very next day after seed synthesis. Growing nanoplates of sizes up to 250 nm involved 4 separate growth steps in which the product of one step was used as the starting material for the subsequent step, as modified from that described by Zou et al.[18] Table 7.1 provides a consolidated chart describing materials needed and observations for the separate growth steps described below.

Sample S1: First, a 20 ml vial was filled with 8.0 ml of DIUF water, 50 μl of 40 :mM trisodium citrate (TSC), and 150 μl of 40 mM L+ascorbic acid. The seeds prepared previously were diluted in water to an optical density (OD) of 0.65 at their peak resonance of 400 nm. Then 1.8 ml of the diluted silver seeds were added to the vial. The mixture was vigorously stirred at room temperature while 5.05 ml of 584 μM $AgNO_3$ was dripped in over 10 min. During the 10 min, the solution turned from bright yellow to orange, red, and maroon. After the $AgNO_3$ addition was complete, the solution was allowed to stir for an additional 10 min and the ultraviolet to visible (UV-vis) spectrum was taken using a DU Series 640 Spectrophotometer (Beckman Coulter). This first solution was called S1.

Sample S2: Second, for the next Ag nanoplate growth step, another 20 ml vial was filled with 4.8 ml of DIUF water, 50 μl of 40 mM TSC, 150 μl of 40 mM L+ascorbic acid, and 5 ml of S1. Again, the mixture was vigorously stirred at room temperature while 5.05 ml of 584 μM $AgNO_3$ was dripped in over 10 min. During the 10 min, the solution turned from maroon to purple to blue to teal. After the $AgNO_3$ addition was complete, the solution was allowed to stir for an additional 10 min and the ultraviolet to visible (UV-vis) spectrum was taken. This second solution was called S2.

Sample S3: Third, for the next Ag nanoplate growth step, another 20 ml vial was filled with 4.8 ml of DIUF water, 50 μl of 40 mM TSC, 150 μl of 40 mM L+ascorbic acid, and 5 ml of S2. Again, the mixture was vigorously stirred at room temperature while 5.05 ml of 584 μM $AgNO_3$ was dripped in over 10 min. During the 10 min, the solution turned from teal to forest green to light forest green with a purple hue. After the $AgNO_3$ addition was complete, the solution was allowed to stir for an additional 10 min and the ultraviolet to visible (UV-vis) spectrum was taken. This third solution was called S3.

Sample S4: For the fourth and final growth step, another 20 ml vial was filled with 4.8 ml of DIUF water, 50 μl of 40 mM TSC, 150 μl of 40 mM L+ascorbic acid, and 5 ml of S3. Again, the mixture was vigorously stirred at room temperature while 5.05 ml of 584 μM $AgNO_3$ was dripped in over 10 min. During the 10 min, the solution turned from forest green/purple to pastel blue/silver. After the $AgNO_3$ addition was complete, the solution was allowed to stir for an additional 10 min and the ultraviolet to visible (UV-vis) spectrum was taken. This fourth and final solution was called S4. All nanoplate solutions were analyzed using a LEO S5500 scanning transmission electron microscope (STEM). A custom designed program was built using the functionality provided by ImageJ to size all of the nanoplate and seed batches.

### 7.2.3 Silver Nanoplate Bioconjugation

Functionalizing silver nanoplates with antibodies and PEG, a process called bioconjugation, is mediated using thiol chemistries and shown schematically in Fig 7.1. Free primary thiols are known to readily react to form covalent thiolate bonds with noble metals such as silver and gold.[19, 20] Since PEG and antibodies do not naturally have an abundance of free thiol groups, preparation steps are required to "thiolate" these compounds in order to bioconjugate them to silver nanoplates. The steps towards thiolation of the antibody are described in detail below. The PEG, however, was purchased as a bifunctional molecule having a methyl terminus and a thiol terminus on each molecule.

#### *7.2.3.1 Antibody-Linker Synthesis*

Preparation, or more specifically "thiolation", of the antibody was the most complicated synthetic step. For optimal antibody activity (interaction between the $F_V$ region with its receptor), the antibody must be bound to the nanoplate in a directional fashion. Therefore, a directional conjugation of the C225 anti-epidermal growth factor receptor antibody (a-EGFR) from Sigma-Aldrich (product number E2156) to nanoplates was performed. Directional procedures were adapted from those previously described for antibody conjugation to gold nanoparticles by Kumar et al.[20] A linker molecule was employed to achieve directionality, meaning that only the Fc region, or nonbinding part of the antibody, attached to the silver. The particular linker used, a hydrazide-polyethylene glycol-dithiol (bottom of Fig 7.1), covalently bound to the glycosylated portion of the antibody (found in the Fc region) through its hydrazide group, while the dithiol groups bound to silver.

For directional conjugation of a-EGFR to Ag nanoplates, the linker molecule was first attached to the antibody. As previously described[20], the antibody was prepped by

changing the buffer to a mono/dibasic sodium phosphate buffer (pH = 7.5) using two wash steps in a 50 kDa molecular weight cut off (MWCO) centrifugal filter from Millipore (centrifuge at 3600 rpm for 15 min at 4°C). The antibody was reconstituted in 1.3 ml of the sodium phosphate buffer and placed in a sterile 2 ml tube. To create an aldehyde group on the glycosylated portion of the antibody, 80 µl of fresh 100 mM $NaIO_4$ was added to the antibody solution and allowed to shake in the dark for 30 min at room temperature. The reaction was quenched by adding 500 µl of 1x phosphate buffered saline. Then, 6 µl of 427.4 mM linker in anhydrous ethanol (kept at -80°C prior to use) was added to the antibody solution and allowed to react for 1 hr while shaking at room temperature. Finally the antibody-linker (AB-linker) conjugate was cleaned using HEPES buffer in the same 50 kDa MWCO Millipore filters described above and then reconstituted in 300 µl HEPES buffer (pH = 8.0) for storage. The AB-linker conjugate can be stored at 4°C and will remain viable for the life of the antibody. A 75% to 85% yield of the AB-linker conjugate can be expected using this technique if strict and clean pipeting techniques are employed throughout the process.

#### *7.2.3.2 Antibody and PEG Conjugation to Nanoplates*

Once the AB-linker conjugate was built, further conjugation to the Ag nanoplates was facile. Briefly, any desired batch (S1 through S4) of nanoplates was placed in a 50 kDa MWCO Millipore centrifugal filter directly after synthesis and spun at 1500 rcf for 5 min at 20°C. The nanoplates were then resuspended in 1 ml of DIUF water, placed in a 2 ml tube, wrapped in foil, and allowed to sit overnight at room temperature. Then, enough of the AB-linker solution was added to account for 0.05 mg of antibody-linker (the exact volume of the AB-linker solution varied based on the final concentration of the AB-linker in HEPES as determined by a Thermo Scientific Nanodrop measurement at a wavelength

of 280 nm with an assumed extinction coefficient of 210,000 $M^{-1}cm^{-1}$). The AB-linker and nanoplates were allowed to shake at room temperature in the dark for 20 min. Slight red shifts (5-10 nm) in peak resonance of the nanoplates was observed after conjugation of the AB-linker to the nanoplates.

To limit opsonization in the bloodstream, the surface area of the silver not covered by antibody was passivated by attachment of mPEG-SH. Specifically, after allowing the AB-linker and Ag nanoplate solution to shake for 20 min, 50 μl of a 2 wt% PEG ($M_n$ = 14 kDa) was added to enhance stability, and 40 μl of 50 mM mPEG-SH (5 kDa) was also added to react with the Ag nanoplates. After shaking in the dark for 20 min, the nanoplates were cleaned using 50 kDa MWCO Millipore centrifugal filters spun at 1500 rcf for 5 min at 4°C. The nanoplates were then resuspended in 500 μl of PBS and sent through a 0.22 μm filter into a sterile 2 ml tube for future use. The antibody conjugated Ag nanoplates can be stored at 4°C for the life of the antibody. A 40 to 60 nm red shift in the peak resonance of the nanoplates was observed directly after the mPEG-SH passivating step.

### 7.2.4 *In Vitro* Characterization with Pancreatic Cancer Cells

Several different human pancreatic cancer cell lines were exposed to the bioconjugated silver nanoplates. *In vitro* tests from cell labeling to cytotoxicity were performed.

#### *7.2.4.1 Cell Labeling*

The human pancreatic cancer cell line MPanc96 was mixed in media with two types of Ag nanoplates: nanoplates conjugated to a-EGFR and mPEG-SH, and nanoplates conjugated only to mPEG-SH. Briefly, approximately 300,000 MPanc96 cells were suspended in 500 μl of media in two separate sterile 2 ml tubes. To each respective tube,

50 μl of the as prepared a-EGFR and mPEG-SH conjugated nanoplates, and the mPEG-SH conjugated nanoplates were added. The tubes were shaken every 30 min over a 4 hr period while in the incubator. After 4 hours, the tubes were centrifuged at 125 rcf for 5 min at 4°C. After the supernatant was removed, the cells were resuspended in 2 wt% formalin in DPBS, allowed to sit for 20 min, and then washed 2x with the 2 wt% formalin in DPBS solution. The cells were fixed on a microscope slide using Vectashield with Dapi mounting solution and imaged in fluorescence and darkfield modes of a Leica DMI3000 B inverted microscope with a Leica DFC 290 kit and a 3 mega pixel color camera.

#### *7.2.4.2 Cytotoxicity*

The human pancreatic cancer cell lines L3.6pl and MPanc96, and the non-cancerous pancreatic line HPNE were incubated with bioconjugated silver nanoplates and tested for cell viability. Both cancer cell lines were cultured *in vitro* using Dulbecco's Modified Eagle Medium (DMEM) (with 4500 mg glucose/L, L-glutamine, $NaHCO_3$ and pyridoxine HCl) supplemented with 10% fetal bovine serum (FBS) and 1% Penicillin-Streptomycin (Pen/Strep) while maintained at 37°C and 5% $CO_2$ in a humidified incubator. For the pancreatic cancer cell lines, the DMEM and the FBS were purchased from Sigma, while the Pen/Strep was purchased from Invitrogen. The non-cancerous pancreatic cell line, HPNE, was cultured *in vitro* using Medium D that contained one volume of medium M3, three volumes of glucose-free DMEM (with L-glutamine, phenol red, and pyridoxine HCl), 5% FBS, 5.5 mM glucose, 10 ng/ml EGF, and 50 μg/ml gentamycin. Medium M3 is a proprietary formulation optimized for the growth of neuroendocrine cells (InCell Corp., San Antonio, TX, USA). For cell viability studies, cells were seeded in a 96 well plate (each well had 5,000 cells per 100 μl of media for the

cancer lines and 10,000 cells per 100 μl of media for the non-cancerous line). The cells were allowed to attach and grow in the 96 well plate for 48 hr, after which the cell media was removed and replaced with suspensions of a-EGFR and mPEG-SH conjugated S4 batches of Ag nanoplates at various concentrations representing 1 mg/ml, 0.5 mg/ml, 0.25 mg/ml, 0.125 mg/ml, 0.0625 mg/ml and 0 mg/ml of silver (at least 5 wells were seeded with each concentration). Note that the highest silver concentration at 1 mg/ml represented ~$1.2\times10^{12}$ nanoplates per ml, while the lowest silver concentration at 0.0625 mg/ml represented ~$7.3\times10^{10}$ nanoplates per ml. After 24 hr of incubation, the media was removed and replaced with fresh media containing no nanoplates. The absorbance of each well in the plate was measured at 490 nm using a Synergy HT Multimode Microplate Reader from BioTek. To perform the assay, 20 μl of a tetrazolium compound [3-(4,5-dimethylthiazol-2-yl)-5-(3-carboxymethoxyphenyl)-2-(4-sulfophenyl)-2H-tetrazolium (MTS) and an electron coupling reagent (phenazine methosulfate) PMS from the CellTiter 96® $AQ_{ueous}$ Non-Radioactive Cell Proliferation Assay (a Promega product) was added to each well. Over a period of 1 hr in the incubator, the MTS was bioreduced by cells into a formazan product that had an absorbance peak at 490 nm. Dehydrogenase enzymes found in metabolically active cells were responsible for the conversion of MTS into the soluble formazan product. Therefore, the absorbance of each well at 490 nm was directly proportional to the number of viable cells. The absorbance of each well at 490 nm taken before adding MTS was subtracted from the post MTS incubation value. Cell viability was determined by comparing the resulting absorbance of wells containing no nanoplates to wells containing nanoplates using an F test for a one-way ANOVA.

### 7.2.5 Animal Model

Xenograft tumors were grown subcutaneously in Nu/Nu mice to test the *in vivo* targeting and imaging capabilities of the a-EGFR conjugated nanoplates (the nanoplates were also passivated with mPEG-SH as described above). Specifically, after administering anesthesia (avertin) to the mouse, the mouse was injected on the back subcutaneously with 50,000 L3.6pl cells suspended in 100 μl of DPBS. After about two weeks of growth, the tumor was mature and the combined ultrasound and photoacoustic imaging experiment was conducted with the mouse situated on a heated eletrocardiogram pad where temperature and heart rate could be monitored while the animal was under anesthesia (isoflurane). After collecting ultrasound and photoacoustic data on the tumor area in what is termed "before" frames, the mouse was injected with ~$10^{12}$ a-EGFR conjugated, mPEG-SH passivated S3 Ag nanoplates in 200 μl of PBS. Ultrasound and photoacoustic data was then collected every hour for the first 6 hr after injection and then again at 24 hr after injection. All procedures were conducted in accordance with the protocols approved by the Institutional Animal Care and Use Committee at the University of Texas at Austin.

### 7.2.6 Biodistribution and Histology

At 112 hr after the mouse was systemically injected with nanoplates, it was sacrificed for histological analysis of the tumor as well as biodistribution of silver throughout the organs. Upon sacrifice, the organs were excavated, weighed, and then dissolved in 5 ml of 70% nitric acid while stirring for 24 hr. The digested organs were diluted by a factor of 10 in water and sent through a 200 nm filter. For analysis, all samples were introduced with a standard glass nebulizer into a GBC Optimass 8000 (GBC Scientific, Hampshire, IL, USA) inductively coupled plasma - time of flight mass spectrometer (ICP-TOFMS). Exact parameters for the ICP-TOFMS measurements can be

found in Table 1 of an article from Rowland et al.[21] Each sample was monitored for Ag content against freshly made standards using silver nitrate.

Histological slices of the tumor were taken after embedding the tumor section in paraffin. Individual tumor slices were mounted on slides and stained with hematoxylin and/or nuclear fast red. Then silver staining was performed to highlight the presence of silver nanoparticles in the tumor. Images of the slides were obtained using a Leica DMI3000 B inverted microscope with a Leica DFC 290 kit and 3 mega pixel color camera using a 1.25X objective.

### 7.2.7 Combined Ultrasound and Photoacoustic (USPA) Imaging Set-up

To perform *in vivo* imaging experiments, a custom designed combined ultrasound and photoacoustic (USPA) imaging system was used as previously described.[7] Briefly, the setup for the combined USPA imaging system was shown in Fig 3.2 in Chapter 3. Pulsed light in the range of wavelengths between 680 nm and 1064 nm was generated by an optical parametric oscillator (OPO) laser system operating at 10 Hz with a 4-6 ns pulse duration. This light was focused onto a 18-fiber bundle that surrounded an array transducer (7.5 MHz center frequency, 14 mm wide, 128 element linear array). To collect radiofrequency (RF) data, the transducer was interfaced with a Cortex ultrasound imaging engine (Winprobe Corp) capable of RF data acquisition for spatially co-registered ultrasound and photoacoustic RF signals. To form the images, RF data was beamformed, and then US images (dB scale) and fluence-compensated PA images (linear scale) were plotted. Three dimensional renderings were obtained by stacking 2D slices using Amira software.

## 7.3 RESULTS AND DISCUSSION

The purpose of the work presented in this chapter is to prove that silver nanoplates can be used as photoacoustic contrast agents. The following sections describe in detail: (1) modeling showing that nanoplates have the high absorption cross-sections required for photoacoustic imaging, (2) silver nanoplate synthesis and bioconjugation, (3) *in vitro* characterization of the nanoplates with pancreatic cancer cells, (4) *in vivo* results showing USPA imaging of nanoplate accumulation in a xenograft tumor mouse model, and (5) the biodistribution of silver in the mouse organs following systemic injection.

### 7.3.1 FDTD Simulations of the Absorption and Scattering from Silver Nanoplates

Figure 7.2 shows the calculated light extinction, absorption, and scattering cross-sections for three silver nanoplates of increasing size. Recall that the extinction cross-section is an additive composite of the absorption and scattering cross-sections. Since higher absorption cross-section leads to higher photoacoustic signal generation (see Chapter 1), the absorption cross-section is the key parameter for photoacoustic imaging contrast agent evaluation. As shown in Fig 7.2, as the edge length of the nanoplate increases, the contribution of the absorption cross-section to the overall extinction cross-section decreases. However, the absorption cross-section absolute value remains fairly constant for the three sizes shown. A quantitative assessment of the absorption cross-section for various silver nanoplates in comparison to gold nanospheres[22] and nanocages[12] is provided in Table 7.2. The absorption cross-section of silver nanoplates is comparable to or better than these other well-established photoacoustic contrast agents. Therefore, modeling results indicate that silver nanoplates have significant potential as photoacoustic contrast agents.

### 7.3.2 Silver Nanoplate "green" Synthesis and Bioconjugation

Researchers have designed numerous methods to synthesize Ag nanoplates.[23-26] Most are accomplished through seed mediated growth mechanisms that can include reducing agents such as hydrazine[18], increases in temperature[27], or even ingenious light mediated methods.[28, 29] Interestingly, even microbes have been shown to produce silver nanoplates upon incubation with $Ag^+$ in solution. Since the silver nanoplates developed here are intended for use in a biological context, the synthesis method was particularly "green". Only biocompatible chemicals were used, such as ascorbic acid (vitamin C) and sodium citrate (a well known preservative). After exploring several different methods of preparing Ag seeds[18, 30], the seeds proposed by Xue et al[17, 28] were found to be the most reproducible; they provided the twinned plane and fault defects necessary for Ag nanoplates synthesis. To grow the Ag nanoplates from these seeds, procedures introduced by Zou et al.[18] were slightly modified. The plates were grown in a step-wise process from 5 nm seeds to large, > 200 nm edge length plates. Figure 7.2 shows the evolution of the synthesis from seeds to large nanoplates in four steps. First, the yellow seeds were grown into 25 nm nanoplates (S1) as shown in Fig 7.2a. Subsequent growth steps increased the edge length of the plates successively (Figs 7.2b-d representing samples S2-S4, respectively). The colors of the resulting solutions changed with their optical extinction properties as depicted in Figs 7.2e and 7.2f. This synthesis method produced mostly nanoplates with edge lengths as shown in Table 7.3, but a small population (< 20%) of Ag nanospheres or other oblong shapes were also synthesized.

### 7.3.3 *In Vitro* Characterization with Pancreatic Cancer Cells

A commonly overexpressed receptor on the surface of cancer cells is the epidermal growth factor receptor (EGFR). The antibody to EGFR (a-EGFR) was used as a model to target Ag nanoplates to pancreatic cancer cells. The directional conjugation

method used for binding a-EGFR to nanoplates was previously described by Kumar et al.[20] This directional method employs linker molecules that bind the Fc portion of the antibody directly to the Ag surface, leaving the entire variable region free to interact with cells. To confirm that the antibody conjugated Ag nanoplates would target pancreatic cancer cells, while PEGylated Ag nanoplates would have limited interaction, pancreatic cancer cells were mixed with both types of particles *in vitro* for 4 hr. The resulting cells imaged using darkfield microscopy are shown in Fig 7.4. The control cells with no nanoplate incubation are seen as blue in darkfield microscopy (Fig 7.4a). The cells incubated with PEGylated Ag nanoplates appear to have no significant accumulation of silver (Fig 7.4b), but the cells incubated with a-EGFR conjugated nanoplates show significant interaction. These *in vitro* results demonstrated the ability of a-EGFR conjugated nanoplate to specifically interact with pancreatic cancer cells.

To determine whether this interaction of a-EGFR conjugated nanoplates with cancer cells induced cytotoxicity, various amounts of a-EGFR conjugated nanoplates were mixed with three different cell lines *in vitro*: MPanc96 and L3.6pl (both pancreatic cancer cell lines shown to overexpress EGFR), and HPNE (a non-cancerous pancreatic cell line). The viability of the cells was tested after incubation with the a-EGFR conjugated nanoplates for 24 hr using the MTS assay. As shown in Fig 7.5, even up to concentrations of 1 mg/ml Ag, no statistically significant cytotoxicity was found with any of the three cells lines. These results were surprising since the cytotoxicity of 5 nm to 10 nm Ag nanospheres has been characterized.[31, 32] The lack of toxicity of these large nanoplates suggests that the cytotoxicity of silver may be size dependent or coating dependent.

### 7.3.4 *In Vivo* Ultrasound and Photoacoustic (USPA) Imaging

All *in vivo* imaging was conducted on Nu/Nu transgenic mice with xenograft human pancreatic cancer subcutaneously grown on their back. Before injection of nanoplates, ultrasound (US) and photoacoustic (PA) imaging was performed across 2D transverse sections of the tumor area by translating the array transducer and fiber optic source across the length of the tumor. Combined ultrasound and photoacoustic USPA imaging of three cross-sections of the tumor region are shown in Fig 7.6. These images provide a basis for the expected endogenous contrast provided by blood and other natural absorbers in tissue (Fig 1.3). Then a-EGFR, mPEG-SH passivated Ag nanoplates were injected (~$10^{12}$ nanoplates in 200 μl of PBS) into the tail vein. Imaging was performed every hour after injection up to 6 hr post injection. At 5 hr post injection, peak accumulation of nanoplates in the tumor was observed as determined by monitoring the photoacoustic signal intensity with time post injection. Individual ultrasound, photoacoustic, and combined USPA images are shown in Fig 7.7. The tumor is clearly outlined in the ultrasound image as the hypoechoic region on top circled in blue (Fig 7.7a). Photoacoustic images captured using the wavelengths of 760 nm, 800 nm, and 900 nm are shown as Figs 7.7b-d, respectively, and the corresponding combined USPA images of these frames are shown in Figs 7.7f-h. The UV-vis extinction spectrum of the nanoplates injected is shown in Fig 7.7e. As expected, the PA signal inside the tumor is strongest at 760 nm since that wavelength matches the LSPR peak of the Ag nanoplates. The PA signal decreased with increasing wavelength corresponding with the UV-vis absorption spectrum of the nanoplates. Also, the distribution of nanoplates in the tumor is heterogeneous. This uneven distribution of nanoplates in the tumor is also depicted in the 3D USPA rendering of the tumor (Fig 7.8). Interestingly, the PA signal is highest at the base of the tumor where large blood vessels appear to be feeding the tumor. These large

blood vessels were confirmed upon tissue dissection. As the nanoplates injected intravenously rely on the bloodstream for transport to the tumor, areas of the tumor with insufficient blood circulation will tend to have minimal nanoplate accumulation. This incomplete distribution of nanoplates in the tumor represents a major challenge for all nanoparticle contrast agents and nanomedicine approaches aimed at imaging or treatment of cancer.

### 7.3.5 Biodistribution of Silver

Systemic injection of any foreign substance in the body will have pharmacological implications. Therefore, it is important to first determine the distribution of the injected agent throughout the body at various time points post injection. For this *in vivo* case study, the mouse was sacrificed at 112 hr post nanoplate injection. The biodistribution of silver throughout the various filtering organs within the body was determined using ICP-MS. The amount of silver per gram of tissue in various organs is displayed in Fig 7.9. As expected and seen in other studies with gold nanoparticles[33, 34], the liver and spleen have high accumulation rates of silver, while the tumor has modest accumulation. Interestingly, the accumulation in the fecal matter is high, indicating that silver clearance from the body via the digestive system might be possible.

Distribution of silver throughout the tumor was also investigated using histology. Histological slices of the tumor stained with silver stain and hematoxylin (Fig 7.10a) or silver stain and nuclear fast red (Fig 7.10b), also confirmed a heterogeneous nanoplate distribution within the tumor. The largest concentration of silver was present at the base of the tumor as indicated by the black arrow in Fig 7.10a. This accumulation was also seen in the PA images of the tumor in which the strongest PA signals were present at the base of the tumor (Fig 7.7).

Since silver nanoplates are carried by the bloodstream, and tumor vasculature is inherently disordered, a nonhomogeneous distribution of nanoparticles within the tumor space is always expected and represents a challenge for all nanoparticle-based medicine. Because nanoparticles cannot reach all areas of a tumor, successful therapeutic outcome may require multiple dosing and/or treatment strategies. Furthermore, in addition to accumulation in the tumor, filtering organs such as the liver and spleen are the most likely sites for silver distribution. Organ specific toxicity studies of the nanoplates in the liver and spleen are needed to determine the safety of using silver nanoplates *in vivo*.

## 7.4 CONCLUSIONS

The results presented indicate that silver nanoplates have excellent potential as a photoacoustic imaging contrast agent. They can be easily synthesized to absorb light from the visible to the near infrared spectrum. FDTD modeling confirmed that they have absorption cross-sections comparable to, and in some cases greater than, conventional gold contrast agents. Silver nanoplates bioconjugated to antibodies showed effective cell labeling and uptake in a tumor model of pancreatic cancer in vivo. Organ specific toxicity associated with silver in the liver and spleen must be addressed prior to widespread adoption as a photoacoustic imaging contrast agent, and clearance through the feces after systemic injection is possible. Overall, this work has solidly demonstrated the feasibility of using silver nanoplates as imaging contrasting agents. Chapter 8 will explore the feasibility of using nanoplates as drug carriers.

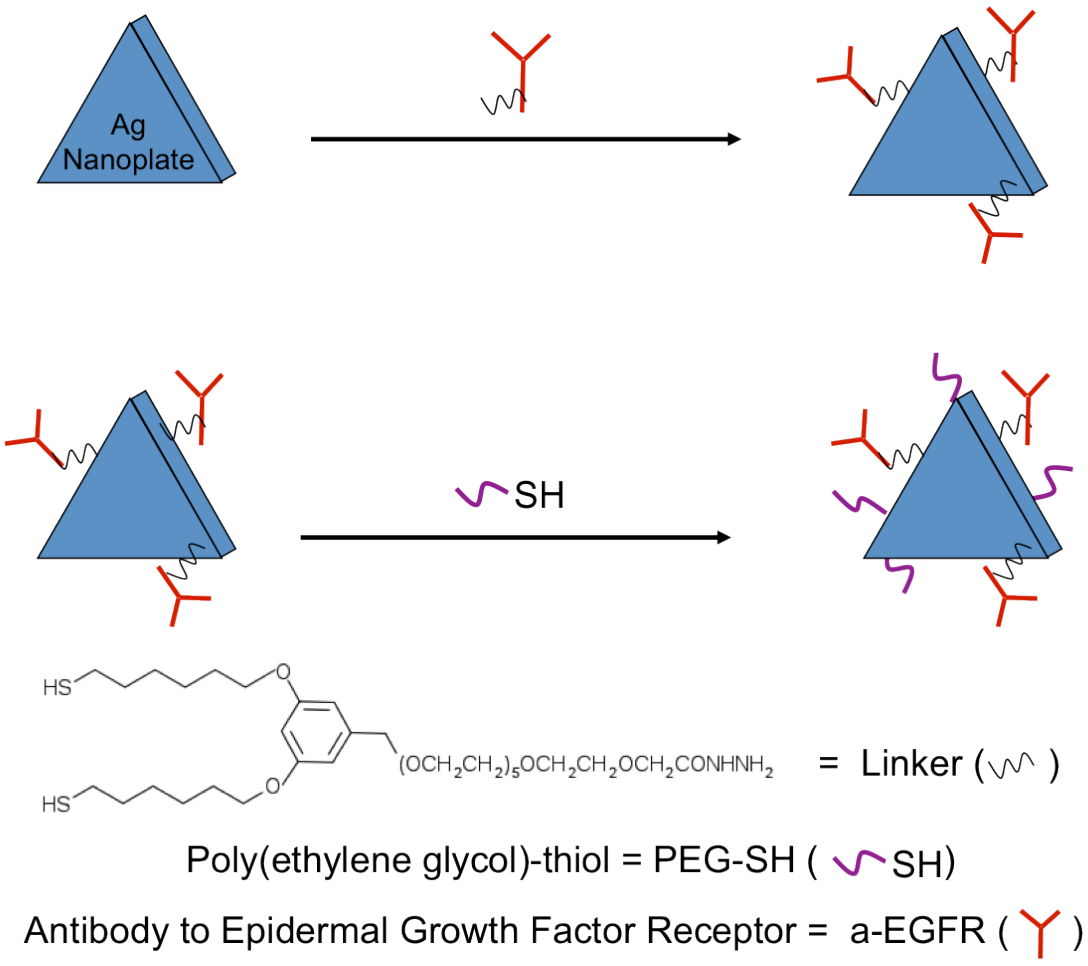


Figure 7.1: Surface grafting of directionally conjugated antibodies and PEG to the surface of silver nanoplates through thiol mediated chemistry.

| Sample Number | S1 | S2 | S3 | S4 |
|---|---|---|---|---|
| Growth Solution | 8.0 ml water<br>0.05 ml TSC<br>0.15 ml AA<br>1.8 ml seeds at OD = 0.65 | 4.8 ml water<br>0.05 ml TSC<br>0.15 ml AA<br>5 ml of S1 | 4.8 ml water<br>0.05 ml TSC<br>0.15 ml AA<br>5 ml of S2 | 4.8 ml water<br>0.05 ml TSC<br>0.15 ml AA<br>5 ml of S3 |
| Color Changes with time | yellow, orange, red, maroon | maroon, purple, blue, teal | teal, forest green, light forest green with purple hue | forest green/purple to pastel blue/silver |
| LSPR peak | 550 nm | 700 nm | 900 nm | 1100 nm |

Table 7.1: Chart showing the growth solutions required for various growth stages of the stepwise nanoplate growth with their associated color changes and resulting longitudinal surface plasmon resonance (LSPR) peaks. Amounts of trisodium citrate (TSC) are from a 40 mM solution, and amounts of ascorbic acid (AA) are from a 40 mM solution. OD = optical density.

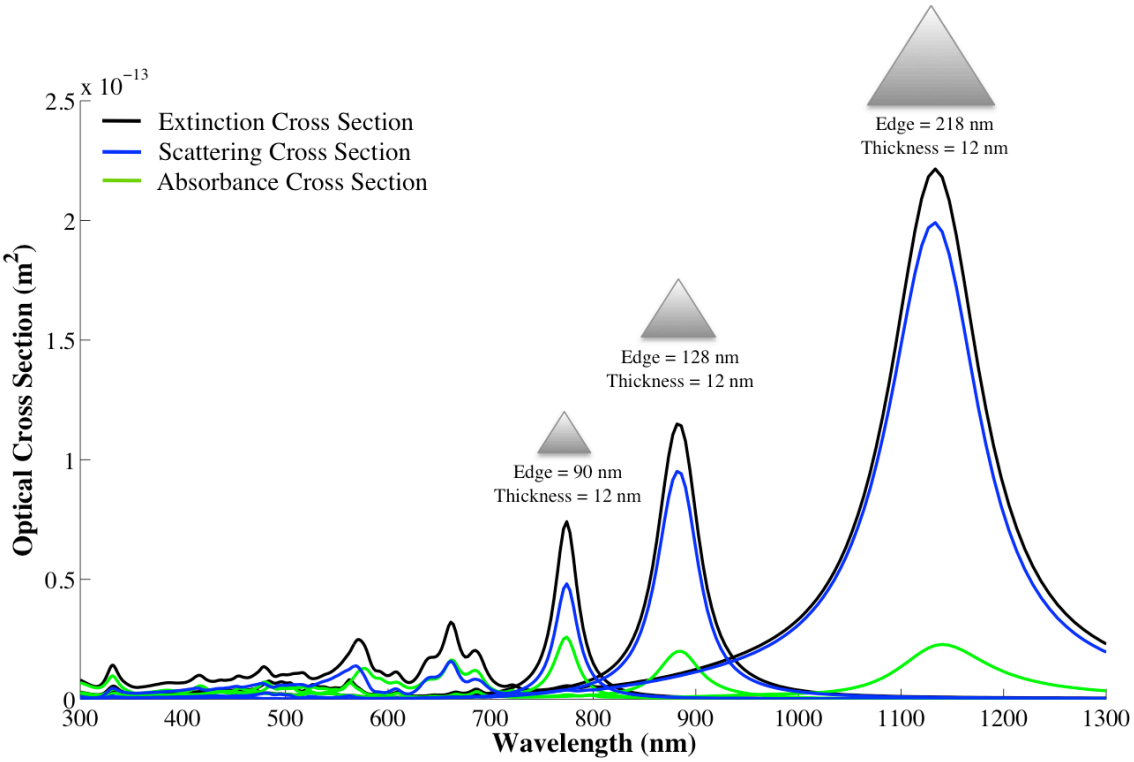


Figure 7.2: FDTD modeling of the extinction, scattering, and absorption cross-section for three silver triangular nanoplates of increasing edge length.

| Nanoparticle Type | Length (nm) | Abs Cross Section ($m^2$) |
|---|---|---|
| Au Nanosphere | 30 | 1.40E-15 |
| Silver Nanoplates (Edge Length x Thickness) | 25x12 | 1.10E-15 |
| | 60x12 | 1.20E-14 |
| | 90x12 | 2.59E-14 |
| | 128x12 | 2.00E-14 |
| | 218x12 | 2.28E-14 |
| Au Nanocages (Edge Length) | 45 | 1.63E-14 |
| | 32 | 6.02E-15 |
| Au Nanorod (Diameter x Length) | 8x34 | 4.31E-15 |

Table 7.2: A comparison of absorbance cross section values for various nanoparticles at their longitudinal surface plasmon resonance. Data for the silver nanoplates and Au nanorods were simulated using FDTD modeling while data for the Au nanospheres and Au nanocages were previously reported.[12, 16, 22]

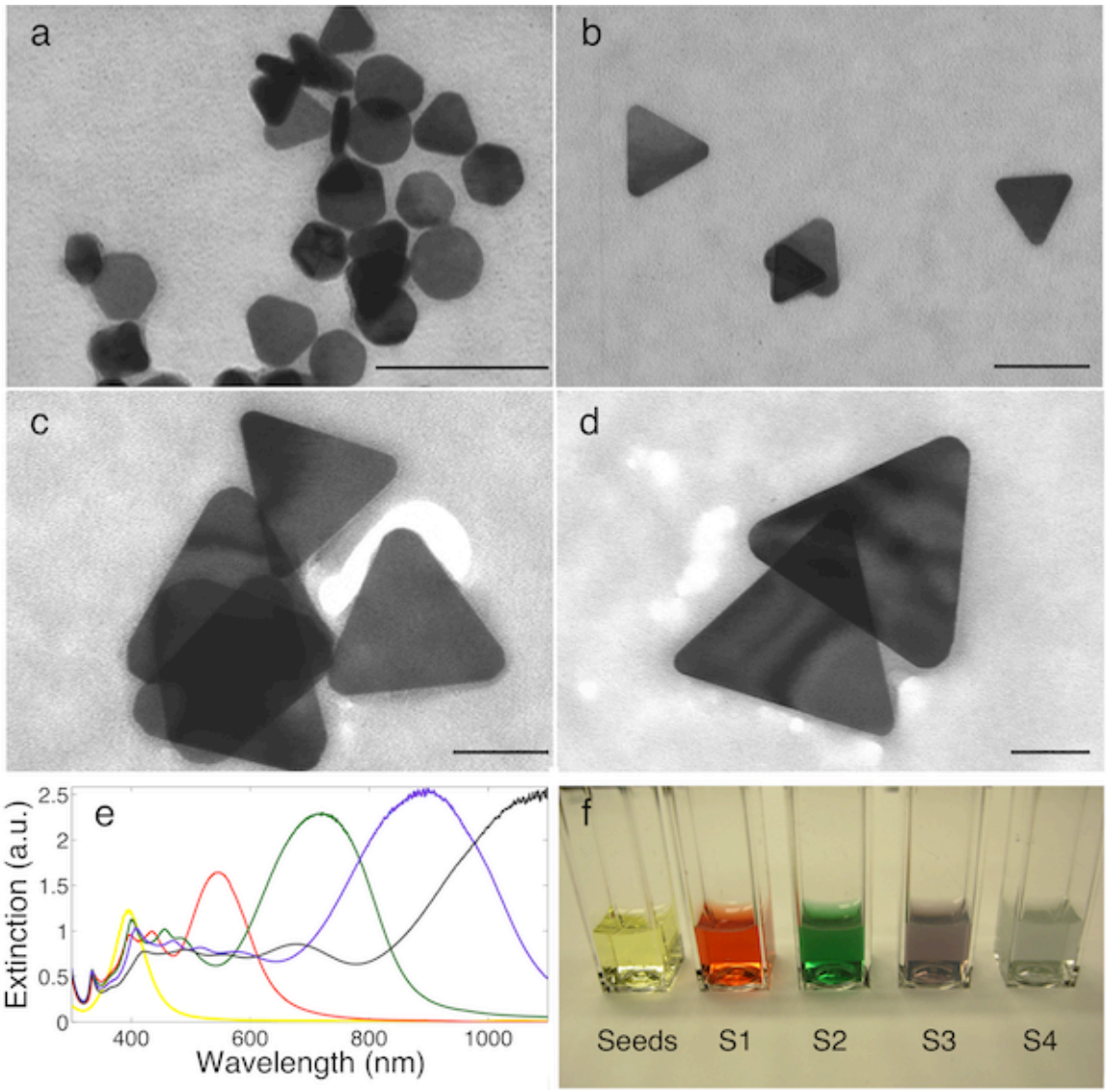


Figure 7.3: Silver nanoplates directly after step-wise growth adding edge length from S1 to S4 (a-d) with their corresponding extinction spectra (e) and color change in solution (f). Scale bars are 100 nm.

| | Edge Length (nm) | Thickness (nm) | % Spheres | Sphere Diameter (nm) |
|---|---|---|---|---|
| S1 | 25.3 ± 5.5 | 10.4 ± 1.6 | 15.5 | 18.5 ± 2.5 |
| S2 | 60.9 ± 10.1 | 12.5 ± 1.9 | 20.0 | 31.9 ± 9.8 |
| S3 | 128.0 ± 25.9 | 18.0 ± 2.7 | 18.2 | 46.0 ± 9.6 |
| S4 | 218.6 ± 35.6 | 25.6 ± 10.6 | 18.3 | 70.9 ± 20.0 |

Table 7.3: Size chart of Ag nanoplate edge length and thickness for each growth step along with the percent population of spheres grown alongside the nanoplates in each batch.

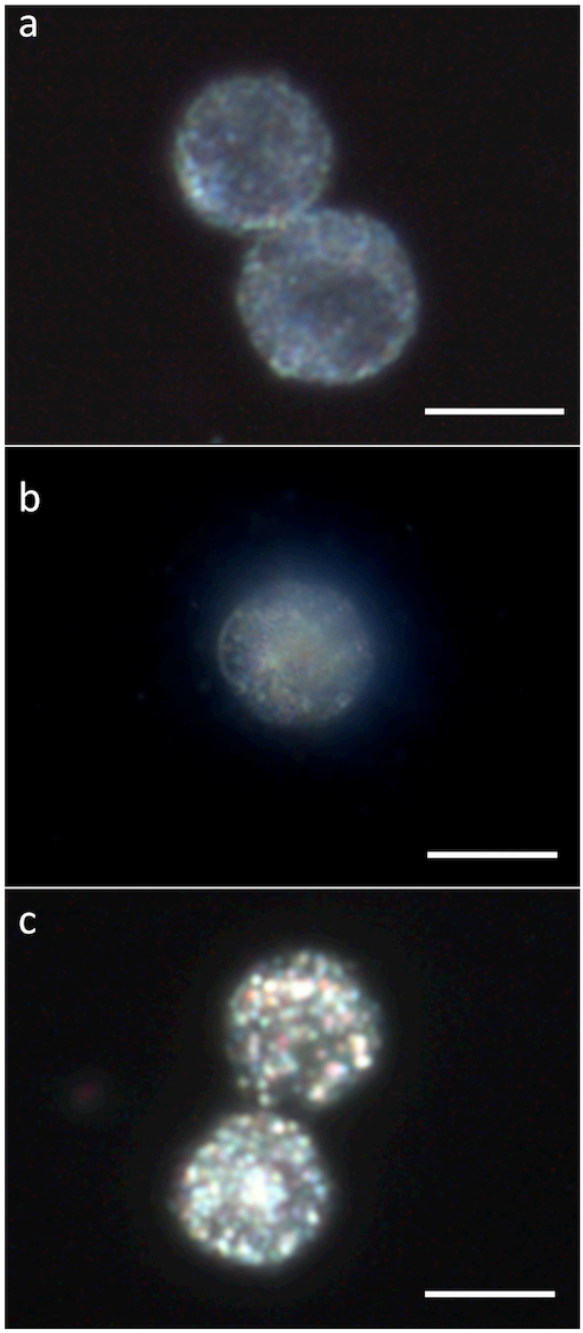


Figure 7.4: Darkfield microscopy of pancreatic cancer cells after incubation with no nanoplates (a), PEGylated nanoplates (b), and a-EGFR conjugated nanoplates (c). All scale bars are 20 μm.

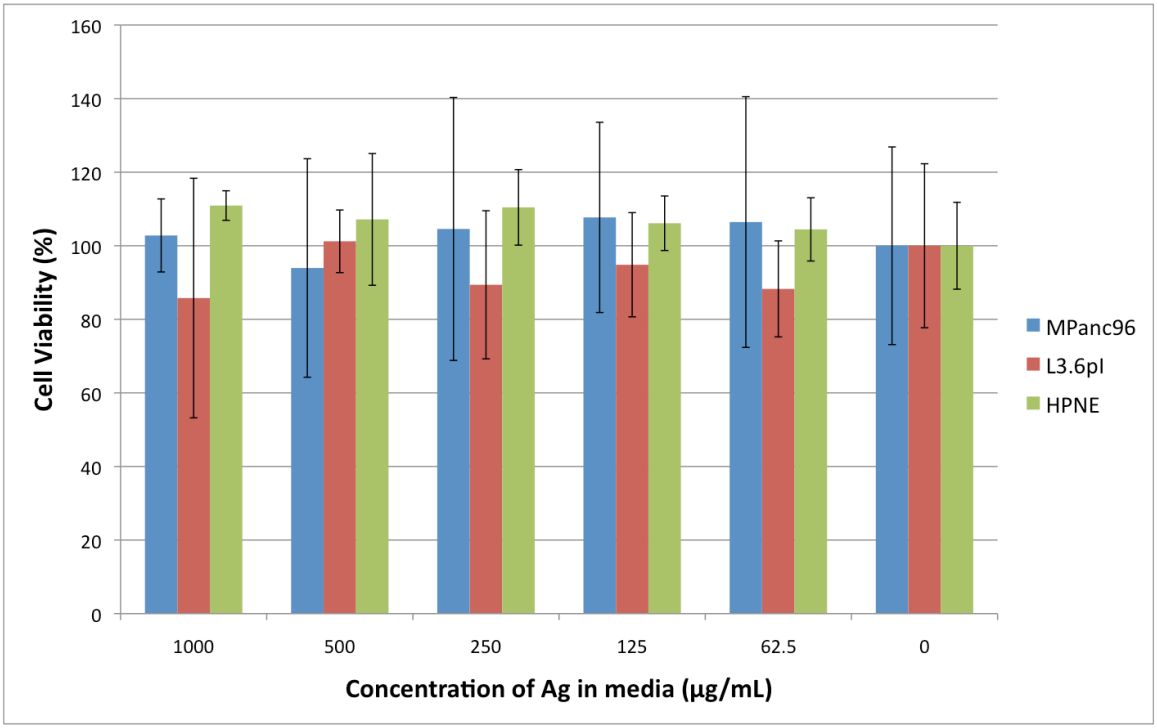


Figure 7.5: Results of the MTS assay for cell viability on three cell lines after incubation for 24 hr with a-EGFR conjugated Ag nanoplates at various concentrations.

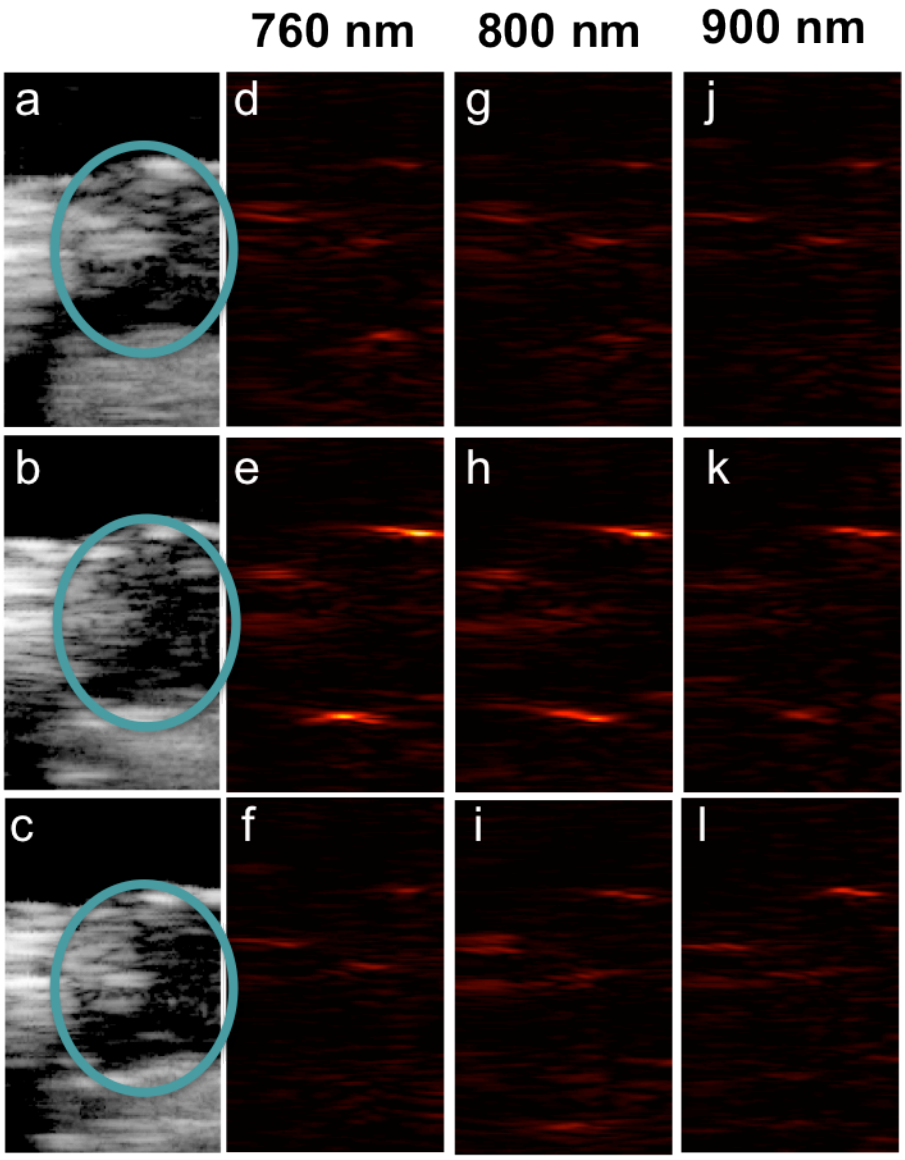


Figure 7.6: Blue circles highlight the position of the tumor in three different 2D cross-sectional planes *in vivo* prior to the silver nanoplate injection. Ultrasound (a-c) and photoacoustic images taken using 760 nm (d-f), 800 nm (g-i), and 900 nm (j-l) wavelengths of light are shown for each cross-section. All images are 17.5 mm by 10.5 mm.

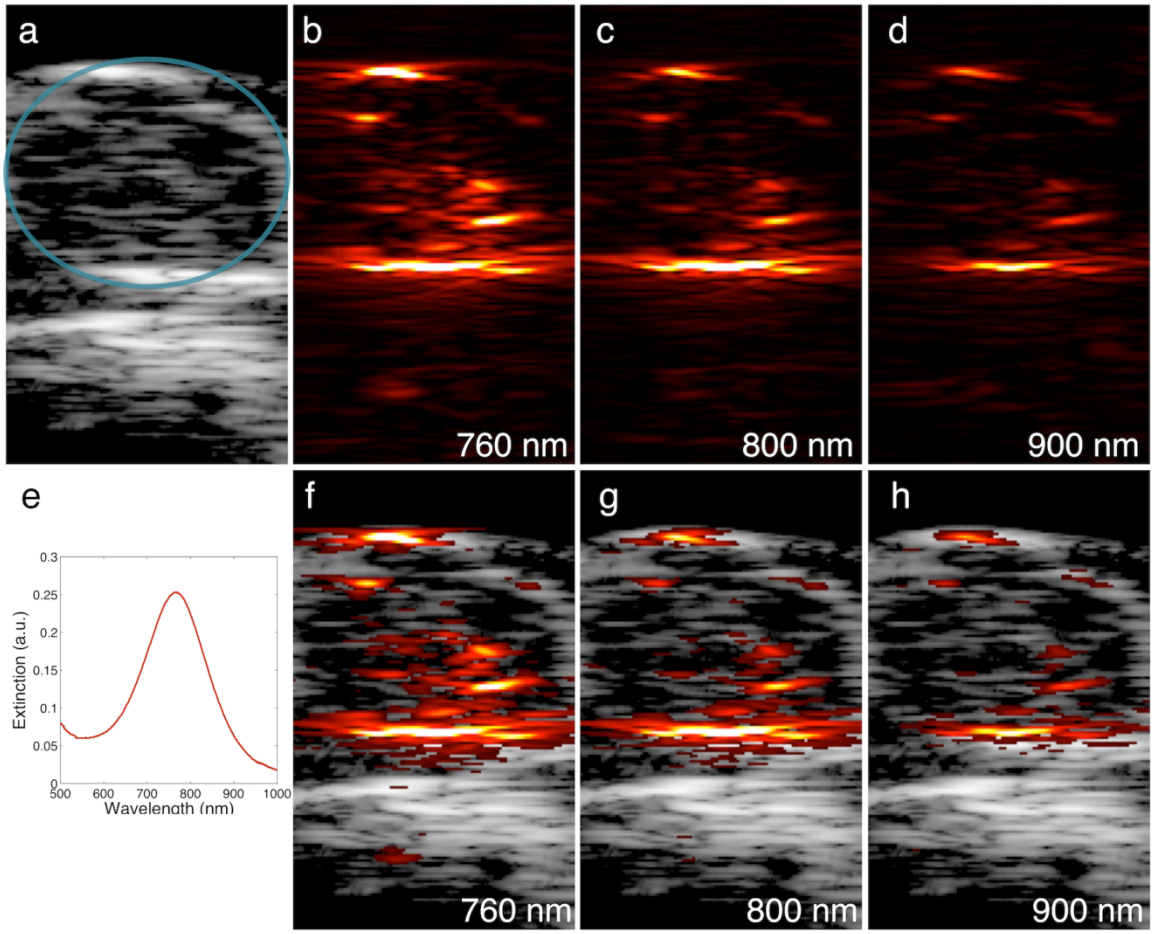


Figure 7.7: Ultrasound (a), photoacoustic (b-d), and combined PAUS (f-h) images of a 2D cross-section of the tumor at 5 hr post injection of a-EGFR and mPEG-SH conjugated Ag nanoplates. The tumor area is circled in blue. All images are 17.5 mm by 10.5 mm. (e) shows the optical extinction spectrum for the Ag nanoplates injected.

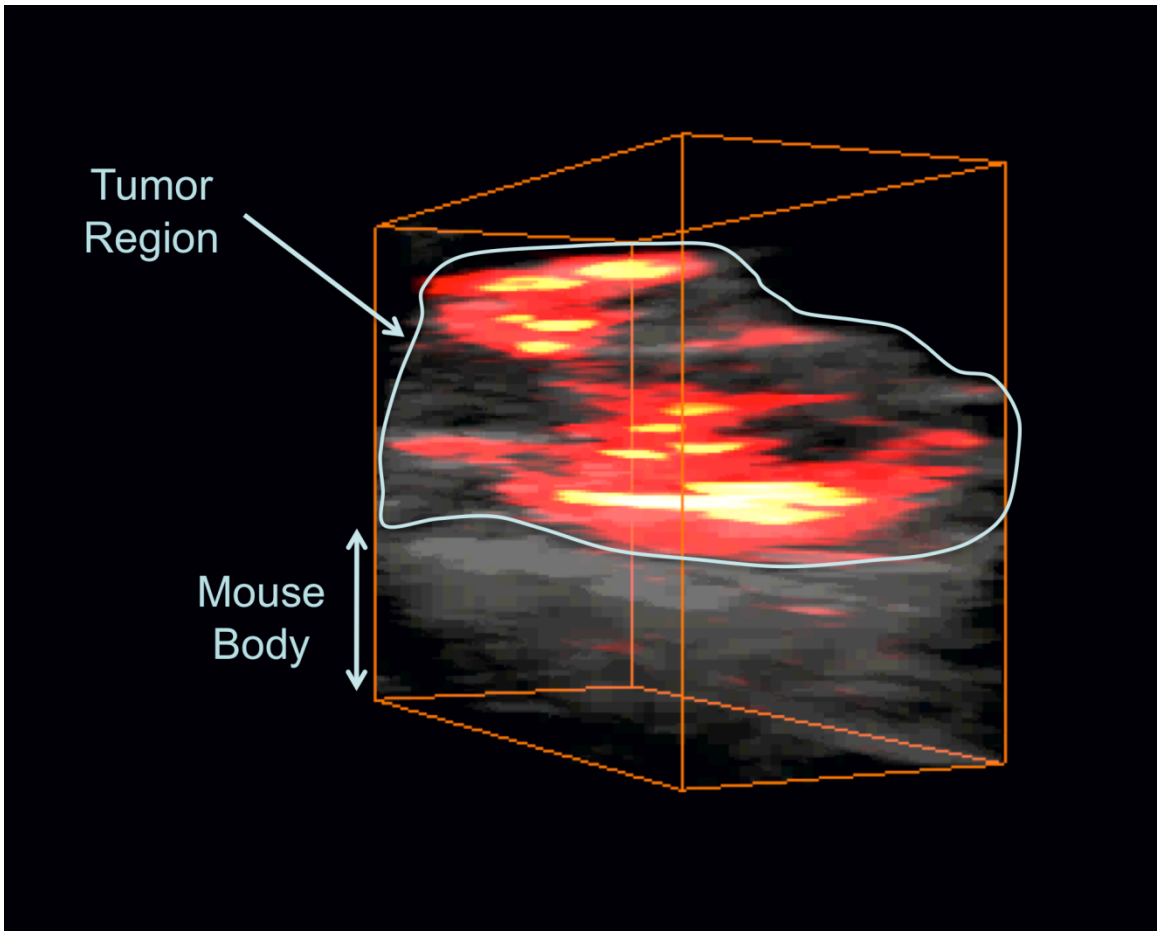


Figure 7.8: A 3D rendering of the entire mouse tumor and the accumulation of a-EGFR conjugated Ag nanoplates within the tumor volume. The image is 17.5 mm by 10.5mm by 12 mm.

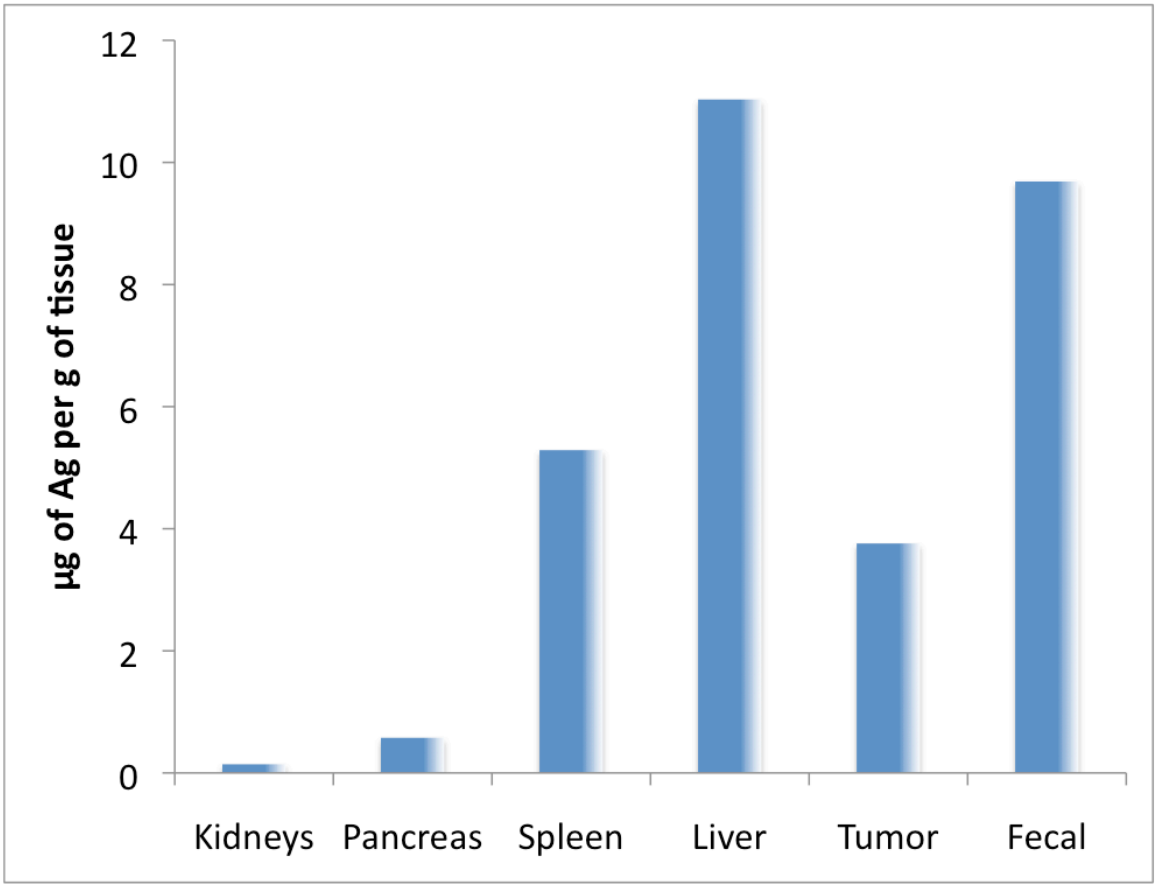


Figure 7.9: The biodistribution of silver in particular mouse organs 112 hr after silver nanoplate injection. Only ~15% of the initial injected dose was accounted for in all the organs tested.

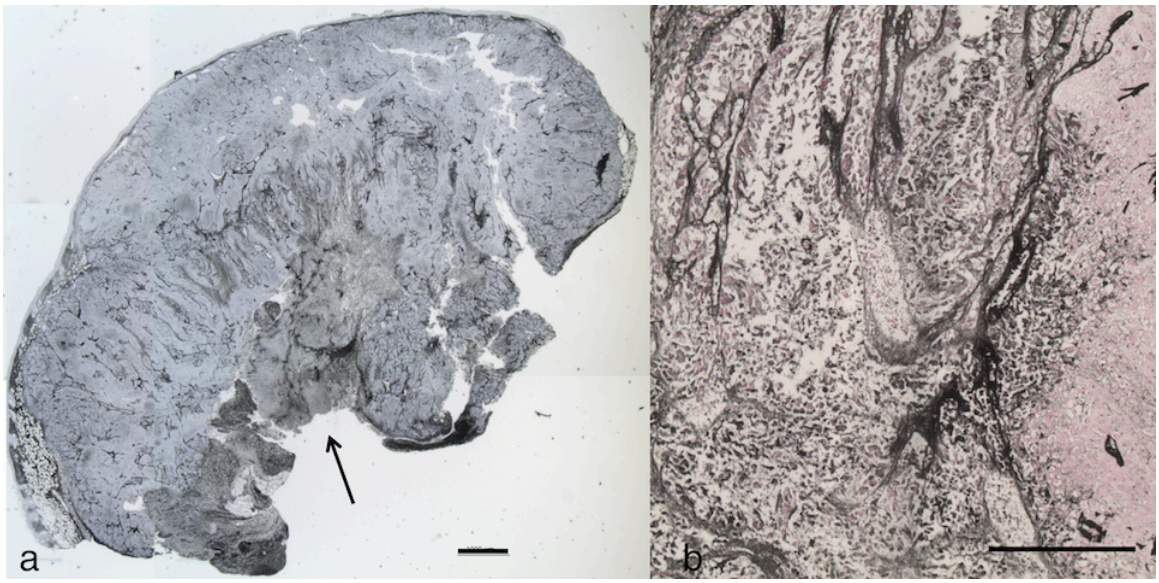


Figure 7.10: Histological slices of the tumor stained with silver stain and hematoxylin (a) and nuclear fast red (b). The scale bar in (a) is 1 mm; scale bar in (b) is 200 μm.

## 7.5 REFERENCES


1. M. A. El-Sayed, "Some interesting properties of metals confined in time and nanometer space of different shapes," Acc Chem Res 34(4), 257-264 (2001)
2. I. Lisiecki, "Size, shape, and structural control of metallic nanocrystals," J Phys Chem B 109(25), 12231-12244 (2005)
3. C. J. Murphy, T. K. Sau, A. M. Gole, C. J. Orendorff, J. Gao, L. Gou, S. E. Hunyadi and T. Li, "Anisotropic metal nanoparticles: Synthesis, assembly, and optical applications," J Phys Chem B 109(29), 13857-13870 (2005)
4. Y. Xia, Y. Xiong, B. Lim and S. E. Skrabalak, "Shape-controlled synthesis of metal nanocrystals: Simple chemistry meets complex physics?," Angew. Chem. Int. Ed. Engl. 48(1), 60-103 (2009)
5. B. Pietrobon, M. McEachran and V. Kitaev, "Synthesis of size-controlled faceted pentagonal silver nanorods with tunable plasmonic properties and self-assembly of these nanorods," ACS Nano 3(1), 21-26 (2009)
6. B. Nikoobakht and M. El-Sayed, "Preparation and growth mechanism of gold nanorods (NRs) using seed-mediated growth method," Chem. Mater. 15(10), 1957-1962 (2003)
7. K. Homan, S. Kim, Y. S. Chen, B. Wang, S. Mallidi and S. Emelianov, "Prospects of molecular photoacoustic imaging at 1064 nm wavelength," Opt Lett 35(15), 2663-2665 (2010)
8. J. B. Jackson and N. J. Halas, "Silver nanoshells: Variations in morphologies and optical properties " J. Phys. Chem. B 105(14), 2743-2746 (2001)
9. R. A. Kruger, P. Liu, Y. R. Fang and C. R. Appledorn, "Photoacoustic ultrasound (PAUS) reconstruction tomography," Med. Phys. 22(10), 1605-1609 (1995)
10. M. Xu and L. V. Wang, "Photoacoustic imaging in biomedicine," Rev. Sci. Instrum. 77(041101 (2006)
11. S. Y. Emelianov, S. R. Aglyamov, J. Shah, S. Sethuraman, W. G. Scott, R. Schmitt, M. Motamedi, A. Karpiouk and A. Oraevsky, "Combined ultrasound, optoacoustic, and elasticity imaging," Proceedings of the SPIE Photonics West 5320(101-112 (2004)
12. E. C. Cho, C. Kim, F. Zhou, C. M. Cobley, K. H. Song, J. Chen, Z. Y. Li, L. V. Wang and Y. Xia, "Measuring the optical absorption cross sections of Au-Ag nanocages and Au nanorods by photoacoustic imaging," J Phys Chem C Nanomater Interfaces 113(21), 9023-9028 (2009)
13. K. Homan, S. Mallidi, E. Cooley and S. Emelianov, "Combined Photoacoustic and Ultrasound Imaging of Metal Nanoparticles In Vivo," in Nanoimaging B. Goins and W. Phillips, Eds., Pan Stanford Publishing, Singapore (2010).

14. P. Li, C. Wang, D. Shieh, C. Wei, C. Liao, C. Poe, S. Jhan, A. Ding and Y. Wu, "In vivo photoacoustic molecular imaging with simultaneous multiple selective targeting using antibody-conjugated gold nanorods," Opt. Express 16(23), 18605-18615 (2008)

15. A. A. Oraevsky, "Gold and silver nanoparticles as contrast agents for optoacoustic imaging," in Photoacoustic Imaging and Spectroscopy L. V. Wang, Ed., Taylor and Francis Group, New York (2009).

16. K. Homan, J. Shah, S. Gomez, H. Gensler, A. Karpiouk, L. Brannon-Peppas and S. Emelianov, "Silver nanosystems for photoacoustic imaging and image-guided therapy," Journal of Biomedical Optics 15(2), 021316 (2010)

17. C. Xue and C. A. Mirkin, "pH-switchable silver nanoprism growth pathways," Angew. Chem. Int. Ed. Engl. 46(12), 2036-2038 (2007)

18. X. Zou, E. Ying, H. Chen and S. Dong, "An approach for synthesizing nanometer-to micrometer-sized silver nanoplates," Colloids Surf. Physicochem. Eng. Aspects 303(3), 226-234 (2007)

19. C. S. Levin, S. W. Bishnoi, N. K. Grady and N. J. Halas, "Determining the conformation of thiolated poly(ethylene glycol) on Au nanoshells by surface-enhanced Raman scattering spectroscopic assay," Anal. Chem. 78(10), 3277-3281 (2006)

20. S. Kumar, J. Aaron and K. Sokolov, "Directional conjugation of antibodies to nanoparticles for synthesis of multiplexed optical contrast agents with both delivery and targeting moieties," Nat Protoc 3(2), 314-320 (2008)

21. A. Rowland and J. Holcombe, "Evaluation and correction of isotope ratio inaccuracy on inductively coupled plasma time-of-flight mass spectrometry," Spectrochimica Acta Part B: Atomic Spectroscopy 64(1), 35-41 (2009)

22. C. M. Pitsillides, E. K. Joe, X. Wei, R. R. Anderson and C. P. Lin, "Selective cell targeting with light-absorbing microparticles and nanoparticles," Biophys. J. 84(6), 4023-4032 (2003)

23. V. Biju, T. Itoh, A. Anas, A. Sujith and M. Ishikawa, "Semiconductor quantum dots and metal nanoparticles: syntheses, optical properties, and biological applications," Anal Bioanal Chem 391(7), 2469-2495 (2008)

24. E. Hao, G. C. Schatz and J. T. Hupp, "Synthesis and optical properties of anisotropic metal nanoparticles," J Fluoresc 14(4), 331-341 (2004)

25. X. C. Jiang, C. Y. Chen, W. M. Chen and A. B. Yu, "Role of Citric Acid in the Formation of Silver Nanoplates through a Synergistic Reduction Approach," Langmuir (2009)

26. B. Wiley, Y. Sun and Y. Xia, "Synthesis of silver nanostructures with controlled shapes and properties," Acc Chem Res 40(10), 1067-1076 (2007)

27. C. Metraux and C. Mirkin, "Rapid thermal synthesis of silver nanoprisms with chemically tailorable thickness," Adv. Mater. 17(4), 412-415 (2005)

28. C. Xue, G. S. Metraux, J. E. Millstone and C. A. Mirkin, "Mechanistic study of photomediated triangular silver nanoprism growth," J. Am. Chem. Soc. 130(26), 8337-8344 (2008)

29. M. Sakamoto, M. Fujistuka and T. Majima, "Light as a construction tool of metal nanoparticles: Synthesis and mechanism," Journal of Photochemistry & Photobiology, C: Photochemistry Reviews 10(1), 33-56 (2009)

30. S. E. Skrabalak, L. Au, X. Li and Y. Xia, "Facile synthesis of Ag nanocubes and Au nanocages," Nat Protoc 2(9), 2182-2190 (2007)

31. P. V. Asharani, M. P. Hande and S. Valiyaveettil, "Anti-proliferative activity of silver nanoparticles," BMC Cell Biol 10(65 (2009)

32. P. V. AshaRani, G. Low Kah Mun, M. P. Hande and S. Valiyaveettil, "Cytotoxicity and genotoxicity of silver nanoparticles in human cells," ACS Nano 3(2), 279-290 (2009)

33. R. Arvizo, R. Bhattacharya and P. Mukherjee, "Gold nanoparticles: Opportunities and challenges in nanomedicine," Expert Opin Drug Deliv 7(6), 753-763 (2010)

34. S. K. Balasubramanian, J. Jittiwat, J. Manikandan, C. N. Ong, L. E. Yu and W. Y. Ong, "Biodistribution of gold nanoparticles and gene expression changes in the liver and spleen after intravenous administration in rats," Biomaterials 31(8), 2034-2042 (2010)

# Chapter 8: Synthesis of the CIT-NpS and *In Vitro* Characterization

The objective of this research is to create nanosystems with the ability to provide both imaging contrast and therapy for pancreatic cancer. In Chapters 2-5 the CIT-NS design was discussed. In Chapter 6, a new and potentially better nanosystem, the CIT-NpS, was proposed. Chapter 7 showed that this nanoplate system could enhance photoacoustic imaging *in vivo*. Finally, this chapter explores synthesis methods and preliminary *in vitro* characterization for the entire CIT-NpS, complete with drugs as depicted in Fig 6.1.

## 8.1 Introduction

This chapter explores the feasibility of using silver nanoplates as drug carriers, thus completing the CIT-NpS design. As discussed in Chapters 2 and 5, Gemcitabine (Gem) remains the chemotherapeutic standard of care for pancreatic cancer patients;[1-4] therefore, attachment of Gem to the silver nanoplate system is the ultimate goal (Fig 6.1). Towards this end, several facets of synthesis and characterization of the CIT-NpS must be addressed: (1) methods of Gem conjugation to the nanoplate, (2) chemical modifications of Gem necessary for the chosen conjugation strategy, and (3) testing of the chemically modified drug (Gem prodrug) for therapeutic efficacy.

Conjugating drugs to metal surfaces can be accomplished through several strategies. Electrostatic interactions, chemisorption, hydrogen bonding, and covalent bonding are some of the ways that drugs can be attached to nanoparticle carriers. Covalent bonds are desired since they form a strong connection between the drug and the metal that is not easily broken or displaced by interactions with molecules in the bloodstream. Primary amine groups, such as those found on Gem (Fig 5.2), can chemically adsorb to silver and gold surfaces. Some argue that the amine-gold connection

is covalent[5, 6], but not as strong as the covalent bond between free thiol groups and silver or gold (a.k.a. thiolate bonds). The nanoplate system was designed to be a systemically injected platform. Therefore, thiolate bonds between the drug and the metal represent the tightest junction with the least likelihood of degrading in the bloodstream. For this thiolate bonding strategy to work, a free sulfhydryl residue (primary thiol) must be present on Gem.

Introduction of sulfhydryl residues to molecules, also called thiolation, is well known. Hermanson describes at least 11 different methods for thiolation of proteins.[7] Seven of these techniques are for modification of amine groups to thiol groups. Following Hermanson's protocols, Gem was thiolated using N-succinimidyl S-acetylthioacetate (SATA) at its primary amine site. Described in this chapter are methods of synthesis and characterization for a Gemcitabine thioamide prodrug formed using SATA. Furthermore, prodrug therapeutic efficacy is tested in comparison to native Gem, and the effect that drug attachment has on the structural stability, drug delivery mechanisms, and imaging contrast potential of the nanoplate system is investigated.

## 8.2 METHODS

This methods section is divided into three major segments: (1) prodrug synthesis, (2) CIT-NpS synthesis, and (3) *in vitro* characterization of the CIT-NpS with pancreatic cancer cells. For reader clarity, the sources for all materials are consolidated here.

Materials: All chemicals were used without further purification and were at minimum ACS grade. Silver nitrate (>99%), pyridine, hydroxylamine, the antibody to Epidermal Growth Factor Receptor (EGFR) clone C225, poly(ethylene glycol) bisphenol A epichlorohydrin $M_n$ = 14 kDa, and Bis (p-sulfonatophenyl) phenylphosphine dihydrate dipotassium salt (BSPP) were purchased from Sigma-Aldrich (St. Louis, MO, USA).

ACS grade L(+) ascorbic acid was a product of Acros (Morris Plains, NJ, USA). Dulbecco's phosphate buffered saline (DPBS) came from Mediatech, Inc. (Herndon, VA, USA). The methyl-poly(ethylene glycol)-thiol (mPEG-SH of 5 kDa) was from Laysan Bio (Arab, AL, USA). All cell culture products, the MTS assay, and N-succinimidyl S-acetylthioacetate (SATA) were purchased from Invitrogen (Carlsbad, CA, USA) unless otherwise specified. Slide mounting media, Vectashield with DAPI stain, was from Vector Laboratories (Burlingame, CA, USA). The linker hydrazide-polyethylene glycol-dithiol (SPT-014B) was a product of Sensopath (Bozeman, MT, USA).

### 8.2.1 Gemcitabine-Thioamide Prodrug Synthesis and Characterization

Several strategies for thiolation of Gem were considered and tested.[7] After several failed attempts, it was deduced that the primary amine on Gem is a very weak nucleophile. Successful thiolation of Gem was only achieved using SATA when pyridine was used as the solvent. The basic nature of pyridine helped facilitate nucleophilic attack by the primary amine on Gem. Specifically, a thiolated version of Gem was synthesized in a two-step reaction as shown in Fig 8.1. Gem (25 mg, 0.0834 mmol) was placed in a small glass vial with 0.8 ml of pyridine and allowed to stir at room temperature. Then SATA (15.43 mg, 0.0667 mmol) was added. Nitrogen was bubbled into the stirring mixture for 1 min and then the reaction was sealed in the nitrogen environment while stirring for 3 hr. Aliquots of the crude mixture were taken for direct analysis by electrospray ionization mass spectroscopy (ESI-MS). For $H^1$ Nuclear Magnetic Resonance (NMR) analysis at 600 MHz, the reaction was performed under $N_2$ in deuterated pyridine and transferred directly to a NMR glass tube for analysis of the crude mixture. NMR analysis of the split doublets in the CH6 and CH5 positions on Gem were used to determine yield of the Gemcitabine acetylthioamide (Gem-ATA) prodrug.

To complete Step 2 of the reaction shown in Fig 8.1, 5.332 μl of the mixture from Step 1 was placed in 944.668 μl of a sodium phosphate buffer (50 mM, pH = 8.0) while stirring. Then 50 μl of a 1 mg/ml solution of hydroxylamine (0.72 μmol – 2x the moles of SATA present) was added and the solution was stirred at room temperature for 2 hr. During those 2 hr, the acetyl group was removed from Gem-ATA, creating the final Gemcitabine Thioamide (Gem-TA) prodrug. Analysis of the crude final product was attempted through ESI-MS following desalting and purification using C-18 Ziptips (a product of Millipore).

### 8.2.2 CIT-NpS Synthesis and Characterization

Using the thiolated version of Gem (Gem-TA), described above, the CIT-NpS can be built. Three molecules were surface grafted to Ag nanoplates via thiolate bonds[8, 9] in the following order: the antibody to EGFR, Gem-TA, and mPEG-SH. The antibody to EGFR (a-EGFR) was added first because it is the largest molecule and therefore has the least mobility in solution. If it were not grafted first, it is likely that a-EGFR would not bind in significant quantities. The Gem-TA prodrug was grafted second to afford as much space for binding on the surface of silver as possible. Finally, mPEG-SH was added to fill in any available surface spaces, adding stability to the nanoplate.

The steps for bioconjugation of the three moieties are described below. Any desired batch (S1 through S4, based on the desired optical properties) of the as prepared nanoplates (see Chapter 7) were placed in a 50 kDa MWCO Millipore centrifugal filter directly after synthesis and spun at 1500 rcf for 3 min at 20°C. The nanoplates were then resuspended in 1 ml of DIUF water, placed in a 2 ml tube, wrapped in foil, and allowed to sit overnight at room temperature. Then 200 μl of a 2 wt% PEG solution was added (poly(ethylene glycol) bisphenol A epichlorohydrin $M_n$ = 14 kDa). Adding the PEG

solution helped limit aggregation of the nanoplates during the bioconjugation process. An ultraviolet to visible (UV-vis) spectrum from 300 nm to 1100 nm was measured using a Beckman Coulter DU 640 spectrophotometer with a 1 cm pathlength cuvette containing 7 μl of the nanoplate solution in 400 μl of DIUF water. Then, enough of the as prepared antibody-linker (AB-linker) solution (see Chapter 7) was added to account for 0.05 mg of antibody-linker. The exact volume of the AB-linker solution varied based on the final concentration of the AB-linker in HEPES as determined by a Thermo Scientific Nanodrop read at a wavelength of 280 nm with an assumed extinction coefficient of 210,000 $M^{-1}cm^{-1}$. The AB-linker and nanoplates were allowed to shake at room temperature in the dark for 20 min, after which the UV-vis spectrum was determined. Slight red shifts (5-10 nm) in peak resonance of the nanoplates were observed after conjugation of the AB-linker to the nanoplates.

The Gem-TA prodrug was conjugated after the AB-linker. Specifically, 40 μl of the as prepared Gem-TA solution (see section 8.2.1) was added to the silver nanoplate/AB-linker solution and allowed to shake at room temperature in the dark for 20 min, after which the UV-vis spectrum was measured. Again, slight red shifts (4-6 nm) in peak resonance of the nanoplates were observed after conjugation of the Gem-TA to the nanoplates.

To limit opsonization in the bloodstream, the surface area of the silver not covered by antibody or Gem-TA was passivated by attachment of mPEG-SH. Specifically, after allowing the AB-linker/Gem-TA/Ag nanoplate solution to react, 40 μl of 50 mM mPEG-SH (5 kDa) was also added to react with the Ag nanoplates. After shaking in the dark for 20 min, the nanoplates were cleaned using a 50 kDa MWCO Millipore centrifugal filter spun at 1500 rcf for 5 min at 4°C. Supernatants were collected for analysis. Then, the nanoplates were resuspended in 500 μl of DPBS and sent through

a 0.22 μm filter into another 50 kDa MWCO Millipore centrifugal filter in 5 ml total of DPBS. The nanoplates were again spun at 1500 rcf for 5 min at 4°C. The sterile nanoplates (the final CIT-Nps) were suspended in 500 μl of DPBS in a sterile 2 ml tube for future use.

Several analytic techniques were used to prove that Gem-TA attached to the nanoplates. To enhance the accuracy of these methods, a set of nanoplates conjugated to Gem-TA, without a-EGFR or mPEG-SH was created. Briefly, an S3 batch of the as prepared nanoplates (see Chapter 7) was placed in a 50 kDa MWCO Millipore centrifugal filter directly after synthesis and spun at 1500 rcf for 3 min at 20°C. The nanoplates were then resuspended in 1 ml of DIUF water, placed in a 2 ml tube, wrapped in foil, and allowed to sit overnight at room temperature. Then, 40 μl of the Gem-TA solution (see section 8.2.1) was added to the silver nanoplate solution and allowed to shake at room temperature in the dark for 20 min, after which the UV-vis spectrum was taken. Then the plates were washed twice using a 50 kDa MWCO Millipore centrifugal filter (1000 fold dilution). For analysis using energy-dispersive X-ray spectroscopy (EDS) on a scanning transmission electron microscope (STEM), nanoplates were drop casted onto formvar/carbon 200 mesh Cu TEM grids. For analysis using X-ray photoelectron spectroscopy (XPS), nanoplates were drop casted onto a silicon wafer and dried in a vacuum oven overnight at 60°C. Lastly, to ensure that Gem-TA was grafting specifically to the nanoplates, Step 2 of the reaction shown in Fig 8.1 was replicated with and without the hydroxylamine reactant. The supernatants after nanoplate attachment for both reactions were analyzed using UV-vis spectroscopy.

### 8.2.3 *In Vitro* Characterization with Pancreatic Cancer Cells

The human pancreatic cancer cell line L3.6pl and the non-cancerous pancreatic line HPNE were incubated with bioconjugated silver nanoplates and tested for cell viability. Since several different conditions were tested using the same assay, the procedure for culturing the cells and the general assay protocol description are consolidated in this section. Specifics of each test are then provided in the following sections 8.2.3.1 through 8.2.3.4.

The L3.6pl cell line was cultured *in vitro* using Dulbecco's Modified Eagle Medium (DMEM) (with 4500 mg glucose/L, L-glutamine, $NaHCO_3$ and pyridoxine HCl) supplemented with 10% fetal bovine serum (FBS) and 1% Penicillin-Streptomycin (Pen/Strep) while maintained at 37°C and 5% $CO_2$ in a humidified incubator. The DMEM and the FBS were purchased from Sigma and the Pen/Strep from Invitrogen. The non-cancerous pancreatic cell line, HPNE, was cultured *in vitro* using Medium D that contained one volume of medium M3, three volumes of glucose-free DMEM (with L-glutamine, phenol red, and pyridoxine HCl), 5% FBS, 5.5 mM glucose, 10 ng/ml EGF, and 50 μg/ml gentamycin. Medium M3 is a proprietary formulation optimized for the growth of neuroendocrine cells (InCell Corp., San Antonio, TX, USA). For cell viability studies, cells were seeded in a 96 well plate (each well had 5,000 cells per 100 μl of media for the L3.6pl line and 10,000 cells per 100 μl of media for the non-cancerous, HPNE line). The cells were allowed to attach and grow in the 96 well plate for 24 hr, after which the cell media was removed and replaced with suspensions of bioconjugated Ag nanoplates or drugs (at least 5 wells were seeded for each concentration). After 48 hr of incubation, the media was removed and replaced with fresh media containing no nanoplates or drugs. The absorbance of each well in the plate was measured at 490 nm using a Synergy HT Multimode Microplate Reader from BioTek. To perform the assay,

20 μl of a tetrazolium compound [3-(4,5-dimethylthiazol-2-yl)-5-(3-carboxymethoxyphenyl)-2-(4-sulfophenyl)-2H-tetrazolium (MTS) and an electron coupling reagent (phenazine methosulfate) PMS from the CellTiter 96® $AQ_{ueous}$ Non-Radioactive Cell Proliferation Assay (a Promega product) was added to each well. Over a period of 1 hr in the incubator, the MTS was bioreduced by cells into a formazan product that had an absorbance peak at 490 nm. Dehydrogenase enzymes found in metabolically active cells were responsible for the conversion of MTS into the soluble formazan product. Therefore, the absorbance of each well at 490 nm was directly proportional to the number of viable cells. The absorbance of each well at 490 nm taken before adding MTS was subtracted from the post MTS incubation value. Cell viability was determined by comparing the resulting absorbance of wells containing no nanoplates or drugs to that of wells containing nanoplates or drugs using an F test for a one-way ANOVA.

#### *8.2.3.1 Cytotoxicity of the Gemcitabine-TA Prodrug*

The efficacy of the Gem-TA prodrug was compared with that of native Gem using the MTS assay on L3.6pl pancreatic cancer cells. Details describing how the MTS assay was performed can be found above (section 8.2.3). For this particular test, Gem was suspended in cell media at 300 nM, sterilized using a 200 nm filter, and mixed with the cells. Dilutions of 1:10 in media were prepared to create all of the Gem conditions tested (30 nM and 3 nM). Similar concentrations of Gem-TA were obtained differently. First, 265 μl of the Gem-TA solution obtained from Step 2 in Fig 8.1 (see section 8.2.1) was added to 1.735 ml of sterile DPBS. The solution was sent through a sterile 200 nm filter. Then 48.9 μl of that sterile solution was added to 1.7511 ml of media to create a 300 nM concentration of Gem-TA in media. Dilutions of 1:10 in media were prepared to create

all of the Gem-TA conditions tested (30 nM and 3 nM). Cells were incubated with drugs in media for 48 hr prior to performing the MTS assay.

#### *8.2.3.2 CIT-NpS Therapeutic Efficacy and Cytotoxicity*

Using the CIT-NpS as a vehicle capable of carrying and delivering drugs to pancreatic cancer cells was evaluated against the efficacy of the free Gem-TA prodrug in solution using the MTS assay. Details describing how the MTS assay was performed can be found above (section 8.2.3). For this particular test, the CIT-NpS was obtained as prepared and described in section 8.2.2. However, in the last wash step instead of resuspending in 500 μl of DPBS, the particles were suspended in 5.5 ml of cell media. This dilution makes ~$1.5x10^{11}$ nanoplates/ml at a Gem-TA concentration of 300 nM. Dilutions of 1:10 in media were prepared to create all of the CIT-NpS conditions tested. The Gem-TA samples were prepared as described in section 8.2.3.1.

#### *8.2.3.3 CIT-NpS Toxicity and Stability under Pulsed Laser Exposure*

Cell viability tests using pancreatic cancer L3.6pl cells were performed to determine if the pulsed laser irradiation associated with photoacoustic imaging would cause either (1) damage to nanoparticle labeled cells or (2) extensive drug release from the silver nanoplates. Details describing how the MTS assay was performed can be found above (section 8.2.3). For this particular test, the CIT-NpS was prepared exactly as described in section 8.2.3.2. Nanoplates with only a-EGFR and mPEG-SH were also created using the same procedures described in sections 8.2.2 and 8.2.3.2 except Gem-TA was excluded. Unlike the first two MTS assays described in sections 8.2.3.1 and 8.2.3.2, no dilutions of the particles were performed. Instead, every well was filled with ~$1.5x10^{11}$ nanoplates/ml in media at a Gem-TA concentration of 300 nM where appropriate. The nanoplates were incubated with cells for 4 hr prior to laser exposure. The condition that

was varied was the fluence of the laser exposed to the particles. Laser light at the peak resonance wavelength of the nanoplates was irradiated in a 0.2 $cm^2$ circular spot corresponding to the area of each well in the 96 well black plate. The light was generated using a SpectraPhysics optical parametric oscillator (OPO) system operating at a pulse repetition frequency of 10 Hz and pulse duration of 4-6 ns. Each well received 1000 pulses of light. The MTS assay was performed at 48 hr post laser exposure.

#### *8.2.3.4 CIT-NpS Toxicity under Continuous Wave Laser Exposure*

Cell viability tests using pancreatic cancer L3.6pl cells were also performed to determine if a continuous wave laser could be used in combination with silver nanoplates to induce photothermal cell damage. Details describing how the MTS assay was performed can be found above (section 8.2.3). For this particular test, nanoplates with only a-EGFR and mPEG-SH were created using the same procedures described in sections 8.2.2 and 8.2.3.2 except Gem-TA was excluded. Similar to the test performed in section 8.2.3.3, no dilutions of the particles were prepared. Instead, every well was filled with ~$1.5x10^{11}$ nanoplates/ml in media. The nanoplates were incubated with cells for 4 hr prior to laser exposure. The condition that was varied was laser irradiation time. Laser light at the peak resonance wavelength of the nanoplates was irradiated in a 0.2 $cm^2$ circular spot corresponding to the area of each well in the 96 well black plate. The measured power of the continuous wave diode 808 nm laser was kept constant at 1.3 $W/cm^2$. The MTS assay was performed at 48 hr post laser exposure.

### 8.3 RESULTS AND DISCUSSION

Other researchers have attached Gem to gold nanoparticles and targeted pancreatic cancer[6]. Presented here is the synthesis of a new Gem prodrug and its subsequent attachment to silver nanoplates for pancreatic cancer treatment. These

preliminary results demonstrate that the CIT-NpS can be synthesized and used as a drug carrier with multifunctional properties.

### 8.3.1 Gemcitabine-TA Prodrug Synthesis and Characterization

Thiolation of Gem was performed to create the prodrug Gem-TA that was successfully grafted to silver nanoplates. The thiolation was achieved using the reactant SATA that had been previously used for protein thiolation.[7] The two-step reaction scheme for Gem-TA synthesis is shown in Fig 8.1. In the first step, Gem-ATA was formed by reacting Gem and SATA in pyridine. Surprisingly, pyridine was the only solvent that allowed for favorable formation of Gem-ATA. Other aqueous solvents such as basic phosphate and carbonate buffers were tried, but ultimately failed to produce Gem-ATA. Interactions between the pyridine solvent and Gem likely increase the nucleophilicity of Gem's primary amine, allowing the reaction with SATA to proceed. However, more investigation would be required for a detailed reaction mechanism to be fully elucidated. ESI-MS results shown in Fig 8.2 demonstrate the presence of both Gem and Gem-ATA in the crude reaction mixture after Step 1. NMR of the crude mixture also confirmed this result where peaks associated with the CH6 and CH5 hydrogens on Gem are still present in the Gem-ATA spectrum (Fig 8.3). Comparing the integrated peak values of the split doublets associated with native Gem at 8.38 ppm and the doublet associated with Gem-ATA at 8.73 ppm, the reaction yield was calculated at only 15%. For the second reaction step, ESI-MS was used to analyze the mixture after reaction with hydroxylamine in aqueous phosphate buffer. After purification and desalting using C18 Ziptips, the ESI-MS did not detect Gem-TA in the sample. Moreover, Gem, NHS, and SATA were also not detected, so it is possible that the desalting using the C18 Ziptips actually filtered out the compounds of interest. Thus, even though confirmation of the

Gem-TA prodrug was difficult; notable changes in the nanoplate properties and supernatants were found, which indicate that Gem-TA must have been formed. Details of these tests are provided in the next section.

### 8.3.2 CIT-NpS Synthesis and Characterization

Results here indicate that the CIT-NpS was formed. Chapter 7 already showed that Ag nanoplates could be created with a-EGFR and mPEG-SH grafted. In this Chapter, Gem-TA was formed and grafted in succession with a-EGFR and mPEG-SH to Ag nanoplates. The most convincing evidence that Gem-TA was formed and did attach to silver came from supernatant analysis. As described in section 8.2.2, the reaction in Step 2 of Fig 8.1 was set up as a test with and without the hydroxylamine (HA). After those reactions were run for 2 hr in phosphate buffer, 40 μl of each was reacted with different batches of silver nanoplates. The nanoplates were then washed twice and the supernatants analyzed using a spectrophotometer. The UV spectrums from the first supernatant washes are shown in Fig 8.4a. Unfortunately, pyridine, Gem, Gem-TA, and NHS all contribute to the collective peak at 255 nm shown in Fig 8.4a. However, a noticeable change in peak height is visible for the supernatant collected for the nanoplates reacted with HA and without HA in Step 2. Therefore, even though absorption in the UV range for multiple reactants did not allow for precise quantification of Gem-TA attachment to Ag nanoplates, the decrease in the overall absorbance for the supernatant captured when HA was used, shows that Gem-TA must have attached to the nanoplates.

Analysis of the Ag nanoplates after conjugation of a-EGFR and Gem-TA also confirmed grafting. As shown in Fig 8.4b, the resonance peak for the Ag nanoplates right shifted with each subsequent grafting step. These small shifts in resonance are consistent

with findings from other researchers who attached molecules to gold using thiolate bonds.[9, 10]

Further qualitative demonstration of Gem-TA attachment to the nanoplates was provided by EDS and XPS analysis. For EDS analysis, nanoplates were washed and drop casted on TEM grids for analysis in the STEM. Figure 8.5 shows the resulting EDS elemental mapping for Ag, F, and S for the single silver nanoplate shown in Fig 8.5a. The colored maps for the various elements show overlap in the signals for the three elements, illustrating that Ag is present and that F and S atoms associated with the Gem-TA prodrug are also present. Lastly, XPS analysis further confirmed the presence of F on the surface of Ag nanoplates. As shown in Fig 8.6, a peak for F 1s was located at a binding energy of 688 eV. That peak was integrated and compared with the corresponding peak for silver. XPS analysis indicated that a Ag:F ratio of 40:1 was calculated from the integrated peak values. However, without having known standards for the XPS measurement, this ratio could not be used quantitatively to determine the exact amount of Gem-TA on the surface of Ag. Thus, though the results are only qualitative, both XPS and EDS showed that Gem-TA was grafted to the surface of Ag nanoplates.

### 8.3.3 Cytotoxicity of the Gemcitabine-TA Prodrug

Once a prodrug like Gem-TA is built, it is important to first test its efficacy *in vitro* in comparison to the native drug Gem. A cell viability test was performed using the MTS assay on the pancreatic cancer cell line L3.6pl, and the results are shown in Fig 8.7. The concentration dependent loss in cell viability is comparable for the two versions of the drug. As discussed in Chapter 5, previous studies[11, 12] have shown that prodrug versions of Gem are more effective than Gem. Most references site the stability of the prodrug forms in plasma as the main reason for increased therapeutic efficacy.[11, 12] The

tests performed in the literature measured inhibition of protein synthesis and used different cells lines than those used here. The MTS assay, which assesses the function of active mitochondria, is a cell viability study only. The results shown in Fig 8.7 indicate that Gem-TA and Gem have toxic effects proportional to concentration. However, for this MTS assay performed on L3.6pl pancreatic cancer cells, there is no evidence of enhanced cytotoxicity for Gem-TA. Instead, these results indicate that Gem-TA and Gem are equally effective. The contradiction between these results and the literature might stem from either the type of cytotoxicity tests performed or the differences between individual cells lines. Protein inhibition testing would need to be performed on the L3.6pl cell line to further elucidate the reason for this difference.

### 8.3.4 Therapeutic Efficacy of the CIT-NpS

As explained above (Section 8.3.3), Gem-TA was proven at least as effective as Gem in inhibiting cell growth; now the therapeutic efficacy of the entire CIT-NpS complex was preliminarily assessed. Again, an MTS assay was performed on pancreatic cancer L3.6pl cells, this time with the CIT-NpS mixed in media as compared with Gem-TA free drug mixed in media. Surprisingly, the CIT-NpS did not perform as well as the free Gem-TA drug. This finding is in contrast to a study from Patra et al.[6] They used the same EGFR antibody (C225) and native Gem loaded on gold nanospheres. Both their *in vitro* and *in vivo* data showed that the bioconjugated gold carriers were significantly more effective than the antibody or Gem used alone or in combination against pancreatic cancer. One possible explanation for the contradictory results is that in the data presented here, the concentration of drug on the surface of the CIT-NpS could be in error. None of the analytical techniques used (EDS, XPS, or UV-vis) could quantitatively determine drug attachment. Another reason for the variation in the studies could be use of different

pancreatic cells lines. Patra et al used AsPC-1, MIA Paca-2, and PANC-1 cell lines, while the L3.6pl pancreatic cancer line was used here. Finally, another explanation is that silver is actually having a survival benefit for cells. This explanation may seem incredible given the body of literature claiming that silver is toxic.[13, 14] However, in most of the MTS assays run to date (data not shown) in which cells were mixed with PEGylated or antibody conjugated silver nanoplates, the cells were up to 20% more viable than controls. This observation appeared to be within experimental error and was thus ignored for years. However, research done by Dr. Levi of Wake Forrest University seems to support the conclusion. Dr. Levi was using silver nanoplates to help prevent infection while sealing wounds. She induced slight hyperthermia in the wound region using continuous wave lasers in conjunction with silver nanoplates. Her unpublished *in vitro* tests also showed a survival benefit when silver nanoplates were present. Ongoing investigation into this topic is underway to determine if these results are credible, but they could indicate that silver is (1) stressing the cell and causing increased activity or (2) having a strong antimicrobial effect that relieves the cell and allows for increased proliferation. Regardless of the cause, the CIT-NpS was not as effective a drug carrier as expected and more tests are required to understand this phenomenon.

### 8.3.5 CIT-NpS Cytotoxicity under Pulsed Laser Exposure

Another reason that the CIT-NpS was not as effective as the free Gem-TA drug could be that drugs were so tightly bound to silver that they did not interact with cells in the same way as free drugs. To test this theory, again MTS assays were run on L3.6pl cells that were mixed in separate wells with the CIT-NpS and a-EGFR/mPEG-SH conjugated silver nanoplates in media. Light energy of various fluences, 1000 pulses of laser irradiation at peak nanoplate resonances, were exposed to the wells to determine if

photoacoustic laser pulses could be used to trigger drug release from the silver nanoplates and enhance therapeutic efficacy. Unfortunately, cell viability at 48 hr post laser exposure remained constant for all conditions tested, as shown in Fig 8.9. This result raises three considerations. First, it is inconclusive whether these laser pulses enhanced drug delivery. The same MTS assay was repeated for an incubation period of 24 hr (data not shown), and losses in cell viability were only barely apparent at that early stage. Thus, since Gem takes so long (at least 48 hr) to exhibit anti-proliferative effects, this test likely cannot accurately measure if drugs were dropped in the 48 hr period by the laser in the beginning or by cell activity slightly later. Conjugation of a fast-acting drug to silver nanoplates and using them in combination with a different assay that can measure cell death would be a better way of testing whether laser pulses can trigger drug release. Secondly, photoacoustic laser pulses had no cytotoxic effect. For example, the cells exposed to only a-EGFR/mPEG-SH conjugated silver nanoplates in media were at least as viable as controls regardless of laser energy. Lastly, for the cases where a-EGFR/mPEG-SH conjugated silver nanoplates were used, they were all more viable than controls. This observation gives credence to the discussion in section 8.3.4 about how silver is somehow enhancing cell viability relative to controls. Therefore, while this test did not show triggered drug release, it did prove that photoacoustic pulsed irradiation of nanoplates had no toxic effect on cells.

### 8.3.6 CIT-NpS Cytotoxicity under Continuous Wave Laser Exposure

Even though the CIT-NpS was not as effective a drug carrier as expected, it was an excellent photothermal agent. In this test, the MTS assay was used on pancreatic cancer L3.6pl cells after incubation with a-EGFR/mPEG-SH conjugated silver nanoplates in media. The MTS assay measured cell viability 48 hr post continuous wave laser

exposure. As shown in Fig 8.10, significant hyperthermic effects were prevalent starting at 2 min of laser exposure. Therefore, a-EGFR targeted silver nanoplates interacted with cells, continuous wave lasers were used to heat the area surrounding the nanoplates, and this heat caused significant cell damage. When targeted to cancer cells, this photothermal damage strategy can be highly effective using silver nanoplates.

### 8.3.7 CIT-NpS Stability

Using Ag nanoplates for any type of biological or imaging contrast agent application requires that they are stable in saline solutions. While Ag has excellent optical properties for use as a sensor, it is silver's lack of stability in salt solutions that has largely limited its use in biomedical applications. As shown previously,[15] when Ag nanoplates are built, the face of the plate takes on the lowest possible energy surface, the (111) plane. A high resolution transmission electron micrograph (TEM) of a silver nanoplate face is shown in Fig 8.11a. The electron diffraction pattern from that same nanoplate face is shown in Fig 8.11b where the first ring of intense spots can be attributed to the (220) Bragg reflections with a lattice spacing of 1.44 Å. This nanoplate surface is most unstable at the tips where its electromagnetic field enhancements are greatest.[16] Usually it is the loss of these tips that causes the longitudinal surface plasmon resonance (LSPR) peak to left-shift (to lower wavelengths, also termed blue-shift), even when Ag nanoplates are suspended in water over time. Therefore, the synthesis technique employed for silver nanoplates synthesis purposefully did not generate perfect Ag nanoplates tips, but instead allowed for rounded tips as shown in Fig 8.11a to be produced. The loss of the tips happened twice in the protocols presented. The first rearrangement of atoms on the silver surface happened during the wash step when Ag nanoplates were removed from their growth media. Centrifuging is a technique known to

left-shift the resonance peak of Ag nanoplates.[17] Secondly, the nanoplates are kept in foil at room temperature overnight in water prior to use. The nanoplates do left-shift ~40-50 nm while sitting overnight in water. However, they stabilize after that and can be kept in water without shifts in resonance for up to two weeks at 4°C.

Employing a synthetic method that generated rounded nanoplate tips was only the first step to solving the stability issue. Even Ag nanoplates with rounded tips will degrade and dissolve in salt solutions without additional passivation. Fortunately, grafting molecules like antibodies and PEG to the surface of silver further passivated the nanostructure. As shown in Fig 8.12, silver nanoplates can be kept for days in media at 37°C in a humidified incubator with little change in resonance. Comparing the data from Figs 8.12a and 8.12b, silver nanoplates with Gem-TA conjugated were less stable than silver nanoplates with only a-EGFR and mPEG-SH. Thus, drug conjugation can make the nanoplates less stable.

Interactions with cells strongly affected nanoplate stability. In the graphs shown in Figs 8.12c and 8.12d, two different cell lines were mixed with ~$1.5x10^{11}$ nanoplates per ml in media. These wells were not exposed to laser irradiation. They were left to incubate with the cells for up to 96 hr; UV-vis spectra of the wells were taken at various time points. Interestingly, the L3.6pl cells caused a 100 nm left shift in the spectrum, indicating that silver was degrading and the aspect ratio of its longitudinal to transverse dimensions was decreasing. Correspondingly, the peak at ~400 nm in Fig 8.12c at 46 hr indicates that formation of silver nanospheres increased over time. Conversely, the non-cancerous HPNE pancreatic cell line caused no such left shift in the spectrum (Fig 8.12d). Instead, the significant loss in the longitudinal peak was caused by cell induced aggregation of silver. Correspondingly, no increase in the peak at 400 nm associated with formation of silver nanospheres was observed. These results suggest that (1) silver can be

degraded by cells and (2) that silver could be used as a sensor for cell interaction. The cells that overexpress a-EGFR, such as L3.6pl cells, will interact with the silver, ultimately causing a left shift in the spectrum that can be detected using photoacoustic techniques. Thus, silver nanoplates could be used to sense cellular interactions non-invasively, *in vivo*.

Using silver nanoplates as a sensor will only be possible if photoacoustic laser pulses do not also induce shape changes in the silver. Photoacoustic laser pulses last 4-6 ns and can deposit so much energy in a nanoparticle that it transiently heats to hundreds of degrees Celsius.[18] Since nanoparticle melting temperatures can be hundreds of degrees lower than the bulk metal's melting temperature, nanoparticles can melt and change shape in response to photoacoustic laser pulses. To test the structural stability of Ag nanoplates to these laser pulses, PEGylated silver nanoplates were suspended in media and placed in a black 96 well plate. The wells were subjected to 1000 pulses of varying laser fluences. Unfortunately, even the smallest laser fluence tested (2.5 $mJ/cm^2$) had a left-shifting effect on the silver nanoplates as shown in the UV-vis spectra in Fig 8.12e. Furthermore, two sizes of silver nanoplates were tested in this manner, one S3 batch and one S4 batch corresponding to Figs 8.12e and 8.12f, respectively. Both batches demonstrated instability in response to laser irradiation (note that the 5 $mJ/cm^2$ plot in Fig 8.12f is not missing, but directly under the 10 $mJ/cm^2$ plot). Therefore, silver nanoplates should be stabilized if they are to be used for photoacoustic imaging in vivo. One method of stabilization already proposed for gold nanorods is silica coating. The connection between silica and gold makes it more difficult for the surface atoms to rearrange under laser irradiation.[19, 20] Similar methods could be employed to further stabilize silver nanoplates.

## 8.4 CONCLUSIONS

A thiolated version of Gemcitabine, Gemcitabine-Thioamide, was synthesized and successfully grafted to silver nanoplates. By grafting a-EGFR, Gem-TA, and mPEG-SH in sequence, the final CIT-NpS was built. Surprisingly, the CIT-NpS's performance as a drug carrier was seemingly not as effective as that for the free drug. Methods for accurate quantification of drug on the nanoplate surface are needed to allow for direct comparison with free drugs; however, the CIT-NpS showed slightly less therapeutic efficacy in the cell viability assay performed. Cell viability assays performed with cells exposed to silver nanoplates and photoacoustic laser pulses showed that photoacoustic pulses caused no toxicity to cells. However, silver nanoplates exhibited instability under pulsed laser irradiation. Therefore, techniques to stabilize their structure, such as silica coating, are needed. Finally, silver nanoplates were excellent photothermal agents, causing cell death after 2 min of continuous wave laser exposure. Overall, the nanoplates have potential since they can interact with cells for photothermal therapy applications as well as sensor applications. The LSPR of silver nanoplates left-shifted in response to interactions with pancreatic cancer cells; while normal pancreatic cells caused a decrease in resonance, but no left or right shift. These shifts are indicative of cellular interactions with nanoparticles that can be detected non-invasively *in vivo* using photoacoustics. Therefore, silver nanoplates can be employed as a degradable, cellular sensor. In summary, though the CIT-NpS is moderately effective as a drug carrier; the multifunctional aspects of its design make it an excellent nanoplatform with possible uses as a photothermal agent and degradable sensor.

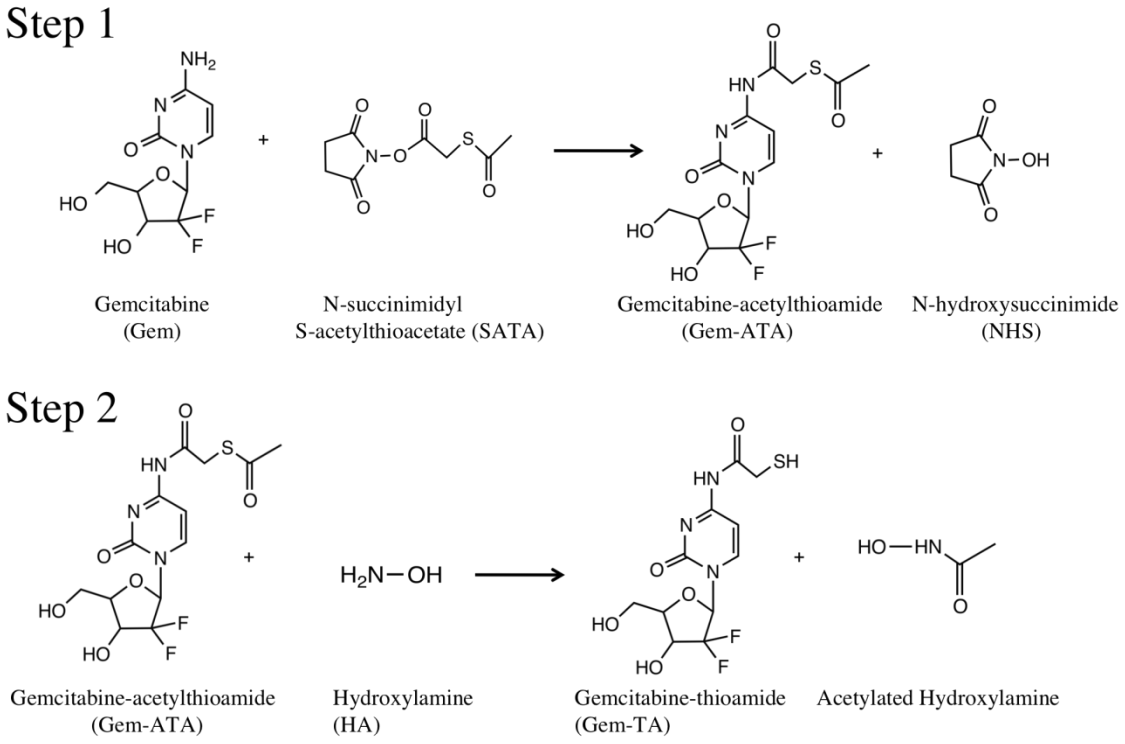


Figure 8.1: Reaction scheme for thiolating Gemcitabine to create Gemcitabine-Thioamide (Gem-TA).

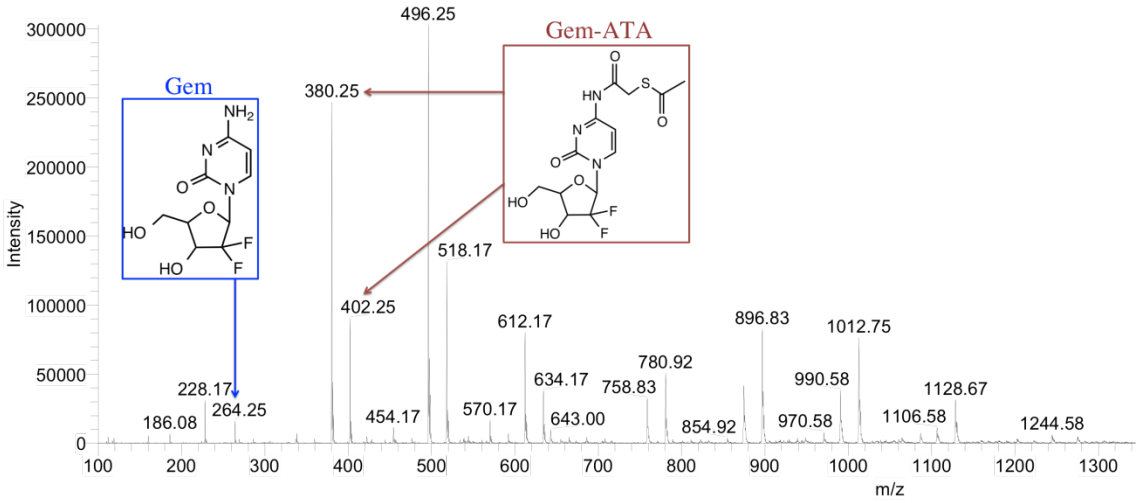


Figure 8.2: Mass Spectroscopy results showing formation of the Gem-ATA prodrug. The large peaks at 496.25 and 518.17 m/z are unreacted Gem and SATA flying as one charged mass with either $H^+$ or $Na^+$.

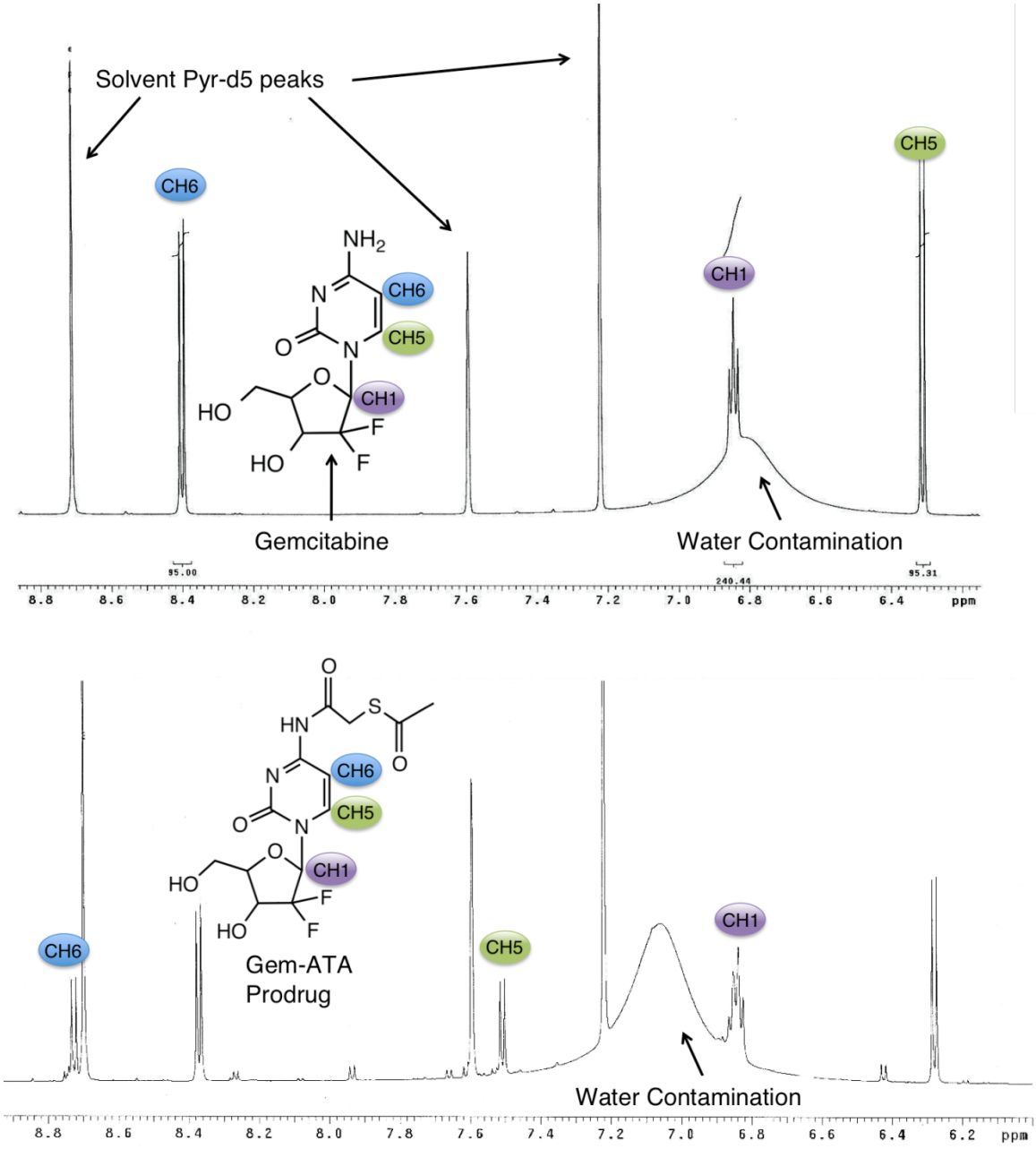


Figure 8.3: NMR of Gem (top) and the Gem-ATA prodrug (bottom). The H shifts that are most noteworthy for Gem-ATA formation are the CH6, CH5, and CH1 as labeled in blue, green, and purple, respectively. The Gem-ATA spectrum shows major shifts in the doublet peaks associated with the CH6 and CH5 hydrogens. The CH1 position shows two overlaid triplets in the Gem-ATA spectra showing that both Gem-ATA and Gem are both present in the sample.

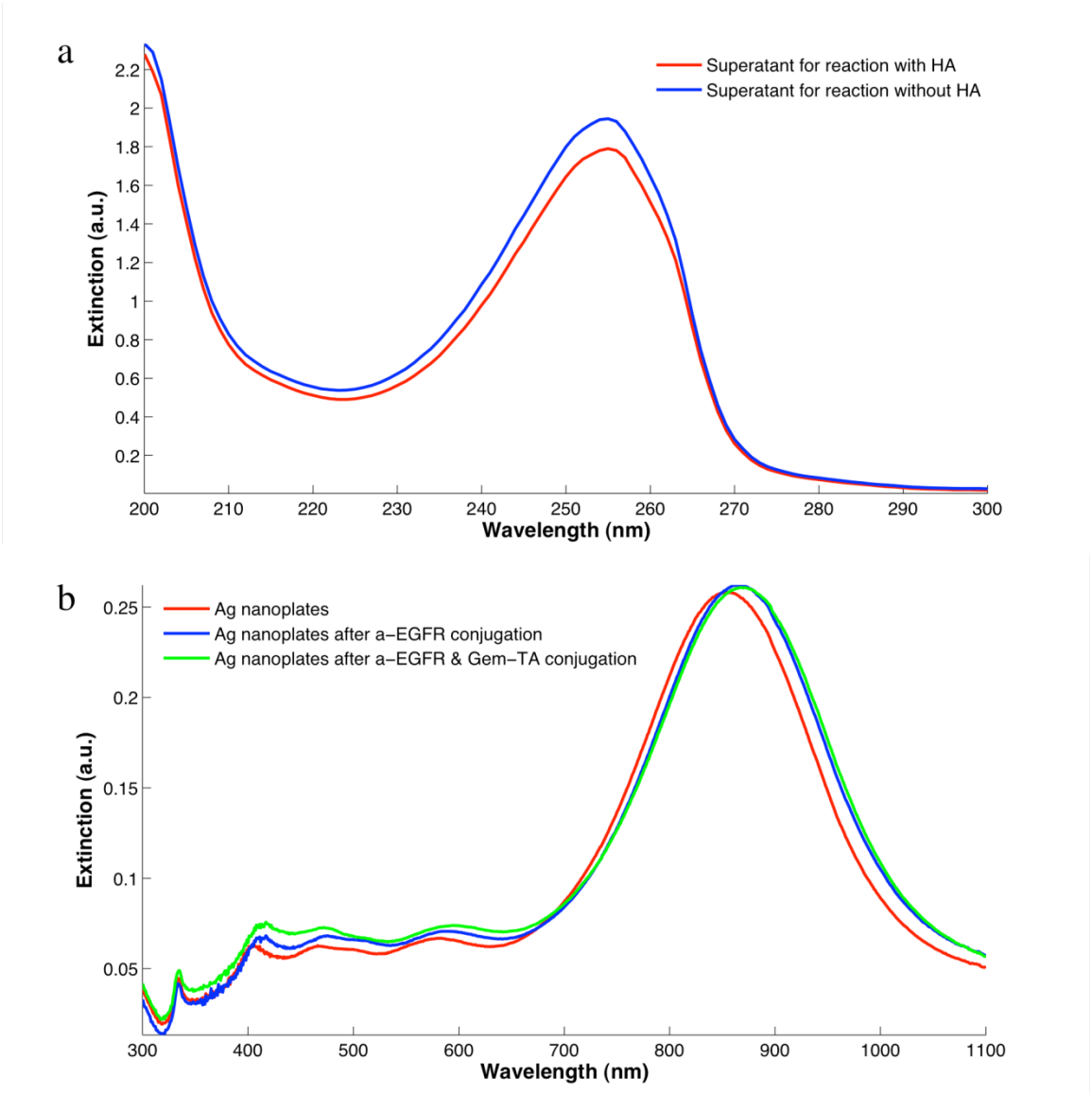


Figure 8.4: UV-vis spectrographs showing (a) the difference in the supernatant after conjugation to Ag nanoplates for a Gem-ATA reaction staged with HA and without HA, and (b) Ag nanoplates after conjugation of antibodies and Gem-TA prodrugs.

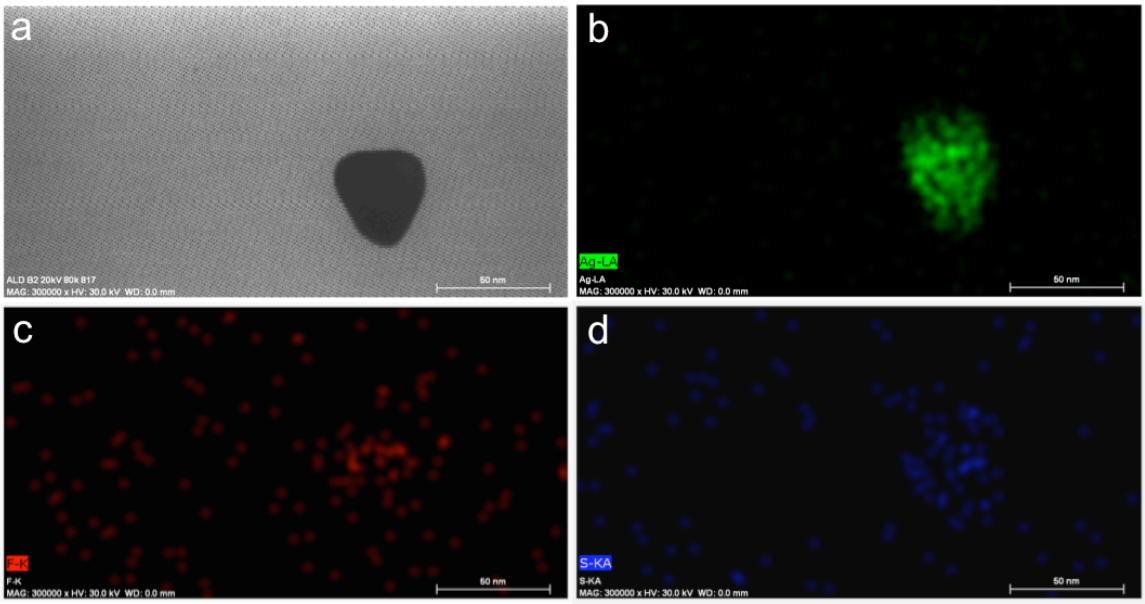


Figure 8.5: Energy-dispersive X-ray spectroscopy results captured using a scanning transmission electron microscope showing a silver nanoplate (a) with an elemental map of the elements Ag (b), F (c), and S (d). The coregistry of F and S with the location of the silver nanoplate in the image shows that Gem-TA is attached to the silver nanoplate.

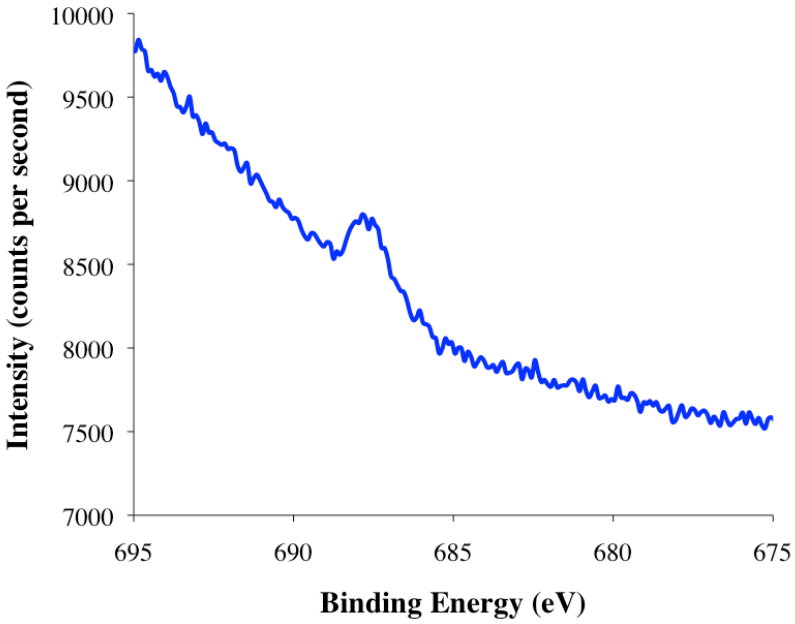


Figure 8.6: X-ray photoelectron spectroscopy results showing the detection of F 1s at a binding energy of 688 eV on the surface of a silver nanoplate sample conjugated to Gem-TA.

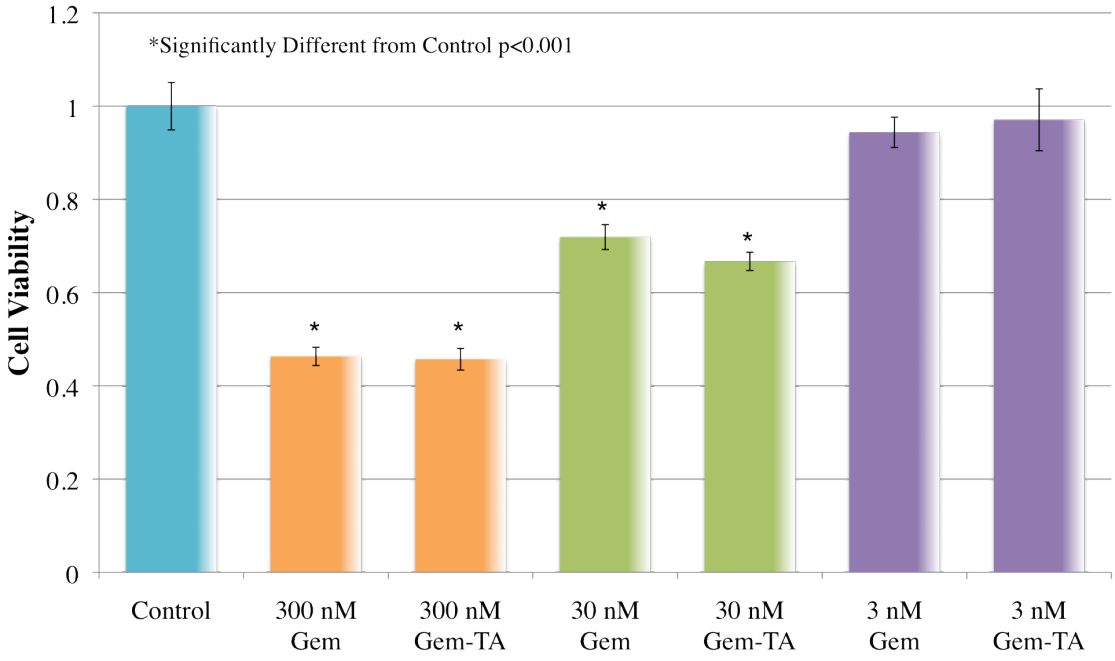


Figure 8.7: A comparison of L3.6pl cell viability after 48 hr of incubation with various concentrations of Gem and Gem-TA in their media.

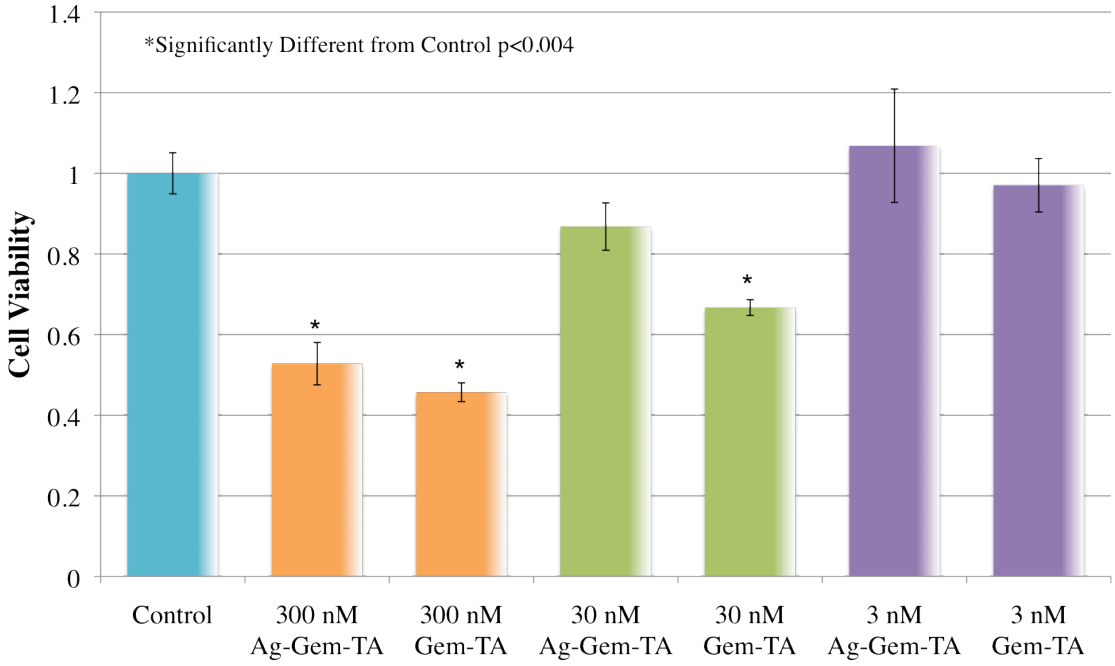


Figure 8.8: A comparison of L3.6pl cell viability after 48 hr of incubation with various drug concentrations either attached to silver nanoplates (Ag-Gem-TA) or free (Gem-TA) in the media.

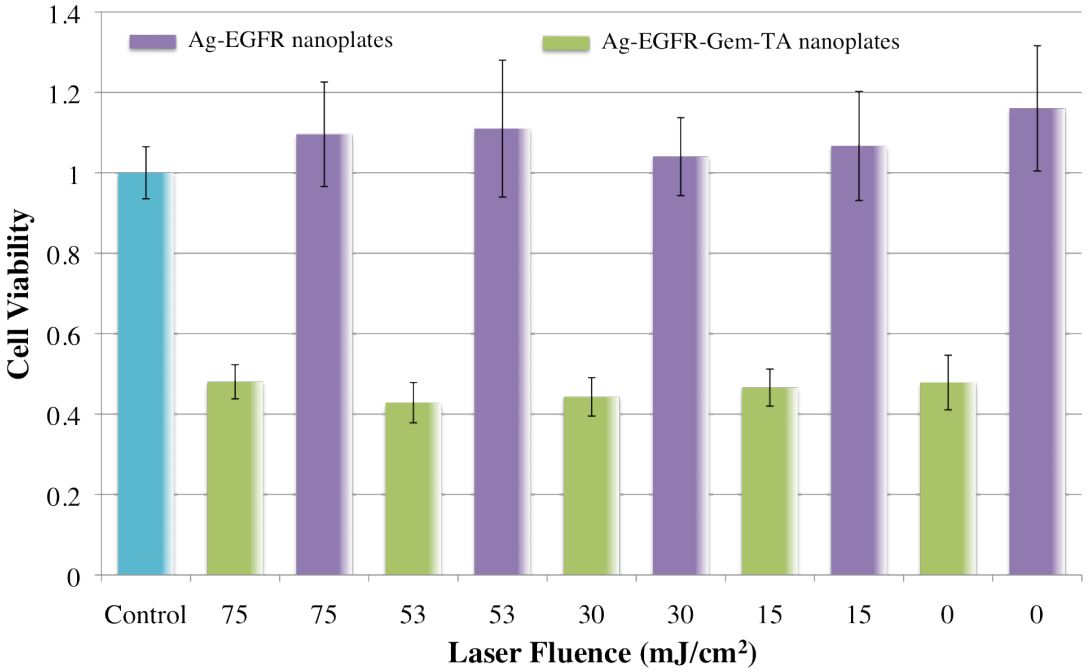


Figure 8.9: A comparison of L3.6pl cell viability after 1000 laser pulses at various light fluences. Cell viability was measured 48 hr after pulsed laser exposure for cells mixed with nanoplates conjugated to EGFR (Ag-EGFR) or nanoplates conjugated to EGFR and Gem-TA (Ag-EGFR-Gem-TA, 300 nM Gem-TA). The concentration of Ag nanoplates was kept constant for each condition at $1.5x10^{11}$ nanoplates per ml of media.

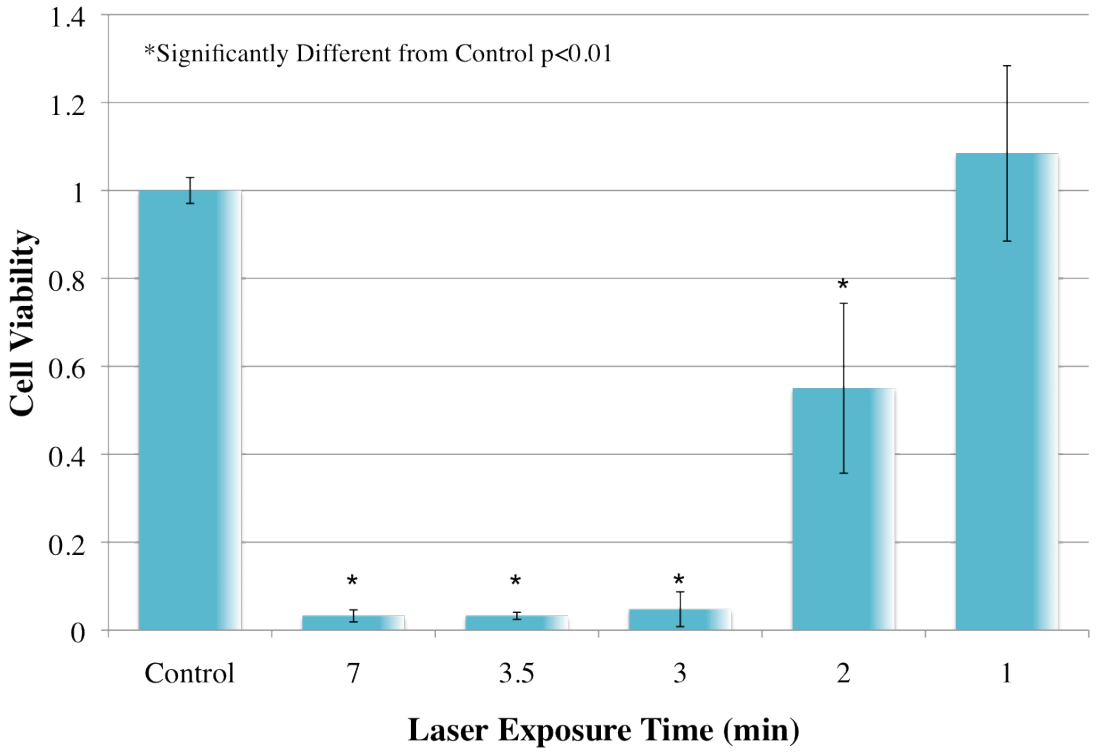


Figure 8.10: Cell viability results for L3.6pl cells mixed with EGFR conjugated silver nanoplates ($1.5x10^{11}$ nanoplates per ml of media) at 48 hr after exposure to a continuous wave laser operating at 1.3 W/cm$^2$ for various times.

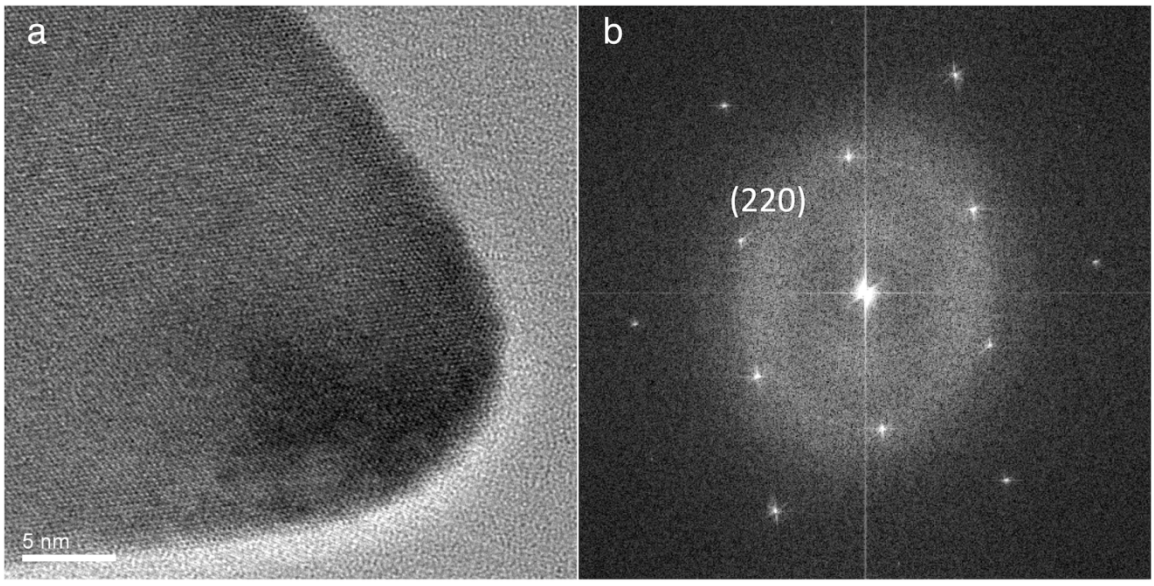


Figure 8.11: High-resolution transmission electron microscope of one Ag nanoplate (a) and its corresponding diffraction pattern (b).

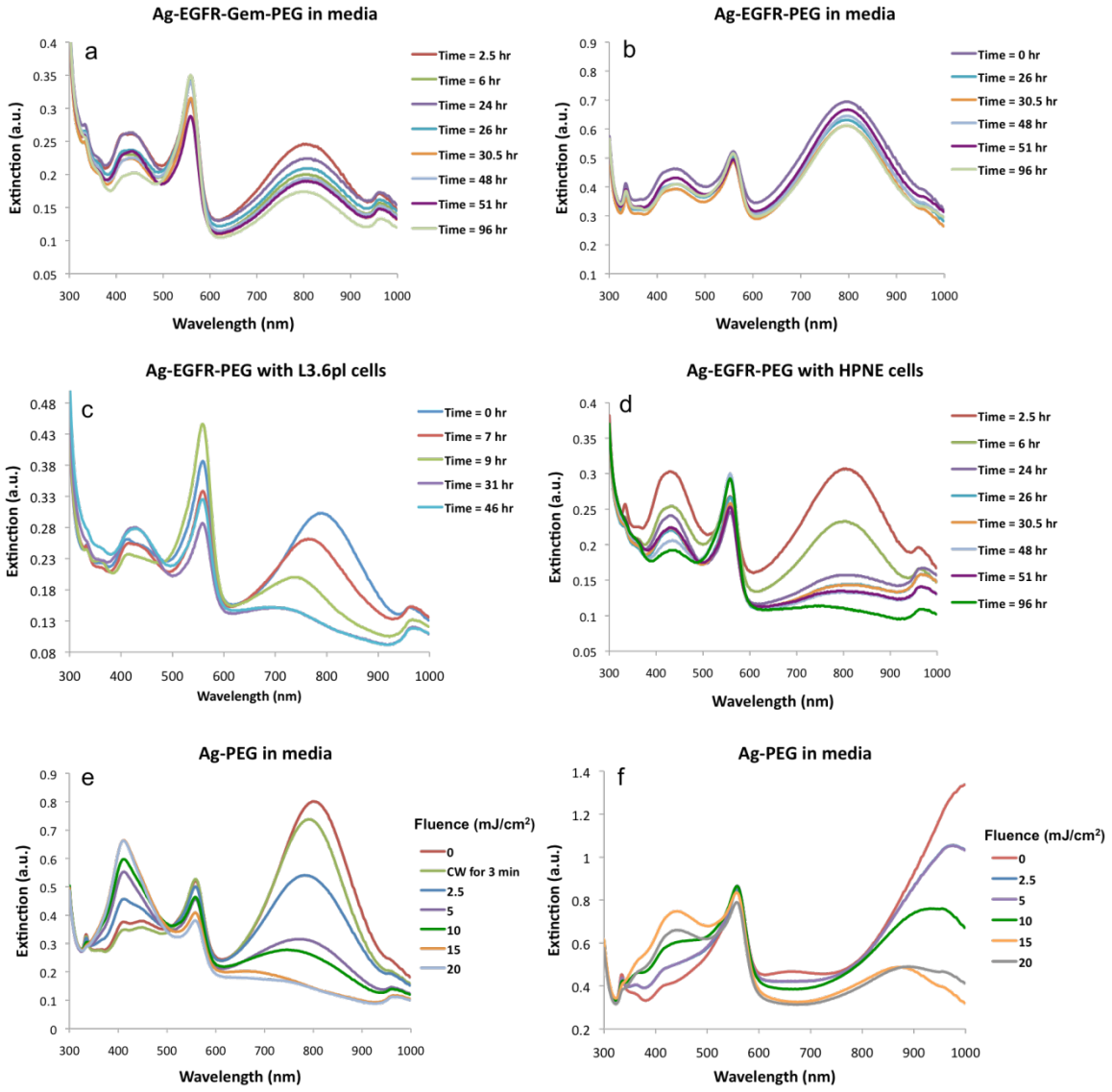


Figure 8.12: Ultra-violet to visible (UV-vis) spectrophotometry results depicting various aspects of silver nanoplate stability with either time or pulsed laser exposure. The UV-vis with time for drug loaded (a) versus non-drug loaded nanoplates (b) kept in media at 37°C for 96 hr; the UV-vis with time for non-drug loaded, but EGFR conjugated nanoplates mixed with either L3.6pl cells (c) or HPNE cells (d); the UV-vis directly after 1000 laser pulses at various fluences for two sizes of nanoplates conjugated only to PEG (e and f).

## 8.5 REFERENCES


1. E. Bria, M. Milella, A. Gelibter, F. Cuppone, M. S. Pino, E. M. Ruggeri, P. Carlini, C. Nistico, E. Terzoli, F. Cognetti and D. Giannarelli, "Gemcitabine-based combinations for inoperable pancreatic cancer: Have we made real progress?: A meta-analysis of 20 phase 3 trials," Cancer 110(3), 525-533 (2007)
2. Y. J. Chua and D. Cunningham, "Chemotherapy for advanced pancreatic cancer," Best Pract Res Clin Gastroenterol 20(2), 327-348 (2006)
3. A. Mancuso, F. Calabro and C. N. Sternberg, "Current therapies and advances in the treatment of pancreatic cancer," Crit. Rev. Oncol. Hematol. 58(3), 231-241 (2006)
4. H. Q. Xiong, K. Carr and J. L. Abbruzzese, "Cytotoxic chemotherapy for pancreatic cancer: Advances to date and future directions," Drugs 66(8), 1059-1072 (2006)
5. L. M. Demers, M. Ostblom, H. Zhang, N. H. Jang, B. Liedberg and C. A. Mirkin, "Thermal desorption behavior and binding properties of DNA bases and nucleosides on gold," J. Am. Chem. Soc. 124(38), 11248-11249 (2002)
6. C. R. Patra, R. Bhattacharya, E. Wang, A. Katarya, J. S. Lau, S. Dutta, M. Muders, S. Wang, S. A. Buhrow, S. L. Safgren, M. J. Yaszemski, J. M. Reid, M. M. Ames, P. Mukherjee and D. Mukhopadhyay, "Targeted delivery of gemcitabine to pancreatic adenocarcinoma using cetuximab as a targeting agent," Cancer Res. 68(6), 1970-1978 (2008)
7. G. T. Hermanson, Bioconjugate techniques, Academic Press, San Diego (1996).
8. A. A. Isab and M. I. Wazeer, "Synthesis and characterization of thiolate-Ag(I) complexes by solid-state and solution NMR and their antimicrobial activity," Spectrochim Acta A Mol Biomol Spectrosc (2006)
9. S. Kumar, J. Aaron and K. Sokolov, "Directional conjugation of antibodies to nanoparticles for synthesis of multiplexed optical contrast agents with both delivery and targeting moieties," Nat Protoc 3(2), 314-320 (2008)
10. S. Kumar, N. Harrison, R. Richards-Kortum and K. Sokolov, "Plasmonic nanosensors for imaging intracellular biomarkers in live cells," Nano Lett 7(5), 1338-1343 (2007)
11. M. L. Immordino, P. Brusa, F. Rocco, S. Arpicco, M. Ceruti and L. Cattel, "Preparation, characterization, cytotoxicity and pharmacokinetics of liposomes containing lipophilic gemcitabine prodrugs," J Control Release 100(3), 331-346 (2004)
12. F. Myhren, B. Brretzen, A. Dalen and M. L. Sandvold, "Gemcitabine derivatives ", (2002)

13. P. V. Asharani, M. P. Hande and S. Valiyaveettil, "Anti-proliferative activity of silver nanoparticles," BMC Cell Biol 10(65 (2009)

14. P. V. AshaRani, G. Low Kah Mun, M. P. Hande and S. Valiyaveettil, "Cytotoxicity and genotoxicity of silver nanoparticles in human cells," ACS Nano 3(2), 279-290 (2009)

15. X. Zou, E. Ying, H. Chen and S. Dong, "An approach for synthesizing nanometer-to micrometer-sized silver nanoplates," Colloids Surf. Physicochem. Eng. Aspects 303(3), 226-234 (2007)

16. L. J. Sherry, R. Jin, C. A. Mirkin, G. C. Schatz and R. P. Van Duyne, "Localized surface plasmon resonance spectroscopy of single silver triangular nanoprisms," Nano Lett 6(9), 2060-2065 (2006)

17. Y. Xia, Y. Xiong, B. Lim and S. E. Skrabalak, "Shape-controlled synthesis of metal nanocrystals: Simple chemistry meets complex physics?," Angew. Chem. Int. Ed. Engl. 48(1), 60-103 (2009)

18. C. M. Pitsillides, E. K. Joe, X. Wei, R. R. Anderson and C. P. Lin, "Selective cell targeting with light-absorbing microparticles and nanoparticles," Biophys. J. 84(6), 4023-4032 (2003)

19. Y.-S. Chen, P. P. Kruizinga, P. P. Joshi, S. Kim, K. A. Homan, K. Sokolov, W. Frey and S. Emelianov, "On stability of molecular therapeutic agents for noninvasive photoacoustic and ultrasound image-guided photothermal therapy," SPIE Photonics West 76541Q, 7564-7571 (2010)

20. Y. S. Chen, W. Frey, S. Kim, K. Homan, P. Kruizinga, K. Sokolov and S. Emelianov, "Enhanced thermal stability of silica-coated gold nanorods for photoacoustic imaging and image-guided therapy," Opt Express 18(9), 8867-8878 (2010)

# Chapter 9: Conclusions and Future Work

## 9.1 MOTIVATION

Pancreatic cancer remains an unsolved health problem, with conventional cancer treatments having little impact on disease course. In the United States, pancreatic cancer represents the fourth leading cause of cancer-related deaths.[1] In fact, for all stages of pancreatic cancer combined, the 5 year survival rate remains at a low 5%, making it arguably the most lethal of all solid tumors.[2] Chemotherapy is a common treatment for pancreatic cancer, but survival benefits from those treatments are measured only in months.[2, 3] The most effective drugs that have formed the basis of chemotherapeutic treatment for pancreatic cancer have been 5-fluorouracil (5-FU) and the more recently approved gemcitabine (Gem).[2] As with most chemotherapeutic regimens, treatment involves systemic intravenous injections. The concentration of Gem used per session is dose-limited by its cytotoxic effect on healthy bone marrow and epithelial tissue.[4] Some hypothesize that the systemic approach is ineffective for most patients because drug concentrations accumulated within the tumor itself are not high enough to realize their estimated therapeutic potential.[5]

The objective of this thesis was to create tools to improve and better understand chemotherapeutic treatment of pancreatic cancer. Thus, nanosystems were designed with a dual purpose: to carry Gem and act as imaging contrast agents for photoacoustic imaging. The strategy is that packaging drugs into nanosystem delivery vehicles will make treatment more effective. Furthermore, synthesizing the nanosystems to be multifunctional imaging contrast agents also facilitates visualization of drug delivery, allowing clinicians to assess whether proper doses of drug arrived at the diseased site. Toward this end, the combined imaging and therapy nanocage system (CIT-NS) and the

combined imaging and therapy nanoplate system (CIT-NpS) were designed, synthesized, and characterized in this work. Specifically, Chapters 2 and 6 explained the design of each nanosystem in depth. Chapter 3 and 7 demonstrated that both nanosystems could act as imaging contrast agents for photoacoustic imaging in *ex vivo* and *in vivo* scenarios. Finally, Chapters 4, 5 and 8 demonstrated that synthesis of these nanosystems as drug carriers and imaging contrast agents was possible. Throughout each chapter, discussions of the advantages and limitations of each respective system was presented; additionally, a critical overview and comparison of these nanosystems from a clinical perspective is provided below.

### 9.2 THE CIT-NS VERSUS THE CIT-NPS: CLINICAL RELEVANCE

The CIT-NS and the CIT-NpS are complex nanosystems built as drug carriers and photoacoustic imaging contrast agents. The clinical advantage of these systems could be the ability to visualize drug delivery to pancreatic cancer *in vivo*, non-invasively. Furthermore, the nanosystems can act as both photothermal therapy agents and as IR-sensitizing agents, providing clinicians even more therapeutic options.

The ideal CIT-NS consisted of a polymer core of poly(lactic-co-glycolic) acid (PLGA) with encapsulated drugs covered with a nanocage of silver. Targeting and stabilizing agents were grafted to the exterior of the nanosystem (Chapter 2, Fig 2.1). The CIT-NS incorporating the model drug doxorubicin (DOX) was successfully synthesized (Chapter 4). Analysis of the *in vitro* properties of the system, such as control over the drug release profile and broad extinction in the near infrared spectrum, indicate that the nanosystem has potential for *in vivo* applications. However, encapsulation of gemcitabine (Gem) or a Gem prodrug (Gemcitabine-$N^4$ Oleoyl Amide) in PLGA was unsuccessful (Chapter 5). Therefore, different encapsulation methods will be required for successful

encapsulation, or a different chemotherapeutic drug for treatment of pancreatic cancer can be used. One such drug, paclitaxel (Taxol), is known to be effective against pancreatic cancer and has been shown to encapsulate in PLGA nanoparticles.[6] Other solutions to this problem could involve updating the CIT-NS design. For instance, the polymer used for encapsulation could be changed to one unaffected by Gem, or liposomes[7] could be used as the core of the CIT-NS. New designs for the CIT-NS could also be considered that incorporate silver and Gem without the polymer, such as the CIT-NpS.

The CIT-NpS consisted of a silver nanoplate with a targeting antibody, a Gem prodrug, and poly(ethylene glycol) (PEG) molecules grafted to its surface (Chapter 6, Fig 6.1). Preliminary results indicated that silver nanoplates were excellent photoacoustic imaging contrast agents (Chapter 7). They were easily synthesized to absorb light from the visible to the near infrared spectrum. Finite difference time domain (FDTD) modeling confirmed that they have absorption cross-sections comparable to, and in some cases greater than, conventional gold contrast agents. Silver nanoplates bioconjugated to antibodies showed effective cell labeling and uptake in a subcutaneous tumor model of pancreatic cancer *in vivo*. Surprisingly, the performance of CIT-NpS as a drug carrier was seemingly not as effective as that for the free drug (Chapter 8). Methods for accurate quantification of drug on the nanoplate surface are needed before a precise comparison can be made; however, the CIT-NpS showed slightly less therapeutic efficacy in the cell viability assay performed. Cell viability assays performed with cells exposed to silver nanoplates and photoacoustic laser pulses showed that photoacoustic pulses caused no toxicity to nanoparticle-labeled cells. Finally, silver nanoplates were excellent photothermal agents, causing cell death after 2 min of continuous wave laser exposure. Overall, though the CIT-NpS is moderately effective as a drug carrier, the multifunctional

aspects of its design make it an excellent nanoplatform with possible uses as a photothermal agent and degradable sensor.

### 9.2.1 Nanosystem Size and Drug Loading

The CIT-NpS may be superior to the CIT-NS since it has the advantages of higher absorption cross section per particle, sharper and more defined LSPR peaks, simplified synthesis, and smaller size that allows for better accumulation and intracellular trafficking at a tumor site. However, the large disadvantage of the nanoplate system is its reduced drug loading capacity compared to the CIT-NS. Achieving a clinically effective dose using the CIT-NS is feasible; while the loading of Gem-TA in the CIT-NpS at 300 nM concentrations for ~$1.5x10^{11}$ nanoplates/ml cannot provide a similar dosage without the injection of excessive amounts of silver. However, the use of other drugs such as Taxol, that require much lower clinical dosages, should be considered for both nanosystems to enhance clinical relevance. Furthermore, the CIT-NpS is more difficult to stabilize due to its high-energy surface that is prone to dissolution and side reactions if not properly passivated. Therefore, a critical design consideration for drug carrier nanosystems in general is the tradeoff between size, drug loading, and stability.

### 9.2.2 Triggered Drug Release

Triggered drug release was not definitely proven for either nanosystem. The cell viability assays used in combination with the CIT-NpS were not definitive. Furthermore, inducing shape change of the CIT-NS system using pulsed lasers was attempted (data not shown) and no shape change was observed. However, using different tests, it is still possible to drop drugs using lasers as has been shown with other nanosystems.[8-10] For instance, it is likely that the pulsed laser used for these tests did not facilitate drug release from the CIT-NpS or shape change of the CIT-NS. Continuous wave lasers that create

sustained heating of the nanosystems could create considerable drug detachment, however. Conjugating dyes or other fast-acting drugs to the nanosystems could provide better experimental conditions for drug release testing. Performing the pulsed laser tests again with those molecules in the nanosystems would provide more definitive proof of triggered drug release.

### 9.2.3 Nanosystem Stability

Nanosystem stability in biological solutions is a critical parameter for clinical application of the investigated system. The CIT-NS shape and optical properties were stable under all conditions tested; however, the CIT-NS has a short shelf life because its large size leads to aggregation in solution. The nanoplate system has longer shelf life (up to two weeks), but suffers from other types of instability. The CIT-NpS exhibited shape instability under pulsed laser irradiation; therefore, techniques to stabilize nanoplate structure, such as silica coating[11], are needed. A preliminary experiment was performed to assess the feasibility of coating PEGylated silver nanoplates with silica. The silica coating was performed using the addition of tetraethyl orthosilicate under basic conditions as previously reported.[12] Energy-dispersive X-ray spectroscopy (EDS) mapping measurements of a silica-coated silver nanoplate is shown in Fig 9.1. Signals for Si and Ag map onto the nanoplate, however, the nanoplate was unstable under the electron beam and was degraded during the measurement. This degradation likely happened because the particles were not sufficiently cleaned from the buffer before drop casting on TEM grids. Nonetheless, this preliminary experiment showed that silica coating is possible. Testing of enhanced stability of silica-coated silver nanoplates under pulsed laser irradiation is a next step for future work.

In addition to instability under pulsed laser irradiation, the CIT-NpS was also unstable upon prolonged cell exposure. This instability is an exciting finding since it infers that silver nanoplates could be used as a cellular biosensor (Chapter 8). For example, the LSPR of silver nanoplates left-shifted in response to interactions with pancreatic cancer cells; while normal pancreatic cells caused a decrease in resonance, with no left or right shift. These shifts are indicative of cellular interactions with nanoparticles and can be detected *in vivo,* non-invasively using photoacoustics. Therefore, silver nanoplates can be employed as a cellular sensor.

Nanoplate instability with prolonged exposure to cells *in vitro* also indicates that silver is degradable. Silver nanoplates as a non-toxic, biodegradable sensor could be an exciting discovery for imaging diagnostics applications. However, *in vivo* tests using silver showed significant accumulation of silver after systemic injection in the tumor, liver, spleen, and feces. Thus, organ specific toxicity associated with degradation of silver in the liver and spleen must be addressed prior to widespread adoption as a photoacoustic imaging contrast agent. Accumulation of silver in feces following systemic injection suggests that this is one mechanism of clearance.

Overall, instability of the nanoplate system presents both advantages and disadvantages. Instability in response to pulsed laser irradiation could degrade photoacoustic signals. However, future work on silica coating of the nanoplates could alleviate this concern. Instability in response to the cellular environment could provide significant opportunities such as using the nanoplates as exogenous, biodegradable sensors.

### 9.2.4 Silver versus Gold

Finite difference time domain (FDTD) simulations performed using Lumerical software corroborates earlier fidnings[13] that longitudinal surface plasmon resonances (LSPR) of silver are stronger and sharper than gold (Fig 9.2). However, for photoacoustic imaging enhancement, it is the absorption cross section of the nanoplate that is most important. For plate sizes with aspect ratios below 90 nm edge length by 12 nm thickness, the absorption cross-section of silver nanoplates exceeds that of gold. However, as illustrated in Fig 9.2, as the plate aspect ratio increases, the absorption cross-section for the gold nanoplates exceeds that of silver. Therefore, at higher resonance wavelengths, gold is more advantageous to use as a photoacoustic contrast agent (assuming a nanoplate shape). Since the absorption cross section of silver and gold vary with respect to size, the best metal to use for nanosystems like the CIT-NS and CIT-NpS will partially depend on the spectral range in which imaging will be conducted.

An even more important factor than the optical properties of silver versus gold, is the biological reaction to one metal or the other. The biocompatibility of gold has been well documented.[14-16] However, complete clearance of gold from the body is unlikely. Silver has been documented as toxic[17, 18] in the form of a salt (silver nitrate) or small 5 nm spherical shapes. Results presented here contradict those findings for silver. In fact, for the five cell lines tested (2 pancreatic cancer lines, 1 breast cancer line, and 2 normal pancreatic lines), silver nanoplates could not be concentrated to a level that showed cytotoxic effects using the MTS assay. Therefore, a size dependent toxicity of silver nanoparticles might exist; but the topic requires further exploration. Assuming that silver is not as toxic in nanoplate form, the real difference between silver and gold is biodegradability. The instability of silver in the body could be used to advantage in cellular sensor applications with this metal. Therefore, using silver versus gold in

nanosystems like the CIT-NpS is not a clear choice. Nanosystem stability, LSPR effects, and biocompatibility should all be considered in the design.

## 9.3 Future Directions for Nanosystems to Treat and Image Pancreatic Cancer

This thesis focused on packaging Gem in or on nanosystems for treatment of pancreatic cancer with some success. Drugs like Taxol are several times more effective in killing pancreatic cancer cells *in vitro* than Gem. However, Taxol has never been approved for pancreatic cancer treatment because the dose required for systemic injections is overly toxic to healthy tissue. A potent drug like Taxol that shows promise therapeutically in cell culture is a perfect candidate for nano-vehicle delivery. Nanosystems have the potential to deliver drugs to diseased tissue while leaving healthy tissue largely unaffected. Therefore, testing this potential using nanosystems like the CIT-NS or CIT-NpS with encapsulated Taxol would be an excellent topic for future work.

A major contributor to the lack of chemotherapeutic efficacy in pancreatic cancer is the tumor's underdeveloped vascular system. Drugs do not reach the tumor in high enough concentrations to be beneficial since the vasculature is not robust. Furthermore, a pancreatic cancer mass actually has very few pancreatic cancer cells. Pancreatic cancer cells induce the formation of stromal cells in the tumor area, and these stromal cells form the bulk of most pancreatic cancer masses. Therefore, a two-pronged strategy might be needed to achieve a therapeutic benefit using nanoparticles as drug delivery vehicles to fight pancreatic cancer.

Nanosystems still have to use the existing vasculature to be delivered in large quantities to the tumor. Ultrasound can assist in this process. Therefore, the first part of the strategy would employ highly focused ultrasound to create pores in the existing

vasculature of the tumor after systemic nanoparticle injection. This procedure will allow for increased accumulation of the nanosystem in the tumor. The second part of the strategy would use nanosystems with grafted antibodies meant to target receptors on the surface of stromal cells in the mass, rather than upregulated receptors on the surface of pancreatic cancer cells. No such antibody target for stromal cells has been created that would be specific to the stromal cells generated in pancreatic cancer, but researchers in the Pancreatic Cancer Research Group at M.D. Anderson Cancer Center are actively searching for them.

Lastly, accurate animal models of pancreatic cancer are needed to test if these nanosystems have potential in humans. The best model available to date is an orthotopic pancreatic cancer mouse model. The work presented here showing *in vivo* uptake of silver nanoplates in a mouse model of pancreatic cancer was a subcutaneous model. The vasculature formed in subcutaneous models is different than that formed in orthotopic models. Therefore, future work using orthotopic pancreatic cancer mouse models to test the efficacy of Taxol loaded nanosystems targeted to stromal cells is an excellent future project. Attempts to deliver gold nanospheres to orthotopic pancreatic tumors in mice has shown some success,[19] so this approach is promising.

### 9.4 Summary of Contributions to the Field

The originality of this thesis is given by the study of the CIT-NS and CIT-NpS, which represent compositions of matter never before tested nor designed. The methods of synthesis and characterization outlined in this work will allow future researchers to recreate or build upon the current designs. Although explanations provided here focus on applicability of these nanosystems for pancreatic cancer, the nanosystems are platform technologies, from which several types of cancer could be treated and imaged. Also

introduced here is the idea of using nanotechnology to help visualize drug delivery. The combination of photoacoustic imaging with these nanosystems presents a new tool for clinicians. Better imaging of the tumor and quantification of drug delivery are both possible with this technique.

Also described in this thesis were steps towards understanding silver nanostructures, which revealed several new findings that contradict current literature. For instance, passivated silver nanostructures are non-toxic to several cancerous and non-cancerous cell lines. Furthermore, silver is biodegradable and could be considered instead of gold for applications such as photothermal therapy and noninvasive cellular sensing. Although future research is required to fully investigate the clinical potential of these systems for pancreatic cancer, the work presented in this dissertation is a significant step towards creation of multifunctional nanosystems that will enable photoacoustic imaging of drug delivery.

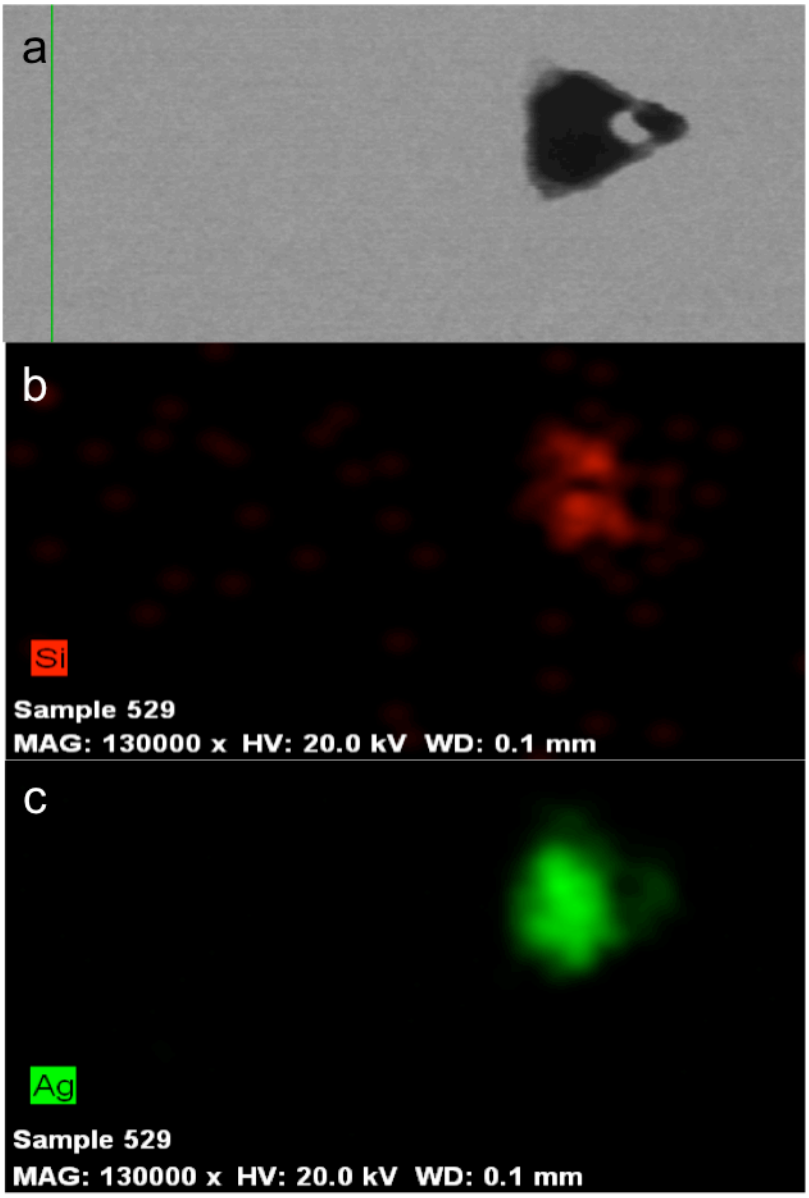


Figure 9.1: Energy-dispersive X-ray spectroscopy results captured using a scanning transmission electron microscope showing a silica-coated silver nanoplate (a) with an elemental map of the elements Si (b) and Ag (c). The coregistry of Si and Ag with the location of the silver nanoplate in the image shows that Gem-TA is attached to the silver nanoplate.

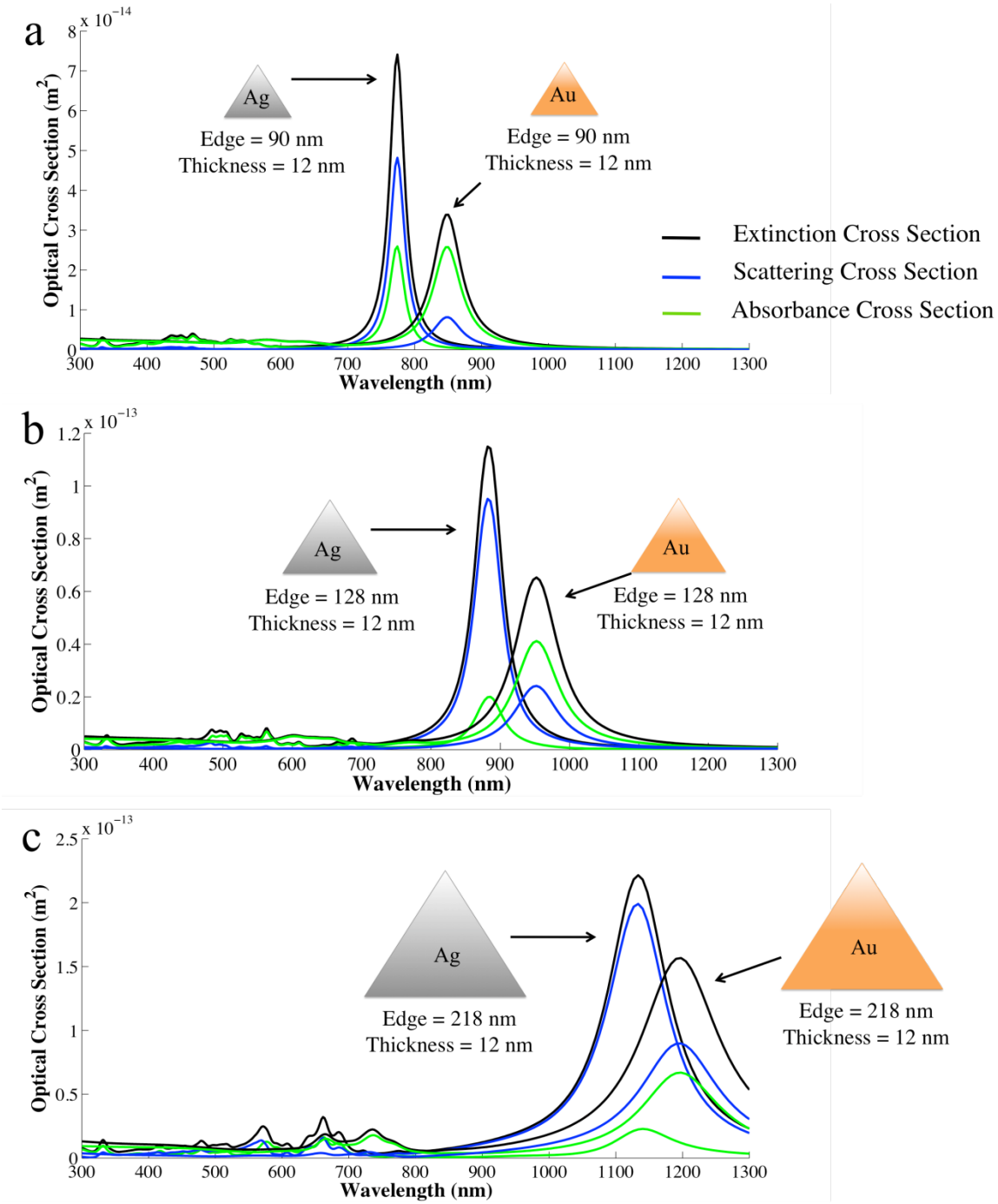


Figure 9.2: Finite difference time domain (FDTD) modeling of the extinction, scattering, and absorption cross-sections for 90x12 nanoplates (a), 128x12 nanoplates (b), and 218x12 nanoplates (c) for silver and gold.

## 9.5 REFERENCES


1. N. J. Nelson, "Pancreatic Cancer Research Matures," J. Natl. Cancer Inst. (2007)
2. E. Bria, M. Milella, A. Gelibter, F. Cuppone, M. S. Pino, E. M. Ruggeri, P. Carlini, C. Nistico, E. Terzoli, F. Cognetti and D. Giannarelli, "Gemcitabine-based combinations for inoperable pancreatic cancer: Have we made real progress?: A meta-analysis of 20 phase 3 trials," Cancer 110(3), 525-533 (2007)
3. H. R. Cardenes, E. G. Chiorean, J. Dewitt, M. Schmidt and P. Loehrer, "Locally advanced pancreatic cancer: Current therapeutic approach," Oncologist 11(6), 612-623 (2006)
4. T. Ishikawa, "Is it relevant that intra-arterial chemotherapy may be effective for advanced pancreatic cancer?," World J Gastroenterol 13(32), 4306-4309 (2007)
5. X. Yu, Y. Zhang, C. Chen, Q. Yao and M. Li, "Targeted drug delivery in pancreatic cancer," Biochim. Biophys. Acta (2009)
6. F. Danhier, N. Lecouturier, B. Vroman, C. Jerome, J. Marchand-Brynaert, O. Feron and V. Preat, "Paclitaxel-loaded PEGylated PLGA-based nanoparticles: In vitro and in vivo evaluation," J Control Release 133(1), 11-17 (2009)
7. M. L. Immordino, P. Brusa, F. Rocco, S. Arpicco, M. Ceruti and L. Cattel, "Preparation, characterization, cytotoxicity and pharmacokinetics of liposomes containing lipophilic gemcitabine prodrugs," J Control Release 100(3), 331-346 (2004)
8. R. R. Patil, S. A. Guhagarkar and P. V. Devarajan, "Engineered nanocarriers of doxorubicin: A current update," Crit. Rev. Ther. Drug Carrier Syst. 25(1), 1-61 (2008)
9. G. Wu, A. Mikhailovsky, H. A. Khant, C. Fu, W. Chiu and J. A. Zasadzinski, "Remotely triggered liposome release by near-infrared light absorption via hollow gold nanoshells," J. Am. Chem. Soc. 130(26), 8175-8177 (2008)
10. J. You, G. Zhang and C. Li, "Exceptionally high payload of doxorubicin in hollow gold nanospheres for near-infrared light-triggered drug release," ACS Nano 4(2), 1033-1041 (2010)
11. Y. S. Chen, W. Frey, S. Kim, K. Homan, P. Kruizinga, K. Sokolov and S. Emelianov, "Enhanced thermal stability of silica-coated gold nanorods for photoacoustic imaging and image-guided therapy," Opt Express 18(9), 8867-8878 (2010)
12. Y. Kobayashi, H. Katakami, E. Mine, D. Nagao, M. Konno and L. M. Liz-Marzan, "Silica coating of silver nanoparticles using a modified Stober method," J. Colloid Interface Sci. 283(2), 392-396 (2005)

13. J. B. Jackson and N. J. Halas, "Silver nanoshells: Variations in morphologies and optical properties " J. Phys. Chem. B 105(14), 2743-2746 (2001)

14. R. Arvizo, R. Bhattacharya and P. Mukherjee, "Gold nanoparticles: Opportunities and challenges in nanomedicine," Expert Opin Drug Deliv 7(6), 753-763 (2010)

15. L. R. Hirsch, A. M. Gobin, A. R. Lowery, F. Tam, R. A. Drezek, N. J. Halas and J. L. West, "Metal nanoshells," Ann. Biomed. Eng. 34(1), 15-22 (2006)

16. T. Jennings and G. Strouse, "Past, present, and future of gold nanoparticles," Adv. Exp. Med. Biol. 620(34-47 (2007)

17. P. V. Asharani, M. P. Hande and S. Valiyaveettil, "Anti-proliferative activity of silver nanoparticles," BMC Cell Biol 10(65 (2009)

18. P. V. AshaRani, G. Low Kah Mun, M. P. Hande and S. Valiyaveettil, "Cytotoxicity and genotoxicity of silver nanoparticles in human cells," ACS Nano 3(2), 279-290 (2009)

19. C. R. Patra, R. Bhattacharya, E. Wang, A. Katarya, J. S. Lau, S. Dutta, M. Muders, S. Wang, S. A. Buhrow, S. L. Safgren, M. J. Yaszemski, J. M. Reid, M. M. Ames, P. Mukherjee and D. Mukhopadhyay, "Targeted delivery of gemcitabine to pancreatic adenocarcinoma using cetuximab as a targeting agent," Cancer Res. 68(6), 1970-1978 (2008)

# Bibliography


Aaron, J., N. Nitin, et al. (2007). "Plasmon resonance coupling of metal nanoparticles for molecular imaging of carcinogenesis in vivo." J Biomed Opt **12**(3): 034007.

Agarwal, B., E. Abu-Hamda, et al. (2004). "Endoscopic ultrasound-guided fine needle aspiration and multidetector spiral CT in the diagnosis of pancreatic cancer." Am J Gastroenterol **99**(5): 844-50.

Aherne, D., D. Ledwith, et al. (2008). "Optical properties and growth aspects of silver nanoprisms produced by a highly reproducible and rapid synthesis at room temperature." Advanced Functional Materials **18**(14): 2005-2016.

An, K. and T. Hyeon (2009). "Synthesis and biomedical applications of hollow nanostructures." Nano Today **4**(4): 359-373.

ANSI (2000). "Orlando: Laser Institute of America " American National Standard for Safe use of Lasers, ANSI Z136.1.

Arepally, A. (2008). "Targeted drug delivery under MRI guidance." J Magn Reson Imaging **27**(2): 292-8.

Arica, B. and A. Lamprecht (2005). "In vitro evaluation of betamethasone-loaded nanoparticles." Drug Dev Ind Pharm **31**(1): 19-24.

Arvizo, R., R. Bhattacharya, et al. (2010). "Gold nanoparticles: Opportunities and challenges in nanomedicine." Expert Opin Drug Deliv **7**(6): 753-63.

Asharani, P. V., M. P. Hande, et al. (2009). "Anti-proliferative activity of silver nanoparticles." BMC Cell Biol **10**: 65.

AshaRani, P. V., G. Low Kah Mun, et al. (2009). "Cytotoxicity and genotoxicity of silver nanoparticles in human cells." ACS Nano **3**(2): 279-290.

Astete, C. E. and C. M. Sabliov (2006). "Synthesis and characterization of PLGA nanoparticles." J Biomater Sci Polym Ed **17**(3): 247-89.

Atiyeh, B. S., M. Costagliola, et al. (2007). "Effect of silver on burn wound infection control and healing: Review of the literature." Burns **33**(2): 139-148.

Bala, I., S. Hariharan, et al. (2004). "PLGA nanoparticles in drug delivery: The state of the art." Crit Rev Ther Drug Carrier Syst **21**(5): 387-422.

Balasubramanian, S. K., J. Jittiwat, et al. (2010). "Biodistribution of gold nanoparticles and gene expression changes in the liver and spleen after intravenous administration in rats." Biomaterials **31**(8): 2034-42.

Barth, B. M., R. Sharma, et al. (2010). "Bioconjugation of calcium phosphosilicate composite nanoparticles for selective targeting of human breast and pancreatic cancers in vivo." ACS Nano **4**(3): 1279-87.

Beger, H. G., B. Rau, et al. (2003). "Treatment of pancreatic cancer: Challenge of the facts." World J Surg **27**(10): 1075-84.

Betancourt, T., B. Brown, et al. (2007). "Doxorubicin-loaded PLGA nanoparticles by nanoprecipitation: Preparation, characterization and in vitro evaluation." Nanomedicine **2**(2): 219-232.

Betancourt, T., B. Brown, et al. (2007). "Doxorubicin-loaded PLGA nanoparticles by nanoprecipitation: Preparation, characterization and in vitro evaluation." Nanomed **2**(2): 219-32.

Bhattacharya, R. and P. Mukherjee (2008). "Biological properties of "naked" metal nanoparticles." Adv Drug Deliv Rev **60**(11): 1289-306.

Bhattacharyya, S., R. Bhattacharya, et al. (2010). "Nanoconjugation modulates the trafficking and mechanism of antibody induced receptor endocytosis." Proc Natl Acad Sci U S A **107**(33): 14541-6.

Biju, V., T. Itoh, et al. (2008). "Semiconductor quantum dots and metal nanoparticles: Syntheses, optical properties, and biological applications." Anal Bioanal Chem **391**(7): 2469-95.

Birnbaum, D. T., J. D. Kosmala, et al. (2000). "Optimization of preparation techniques for poly(lactic acid-co-glycolic acid) nanoparticles." Journal of Nanoparticle Research **2**: 173-181.

Blanco, D. and M. Alonso (1998). "Protein encapsulation and release from poly (lactide-co-glycolide) microspheres: Effect of the protein and polymer properties and of the co-encapsulation of surfactants." European Journal of Pharmaceutics and Biopharmaceutics **45**(3): 285-294.

Bosetti, M., A. Masse, et al. (2002). "Silver coated materials for external fixation devices: in vitro biocompatibility and genotoxicity." Biomaterials **23**(3): 887-92.

Brannon-Peppas, L. (1995). "Recent advances on the use of biodegradable microparticles and nanoparticles in controlled drug delivery." International Journal of Pharmaceutics **116**(1): 1-9.

Brannon-Peppas, L. (1997). "Polymers in Controlled Drug Delivery." Medical Plastics and Biomaterials **4**: 34-44.

Brannon-Peppas, L. and D. T. Birnbaum (2000). "Process to scale-up the production of biodegradable nanoparticles." Abstract, American Institute of Chemical Engineers Meeting.

Brannon-Peppas, L. and J. O. Blanchette (2004). "Nanoparticle and targeted systems for cancer therapy." Adv Drug Deliv Rev **56**(11): 1649-59.

Brett, D. W. (2006). "A discussion of silver as an antimicrobial agent: Alleviating the confusion." Ostomy Wound Manage **52**(1): 34-41.

Bria, E., M. Milella, et al. (2007). "Gemcitabine-based combinations for inoperable pancreatic cancer: Have we made real progress?: A meta-analysis of 20 phase 3 trials." Cancer **110**(3): 525-33.

Brigger, I., C. Dubernet, et al. (2002). "Nanoparticles in cancer therapy and diagnosis." Adv Drug Deliv Rev **54**(5): 631-51.

Brusa, P., M. L. Immordino, et al. (2007). "Antitumor activity and pharmacokinetics of liposomes containing lipophilic gemcitabine prodrugs." Anticancer Res **27**(1A): 195-9.

Brussieux, J., A. Boisivon, et al. (1991). "Prevention of neonatal conjunctivitis. A comparative clinical and bacteriologic study of 2 eyedrops: Silver nitrate and oxytetracycline chlorhydrate." Ann Pediatr (Paris) **38**(9): 637-41.

Cai, S., S. Thati, et al. (2010). "Localized doxorubicin chemotherapy with a biopolymeric nanocarrier improves survival and reduces toxicity in xenografts of human breast cancer." J Control Release **146**(2): 212-8.

Cardenes, H. R., E. G. Chiorean, et al. (2006). "Locally advanced pancreatic cancer: Current therapeutic approach." Oncologist **11**(6): 612-23.

Cascante, A., D. Abate-Daga, et al. (2007). "GCV modulates the antitumoural efficacy of a replicative adenovirus expressing the TAT8-TK as a late gene in a pancreatic tumour model." Gene Ther **14**(20): 1471-80.

Chamberland, D., A. Agarwal, et al. (2008). "Photoacoustic tomography of joints aided by an Etanercept-conjugated gold nanoparticle contrast agent: An ex vivo preliminary rat study." Nanotechnology **19**: 095101.

Chasin, M. and R. S. Langer (1990). Biodegradable polymers as drug delivery systems. New York, Marcel Dekker.

Chen, R. F., Z. H. Li, et al. (2007). "In vivo Radioiodide Imaging and Treatment of Pancreatic Cancer Xenografts after MUC1 Promoter-Driven Expression of the Human Sodium-Iodide Symporter." Pancreatology **7**(5-6): 505-513.

Chen, X. and H. J. Schluesener (2008). "Nanosilver: A nanoproduct in medical application." Toxicol Lett **176**(1): 1-12.

Chen, Y.-S., P. P. Kruizinga, et al. (2010). "On stability of molecular therapeutic agents for noninvasive photoacoustic and ultrasound image-guided photothermal therapy." SPIE Photonics West **7654**: 7564-7571.

Chen, Y. S., W. Frey, et al. (2010). "Enhanced thermal stability of silica-coated gold nanorods for photoacoustic imaging and image-guided therapy." Opt Express **18**(9): 8867-78.

Cheng, X., F. Zhang, et al. (2009). "DNA/chitosan nanocomplex as a novel drug carrier for doxorubicin." Drug Deliv **16**(3): 135-44.

Cho, E. C., C. Kim, et al. (2009). "Measuring the optical absorption cross sections of Au-Ag nanocages and Au nanorods by photoacoustic imaging." J Phys Chem C Nanomater Interfaces **113**(21): 9023-9028.

Chu, C., Y. Wang, et al. (2010). "Surface deformation of gold nanorod-loaded poly (dl-lactide-co-glycolide) nanoparticles after near infrared irradiation: an active and controllable drug release system." Journal of Materials Chemistry **20**(16): 3260-3264.

Chua, Y. J. and D. Cunningham (2006). "Chemotherapy for advanced pancreatic cancer." Best Pract Res Clin Gastroenterol **20**(2): 327-48.

Clement, J. L. and P. S. Jarrett (1994). "Antibacterial silver." Metal-Based Drugs **1**: 467-482.

Cobley, C. M., L. Au, et al. (2010). "Targeting gold nanocages to cancer cells for photothermal destruction and drug delivery." Expert Opin Drug Deliv **7**(5): 577-87.

Collinge, C. A., G. Goll, et al. (1994). "Pin tract infections: Silver vs uncoated pins." Orthopedics **17**(5): 445-8.

Copland, J. A., M. Eghtedari, et al. (2004). "Bioconjugated gold nanoparticles as a molecular based contrast agent: Implications for imaging of deep tumors using optoacoustic tomography." Mol Imaging Biol **6**(5): 341-9.

Copland, J. A., M. Eghtedari, et al. (2004). "Bioconjugated gold nanoparticles as a molecular based contrast agent: implications for imaging of deep tumors using optoacoustic tomography." Molecular Imaging And Biology: MIB: The Official Publication Of The Academy Of Molecular Imaging **6**(5): 341-9.

DaCosta, R. S., L.Lilge, et al. (1997). " Confocal fluorescence microscopy/macroscopy and microspectrofluorimetry analysis of human colorectal tissues." J. Anal. Morphol. Cell Vision **4**: 24-29.

Danhier, F., N. Lecouturier, et al. (2009). "Paclitaxel-loaded PEGylated PLGA-based nanoparticles: In vitro and in vivo evaluation." J Control Release **133**(1): 11-7.

Darouiche, R. O. (1999). "Anti-infective efficacy of silver-coated medical prostheses." Clin Infect Dis **29**(6): 1371-7.

Darouiche, R. O. (2004). "Treatment of infections associated with surgical implants." N Engl J Med **350**(14): 1422-9.

Das, M., N. Sanson, et al. (2007). "Microgels loaded with gold nanorods: photothermally triggered volume transitions under physiological conditions." Langmuir **23**(1): 196-201.

Dax, S. L., J. J. McNally, et al. (1999). "Multi-component methodologies in solid-phase organic synthesis." Curr Med Chem **6**(3): 255-70.

De Angelis, C., A. Repici, et al. (2007). "Pancreatic cancer imaging: The new role of endoscopic ultrasound." Journal of the Pancreas **8**(1 Suppl): 85-97.

Decuzzi, P., R. Pasqualini, et al. (2009). "Intravascular delivery of particulate systems: Does geometry really matter?" Pharm Res **26**(1): 235-43.

Demers, L. M., M. Ostblom, et al. (2002). "Thermal desorption behavior and binding properties of DNA bases and nucleosides on gold." J Am Chem Soc **124**(38): 11248-9.

Diebold, G., M. Khan, et al. (1990). "Photoacoustic "signatures" of particulate matter: Optical production of acoustic monopole radiation." Science **250**(4977): 101.

Doiron, A. L., K. Chu, et al. (2008). "Preparation and initial characterization of biodegradable particles containing gadolinium-DTPA contrast agent for enhanced MRI." Proc Natl Acad Sci U S A **105**(45): 17232-7.

Doiron, A. L., K. A. Homan, et al. (2009). "Poly(Lactic-co-Glycolic) Acid as a Carrier for Imaging Contrast Agents." Pharm Res **26**(3): 674-82.

Dorwald, F. (2002). Organic synthesis on solid phase: Supports, linkers, reactions, Wiley-VCH Verlag GmbH.

Drake, P. L. and K. J. Hazelwood (2005). "Exposure-related health effects of silver and silver compounds: A review." Ann Occup Hyg **49**(7): 575-85.

Eck, W., G. Craig, et al. (2008). "PEGylated gold nanoparticles conjugated to monoclonal F19 antibodies as targeted labeling agents for human pancreatic carcinoma tissue." ACS Nano **2**(11): 2263-72.

Eghtedari, M., A. Oraevsky, et al. (2007). "High sensitivity of in vivo detection of gold nanorods using a laser optoacoustic imaging system." Nano Lett **7**(7): 1914-1918.

Eichmiller, F. (2001). "Research into non-mercury containing metallic alternatives." Operative Dentistry **6**: 111-118.

El-Sayed, I. H., X. Huang, et al. (2005). "Surface plasmon resonance scattering and absorption of anti-EGFR antibody conjugated gold nanoparticles in cancer diagnostics: Applications in oral cancer." Nano Lett **5**(5): 829-34.

El-Sayed, M. A. (2001). "Some interesting properties of metals confined in time and nanometer space of different shapes." Acc Chem Res **34**(4): 257-64.

Elechiguerra, J. L., J. L. Burt, et al. (2005). "Interaction of silver nanoparticles with HIV-1." J Nanobiotechnology **3**: 6.

Emelianov, S. Y., S. R. Aglyamov, et al. (2004). "Combined ultrasound, optoacoustic, and elasticity imaging." Proceedings of the SPIE Photonics West **5320**: 101-112.

Farrell, J. J., N. Senzer, et al. (2006). "Long-Term data for endoscopic ultrasound (EUS) and percutanous (PTA) guided intratumoral TNFerade gene delivery combined with chemoradiation in the treatment of locally advanced pancreatic cancer (LAPC)." Gastrointestinal Endoscopy **63**(5): AB93.

Feng, S. S., L. Mu, et al. (2004). "Nanoparticles of biodegradable polymers for clinical administration of paclitaxel." Curr Med Chem **11**(4): 413-24.

Fogar, P., F. Navaglia, et al. (2007). "Suicide gene therapy with the yeast fusion gene cytosine deaminase/uracil phosphoribosyltransferase is not enough for pancreatic cancer." Pancreas **35**(3): 224-31.

Folkman, J. (1990). "What is the evidence that tumors are angiogenesis dependent?" J. Natl. Cancer Inst. **82**(1): 4-6.

Fox, C. L., Jr. and S. M. Modak (1974). "Mechanism of silver sulfadiazine action on burn wound infections." Antimicrob Agents Chemother **5**(6): 582-8.

Frutos, A., J. Brockman, et al. (2000). "Reversible protection and reactive patterning of amine-and hydroxyl-terminated self-assembled monolayers on gold surfaces for the fabrication of biopolymer arrays." Langmuir **16**(5): 2192-2197.

Fung, L. C., A. E. Khoury, et al. (1996). "Biocompatibility of silver-coated peritoneal dialysis catheter in a porcine model." Perit Dial Int **16**(4): 398-405.

Furno, F., K. S. Morley, et al. (2004). "Silver nanoparticles and polymeric medical devices: A new approach to prevention of infection?" J Antimicrob Chemother **54**(6): 1019-24.

Gobin, A. M., M. H. Lee, et al. (2007). "Near-infrared resonant nanoshells for combined optical imaging and photothermal cancer therapy." Nano Lett **7**(7): 1929-34.

Gosheger, G., J. Hardes, et al. (2004). "Silver-coated megaendoprostheses in a rabbit model--an analysis of the infection rate and toxicological side effects." Biomaterials **25**(24): 5547-56.

Gref, R., A. Domb, et al. (1995). "The controlled intravenous delivery of drugs using PEG-coated sterically stabilized nanospheres." Long-circulating Drug Delivery Systems **16**(2-3): 215-233.

Gress, F. G., R. H. Hawes, et al. (1999). "Role of EUS in the preoperative staging of pancreatic cancer: A large single-center experience." Gastrointest Endosc **50**(6): 786-91.

Gupta, A. and S. Silver (1998). "Silver as a biocide: will resistance become a problem?" Nat Biotechnol **16**(10): 888.

Hancock, H., M. R. Dreher, et al. (2009). "Evaluation of pulsed high intensity focused ultrasound exposures on metastasis in a murine model." Clin Exp Metastasis **26**(7): 729-38.

Hao, E., G. C. Schatz, et al. (2004). "Synthesis and optical properties of anisotropic metal nanoparticles." J Fluoresc **14**(4): 331-41.

Hermanson, G. T. (1996). Bioconjugate techniques. San Diego, Academic Press.

Hill, J. (2004). Colloidal silver: a literature review: medical uses, toxicology & manufacture, Clear Springs Press, LLC.

Hippocrates (1994-2000). On Ulcers, 400 B.C.E.; Translated by Francis Adams, ©.

Hirsch, L. R., A. M. Gobin, et al. (2006). "Metal nanoshells." Ann Biomed Eng **34**(1): 15-22.

Hirsch, L. R., R. J. Stafford, et al. (2003). "Nanoshell-mediated near-infrared thermal therapy of tumors under magnetic resonance guidance." Proc Natl Acad Sci U S A **100**(23): 13549-54.

Hobbs, S. K., W. L. Monsky, et al. (1998). "Regulation of transport pathways in tumor vessels: role of tumor type and microenvironment." Proceedings Of The National Academy Of Sciences Of The United States Of America **95**(8): 4607-12.

Homan, K., S. Emelianov, et al. (2008). Compositions for Therapy and Imaging of Cancer and Associated Methods. US; WPO, University of Texas at Austin.

Homan, K., S. Gomez, et al. (2009). "Design and development of multifunctional contrast agents for photoacoustic imaging." Reporters, Markers, Dyes, Nanoparticles, and Molecular Probes for Biomedical Applications: Proceedings of the SPIE **7190**: 71900I-71900I.

Homan, K., S. Kim, et al. (2010). "Prospects of molecular photoacoustic imaging at 1064 nm wavelength." Opt Lett **35**(15): 2663-5.

Homan, K., S. Mallidi, et al. (2010). Combined photoacoustic and ultrasound imaging of metal nanoparticles in vivo. Nanoimaging. B. Goins and W. Phillips. Singapore, Pan Stanford Publishing. **3**.

Homan, K., J. Shah, et al. (2010). "Silver nanosystems for photoacoustic imaging and image-guided therapy." Journal of Biomedical Optics **15**(2): 021316.

Hong, R.-L., C.-J. Huang, et al. (1999). "Direct comparison of liposomal doxorubicin with or without polyethylene glycol coating in C-26 tumor-bearing mice: Is surface coating with polyethylene glycol beneficial?" Clin Cancer Res **5**(11): 3645-3652.

Huang, X., I. H. El-Sayed, et al. (2006). "Cancer cell imaging and photothermal therapy in the near-infrared region by using gold nanorods." Journal Of The American Chemical Society **128**(6): 2115-20.

Huang, X., S. Neretina, et al. (2009). "Gold nanorods: From synthesis and properties to biological and biomedical applications." Advanced Materials **21**(48): 4880-4910.

Huang, Y. F., K. Sefah, et al. (2008). "Selective photothermal therapy for mixed cancer cells using aptamer-conjugated nanorods." Langmuir **24**(20): 11860-5.

Immordino, M. L., P. Brusa, et al. (2004). "Preparation, characterization, cytotoxicity and pharmacokinetics of liposomes containing lipophilic gemcitabine prodrugs." J Control Release **100**(3): 331-46.

Ip, M., S. L. Lui, et al. (2006). "Antimicrobial activities of silver dressings: An in vitro comparison." Journal of Medical Microbiology **55**: 59-63.

Isab, A. A. and M. I. Wazeer (2006). "Synthesis and characterization of thiolate-Ag(I) complexes by solid-state and solution NMR and their antimicrobial activity." Spectrochim Acta A Mol Biomol Spectrosc.

Ishikawa, T. (2007). "Is it relevant that intra-arterial chemotherapy may be effective for advanced pancreatic cancer?" World J Gastroenterol **13**(32): 4306-9.

Jackson, J. B. and N. J. Halas (2001). "Silver nanoshells: Variations in morphologies and optical properties " J. Phys. Chem. B **105**(14): 2743-2746.

Jain, P. K. and M. A. El-Sayed (2007). "Universal scaling of plasmon coupling in metal nanostructures: Extension from particle pairs to nanoshells." Nano Lett **7**(9): 2854-8.

Jain, P. K., K. S. Lee, et al. (2006). "Calculated absorption and scattering properties of gold nanoparticles of different size, shape, and composition: Applications in biological imaging and biomedicine." J Phys Chem B **110**(14): 7238-48.

Jain, R. A. (2000). "The manufacturing techniques of various drug loaded biodegradable poly(lactide-co-glycolide) (PLGA) devices." Biomaterials **21**(23): 2475-90.

Jain, R. K. (1999). "Transport of molecules, particles, and cells in solid tumors." Annu Rev Biomed Eng **1**: 241-263.

Jemal, A., L. X. Clegg, et al. (2004). "Annual report to the nation on the status of cancer, 1975-2001, with a special feature regarding survival." Cancer **101**(1): 3-27.

Jennings, T. and G. Strouse (2007). "Past, present, and future of gold nanoparticles." Adv Exp Med Biol **620**: 34-47.

Jiang, W., B. Y. Kim, et al. (2008). "Nanoparticle-mediated cellular response is size-dependent." Nat Nanotechnol **3**(3): 145-50.

Jiang, X. C., C. Y. Chen, et al. (2009). "Role of citric acid in the formation of silver nanoplates through a synergistic reduction approach." Langmuir.

Jiang, Z.-j. and C.-y. Liu (2003). "Seed-mediated growth technique for the preparation of a silver nanoshell on a silica sphere." J. Phys. Chem. B **107**: 12411-12415.

Johnston, M. J., K. Edwards, et al. (2008). "Influence of drug-to-lipid ratio on drug release properties and liposome integrity in liposomal doxorubicin formulations." J Liposome Res **18**(2): 145-57.

Kataoka, M. and Y. Hayakawa (1999). "A convenient method for the synthesis of N-free 5-O-(p, p-Dimethoxytrityl)-2-deoxyribonucleosides via the 5-O-Selective tritylation of the parent substances." J. Org. Chem **64**(16): 6087-6089.

Key, F. "A brief history of the health support uses of silver." from http://www.silver-colloids.com/Pubs/history-silver.html.

Kinsler, L. E., A. R. Frey, et al. (2000). Fundamentals of Acoustics. New York, John Wiley and Sons, Inc.

Klasen, H. J. (2000). "A historical review of the use of silver in the treatment of burns. II. Renewed interest for silver." Burns **26**(2): 131-8.

Klasen, H. J. (2000). "Historical review of the use of silver in the treatment of burns. I. Early uses." Burns **26**(2): 117-30.

Kobayashi, Y., H. Katakami, et al. (2005). "Silica coating of silver nanoparticles using a modified Stober method." J Colloid Interface Sci **283**(2): 392-6.

Konerding, M. A., A. J. Miodonski, et al. (1995). "Microvascular corrosion casting in the study of tumor vascularity: A review." Scanning Microscopy **9**(4): 1233-44.

Kong, G., R. D. Braun, et al. (2000). "Hyperthermia enables tumor-specific nanoparticle delivery: Effect of particle size." Cancer Research **60**(16): 4440-5.

Kraft, C. N., M. Hansis, et al. (2000). "Striated muscle microvascular response to silver implants: A comparative in vivo study with titanium and stainless steel." J Biomed Mater Res **49**(2): 192-9.

Kruger, R. A. (1994). "Photoacoustic ultrasound." Med Phys **21**(1): 127-31.

Kruger, R. A. and P. Liu (1994). "Photoacoustic ultrasound: Pulse production and detection of 0.5% Liposyn." Med Phys **21**(7): 1179-84.

Kruger, R. A., P. Liu, et al. (1995). "Photoacoustic ultrasound (PAUS) reconstruction tomography." Med Phys **22**(10): 1605-9.

Ku, G., X. Wang, et al. (2005). "Imaging of tumor angiogenesis in rat brains in vivo by photoacoustic tomography." Appl Opt **44**(5): 770-5.

Kumar, S., J. Aaron, et al. (2008). "Directional conjugation of antibodies to nanoparticles for synthesis of multiplexed optical contrast agents with both delivery and targeting moieties." Nat Protoc **3**(2): 314-20.

Kumar, S., N. Harrison, et al. (2007). "Plasmonic nanosensors for imaging intracellular biomarkers in live cells." Nano Lett **7**(5): 1338-43.

Kwon, R. S. and J. M. Scheiman (2006). "New advances in pancreatic imaging." Curr Opin Gastroenterol **22**(5): 512-9.

Lansdown, A. B. (2007). "Critical observations on the neurotoxicity of silver." Crit Rev Toxicol **37**(3): 237-50.

Larina, I. V., B. M. Evers, et al. (2005). "Enhancement of Drug Delivery in Tumors by Using Interaction of Nanoparticles with Ultrasound Radiation." Technology in Cancer Research and Treatment **4**(2): 217-226.

Larina, I. V., B. M. Evers, et al. (2005). "Optimal drug and gene delivery in cancer cells by ultrasound-induced cavitation." Anticancer Res **25**(1A): 149-56.

Lassalle, V. and M. Ferreira (2007). "PLA nano and microparticles for drug delivery: An overview of the methods of preparation." Macromolecular Bioscience **7**(6): 767-783.

Levin, C. S., S. W. Bishnoi, et al. (2006). "Determining the conformation of thiolated poly(ethylene glycol) on Au nanoshells by surface-enhanced Raman scattering spectroscopic assay." Anal Chem **78**(10): 3277-81.

Li, M. L., J. C. Wang, et al. (2009). "In-vivo photoacoustic microscopy of nanoshell extravasation from solid tumor vasculature." J Biomed Opt **14**(1): 010507.

Li, P., C. Wang, et al. (2008). "In vivo photoacoustic molecular imaging with simultaneous multiple selective targeting using antibody-conjugated gold nanorods." Optics Express **16**(23): 18605-18615.

Liao, H., C. Nehl, et al. (2006). "Biomedical applications of plasmon resonant metal nanoparticles." Nanomedicine **1**(2): 201-208.

Link, S. and M. El-Sayed (1999). "Spectral properties and relaxation dynamics of surface plasmon electronic oscillations in gold and silver nanodots and nanorods." Journal of Physical Chemistry B **103**(40): 8410-8426.

Lisiecki, I. (2005). "Size, shape, and structural control of metallic nanocrystals." J Phys Chem B **109**(25): 12231-44.

Liu, Z., H. Song, et al. (2005). "Fabrication and near-infrared photothermal conversion characteristics of Au nanoshells." Applied Physics Letters **86**: 113109.

Loo, C., A. Lin, et al. (2004). "Nanoshell-enabled photonics-based imaging and therapy of cancer." Technology In Cancer Research & Treatment **3**(1): 33-40.

Loo, C., A. Lin, et al. (2004). "Nanoshell-enabled photonics-based imaging and therapy of cancer." Technol Cancer Res Treat **3**(1): 33-40.

Lu, D., X. Wen, et al. (2009). "A pH-sensitive nano drug delivery system derived from pullulan/doxorubicin conjugate." J Biomed Mater Res B Appl Biomater **89**(1): 177-83.

Lu, Y., G. L. Liu, et al. (2005). "Nanophotonic crescent moon structures with sharp edge for ultrasensitive biomolecular detection by local electromagnetic field enhancement effect." Nano Lett **5**(1): 119-24.

Mahmud, A., X. B. Xiong, et al. (2008). "Development of novel polymeric micellar drug conjugates and nano-containers with hydrolyzable core structure for doxorubicin delivery." Eur J Pharm Biopharm **69**(3): 923-34.

Mallidi, S., T. Larson, et al. (2007). "Molecular specific photoacoustic imaging with plasmonic nanoparticles." Optics Express **15**(11): 6583-6588.

Mallidi, S., T. Larson, et al. (2009). "Multiwavelength photoacoustic imaging and plasmon resonance coupling of gold nanoparticles for selective detection of cancer." Nano Lett **9**(8): 2825-2831.

Mancuso, A., F. Calabro, et al. (2006). "Current therapies and advances in the treatment of pancreatic cancer." Crit Rev Oncol Hematol **58**(3): 231-41.

Matzler, C. (2002). "MATLAB Functions for Mie Scattering and Absorption." from www.iap.unibe.ch/publications/download/199/en/.

Metraux, C. and C. Mirkin (2005). "Rapid thermal synthesis of silver nanoprisms with chemically tailorable thickness." Advanced Materials **17**(4): 412-415.

Michl, P., C. Barth, et al. (2003). "Claudin-4 expression decreases invasiveness and metastatic potential of pancreatic cancer." Cancer Res **63**(19): 6265-71.

Michl, P., S. Pauls, et al. (2006). "Evidence-based diagnosis and staging of pancreatic cancer." Best Pract Res Clin Gastroenterol **20**(2): 227-51.

Mueller, H. J. (2001). "In vitro tarnish and corrosion of a consolidated silver material for direct filling applications." Dent Mater **17**(1): 60-70.

Mundargi, R. C., V. R. Babu, et al. (2008). "Nano/micro technologies for delivering macromolecular therapeutics using poly(D,L-lactide-co-glycolide) and its derivatives." J Control Release **125**(3): 193-209.

Murphy, C. J., T. K. Sau, et al. (2005). "Anisotropic metal nanoparticles: Synthesis, assembly, and optical applications." J Phys Chem B **109**(29): 13857-70.

Myhren, F., B. Brretzen, et al. (2002). Gemcitabine derivatives US, Norsk Hydro ASA. **US6384019**.

Nau, W. H., R. J. Roselli, et al. (1999). "Measurement of thermal effects on the optical properties of prostate tissue at wavelengths of 1,064 and 633 nm." Lasers in Surgery and Medicine **24**(1): 38-47.

NCI. (2010). "Surveillance Epidemiology and End Results." SEER Stat Fact Sheets, from http://seer.cancer.gov/statfacts/html/pancreas.html.

Nel, A. E., L. Madler, et al. (2009). "Understanding biophysicochemical interactions at the nano-bio interface." Nat Mater **8**(7): 543-57.

Nelson, N. J. (2007). "Pancreatic Cancer Research Matures." J Natl Cancer Inst.

Nichols, L. S., R. Ashfaq, et al. (2004). "Claudin 4 protein expression in primary and metastatic pancreatic cancer: support for use as a therapeutic target." Am J Clin Pathol **121**(2): 226-30.

Nie, S., Y. Xing, et al. (2007). "Nanotechnology applications in cancer." Annu Rev Biomed Eng **9**: 257-88.

Nikoobakht, B. and M. El-Sayed (2003). "Preparation and growth mechanism of gold nanorods (NRs) using seed-mediated growth method." Chemistry of Materials **15**(10): 1957-1962.

O'Neal, D. P., L. R. Hirsch, et al. (2004). "Photo-thermal tumor ablation in mice using near infrared-absorbing nanoparticles." Cancer Lett **209**(2): 171-6.

Oraevsky, A., R. Esenaliev, et al. (1995). Lateral and z-axial resolution in laser optoacoustic imaging with ultrasonic transducers. Proc. SPIE.

Oraevsky, A., S. Jacques, et al. (1994). Time-Resolved Optoacoustic Imaging in Layered Biological Tissues. Advances in Optical Imaging and Photon Migration. R. R. Alfano. New York, Academic Press. **21:** 161-165.

Oraevsky, A., S. Jacques, et al. (1993). Determination of tissue optical properties by time-resolved detection of laser-induced stress waves. Proc. SPIE.

Oraevsky, A., A. Karabutov, et al. (2001). Enhancement of optoacoustic tissue contrast with absorbing nanoparticles. European Conference on Biomedical Optics, Proc. SPIE, SPIE, San Jose, CA, USA, Proc of SPIE.

Oraevsky, A. A. (2009). Gold and silver nanoparticles as contrast agents for optoacoustic imaging. Photoacoustic Imaging and Spectroscopy. L. V. Wang. New York, Taylor and Francis Group.

Oraevsky, A. A., S. L. Jacques, et al. (1997). "Measurement of tissue optical properties by time-resolved detection of laser-induced transient stress." Appl Opt **36**(1): 402-15.

Oraevsky, A. A., S. L. Jacques, et al. (1997). " Measurement of tissue optical properties by time-resolved detection of laser-induced transient stress." Appl. Optics **36**(1): 402-415.

Oraevsky, A. A. and A. A. Karabutov (2003). Optoacoustic Tomography, CRC Press.

Ovington, L. G. (1999). "The value of silver in wound management." Podiatry Today **12**: 59-62.

Owens, D. E., 3rd and N. A. Peppas (2006). "Opsonization, biodistribution, and pharmacokinetics of polymeric nanoparticles." Int J Pharm **307**(1): 93-102.

Panyam, J. and V. Labhasetwar (2003). "Biodegradable nanoparticles for drug and gene delivery to cells and tissue." Advanced Drug Delivery Reviews **55**(3): 329-347.

Panyam, J., W. Z. Zhou, et al. (2002). "Rapid endo-lysosomal escape of poly(DL-lactide-co-glycolide) nanoparticles: Implications for drug and gene delivery." FASEB J **16**(10): 1217-26.

Park, S. and H. S. Yoo (2009). "In vivo and in vitro anti-cancer activities and enhanced cellular uptakes of EGF fragment decorated doxorubicin nano-aggregates." Int J Pharm **383**(1-2): 178-85.

Patel, C. K. N. and A. C. Tam (1981). "Pulsed optoacoustic spectroscopy of condensed matter." Reviews of Modern Physics **53**(3): 517-550.

Patil, R. R., S. A. Guhagarkar, et al. (2008). "Engineered nanocarriers of doxorubicin: A current update." Crit Rev Ther Drug Carrier Syst **25**(1): 1-61.

Patra, C. R., R. Bhattacharya, et al. (2008). "Targeted delivery of gemcitabine to pancreatic adenocarcinoma using cetuximab as a targeting agent." Cancer Res **68**(6): 1970-8.

Pausawasdi, N. and J. Scheiman (2007). "Endoscopic evaluation and palliation of pancreatic adenocarcinoma: Current and future options." Curr Opin Gastroenterol **23**(5): 515-21.

Peterson, M. S., J. Bouwman, et al. (2007). "Inorganic metallodielectric materials fabricated using two single-step methods based on the Tollen's process." J Colloid Interface Sci **306**(1): 41-9.

Pietrobon, B., M. McEachran, et al. (2009). "Synthesis of size-controlled faceted pentagonal silver nanorods with tunable plasmonic properties and self-assembly of these nanorods." ACS Nano **3**(1): 21-6.

Pitsillides, C. M., E. K. Joe, et al. (2003). "Selective cell targeting with light-absorbing microparticles and nanoparticles." Biophys J **84**(6): 4023-32.

Prokopowicz, M., J. Lukasiak, et al. (2004). "Utilization of a sol-gel method for encapsulation of doxorubicin." J Biomater Sci Polym Ed **15**(3): 343-56.

Qian, J., K. T. Yong, et al. (2007). "Imaging pancreatic cancer using surface-functionalized quantum dots." J Phys Chem B **111**(25): 6969-72.

Reni, M. and S. Cereda (2007). "New therapies for pancreatic cancer: Current standard." Journal of the Pancreas **8**(1 Suppl): 98-101.

Rentz, E. "Historic perspectives on clinical use and efficacy of silver." from http://lifesilver.com/history.htm.

Rhim, J. W., S. I. Hong, et al. (2006). "Preparation and characterization of chitosan-based nanocomposite films with antimicrobial activity." J Agric Food Chem **54**(16): 5814-22.

Rosenman, K. D., A. Moss, et al. (1979). "Argyria: Clinical implications of exposure to silver nitrate and silver oxide." J Occup Med **21**(6): 430-5.

Rowland, A. and J. Holcombe (2009). "Evaluation and correction of isotope ratio inaccuracy on inductively coupled plasma time-of-flight mass spectrometry." Spectrochimica Acta Part B: Atomic Spectroscopy **64**(1): 35-41.

Rubin, M. A., M. Buyyounouski, et al. (1999). "Microvessel density in prostate cancer: lack of correlation with tumor grade, pathologic stage, and clinical outcome." J.Urology **53**(3): 542-547.

Saif, M. W. (2007). "Controversies in the adjuvant treatment of pancreatic adenocarcinoma." Journal of the Pancreas **8**(5): 545-52.

Sakamoto, M., M. Fujistuka, et al. (2009). "Light as a construction tool of metal nanoparticles: Synthesis and mechanism." Journal of Photochemistry & Photobiology, C: Photochemistry Reviews **10**(1): 33-56.

SAMSUNG. (2006). "SAMSUNG Laundry Featuring SilverCare™ Technology." from http://www.samsung.com/PressCenter/PressRelease/PressRelease.asp?seq=20060213_0000233684.

Schierholz, J. M., L. J. Lucas, et al. (1998). "Efficacy of silver-coated medical devices." J Hosp Infect **40**(4): 257-62.

Seipelt, R. G., J. F. Vazquez-Jimenez, et al. (2001). "The St. Jude "Silzone" valve: Midterm results in treatment of active endocarditis." Ann Thorac Surg **72**(3): 758-62; discussion 762-3.

Sethuraman, S., S. R. Aglyamov, et al. (2008). "Remote temperature estimation in intravascular photoacoustic imaging." Ultrasound Med Biol **34**(2): 299-308.

Shah, J., S. R. Aglyamov, et al. (2006). Ultrasound-based Thermal and Elasticity Imaging to Assist Photothermal Cancer Therapy - Preliminary Study. Proceeding of the 2006 IEEE Ultrasonics Symposium.

Shah, J., S. R. Aglyamov, et al. (2008). "Ultrasound imaging to monitor photothermal therapy - feasibility study." Opt Express **16**(6): 3776-85.

Shah, J., S. Park, et al. (2008). "Photoacoustic imaging and temperature measurement for photothermal cancer therapy." J Biomed Opt **13**(3): 034024.

Sherry, L. J., R. Jin, et al. (2006). "Localized surface plasmon resonance spectroscopy of single silver triangular nanoprisms." Nano Lett **6**(9): 2060-5.

Shive, M. S. and J. M. Anderson (1997). "Biodegradation and biocompatibility of PLA and PLGA microspheres." Adv Drug Deliv Rev **28**(1): 5-24.

Silva, G., P. Ducheyne, et al. (2007). "Materials in particulate form for tissue engineering. 1. Basic concepts." Journal of Tissue Engineering and Regenerative Medicine **1**(1): 4-24.

Silver, S. (2003). "Bacterial silver resistance: molecular biology and uses and misuses of silver compounds." FEMS Microbiol Rev **27**(2-3): 341-53.

Silver, S., T. Phung le, et al. (2006). "Silver as biocides in burn and wound dressings and bacterial resistance to silver compounds." J Ind Microbiol Biotechnol **33**(7): 627-34.

Simon, B. and H. Printz (2001). "Epidemiological trends in pancreatic neoplasias." Dig Dis **19**(1): 6-14.

Skrabalak, S. E., L. Au, et al. (2007). "Facile synthesis of Ag nanocubes and Au nanocages." Nat Protoc **2**(9): 2182-90.

Skrabalak, S. E., J. Chen, et al. (2008). "Gold nanocages: Synthesis, properties, and applications." Acc Chem Res **41**(12): 1587-95.

Sokolov, K., J. Aaron, et al. (2003). "Optical systems for in vivo molecular imaging of cancer." Technol Cancer Res Treat **2**(6): 491-504.

Sokolov, K., M. Follen, et al. (2003). "Real-time vital optical imaging of precancer using anti-epidermal growth factor receptor antibodies conjugated to gold nanoparticles." Cancer Res **63**(9): 1999-2004.

Son, Y. J., J. S. Jang, et al. (2003). "Biodistribution and anti-tumor efficacy of doxorubicin loaded glycol-chitosan nanoaggregates by EPR effect." J Control Release **91**(1-2): 135-45.

Steger, M., C. Hubschwerlen, et al. (2001). "Solid-and solution-Phase synthesis of highly-Substituted-Pyrrolidine libraries." Bioorganic & Medicinal Chemistry Letters **11**(18): 2537-2540.

Sun, R. W., R. Chen, et al. (2005). "Silver nanoparticles fabricated in Hepes buffer exhibit cytoprotective activities toward HIV-1 infected cells." Chem Commun (Camb)(40): 5059-61.

Taille, A. E. d. l., E. Katz, et al. (2000). "Microvessel density as a predictor of PSA recurrence after radical prostatectomy. A comparison of CD34 and CD31." Am. J. Clin. Pathol. **113**(4): 555-562.

Tamm, E. and C. Charnsangavej (2001). "Pancreatic cancer: Current concepts in imaging for diagnosis and staging." Cancer J **7**(4): 298-311.

Tang, N., G. Du, et al. (2007). "Improving penetration in tumors with nanoassemblies of phospholipids and doxorubicin." J Natl Cancer Inst **99**(13): 1004-15.

Thompson, L. and J. Ellman (1994). "Straightforward and general method for coupling alcohols to solid supports." Tetrahedron Letters **35**(50): 9333-9336.

Tong, R., L. Tang, et al. (2009). "Controlled formulation of doxorubicin-polylactide nanoconjugates for cancer drug delivery." Conf Proc IEEE Eng Med Biol Soc **2009**: 2400-2.

Ulanet, D. B., D. L. Ludwig, et al. (2010). "Insulin receptor functionally enhances multistage tumor progression and conveys intrinsic resistance to IGF-1R targeted therapy." Proc Natl Acad Sci U S A **107**(24): 10791-8.

Valinas, R., A. Barrier, et al. (2002). "18 F-fluorodeoxyglucose positron emission tomography for characterization and initial staging of pancreatic tumors." Gastroenterol Clin Biol **26**(10): 888-92.

Varadhachary, G. R., E. P. Tamm, et al. (2006). "Borderline resectable pancreatic cancer: Definitions, management, and role of preoperative therapy." Ann Surg Oncol **13**(8): 1035-46.

Vasir, J. K. and V. Labhasetwar (2007). "Biodegradable nanoparticles for cytosolic delivery of therapeutics." Adv Drug Deliv Rev **59**(8): 718-28.

Vert, M., S. Li, et al. (1995). "Recent advances in the field of lactic acid/glycolic acid polymer-based therapeutic systems." Macromol Symp **98**: 633.

von Maltzahn, G., J. H. Park, et al. (2009). "Computationally guided photothermal tumor therapy using long-circulating gold nanorod antennas." Cancer Res **69**(9): 3892-900.

Walker, M., C. A. Cochrane, et al. (2006). "Silver deposition and tissue staining associated with wound dressings containing silver." Ostomy Wound Manage **52**(1): 42-4, 46-50.

Wang, X., Y. Xu, et al. (2002). "Photoacoustic tomography of biological tissues with high cross-section resolution: Reconstruction and experiment." Med Phys **29**(12): 2799-805.

Wang, X., L. Yang, et al. (2008). "Application of nanotechnology in cancer therapy and imaging." CA Cancer J Clin **58**(2): 97-110.

Weissleder, R. (2001). "A clearer vision for in vivo imaging." Nat Biotechnol **19**(4): 316-7.

West, J. and N. Halas (2003). "Engineered nanomaterials for biophotonics applications: improving sensing, imaging, and therapeutics." Annual Review of Biomedical Engineering **5**: 285-292.

Wiley, B., Y. Sun, et al. (2007). "Synthesis of silver nanostructures with controlled shapes and properties." Acc Chem Res **40**(10): 1067-76.

Wilson, K., K. Homan, et al. (2010). "Synthesis of a dual contrast agent for ultrasound and photoacoustic imaging." Reporters, Markers, Dyes, Nanoparticles, and Molecular Probes for Biomedical Applications II Proc. SPIE **7576**: 75760M.

Wray, M. Cope, et al. (1988). "Characterization of the near infrared absorption spectra of cytochrome aa3 and hemoglobin for the non-invasive monitoring of cerebral oxygenation." Biochim. et Biophys. Acta **933**: 184-192.

Wu, G., A. Mikhailovsky, et al. (2008). "Remotely triggered liposome release by near-infrared light absorption via hollow gold nanoshells." Journal of the American Chemical Society **130**(26): 8175-7.

Wu, G., A. Mikhailovsky, et al. (2008). "Remotely triggered liposome release by near-infrared light absorption via hollow gold nanoshells." J Am Chem Soc **130**(26): 8175-7.

Xia, Y., Y. Xiong, et al. (2009). "Shape-controlled synthesis of metal nanocrystals: Simple chemistry meets complex physics?" Angew Chem Int Ed Engl **48**(1): 60-103.

Xie, X., W. Xia, et al. (2007). "Targeted expression of BikDD eradicates pancreatic tumors in noninvasive imaging models." Cancer Cell **12**(1): 52-65.

Xiong, H. Q., K. Carr, et al. (2006). "Cytotoxic chemotherapy for pancreatic cancer: Advances to date and future directions." Drugs **66**(8): 1059-72.

Xu, D. H., J. Q. Gao, et al. (2008). "Liposome-based intracellular kinetics of doxorubicin in K562/DOX cells." Pharmazie **63**(9): 646-9.

Xu, M. and L. V. Wang (2006). "Photoacoustic imaging in biomedicine." Review of Scientific Instruments **77**: 041101.

Xu, R., J. Ma, et al. (2009). "Ag nanoparticles sensitize IR-induced killing of cancer cells." Cell Res **19**(8): 1031-4.

Xue, C., G. S. Metraux, et al. (2008). "Mechanistic study of photomediated triangular silver nanoprism growth." J Am Chem Soc **130**(26): 8337-44.

Xue, C. and C. A. Mirkin (2007). "pH-switchable silver nanoprism growth pathways." Angew Chem Int Ed Engl **46**(12): 2036-8.

Yang, X., S. Skrabalak, et al. (2007). "Photoacoustic tomography of a rat cerebral cortex in vivo with Au nanocages as an optical contrast agent." Nano Lett **7**(12): 3798-3802.

Yokoe, J., S. Sakuragi, et al. (2008). "Albumin-conjugated PEG liposome enhances tumor distribution of liposomal doxorubicin in rats." Int J Pharm **353**(1-2): 28-34.

Yong, K. T., Y. Sahoo, et al. (2006). "Synthesis and plasmonic properties of silver and gold nanoshells on polystyrene cores of different size and of gold–silver core–shell nanostructures." Colloids and Surfaces A: Physicochemical and Engineering Aspects **290**(1-3): 89-105.

Yoo, H. S., K. H. Lee, et al. (2000). "In vitro and in vivo anti-tumor activities of nanoparticles based on doxorubicin-PLGA conjugates." J Control Release **68**(3): 419-31.

Yoshida, T., T. Kondo, et al. (2007). "Combination of doxorubicin and low-intensity ultrasound causes a synergistic enhancement in cell killing and an additive enhancement in apoptosis induction in human lymphoma U937 cells." Cancer Chemother Pharmacol.

You, J., G. Zhang, et al. (2010). "Exceptionally high payload of doxorubicin in hollow gold nanospheres for near-infrared light-triggered drug release." ACS Nano **4**(2): 1033-41.

Youtie, J., P. Shapira, et al. (2008). "Nanotechnology publications and citations by leading countries and blocs." Journal of Nanoparticle Research **10**(6): 981-986.

Yu, J. J., H. A. Lee, et al. (2007). "Bio-distribution and anti-tumor efficacy of PEG/PLA nano particles loaded doxorubicin." J Drug Target **15**(4): 279-84.

Yu, X., Y. Zhang, et al. (2009). "Targeted drug delivery in pancreatic cancer." Biochim Biophys Acta.

Zhou, S., X. Liao, et al. (2003). "Poly-D,L-lactide-co-poly(ethylene glycol) microspheres as potential vaccine delivery systems." J Control Release **86**(2-3): 195-205.

Zhu, M., G. Qian, et al. (2006). "Plasma resonance of silver nanoparticles deposited on the surface of submicron silica spheres." Materials Chemistry and Physics **96**: 489-493.

Zou, X., E. Ying, et al. (2007). "An approach for synthesizing nanometer-to micrometer-sized silver nanoplates." Colloids and Surfaces A: Physicochemical and Engineering Aspects **303**(3): 226-234.